ILMATIETEEN LAITOS
METEOROLOGISKA INSTITUTET
FINNISH METEOROLOGICAL INSTITUTE

165
CONTRIBUTIONS

DIAGNOSTIC STUDIES OF EXTRATROPICAL CYCLONES IN THE PRESENT AND WARMER CLIMATE

MIKA RANTANEN

FINNISH METEOROLOGICAL INSTITUTE
CONTRIBUTIONS

No. 165

DIAGNOSTIC STUDIES OF EXTRATROPICAL CYCLONES IN THE PRESENT AND WARMER CLIMATE

Mika Rantanen

Institute for Atmospheric and Earth System Research / Physics
Faculty of Science
University of Helsinki

Academic dissertation

To be presented, with the permission of the Faculty of Science of the University of Helsinki, for public criticism in auditorium E204, Gustaf Hällströmin katu 2, on April 24th, 2020, at 12 o'clock noon.

Helsinki 2020

Author's Address: Finnish Meteorological Institute
P.O. Box 503
FI-00101 Helsinki
mika.rantanen@fmi.fi

Supervisors: Docent Jouni Räisänen, Ph.D.
Institute for Atmospheric and Earth System Research
University of Helsinki

Docent Victoria Sinclair, Ph.D.
Institute for Atmospheric and Earth System Research
University of Helsinki

Professor Heikki Järvinen, Ph.D.
Institute for Atmospheric and Earth System Research
University of Helsinki

Reviewers: University Lecturer Jennifer Catto, Ph.D.
College of Engineering, Mathematics and Physical Sciences
University of Exeter, United Kingdom

Senior Researcher Christian Grams, Ph.D.
Institute of Meteorology and Climate Research
Karlsruhe Institute of Technology, Germany

Opponent: Professor Heini Wernli, Ph.D.
Institute for Atmospheric and Climate Science
ETH Zurich, Switzerland

ISBN 978-952-336-105-8 (paperback)
ISBN 978-952-336-106-5 (pdf)
ISSN 0782-6117

Edita Prima Oy
Helsinki 2020

ILMATIETEEN LAITOS
METEOROLOGISKA INSTITUTET
FINNISH METEOROLOGICAL INSTITUTE

Published by **Finnish Meteorological Institute**
(Erik Palménin aukio 1), P.O. Box 503
FIN-00101 Helsinki, Finland

Series title, number and report code of publication
FMI Contributions 165, FMI-CONT-165
Date: April 2020

Author
Mika Rantanen

ORCID iD
0000-0003-4279-0322

Title

Diagnostic Studies of Extratropical Cyclones in the Present and Warmer Climate

Abstract

Extratropical cyclones are among the most important weather phenomena at mid- and high latitudes. They drive the weather variability on daily basis, and the passage of a strong extratropical cyclone can occasionally cause damage for society in general and, as a specific example, forestry due to strong winds, flooding and snow load. Furthermore, extratropical cyclones are a crucial component of the atmospheric general circulation due to their ability to transport large amounts of heat and momentum.

Because of climate change, the environment in which extratropical cyclones form will change. For example, the increase of available moisture for extratropical cyclones with the warming enhances the latent heat release in the clouds, affecting thus potentially the intensity and deepening rate of extratropical cyclones, and eventually the impacts which are felt at the surface. Therefore, studying the various effects of climate change on the dynamics of extratropical cyclones is of great importance.

In this thesis, a diagnostic method was developed to analyse the physical causes of vertical motion, geopotential height tendency and relative vorticity tendency within extratropical cyclones. Information on the physical causes gives insight into the relative contribution of different moist and dry processes to the evolution of extratropical cyclones. The thesis covers studies of both an idealized, traditional type of cyclone driven by both adiabatic and diabatic dynamics, and a real-world cyclone which was transitioned from a hurricane and was found to be strongly dependent on moist processes. Information on such dynamical differences is essential during the era of changing climate, when the atmospheric moisture content is continuously increasing due to global warming.

Furthermore, the changes in the characteristics and structure of extratropical cyclones with the warming were investigated. In a model simulation in which sea surface temperatures were increased by 4 K, the precipitation associated with the cyclones increased up to 50 %, and the area of rainfall moved further away from the cyclone's centre. It was also discovered that extratropical cyclones tend to respond differently to the changes in lower-level and upper-level temperature gradient. The decrease of lower-level temperature gradient, as anticipated in northern mid-latitudes with climate change, tends to decrease the strength of extratropical cyclones in a robust way. The response of extratropical cyclones to the increase of upper-level temperature gradient seems to be, in turn, more sensitive to the presence of atmospheric moisture, which highlights the importance of mid-tropospheric latent heat release for the development of extratropical cyclones.

Publishing unit

Weather and Climate Change Impact Research

Classification (UDC)
551.515.1

Keywords: extratropical cyclones, diabatic heating, numerical models, omega equation

ISSN and series title
0782-6117
Finnish Meteorological Institute Contributions

ISBN
978-952-336-105-8 (paperback)
978-952-336-106-5 (pdf)

DOI
10.35614/isbn.9789523361065

Language
English

Pages
52

ILMATIETEEN LAITOS
METEOROLOGISKA INSTITUTET
FINNISH METEOROLOGICAL INSTITUTE

Julkaisija **Ilmatieteen laitos**
(Erik Palménin aukio 1), PL 503
00101 Helsinki

Julkaisun sarja, numero ja raporttikoodi
FMI Contributions 165, FMI-CONT-165
Päivämäärä: Huhtikuu 2020

Tekijä
Mika Rantanen

ORCID iD
0000-0003-4279-0322

Nimeke

Diagnostisia tutkimuksia keskileveysasteiden matalapaineista sekä nykyisessä että lämpimässä ilmastossa

Tiivistelmä

Liikkuvat matalapaineet ovat keski- sekä korkeiden leveysasteiden tärkeimpiä sääilmiöitä. Niiden ansiosta päivittäinen säämme on vaihtelevaa, mutta toisaalta voimakkaat matalapaineet voivat aiheuttaa vahinkoja yhteiskunnalle ja esimerkiksi metsätaloudelle myrskytuulien, tulvimisen tai lumisateiden takia. Keskileveysasteiden liikkuvat matalapaineet ovat myös tärkeä osa koko ilmakehän yleistä kiertoliikettä, koska ne kuljettavat liikemäärää ja esimerkiksi tasaavat päiväntasaajan ja korkeiden leveysasteiden suurta lämpötilaeroa.

Ilmaston lämpenemisen myötä matalapaineiden kasvuympäristö tulee muuttumaan. Esimerkiksi lämpötilan noususta johtuva ilmakehän kosteussisällön kasvu voimistaa pilvissä tapahtuvaa latentin lämmön vapautumista, mikä vaikuttaa myrskyjen voimakkuuteen, voimistumisnopeuteen ja lopulta myös niiden aiheuttamiin tuhoihin. On siis tärkeää tutkia tarkasti mitä vaikutuksia ilmastonmuutoksella on liikkuvien matalapaineiden dynamiikkaan.

Tässä tutkimuksessa kehitettiin diagnostinen työkalu jolla voitiin tutkia matalapaineissa ilmakehän pystyliikkeen sekä geopotentiaalikorkeuden ja suhteellisen pyörteisyyden muutosnopeuden fysikaalisia syitä. Tämän tiedon avulla saadaan selville miten adiabaattinen dynamiikka ja toisaalta diabaattiset prosessit vaikuttavat matalapaineiden kehitykseen, ja mikä on näiden tekijöiden keskinäinen suuruusluokka. Työssä tutkittiin sekä ideaalista, oppikirjamaista matalapainetta, sekä todellista, hurrikaanista muuntautunutta matalapainetta. Idealisoidussa tapauksessa sekä adiabaattiset että diabaattiset prosessit olivat voimakkaita, kun taas myrsky joka muuntui hurrikaanista keskileveysasteiden matalapaineeksi osoittautui vahvasti diabaattiseksi. Tällainen tieto eroavaisuuksissa myrskyjen dynamiikassa on keskeistä ilmastonmuutoksen aikakaudella, erityisesti kasvavan ilmakehän kosteussisällön takia.

Väitöskirjatyössä tutkittiin myös miten keskileveysasteiden matalapaineiden ominaisuudet ja rakenne muuttuu ilmaston lämpenemisen myötä. Tulosten mukaan neljän asteen lämpeneminen kasvatti matalapaineisiin liittyvää sateisuutta jopa 50 %. Havaittiin myös että sadealue siirtyi lämpenemisen myötä kauemmaksi myrskyn keskustasta. Lisäksi huomattiin että myrskyjen dynamiikka riippuu eri tavalla ala- ja yläilmakehän lämpötilagradienteista, jotka muuttuvat pohjoisella pallonpuoliskolla ilmaston lämmetessä. Alailmakehän lämpötilagradientin heikkeneminen vähensi matalapaineiden voimakkuutta hyvin selkeästi, kun taas yläilmakehän lämpötilagradientin kasvattaminen voimisti matalapaineita, mutta voimistumisen suuruus oli herkkä ilmakehän kosteussisällölle. Saatu tulos korostaa latentin lämmön vapautumista matalapaineiden kehityksessä.

Julkaisijayksikkö

Sään ja ilmastonmuutoksen vaikutustutkimus

Luokitus (UDK)
551.515.1

Asiasanat: keskileveysasteiden matalapaineet, diabaattinen lämmitys, numeeriset mallit, omegayhtälö

ISSN ja avainnimike
0782-6117
Finnish Meteorological Institute Contributions

ISBN
978-952-336-105-8 (nid.)
978-952-336-106-5 (pdf)

DOI
10.35614/isbn.9789523361065

Kieli
Englanti

Sivumäärä
52

Acknowledgements

I would like to first thank my supervisors, Doc. Jouni Räisänen, Doc. Victoria Sinclair and Prof. Heikki Järvinen. Jouni, your endless knowledge of atmospheric dynamics and climate change has been of great help to me. Your door has been always open for my questions and every time after our discussions I have got more faith in this work. Victoria, thanks for helping me especially in numerous technical issues, but also giving me more insight in meteorology and atmospheric sciences. Heikki, thanks for your support and mentorship during these years.

I want to thank also Dr. Juha Lento, who has been always very helpful when I have been stuck with computers. Thanks for teaching me how to do things in a "right" way in programming. Without your help this work would have never been done. I am also grateful to Prof. Heini Wernli for serving as opponent in my defence, and Dr. Jennifer Catto and Dr. Christian Grams for pre-examining this thesis.

This whole research was conducted in the Institute for Atmospheric and Earth System Research (INAR) (formerly Division of Atmospheric Sciences). I would like to thank the director of INAR, Prof. Markku Kulmala for providing me the opportunity to work in one of the world's leading atmospheric research groups. Many thanks also for Dynamic Meteorology group for giving me the wonderful working environment which was honestly the best possible place for me to carry out this research. In addition, Doctoral Programme of Atmospheric Sciences deserves special acknowledgements for financially funding this work.

Thanks for all the friends and fellow PhD students for all the fun moments, and not only during the last four years, but during the all nine years which I have been hanging out in Kumpula studying meteorology. The peer support which I have got from you has been very valuable. In addition, special thanks also to my office roommates, Meri, Madeleine and Lauri, for the all helpful discussions which we have had.

Finally, I would like to express my deepest gratitude to the love of my life, Jessica, who has been raising our two daughters, Olivia and Ellen, at home when I have been spending long days at work. I want to thank you for all of your support and sacrifices you have made for me throughout these years.

Mika Rantanen
Lahti, February 2020

Contents

List of publications

This thesis consists of an introductory review, followed by four research articles. In the introductory part, these papers are cited according to their roman numerals. **Paper I** is reprinted under the Creative Commons Attribution 3.0 license, **Paper II** is printed by permission from Springer Nature (licence number 4750131311239), **Paper III** is reprinted under the Creative Commons Attribution-NonCommercial 4.0 License and **Paper IV** is reprinted under the Creative Commons Attribution 4.0 license.

I **Rantanen, M.**, Räisänen, J., Lento, J., Stepanyuk, O., Räty, O., Sinclair, V. A., and Järvinen, H. (2017). OZO v.1.0: software for solving a generalised omega equation and the Zwack-Okossi height tendency equation using WRF model output, *Geoscientific Model Development*, 10, 827-841, doi:10.5194/gmd-10-827-2017

II **Rantanen, M.**, Räisänen, J., Sinclair, V.A. and Järvinen, H. (2019). Sensitivity of idealised baroclinic waves to mean atmospheric temperature and meridional temperature gradient changes, *Climate Dynamics* 52: 2703. doi:10.1007/s00382-018-4283-3

III **Rantanen, M.**, Räisänen, J., Sinclair, V.A. and Järvinen, H. (2020). The extratropical transition of Hurricane Ophelia (2017) as diagnosed with a generalized omega equation and vorticity equation, *Tellus A: Dynamic Meteorology and Oceanography*, 72, 1-26 doi:10.1080/16000870.2020.1721215

IV Sinclair, V.A., **Rantanen, M.**, Haapanala, P., Räisänen, J. and Järvinen, H. (2020). The structure of extratropical cyclones in warmer climates, *Weather and Climate Dynamics*, 1, 1-25 doi:10.5194/wcd-1-1-2020

1 Introduction

1.1 What is an extratropical cyclone?

Extratropical cyclones (hereafter ETCs), often called also as mid-latitude cyclones, are weather systems ranging in size from several hundreds of kilometres to a few thousand kilometres. They form due to atmospheric baroclinicity (i.e. temperature difference in north-south direction), and are thus most abundant and strongest in the winter season when the temperature differences between low- and high latitudes are greatest. ETCs are the main cause of weather variability at mid- and high latitudes. They bring precipitation and winds, and the strongest ETCs can cause societal damage (e.g. Wernli et al., 2002; Liberato et al., 2011, 2013), such as traffic disruption or power outages. The low-level airflows associated with ETCs can form so called atmospheric rivers (Dacre et al., 2019), which can lead to serious flooding for example in UK (Lavers et al., 2011) and the west coast of USA (Ralph et al., 2006).

Because ETCs typically form in the area of strong baroclinicity, they are associated with fronts and thus their appearance looks asymmetric. This is one of the main characteristics distinguishing them from tropical cyclones, which are usually more symmetric by their appearance. In addition, tropical cyclones develop through latent heat release in deep convective clouds and thus their occurrence is restricted to lower latitudes where the sea surface temperatures are higher. Extratropical cyclogenesis instead, tends to occur at mid- and high latitudes, in the Northern Hemisphere most frequently in the so-called North Pacific and North Atlantic storm tracks (Wernli and Schwierz, 2006). Furthermore, tropical cyclones can sometimes curve poleward, enter mid-latitudes and transform into ETCs. These post-tropical storms can cause high-impact weather downstream via amplification of the mid-latitude flow (e.g. Grams and Blumer, 2015; Grams and Archambault, 2016).

ETCs have an important role in atmospheric general circulation. They transport both sensible heat (warm air) and latent heat (moisture) from lower latitudes towards the poles, and at mid-latitudes, they are actually more efficient meridional heat transporters than ocean currents (e.g. Hartmann, 2015). Therefore, without ETCs, the temperature difference between the tropics and poles would be considerably higher. Furthermore, ETCs participate to the energy cycle of our climate system by converting the atmospheric available potential energy to kinetic energy (Lorenz, 1955), which

can be felt at the surface as winds.

In summary, although ETCs are often associated with undesirable weather, they are a crucial part of our climate system. Moreover, due to climate change, the structure and dynamics, and thus potentially the impacts of ETCs on our society may change. For all these reasons, studying the dynamics of ETCs in our changing climate is of great interest.

1.2 Different diagnostic methods

Various studies during the past century have contributed to understanding the role of different physical processes in the development of ETCs (Schultz et al., 2019). The baroclinic theory and the adiabatic processes thereof became well-known during the mid-20th century (Charney, 1947; Eady, 1949). Since then, the role of latent heat release due to formation of clouds and precipitation in baroclinic disturbances has gained attention among the researchers (e.g. Tracton, 1973; Kuo et al., 1991; Stoelinga, 1996). Nowadays it is well understood that diabatic processes can considerably affect the strength of ETCs (e.g. Ahmadi-Givi et al., 2004; Büeler and Pfahl, 2017), especially in warm season (Martínez-Alvarado et al., 2016) and marine cyclones (Roebber and Schumann, 2011).

Diagnostic methods to identify the contributions of various adiabatic and diabatic processes to the development of ETCs have been developed during the years. The key variable to diagnose the effect of diabatic heating is potential vorticity (PV; Rossby, 1939; Ertel, 1942) due to its conservativity in adiabatic and frictionless conditions. Hoskins et al. (1985) later established the use of PV in modern atmospheric dynamics. Because PV can be only modified by diabatic and frictional processes, the appliance of PV inversion techniques allows to determine explicitly the contribution of diabatic processes to the circulation and intensity of ETCs (Davis and Emanuel, 1991; Stoelinga, 1996).

Because the low-level PV anomalies associated with ETCs are strongly coupled to cyclone intensity, diagnostic methods using PV alone are also useful to explain the role of latent heating especially in explosive cyclogenesis. Using the PV framework, Büeler and Pfahl (2017) developed a diagnostic approach to systematically quantify the contribution of latent heating to cyclone intensification. They applied the method

further to surrogate climate change simulations (Büeler and Pfahl, 2019) and found that enhanced diabatic heating was able to largely explain the varying increase in intensity and impacts of most of the studied cyclones. The PV framework was also employed by Chagnon et al. (2013) and Martínez-Alvarado et al. (2016), who used PV tracers to investigate the effect of diabatic processes on the evolution of ETCs. The use of tracers allowed to identify which diabatic processes in the clouds (such as evaporation and condensation) were responsible for the generation of PV anomalies within ETC.

In addition to the PV framework, the roles of different physical processes on ETC evolution can be quantified with various other techniques. Fink et al. (2012) diagnosed the influence of diabatic processes on explosive cyclogenesis using a novel version of surface pressure tendency equation (Knippertz and Fink, 2008; Knippertz et al., 2009). They applied the tool for five selected European windstorms (Storms Lothar, Martin, Klaus, Kyrill and Xynthia) and discovered that Kyrill and Martin were more baroclinically-driven storms than Lothar, Klaus and Xynthia. A more systematic analysis with the same diagnostic tool was performed later in Pirret et al. (2017), who examined 58 different European windstorms using ERA-Interim reanalysis data. According to their results, the contribution of diabatic processes varied considerably from case to case, with baroclinic processes still being the dominant forcing in the majority of storms.

The role of physical forcing mechanisms in the relative vorticity budgets of North Atlantic ETCs was studied by Azad and Sorteberg (2014a,b). They employed a generalized omega equation to decompose the vertical motion into contributions from different forcing terms: vorticity advection, temperature advection, diabatic heating, ageostrophic vorticity tendency and friction (see Section 2.2). They followed mainly the method presented earlier in Pagé et al. (2007), Räisänen (1995) and Pauley and Nieman (1992). After this, the vorticity tendency budget was partitioned into the same components representing the earlier listed physical processes, analogously with the vertical motion, and similarly as in Räisänen (1997). However, while Räisänen (1997) applied the nonlinear balance equation to further convert the vorticity tendencies to geopotential height tendencies, Azad and Sorteberg (2014a,b) relied purely on vorticity diagnostics calculated with the Zwack-Okossi equation (Zwack and Okossi, 1986; Lupo et al., 1992). Besides the papers by Azad and Sorteberg (2014a,b), the Zwack-Okossi equation has been applied successfully in numerous other diagnostic studies on ETC dynamics (e.g. Yoshida and Asuma, 2004; Azad and Sorteberg, 2009; Kuwano-Yoshida and Enomoto, 2013; Fu et al., 2018).

In conclusion, this literature review reveals that several diagnostic equations have been developed to investigate ETCs. The common denominator of these methods is that they all aim to diagnose the role of different adiabatic and diabatic processes in the life cycle of ETCs. However, the used variable can be PV tendency (e.g. Chagnon et al., 2013; Büeler and Pfahl, 2017), surface pressure tendency (e.g. Fink et al., 2012; Pirret et al., 2017), geopotential height tendency (**Paper I**, Räisänen, 1997) or vorticity tendency (e.g. **Paper III**, Azad and Sorteberg, 2014a).

Each of the listed methodologies have their own advantages and disadvantages, and depending on the properties of the used dataset and the specific aim of the research, any of these methods can be beneficial. For example, if one wants to study specifically the impact of free-tropospheric moist processes to ETCs, applying PV diagnostic could be useful because in the free troposphere PV can only be modified by diabatic heating, which largely consists of the latent heat release in the clouds. Instead, the benefit of applying the vorticity- or geopotential height tendency methodology (**Paper I**, **Paper III**) is that they allow to decompose also the adiabatic processes into the contributions from vorticity advection, thermal advection, and ageostrophic vorticity tendency. This would not be possible using PV tendency alone.

1.3 Implications of warmer climate on extratropical cyclones

The ongoing climate change can affect the behaviour of ETCs in several different ways: (1) by increasing the atmospheric moisture content due to increasing temperatures (Hartmann et al., 2013); (2) by decreasing the lower level meridional temperature gradient due to larger warming trend in Arctic regions (known as Arctic amplification, e.g. Serreze et al., 2009) than elsewhere in the globe; and (3) by increasing the upper level meridional temperature gradient due to enhanced warming in the tropical upper troposphere (e.g. Allen and Sherwood, 2008) and cooling in the polar lower stratosphere (e.g. Thompson and Solomon, 2005). The changes (2) and (3) constitute a balanced tug-of-war between two competing effects for the strength of the jet stream, as verified recently by reanalysis datasets (Lee et al., 2019). Because these changes (1)-(3) are occurring simultaneously in the atmosphere, and given the nonlinear responses of ETCs to these changes, it is not surprising that confident future projections of midlatitude storm tracks remain challenging. Accordingly, The Intergovernmental Panel on Climate Change (IPCC) states in its 5th assessment report that "Substantial uncertainty and

thus low confidence remains in projecting changes in NH winter storm tracks, especially for the North Atlantic basin." (Collins et al., 2013).

The latest research on the implications of climate change on the structure and dynamics of ETCs were recently brought together in a review paper by Catto et al. (2019). According to the review, the most robust outcome in the recent studies is that in a warmer climate, the precipitation associated with ETCs will increase (e.g. **Paper IV**, Yettella and Kay, 2017; Hawcroft et al., 2018). What remains still unclear is how the enhanced latent heating associated with increased precipitation will materialize in the intensity of ETCs. This research question is particularly challenging because there are different ways to define the intensity of ETCs, such as surface winds, eddy kinetic energy, minimum surface pressure or the deepening rate (Catto et al., 2019).

Numerical experiments performed with idealized climate change simulations have provided insights on the effect of increasing atmospheric moisture content on ETC intensity (e.g. **Paper II**, **Paper IV**, Booth et al., 2013; Kirshbaum et al., 2018; Tierney et al., 2018). One common aspect seems to be that the eddy kinetic energy is very close to its maximum with present-day climate conditions and is expected to decrease with further warming (**Paper III**, O'Gorman and Schneider, 2008; Pfahl et al., 2015; Kirshbaum et al., 2018; Tierney et al., 2018). One explanation for this could be structural changes in ETCs, such as worse phasing between the warm-frontal ascent and the buoyancy in the warm sector, as found in Kirshbaum et al. (2018) and confirmed later in **Paper III**.

Climate models in Coupled Model Intercomparison Project 5 (CMIP5) predict that the number of strong cyclones would decrease in the North Atlantic by 8 % $\pm$ 3 % (in winter) or 6 % $\pm$ 3 % (in summer) in RCP4.5 scenario by the end of 21st century (Zappa et al., 2013b). Furthermore, under the high-emission RCP8.5 scenario, the extreme winds associated ETCs are projected to decrease 17 % for the entire Northern Hemisphere by the end of the 21st century (Chang, 2018). However, the sign of change is the opposite in the Southern Hemisphere, where CMIP5 models project an increase in the number of strong cyclones (Chang et al., 2012). The deepening rate of ETCs in warmer climates does not seem to change significantly in idealized simulations (Pfahl et al., 2015) or in CMIP5 models in the Northern Hemisphere (Seiler and Zwiers, 2016). However, according to the results of **Paper IV**, and consistent with the Southern Hemisphere CMIP5 projections (Chang et al., 2012), the deepening rate of particularly strong ETCs may increase with the warming.

There is evidence that CMIP5 models have systematic biases in the number and intensity of North Atlantic ETCs (Zappa et al., 2013a; Pithan et al., 2016). Furthermore, it has been shown that diabatic heating in the clouds is sensitive to the model resolution (Willison et al., 2013, 2015). Thus, more research on this subject is clearly needed, especially with high-resolution models using state-of-the-art physics parametrizations. In their review paper on the future of ETCs Catto et al. (2019) emphasize that "Future research could focus on bridging the gap between idealized models and complex climate models, as well as better understanding of the regional impacts of future changes in extratropical cyclones."

1.4 Aims of the thesis

The general aim of this thesis is to increase the understanding on how different atmospheric physical processes can affect the intensity and structure of ETCs, both in present-day climate conditions and in a warmer climate. This aim has been addressed in four research articles, with the following more specific research questions:

1. How much do different adiabatic and diabatic processes contribute to the evolution of ETCs? For this purpose, a diagnostic tool has been developed, and the contributions of different adiabatic and diabatic processes were analysed quantitatively using idealized and real-world case studies in **Paper I** and **III**.

2. How sensitive are ETCs to different aspects of changes in the mean temperature distribution, which are anticipated with climate change in the Northern Hemisphere? This specific aim was addressed in **Paper II** with model simulations in which the large-scale temperature environment experienced by a developing ETC was altered. The simulations were compared to a control run where no changes were performed.

3. Which structural changes are expected to occur in ETCs in a warmer climate, if any, and which physical processes are responsible for these changes? This final aim was investigated with 10-year long simulations with global atmospheric model in **Paper IV**. The structural changes were identified with a cyclone-compositing method.

2 Diagnostic methods and model simulations

In this section, the equations and the model simulations used in this thesis are presented. The diagnostic tool employed in **Paper I** and **III** is based on the decomposition of vertical motion into its physical causes. The method for the decomposition is presented first, in Section 2.1. The strengthening and weakening rate of ETCs was studied using time tendencies of both geopotential height and relative vorticity. The decomposition of these variables is presented in Section 2.2. In addition, the validation of both diagnostic methods is demonstrated in Section 2.3. Then, the basic concept of the energy cycle in the atmosphere and its relation to ETCs is expressed in Section 2.4, and finally, the used numerical weather models and the experiments are briefly introduced in Section 2.5.

2.1 The decomposition of vertical motion

Albeit being often orders of magnitude weaker than the horizontal wind, the vertical wind is a vital part of the atmospheric general circulation. In ETCs, vertical motions are tightly linked to the development of the system: rising motions generate low-level cyclonic vorticity, and when occurring near the cyclone centre, they act to increase the intensity of the system. Furthermore, upward motions lead to adiabatic cooling and consequently to condensation of water vapour. Thus, upward motions are an essential ingredient of the precipitation and latent heat release in ETCs. Moreover, the ascent of warm air and descent of cold air in the eddies convert the available potential energy to kinetic energy, and hence influence the whole energy cycle of the atmosphere. For these reasons, understanding the physical and dynamical causes of the vertical motions in the ETCs is of great importance.

A practical and broadly used way to examine the causes of atmospheric vertical motion is to apply the omega equation. Various forms of the omega equation exist, ranging from the simplest quasi-geostrophic (QG) omega equation to the most complex, generalized version of the omega equation. In this thesis, the main diagnostic tool is based on the generalized omega equation, but two simpler forms of omega equations have also been utilized.

The QG omega equation, which is briefly used in **Paper I**, is presented first:

$$L_{QG}(\omega) = F_{V(QG)} + F_{T(QG)} \tag{1}$$

where

$$L_{QG}(\omega) = \sigma_0(p)\,\nabla^2\omega + f^2\frac{\partial^2\omega}{\partial p^2} \tag{2}$$

and the two right-hand-side (RHS) terms are

$$F_{V(QG)} = f\frac{\partial}{\partial p}\left[\vec{V}_g \cdot \vec{\nabla}\left(\zeta_g + f\right)\right] \tag{3}$$

$$F_{T(QG)} = \frac{R}{p}\nabla^2\left(\vec{V}_g \cdot \vec{\nabla}T\right). \tag{4}$$

The explanations of all mathematical symbols are listed in Table 1. The QG omega equation tells that rising motion in the atmosphere occurs if the cyclonic vorticity advection increases upwards (Eq. 3) or if there is advection of warm air (Eq. 4). The opposite is true for the sinking motion.

The main advantage of the QG omega equation is that it is computationally light to solve and gives still a relatively good approximation of the mid-tropospheric vertical motion decomposed into the contributions from vorticity advection and thermal advection. However, for detailed analysis of the causes of vertical motion, especially in systems which are strongly diabatically-driven, the QG approximations become inevitably problematic. To avoid the QG approximations, one can derive a generalized omega equation directly from the primitive equations (e.g. Räisänen, 1995). Hence, the generalized omega equation does not involve any simplifying assumptions except the hydrostatic balance, which is implicitly assumed when isobaric coordinates are used.

In **Papers I** and **III**, we used the following formulation of the generalized omega equation:

$$L(\omega) = F_V + F_T + F_F + F_Q + F_A \tag{5}$$

where

$$L(\omega) = \nabla^2(\sigma\omega) + f(\zeta + f)\frac{\partial^2\omega}{\partial p^2} - f\frac{\partial^2\zeta}{\partial p^2}\omega + f\frac{\partial}{\partial p}\left[\vec{k}\cdot\left(\frac{\partial\vec{V}}{\partial p}\times\nabla\omega\right)\right] \tag{6}$$

and the RHS terms are

$$F_V = f\frac{\partial}{\partial p}\left[\vec{V}\cdot\nabla\left(\zeta + f\right)\right], \tag{7}$$

$$F_T = \frac{R}{p}\nabla^2\left(\vec{V}\cdot\nabla T\right), \tag{8}$$

$$F_F = -f\frac{\partial}{\partial p}\left[\vec{k}\cdot\left(\nabla\times\vec{F}\right)\right], \tag{9}$$

$$F_Q = -\frac{R}{c_p p}\nabla^2 Q, \tag{10}$$

$$F_A = f\frac{\partial}{\partial p}\left(\frac{\partial\zeta}{\partial t}\right) + \frac{R}{p}\nabla^2\left(\frac{\partial T}{\partial t}\right). \tag{11}$$

The RHS forcing terms represent the effects of vorticity advection (F_V, Eq. 7), thermal advection (F_T, Eq. 8), friction (F_F, Eq. 9), diabatic heating (F_Q, Eq. 10), and an imbalance between vorticity tendency and temperature tendency (hereafter imbalance term, F_A, Eq. 11).

Finally, in **Paper IV**, an intermediate form of the omega equation, which employs the main forcing terms of the generalized omega equation (vorticity advection, thermal advection and diabatic heating), but the simplified LHS operators from the QG omega equation (Eq. 2), was used:

$$\sigma_0(p)\nabla^2\omega + f^2\frac{\partial^2\omega}{\partial p^2} = f\frac{\partial}{\partial p}\left(\vec{V}\cdot\nabla\left(\zeta+f\right)\right) + \frac{R}{p}\nabla^2\left(\vec{V}\cdot\nabla T\right) - \frac{R}{c_p p}\nabla^2 Q. \tag{12}$$

Here the friction term was neglected as is was assumed to be small in an aquaplanet configuration where only ocean exists. In addition, as the horizontal resolution was rather coarse (around 125 km), the imbalance term in synoptic-scale systems can be expected to be relatively small and thus could be ignored.

With homogenous boundary conditions (ω=0 at the lower and upper boundary of the atmosphere), the vertical motion contributions of the individual RHS terms can be solved separately because the LHS operators (Eq. 2 and 6) are linear with respect to ω. As a result, the total vertical motion is decomposed into contributions from different physical processes. For the QG omega equation, this means that the total vertical motion consists of two omega terms:

$$\omega_{QG} = \omega_{V(QG)} + \omega_{T(QG)} \tag{13}$$

Here $\omega_{V(QG)}$ means vertical motion that is due to the vorticity advection term and $\omega_{T(QG)}$ vertical motion that is due to the thermal advection term.

For the generalized omega equation (Eq. 5), the calculated total vertical motion field consists of five omega terms:

$$\omega = \omega_V + \omega_T + \omega_F + \omega_Q + \omega_A \tag{14}$$

In this case, the different ω-terms on the RHS mean vertical motion due to vorticity advection (ω_V), thermal advection (ω_T), friction (ω_F), diabatic heating (ω_Q) and imbalance term (ω_A), analogously to Eq. 5.

All the data needed for solving the equations were obtained directly from the model output, which was vertically interpolated to pressure coordinates. In **Paper I**, we solved the omega equations (both QG and generalized) on a Cartesian grid with a so-called multigrid algorithm. In **Paper III**, the generalized omega equation was applied in spherical coordinates, which meant that we could not utilize the same solver as in **Paper I**. Thus, the solving was performed with Portable, Extensible Toolkit for Scientific Computation (PETSc) differential equation solvers, which allowed us to use parallel computing with supercomputer resources. Finally, the intermediate form of omega equation used in **Paper IV** was solved in spectral space, using the method from Räisänen (1995). In summary, in all of the papers slightly different solving methods for the omega equation were applied, due to the fact that the LHS operators and the used coordinate system varied between the studies.

The generalized omega equation has been used only in a few earlier studies which have aimed to diagnose the different forcing terms affecting ETCs. The method used here builds on Räisänen (1997), nearly similarly as has been done in Caron et al. (2006) and Azad and Sorteberg (2014a,b). However, some technical differences between the methodologies exists. For example, Caron et al. (2006) and Azad and Sorteberg (2014a,b) calculate the frictional tendencies $\vec{F}$ assuming balance between pressure gradient and the frictional and Coriolis forces in the lowest 150 hPa (Caron et al., 2006) or below 850 hPa (Azad and Sorteberg, 2014a,b). In addition, in these studies the diabatic heating rate Q was estimated using the total surface precipitation flux and positive diabatic residuals estimated by the thermodynamic equation. In **Papers I, III** and **IV**, however, $\vec{F}$ and Q were obtained directly from the model output, which simplifies the workflow and increases the numerical accuracy of these tendencies.

Table 1: List of mathematical symbols.

$c_p = 1004$ J kg^{-1}	specific heat of dry air at constant volume
f	Coriolis parameter
F	forcing in the omega equation
$\vec{F}$	friction force per unit mass
$g = 9.81$ m s^{-2}	gravitational acceleration
$\vec{k}$	unit vector along the vertical axis
L	linear operator on the left-hand-side of the omega equation
p	pressure
Q	diabatic heating rate per mass
$R = 287$ J kg^{-1}	gas constant of dry air
$S = -T\frac{\partial ln\theta}{\partial p}$	stability parameter in pressure coordinates
t	time
T	temperature
$\vec{V}$	horizontal wind vector
$\vec{V_g}$	geostrophic wind vector
$\sigma = -\frac{RT}{p\theta}\frac{\partial \theta}{\partial p}$	hydrostatic stability
σ_0	isobaric mean of hydrostatic stability
ζ	vertical component of relative vorticity
ζ_g	relative vorticity of geostrophic wind
ζ_{ag}	relative vorticity of ageostrophic wind
$\omega = \frac{dp}{dt}$	isobaric vertical motion
∇	horizontal nabla operator
∇^2	horizontal laplacian operator

2.2 The decomposition of geopotential height tendency and vorticity tendency

In addition to atmospheric vertical motion, the tendencies of geopotential height and relative vorticity are key variables in studying ETCs because these variables are directly linked to the strengthening or weakening rate of ETCs. With constant Coriolis parameter, the relation between geopotential height tendency and geostrophic vorticity

tendency is as follows:

$$\frac{\partial \zeta_g}{\partial t} = \frac{g}{f}\nabla^2 \frac{\partial Z}{\partial t} \tag{15}$$

Thus, in the Northern Hemisphere, the first order approximation is that positive height tendency means negative vorticity tendency and vice versa.

In **Paper I**, we used the so-called Zwack-Okossi equation (Zwack and Okossi, 1986; Lupo and Smith, 1998)

$$\frac{\partial \zeta_g}{\partial t}(p_L) = \frac{1}{p_s - p_t}\left[\int_{p_t}^{p_s}\left(\frac{\partial \zeta}{\partial t} - \frac{\partial \zeta_{ag}}{\partial t}\right)dp - \frac{R}{f}\int_{p_t}^{p_s}\left(\int_{p}^{p_L}\nabla^2 \frac{\partial T}{\partial t}\frac{dp}{p}\right)dp\right] \tag{16}$$

to decompose the tendency of geostrophic vorticity into components of various forcing terms. Here p_L is the level for which the tendency is calculated, and p_s and p_t are the lower and the upper boundaries of the model domain. The vorticity tendency $\frac{\partial \zeta}{\partial t}$ in the first term of Eq. 16 was calculated using the vorticity equation

$$\frac{\partial \zeta}{\partial t} = -\vec{V}\cdot\nabla(\zeta + f) - \omega\frac{\partial \zeta}{\partial p} + (\zeta + f)\frac{\partial \omega}{\partial p} + \vec{k}\cdot\left(\frac{\partial \vec{V}}{\partial p}\times\nabla\omega\right) + \vec{k}\cdot\nabla\times F, \tag{17}$$

and temperature tendency $\frac{\partial T}{\partial t}$ in the second term of Eq. 16 was calculated using the thermodynamic equation:

$$\frac{\partial T}{\partial t} = -\vec{V}\cdot\nabla T + S\omega + \frac{Q}{c_p} \tag{18}$$

The ageostrophic vorticity tendency was estimated using central time differences

$$\frac{\partial \zeta_{ag}}{\partial t} \approx \frac{\Delta(\zeta - \zeta_g)}{2\Delta t}. \tag{19}$$

with $\Delta t = 1800\ s$.

When substituting the vorticity equation (Eq. 17) and the thermodynamic equation (Eq. 18) into Eq. 16, utilizing the different omega terms from Eq. 14, and finally combining the result with Eq. 15, the different geopotential height tendency terms can be derived, analogously with the vertical motion:

$$\frac{\partial Z}{\partial t} = \left(\frac{\partial Z}{\partial t}\right)_V + \left(\frac{\partial Z}{\partial t}\right)_T + \left(\frac{\partial Z}{\partial t}\right)_F + \left(\frac{\partial Z}{\partial t}\right)_Q + \left(\frac{\partial Z}{\partial t}\right)_A. \tag{20}$$

Here the RHS terms mean geopotential height tendencies that are due to vorticity advection, thermal advection, friction, diabatic heating and imbalance term, respectively. See **Paper I** for the full forms of the RHS terms of Eq. 20.

In **Paper III**, the cyclone development was analysed using vorticity tendencies. The decomposition was similar to that in Räisänen (1995):

$$\frac{\partial \zeta}{\partial t} = \left(\frac{\partial \zeta}{\partial t}\right)_V + \left(\frac{\partial \zeta}{\partial t}\right)_T + \left(\frac{\partial \zeta}{\partial t}\right)_F + \left(\frac{\partial \zeta}{\partial t}\right)_Q + \left(\frac{\partial \zeta}{\partial t}\right)_A . \tag{21}$$

where

$$\left(\frac{\partial \zeta}{\partial t}\right)_V = -\vec{V} \cdot \nabla(\zeta + f) - \omega_V \frac{\partial \zeta}{\partial p} + (\zeta + f)\frac{\partial \omega_V}{\partial p} + \vec{k} \cdot \left(\frac{\partial \vec{V}}{\partial p} \times \nabla \omega_V\right), \tag{22}$$

$$\left(\frac{\partial \zeta}{\partial t}\right)_F = \vec{k} \cdot \nabla \times \vec{F} - \omega_F \frac{\partial \zeta}{\partial p} + (\zeta + f)\frac{\partial \omega_F}{\partial p} + \vec{k} \cdot \left(\frac{\partial \vec{V}}{\partial p} \times \nabla \omega_F\right), \tag{23}$$

and

$$\left(\frac{\partial \zeta}{\partial t}\right)_X = -\omega_X \frac{\partial \zeta}{\partial p} + (\zeta + f)\frac{\partial \omega_X}{\partial p} + \vec{k} \cdot \left(\frac{\partial \vec{V}}{\partial p} \times \nabla \omega_X\right), \; X = T, Q, A \tag{24}$$

Similarly as in Eq. 20, the RHS terms of Eq. 21 describe the vorticity tendencies due to vorticity advection, thermal advection, diabatic heating, friction and the imbalance term, respectively.

2.3 Model simulations

The results presented in this thesis are based on simulations performed with numerical weather models. In **Paper I** and **II**, we used the Weather Research and Forecasting (WRF) model (Shamarock et al., 2008) with its baroclinic wave channel mode. In **Paper III** and **IV**, the Open Integrated Forecast System (OpenIFS) model was used. Short technical information about these two models and the model simulations is presented next.

2.3.1 Baroclinic wave simulations

The WRF model can be used for simulating atmospheric conditions using either real data or idealised cases. In **Paper I** and **II**, an idealised moist baroclinic wave simulation was used. This baroclinic wave configuration is a highly controlled model set-up, which simulates the evolution of only one ETC within a baroclinically unstable jet in the

Northern Hemisphere under constant Coriolis parameter. In both **Paper I** and **II**, the value of the Coriolis parameter was set to 10^{-4}, which corresponds to the latitude of 43°N. The evolution of the baroclinic wave was triggered by inserting a 1-K temperature perturbation to the mid-tropospheric temperature field.

The boundaries of the model domain were periodic in east-west direction. This means that we did not need to have an exceedingly wide model domain in order to simulate the whole life cycle of the eastward-propagating cyclone. In the north-south direction, symmetric boundaries were used. In **Paper I**, the size of the model domain was 4000 km x 8000 km x 16 km, in the x, y and z directions, respectively. In **Paper II**, the length was 5000 km in the x direction with the other directions the same as in **Paper I**.

The model simulations in **Papers I and II** featured full physics schemes, except that the radiation scheme was switched off. The choice of leaving radiation off is a widely used procedure in baroclinic wave simulations (e.g. in Booth et al., 2013; Kirshbaum et al., 2018; Tierney et al., 2018) in order to help the interpretation of diabatic heating, as the latent heat release becomes the only major source of diabatic heating in the free atmosphere. See **Paper I** and **II** for detailed descriptions of the used model parametrizations schemes.

The main aim in **Paper I** was to document the diagnostic software and test its applicability for baroclinic wave simulations. For this reason, the simulation used to demonstrate the usability of the software was based largely on the standard baroclinic wave simulation which comes along with the WRF model package. The horizontal grid spacing was 25 km and there were 64 sigma levels in the vertical dimension.

In **Paper II**, we investigated the changes of cyclone energetics using three scenarios which are expected to occur with climate change in the Northern Hemisphere: (1) uniform increase of temperature; (2) decrease of the lower level meridional temperature gradient; and (3) increase of the upper level temperature gradient. The uniform increase of temperature in (1) was performed by raising the atmospheric temperature stepwise by 2, 4 and 6 K in the initial state of the model run. In (2), we decreased the low-level temperature gradient by warming the southern part of the domain and cooling the northern part of the domain by 2, 4 and 6 K. This acted to decrease the gradient by 4, 8, and 12 K, respectively. A similar procedure was done in (3), but to the opposite direction and at upper levels. More details about the experiments are

presented in **Paper II**.

Even though the changes (1) - (3) are occurring simultaneously in the real world, their effects to the intensity and energy cycle of the simulated ETC were studied separately. Moreover, we conducted the simulations first without moisture in the atmosphere, and then with more realistic, moist environment. The justification for this practise was that we wanted to identify the underlying adiabatic mechanisms which drive the response of ETCs to different types of changes in environmental temperature.

2.3.2 Global model simulations

OpenIFS is a global model developed by the European Centre for Medium-Range Weather Forecasts (ECMWF). OpenIFS has exactly same dynamical core and the physics parametrizations as the full Integrated Forecast System (IFS) model, which is used operationally for weather forecasting at ECMWF. OpenIFS does not have data assimilation capacity, but the model can be used for research purposes with externally generated initial conditions. OpenIFS is tailored to simulate real world cases, such as Storm Ophelia in **Paper III**, but it is also possible to employ OpenIFS with idealised set-up, such as the aquaplanet configuration in **Paper IV**. The version of OpenIFS used in this thesis was Cy40r1, documentation of which is available in ECMWF (2014).

In **Paper III**, we applied OpenIFS for simulating the extratropical transition of Hurricane Ophelia. The spectral resolution of the model was T639, which corresponds to approximately 31 km grid spacing at equator. Vertically there were 137 levels. The initial conditions were generated from ECMWF operational analyses, and a 6-day model simulation was initialized at 12 UTC 13 October 2017. The chosen initialization time was a compromise between the accuracy of the forecast and the length of the tropical phase of Ophelia in the simulation.

The model simulations in **Paper IV** were performed in an aquaplanet mode, a special configuration in which the surface of the Earth is all ocean. The sea surface temperatures (SST) were zonally uniform and symmetric about the equator. The atmosphere was initialized from a randomly selected real analysis from ECMWF. Two model simulations were carried out: the control simulation in which SSTs resembled the real, observed values, and a perturbed experiment in which SSTs were uniformly warmed by 4 K everywhere. These two experiments were run for 11 years, but the first year in

both experiments was discarded to make sure that the model had reached a balanced state. The experiments featured the diurnal cycle but no seasonal cycle; the incoming solar radiation was fixed to its equinoctial value. The model was run at T159 resolution (corresponding to approximately 125 km grid spacing) and with 60 model levels.

In both **Papers III** and **IV**, an objective cyclone tracking algorithm, TRACK (Hodges, 1994, 1995) was applied. TRACK was used to identify ETCs as localised maximum of 850-hPa relative vorticity truncated to T42 (**Paper IV**) or T63 (**Paper III**) resolution. In **Paper III**, TRACK was used to objectively determine the track of Ophelia in the OpenIFS simulation, and to calculate various diagnostic variables following the centre of the storm. In **Paper IV**, TRACK was applied to identify all ETCs occurring at 20°N - 90°N, travelling at least 1000 km and lasting at least for two days. These criteria were applied in order to avoid including tropical, stationary and mesoscale systems to the analysis.

After identifying the cyclone tracks in **Paper IV**, the structural changes were investigated with composite averages of the cyclones. These composites were created from the 200 strongest ETCs in both the control and the warm experiments. The method of creating the composites was the same as in Catto et al. (2010) and Dacre et al. (2012), and is briefly explained as follows. First, the tracks of the 200 strongest cyclones were identified from the model output data. Then, along the tracks, relevant meteorological variables were interpolated to a spherical grid centered on the cyclone centre, and after this, the tracks were rotated so that all the cyclones were travelling to the same direction. Finally, before taking the composite averages, the life cycles of the storms were offset with respect to the time of maximum intensity. With these procedures, we avoided the smoothing errors which would arise from averaging together cyclones which were travelling to the opposite directions, or were in a totally different stage in their life cycle.

2.4 Validation of the diagnostic methods

2.4.1 Vertical motion

In order to validate the diagnostic method, the vertical motion calculated by the omega equation was compared to the model-resolved vertical motion in **Paper I**, **III** and **IV**. As seen from Fig. 1d, the QG omega equation gives a reasonably good estimate of

the areas of strongest upward and downward motion, but many small-scale details are missing compared to ω from the WRF model (Fig. 1b). For this reason, the time-averaged correlation between the QG omega equation and ω from WRF in the simulation represented in **Paper I** was only 0.53 at 700 hPa (not shown). In the upper troposphere, where the effect of neglected terms (diabatic heating and friction) is smaller, the correlation was slightly better, being around 0.65. The intermediate form of omega equation used in **Paper IV** was found to describe vertical motion clearly better than the QG omega equation. In the latitude band of 30-60°N we documented correlation coefficients of 0.84 at 700 hPa and over 0.9 at 500 hPa (not shown).

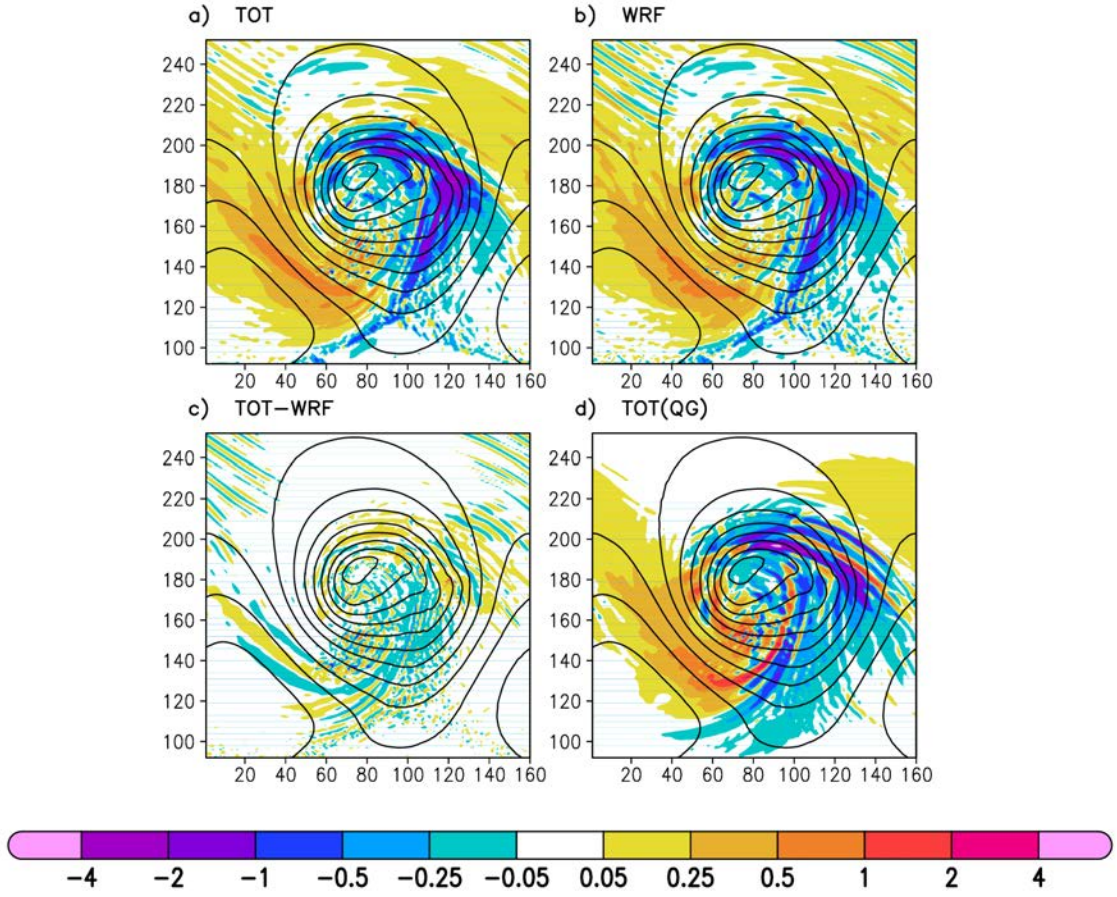

Figure 1: (a) The solution of the generalized omega equation (Eq. 14), (b) the simulated ω directly from the WRF model, (c) their difference, and (d) the solution of the QG omega equation (Eq. 1) at 700 hPa nearly at the time of maximum intensity of the storm simulated in **Paper I**. The contours show the geopotential height at 900 hPa. The labels on the x and y axes indicate grid point numbers. Figure adopted from **Paper I**.

Because the generalized omega equation has been derived directly from the primitive equations, it characterizes atmospheric vertical motion without any simplifying assumptions. Thus, ideally, the correlation against model-resolved vertical motion should be close to 1.0. In fact, this was actually the case in the mid-troposphere, where we documented correlation of 0.95 (**Paper I**) and 0.92 (**Paper III**, blue line in Fig. 2). Near the surface and higher up in the atmosphere the correlation between the generalized omega equation and the model-resolved ω is weaker due to the homogeneous

boundary conditions used in solving the omega equation. Note that in both papers, the correlation was calculated from the area centred at the ETC where the vertical motions are naturally stronger than on average in the atmosphere. When comparing the spatial fields of the solution of generalized omega equation (Fig. 1a) and ω from the WRF model (Fig. 1b), the agreement is excellent. The existing small discrepancies originate from numerical errors, such as the ones arising from the estimation of time derivatives in Eq. 11.

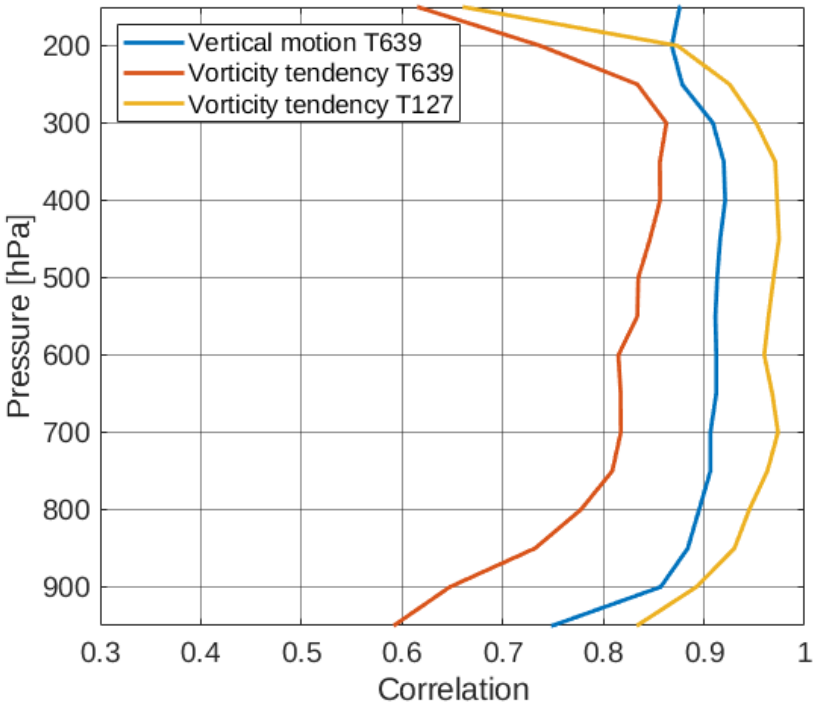

Figure 2: The correlation between the solution of the generalized omega equation and ω from the OpenIFS model (blue), and correlation between the solution of the vorticity equation and the vorticity tendency from OpenIFS at T639 resolution (red) and smoothed to T127 resolution (yellow). The values have been calculated from a 10°x10° moving box centred to the centre of storm Ophelia. Figure adopted from **Paper III**.

2.4.2 Geopotential height tendency and vorticity tendency

As regards the validation of calculated geopotential height tendencies (the sum of the RHS terms in Eq. 20) and vorticity tendencies (the sum RHS terms in Eq. 21), the comparison was made to time derivatives of geopotential height and vorticity fields. The time derivatives were estimated with the central difference method from the actual geopotential height and vorticity fields from the model output. This made the comparison sensitive to the output interval of the model data, since the estimation of the time derivatives improves when the output interval becomes smaller. 30-min output interval was used In **Paper I** and one-hour in **Paper III**, which were compromises between accuracy and the resulting data volume.

For the geopotential height tendency, our diagnostic tool reproduced the time derivative of geopotential height from the model very well, with correlation of 0.95 at 900 hPa and 0.97 at the upper troposphere (not shown) in **Paper I**. Vorticity tendency contains much more small-scale noise than the geopotential height tendency, and thus the correlation is more vulnerable to numerical errors. At T639 resolution, which corresponds to about 30 km grid spacing, the correlation between the solution of the vorticity equation and the time derivative of model-resolved relative vorticity in **Paper III** was 0.65 at 900 hPa, but exceeded 0.85 in the upper troposphere (red line in Fig. 2). When the vorticity tendency fields were smoothed to T127 resolution, the correlation improved to 0.90-0.96 in the free troposphere (yellow line in Fig. 2).

In summary, our diagnostic methods for geopotential height tendency and relative vorticity tendency closed the tendency budgets reasonably well with no considerable residuals. The same was true for the vertical motion calculated with the generalized omega equation (Fig. 1c), but not for the QG omega equation in **Paper I**. Thus, the QG equation was not used further in the meteorological analysis. Our validation results indicate that the equations as well as the numerical methods used in solving them are credible and they can be employed for studying the dynamics of ETCs.

2.5 Cyclone energetics

The cycle of "mechanical energy" in the atmosphere can be depicted with the simple 4-component diagram (Lorenz, 1955) shown in Fig. 3. The two upper boxes describe the storages of available potential energy of the zonal mean flow (A_Z) and the kinetic

energy of the zonal mean flow (K_Z). The lower boxes represent the storages of available potential energy and kinetic energy associated with the atmospheric eddies (A_E and K_E, respectively). The energy of eddies is sometimes decomposed further into the parts associated with stationary and transient eddies (e.g. in Hernández-Deckers and von Storch, 2011), but for simplicity, this division is not made here.

The energy generation terms, the conversion terms between the storages, and the energy dissipation terms have been marked in Fig. 3 with the arrows. The approximate numerical values, according to Boer and Lambert (2008), for both the storages and the conversion terms have also been given.

The main flow of mechanical energy in the atmosphere is marked with the bold arrows in Fig. 3, and can be qualitatively explained as follows:

1) Available potential energy of the zonal mean flow (A_Z), which is the measure of the baroclinicity, is generated (G_Z) continuously when the solar heating tends to increase the meridional temperature differences between low and high latitudes.

2) A_Z is converted into available potential energy of the eddies (A_E) via the conversion term between A_Z and A_E ($C(A_Z, A_E)$), if the meridional heat flux in the eddies is directed towards lower temperatures. This means that the disturbances tend to reduce the meridional temperature differences but increase them in the zonal direction.

3) Within the eddies, if the relatively warm air rises and the cold air sinks, A_E is further converted into kinetic energy of the eddy (K_E). This process is described by the conversion term $C(A_E, K_E)$ in Fig. 3.

4) Finally, most the K_E is destroyed through the dissipation of K_E (D_E). However, about 20 % of the eddy kinetic energy is converted to the kinetic energy of the zonal mean flow via $C(K_E, K_Z)$.

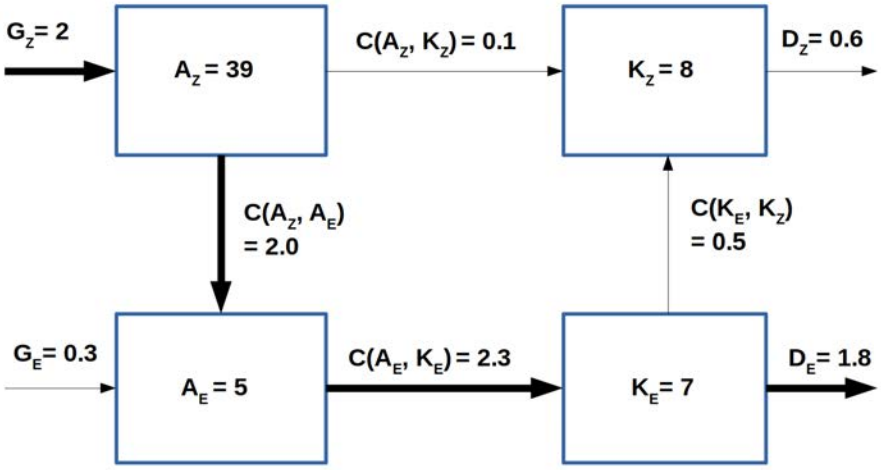

Figure 3: The globally and annually averaged cycle of mechanical energy in the atmosphere. The numerical values are averaged over two reanalysis datasets (Boer and Lambert, 2008). The upper row describes the available potential energy (A_Z) and the kinetic energy (K_Z) of the zonal mean flow, and the lower row describes the available potential energy (A_E) and the kinetic energy (K_E) of the eddies. The unit for storages is 10^5 J/m^2 and for conversions W/m^2. The figure is modified from Fig 4. in Boer and Lambert (2008).

In **Paper II**, the storages A_Z, A_E, and K_E as well as the conversion terms $C(A_Z, A_E)$, $C(A_E, K_E)$ and the dissipation rate D_E were calculated for the model-simulated cyclone in both present-day climate conditions and for three different experiments where the initial temperature distribution was altered. The equations used for the calculation are based on Lorenz (1955) and Oort (1964), and can be found from Section 2.3 of **Paper II**.

3 Physical processes affecting the evolution of extratropical cyclones

The physical processes affecting the evolution of the simulated ETC were studied in **Paper I** and **III**, and partially also in **Paper IV**. In **Paper I**, the contributions of the different physical processes on the life cycle of the ETC were studied using a highly

controlled model configuration where only one ETC was simulated (see Section 2.3.1). In **Paper III**, the main target was to apply the diagnostic method to the extratropical transition of a tropical cyclone, and investigate what is the role of the different processes in an ETC which originates from a strongly diabatically-driven hurricane.

3.1 Idealised simulations

Figure 4 shows the decomposition of atmospheric vertical motion at 700 hPa associated with an idealised ETC in the baroclinic life cycle simulation at the time when the cyclone is close to its maximum intensity. The total vertical motion, which is presented in Fig. 4f, has been obtained by summing the individual terms (Fig. 4a-e) together. The total field is in a very close agreement with the model-resolved vertical motion (as shown earlier in Fig. 1a and b).

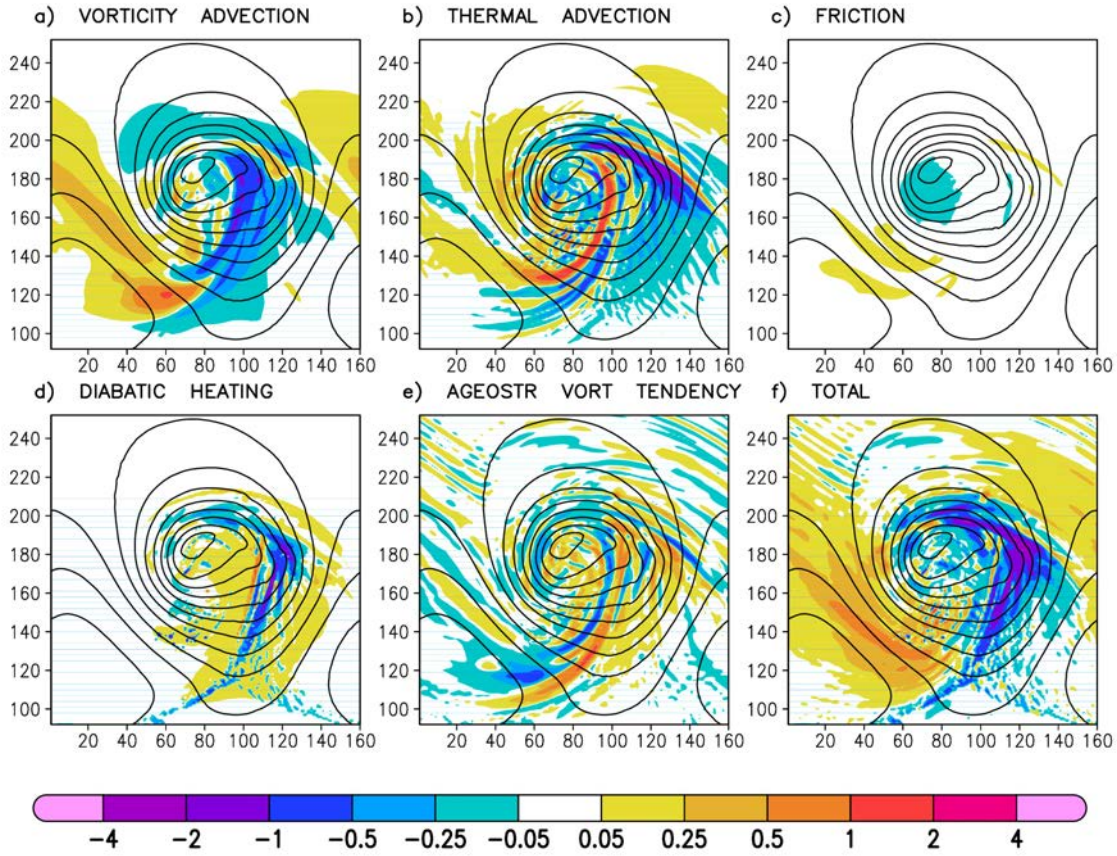

Figure 4: Pressure coordinate vertical motion ω at 700 hPa (colours, with unit of Pa s^{-1}) induced by (a) vorticity advection, (b) thermal advection, (c) friction, (d) diabatic heating, (e) imbalance term, and (f) the total vertical motion. The contours show 900 hPa geopotential height. Figure adopted from **Paper I**.

Omega due to vorticity advection (Fig. 4a) shows large-scale ascent mostly on the southeastern flank of the surface low. In this area, the non-divergent vorticity advection ahead of the upper trough increases upwards which in turn forces ascent in order to maintain hydrostatic balance. The ascent due to thermal advection (Fig. 4b) has more small-scale features, and is maximized in the area of the warm front where the warm air advection is strongest. In the vicinity of the cold front, the effects of vorticity advection and thermal advection seem to compensate each other. This area of cancellation is a well-known feature in ETCs (visible also in Fig. 10 in **Paper IV**) and results from the fact that upward increasing cyclonic vorticity advection and cold-air advection take place in the same area.

Friction causes upward motion near the centre of the low (Fig. 4c) due to the frictional convergence of surface winds and the subsequent Ekman pumping (e.g. Beare, 2007). The magnitude of the ascent is quite weak at 700 hPa, partly due to the fact that the vertical motions induced by friction reach their maximum at lower levels, usually at 900-800 hPa (Stepanyuk et al., 2017). In **Paper III**, we found that the maximum of ascent associated with Ekman pumping rose from 950 hPa to 850 hPa during the extratropical transition of Storm Ophelia.

Diabatic heating, which in the free troposphere in this simulation results from the latent heat release associated with condensation and freezing of water vapor, enhances the rising motion considerably within the frontal zones (Fig. 4d). There are also some small-scale regions of ascent behind the cold front, which are related to the shallow convection taking place when cold air flows above the warm sea surface. Note that latent heat release cannot be considered a totally independent cause of rising motion, but it rather acts as a positive feedback phenomenon which typically requires pre-existing rising motion to occur.

The vertical motion field attributed to the imbalance term (Fig. 4e) is substantial but noisy. One can note the tendency of this term to cancel out the effect of thermal advection (Fig. 4b), especially in the vicinity of the cold front. The reason for this behaviour is that in the atmosphere the temperature tendencies induced by thermal advection are usually small by their temporal and spatial scales, particularly at low levels. However, often the atmosphere does not have time to adjust to these imbalance situations between temperature and vorticity tendencies and thus the compensating vertical motion does not occur. These situations are taken into account by the imbalance term, which often cancels out the effects of thermal advection.

Although these results are directly applicable to the idealised cyclone used in **Paper I**, they reflect the typical distributions of the vertical motions caused by the forcing terms for ETC developed within a baroclinic jet at mid-latitudes over sea surface. In the real world, however, ETCs can be far away from the beautiful, textbook-type cyclones studied in **Paper I**. The variability in the structure and intensity among ETCs stems from the changing contributions of the different forcing mechanisms affecting their evolution. For example, continental cold-season ETCs have often limited access to atmospheric moisture, and thus they are driven more by the dynamical terms (e.g. by vorticity advection in the study by Rolfson and Smith, 1996). On the other hand, ETCs formed above sea surface, and especially those which have tropical origins, are

more diabatically-driven. One example of such a system was Hurricane Ophelia, which underwent an extratropical transition and transformed into a powerful ETC when it hit Europe in October 2017. The contributions of the different physical processes for the low-level cyclone were analysed in **Paper III**, and the main results are presented in the next section.

3.2 Extratropical cyclone transformed from a tropical cyclone

Hurricane Ophelia was a category 3 hurricane which developed over the eastern North Atlantic in October 2017. Ophelia was exceptionally strong for its longitude - National Hurricane Center stated in their post-season report (Stewart, 2018) that Ophelia was the easternmost major hurricane observed in the satellite era. Ophelia underwent an extratropical transition (ET; Sekioka, 1956; Palmén, 1958), a process where the tropical characteristics of the cyclone are replaced by the features typical for ETCs, such as cold core and fronts. The ET of Ophelia was fairly classic; the storm interacted with a positively tilted mid-latitude trough, and the enhanced upper-level divergence due to a favorable position at the right entrance region of the jet stream ensured that Ophelia remained a very strong storm during the ET period. For more detailed synoptic overview of the event, see **Paper III**.

There were two main reasons why we chose a cyclone that transitions from tropical to extratropical as the subject of the case study in **Paper III**. First, we wanted to study a case which would provide a large variety of physical processes affecting to the evolution of the cyclone. Transitioning cyclones are often strongly involved with both thermodynamic and dynamic processes, and thus they can act as good example of such a case. Secondly, to our knowledge, there are no existing literature where the generalized omega equation has been applied to a cyclone with tropical origin.

Figure 5 shows the time series of vorticity tendencies induced by the different forcing terms (RHS terms of Eq. 21) at the cyclone centre. The vorticity tendencies have been averaged over a small circular area following the cyclone centre, which helps to eliminate the vorticity tendency component related to the movement of the storm. Thus, the values in Fig. 5 should represent the changes in the cyclone's intensity. A positive vorticity tendency means that the low-level vorticity at the storm's centre is increasing, which in turn reflects an increased intensity of the cyclone. The approximate times of tropical, transition, and extratropical phases of Ophelia were determined using

a cyclone phase space diagram (Hart, 2003; Evans and Hart, 2003) and the post-season report by the National Hurricane Center (Stewart, 2018).

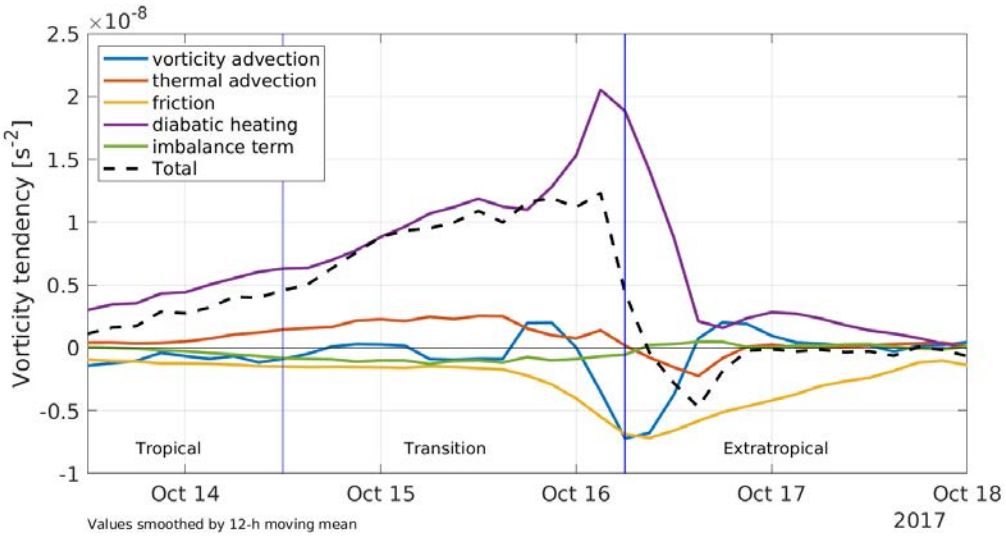

Figure 5: The time evolution of vorticity tendencies due to different forcing terms. The values have been averaged over the 900–800-hPa layer and over a circular area with a 1.5° radius centred on the maximum of the T127 vorticity field. In addition, the values are 12-hour moving averages. The vertical lines mark the approximate times of tropical, transition, and extratropical phases of the storm. Figure is modified from **Paper III**.

The striking feature in Fig. 5 is the dominance of diabatic heating (purple line) during the tropical, transition and extratropical phases of the storm. Furthermore, the contribution of diabatic heating increased during the life cycle, and peaked just when Ophelia was reaching its extratropical phase. In **Paper III**, we found that most of the low-level vorticity tendency at the centre of the cyclone in the tropical phase was generated via the convection scheme of the model. In contrast, the microphysics scheme was responsible for most of the low-level vorticity tendency at the cyclone's centre in the extratropical phase. This shift from convection scheme to microphysics scheme illustrates how the near-core convection transformed into large-scale ascent during the ET of Ophelia. Furthermore, it would be interesting to perform a more comprehensive analysis of whether this feature could be used as a proxy in objectively identifying the tropical, transition and extratropical phases of the transitioning storms.

Another interesting finding was the neutral, or even negative contribution from the vorticity advection (blue line in Fig. 5) to the evolution of the low-level vortex. In the tropical phase and during most of the transition period, the vorticity tendency by vorticity advection at the cyclone centre was close to zero. However, when the cyclone reached its extratropical phase, the low-level vorticity tendency that was due to vorticity advection became markedly negative, to the level of magnitude attributed to the friction term. We found that this behaviour was due to the secondary circulation of the cyclone. The low-level convergent winds transported air with lower cyclonic vorticity to the centre of the storm, and, thus, reduced effectively the vorticity maximum associated with the storm's centre. Similar results have been found earlier for example by DiMego and Bosart (1982) and Räisänen (1997). In **Paper III**, we speculate that the importance of non-divergent vorticity advection is probably larger higher up in the atmosphere in triggering the vertical motion required for the formation of latent heat release above the low-level vortex. This hypothesis is supported by the favourable interaction of Ophelia with the upper-level trough, as explained in more detail in **Paper III**.

Thermal advection was contributing positively particularly during the transition period (red line in Fig. 5), when warm, subtropical airmass was pushed towards mid-latitudes along with Ophelia. The situation changed during the extratropical phase, when the storm occluded and polar maritime airmass wrapped around the cyclone's warm core. The overall contribution from thermal advection is however quite weak, as the advection term right at the low-level centre must be zero by definition.

To conclude the results from **Paper III**, it can be stated that baroclinic processes played a relatively small role for the generation of low-level vorticity during the post-ET intensification period of Ophelia. Instead, we find that diabatic heating, dominated by the convection in the tropical phase and the large-scale ascent in the extratropical phase, was the leading forcing in the strengthening of Ophelia. However, it should be kept in mind that we analysed the vorticity tendencies only for the surface cyclone, and thus the results are not applicable at higher levels, where the baroclinic forcings were presumably more important. Based on only one case study, it is difficult to say whether our results are typical for transitioning tropical cyclones. In **Paper I** we performed similar analysis for a regular, idealized ETC, and found that adiabatic processes played approximately an equally important role as diabatic processes.

4 Effect of warmer climate

This section focuses on how the structure and energy cycle of ETCs will change with climate change. In the first subsection, the changes in the structure of the cyclones with the warming are discussed. The changes in the structure of ETCs were investigated partly in **Paper II** with WRF model, but more comprehensively in **Paper IV** with OpenIFS model. These structural changes in the cyclones with the warming lead to changes also in their energy cycle, which was investigated in **Paper II**.

4.1 Changes in the characteristics and structure of the cyclones

In **Paper II** and **IV**, and in line with the existing literature, we found that ETCs which form in a warmer environment have some characteristics that are different from those that form in a colder environment. The main reason for the differences is the increased atmospheric moisture content, as the warmer air can naturally hold more moisture. In short, the higher moisture content means that diabatic processes in the cyclone become more prevalent during its evolution.

In **Paper II**, the cyclone which developed in 6 K warmer environment deepened more rapidly and ended up being about 7 hPa deeper than the cyclone in the control simulation. The faster deepening was linked to the enhanced release of latent heat above the surface low. Moreover, the heating above the low and the subsequent deepening did not occur steadily, but there were clearly identifiable deepening periods during the life cycle of the storm. In contrast, the cyclone in the present-day environment deepened more gradually, owing this behaviour to more dynamic influences rather than diabatic processes. The faster deepening rate in ETCs formed in warmer and moister conditions is also supported by the findings of **Paper IV**: the strongest 200 cyclones in the warmer climate deepened approximately 25 % faster than the strongest 200 in the present climate. However, when all ETCs were considered (instead of the strongest 200), on average there was no change in the deepening rate.

When looking at the structural changes of ETCs with the warming, a common result from the numerical simulations in **Paper II** and **IV** was the expansion of the area of ascent to downstream of the cyclone centre. This feature is well seen in Figure

6, which shows the 700-hPa vertical motion and its response for the warming in the composite ETC 24 hours before the time of maximum intensity (Fig. 6a) and at the time of maximum intensity (Fig. 6b). The ascent at both panels is maximised to the eastern side of the low (similarly as in Fig. 4f), in the warm sector region where the warm conveyor belt of the low is situated. However, in the experiment where the SSTs were warmed by 4 K, the ascent does not increase precisely at its maximum area, but rather on the poleward and downstream side of the present-day maximum. This result is in line with **Paper II**, where we found that the area of warm-frontal ascent migrated eastward and coincided less well with the warm sector when the atmospheric temperature was increased (see Fig. 6 in **Paper II**).

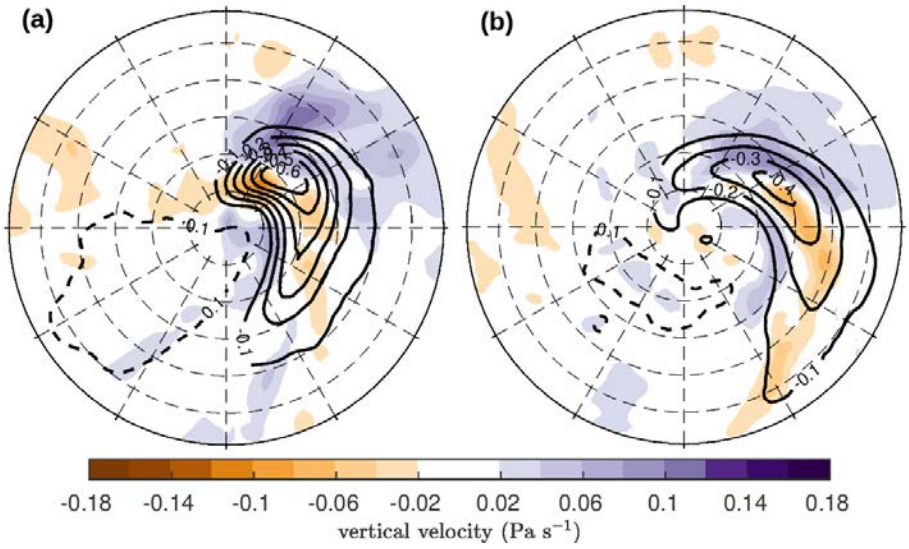

Figure 6: Composite mean and change in 700-hPa vertical velocity in pressure coordinates at (a) 24 hours before the time of maximum intensity and (b) at the time of maximum intensity. Contours show the control values and shading the difference with the warming. Both panels are the composites of the strongest 200 ETCs in each experiment. Modified from **Paper IV**.

A natural follow-up question is then which processes cause the expansion of ascent downstream of the cyclone centre. We discovered that the cyclone-related ascent changes in a complex manner. Firstly, the ascent attributed to thermal advection shifts more poleward relative to the cyclone centre (Fig. 7a). We conclude that this is related to movement of the warm front further away from the cyclone centre with the warming, resulting in a decrease of ascent (or increase of descent) near the cy-

clone centre. However, the primary reason for the downstream increase of ascent is the broadening of the upper-level trough, which induces more upward motion via forcing of vorticity advection (Fig. 7b). Finally, due to increased moisture content, the release of latent heat and thus ω attributed to diabatic heating will strengthen. This is projected to occur mainly within the warm front where the precipitation is strongest. In summary, all these three processes contribute to the increase of ascent downstream and poleward relative to the center of the composite cyclone, but the most pronounced and geographically widest response seems to originate from the vorticity advection term.

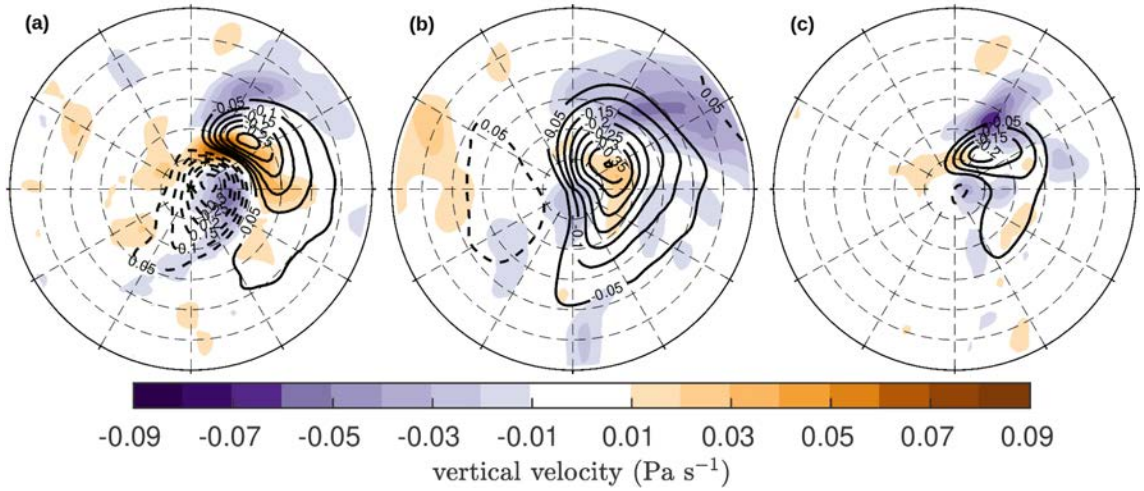

Figure 7: Composite mean and change in 700-hPa vertical velocity in pressure coordinates due to a) thermal advection, b) vorticity advection and c) diabatic heating at 24 hours before the time of maximum intensity. Contours show the control values and shading the difference with the warming. All composites are of the strongest 200 extra-tropical cyclones in each experiment.Modified from **Paper IV**.

While the area of ascent caused by vorticity advection moves slightly downstream due to the broader upper-level trough, the absolute maximum of ascent attributed to vorticity advection decreases slightly. Furthermore, a small decrease in the maximum values of ascent due to thermal advection was also found to take place with the warming. In contrast, the maximum of ascent attributed to diabatic heating increased slightly. Thus, the upward motion in ETCs is expected to become more diabatically-driven in the warmer climate. The numerical values for the maximum values are given in Table 2 of **Paper IV**.

We also found in **Paper IV** that vertical motions in ETCs became slightly more

asymmetric with the warming (not shown). Specifically, the increased asymmetry stems from the fact that the mean upward motion averaged over the composite cyclone area was found to grow in absolute terms, while the mean downward motion was found to weaken. No changes in the fractional area of ascent in ETCs were observed.

As a natural consequence of the fact that there is more moisture in the warmer climate, the precipitation associated with ETCs will increase. According to the simulations performed in **Paper IV**, the cyclone-related total precipitation increased by up to 50 % with the 4-K warming. Furthermore, the response of total precipitation was partitioned into contributions from large-scale precipitation and convective precipitation. It was found out that the maximum of large-scale precipitation moves spatially poleward with the warming, while the area of convective precipitation remains approximately at the same area. The poleward shift in large-scale precipitation is in line with the changes in the area of large-scale ascent presented earlier.

Finally, the 900–700-hPa potential vorticity (PV) was found to increase at all stages of the cyclone evolution. The largest increase of PV is expected to occur slightly poleward from the cyclone centre, which results from the expansion of ascent and the consequent enhanced large-scale precipitation. This induces diabatically more low-level PV in that region via enhanced latent heating. Elsewhere in the surroundings of the storm centre, a small increase of PV was found to take place due to increased stratification.

4.2 Changes in the energy cycle of cyclones

As seen from Fig. 3, the main energy cycle of the atmosphere is dependent on the existence of eddies. These eddies, which consist largely of ETCs, are a crucial part of the atmospheric general circulation. In a warmer climate, the structure of ETCs, and hence their ability to convert atmospheric potential energy into kinetic energy could be changed, which has effects eventually for the whole general circulation. In **Paper II**, the energy cycle of the WRF-simulated ETC was investigated using three different climate change scenarios which were incorporated to the initial state of the model one at a time (see Section 2.3.1).

The main outcome in the simulations conducted in the warmer environment was that the increased atmospheric temperature and hence the moisture content compared to typical present-day values decreased the capability of the cyclone to exploit the avail-

able potential energy of the zonal mean flow (A_Z). This can be seen from Fig. 8a as a smaller decrease of A_Z with time in the warmer simulation (red solid line) compared to the control simulation (blue solid line), and from Fig. 8d as a weaker conversion of A_Z to available potential energy of the eddy (A_E).

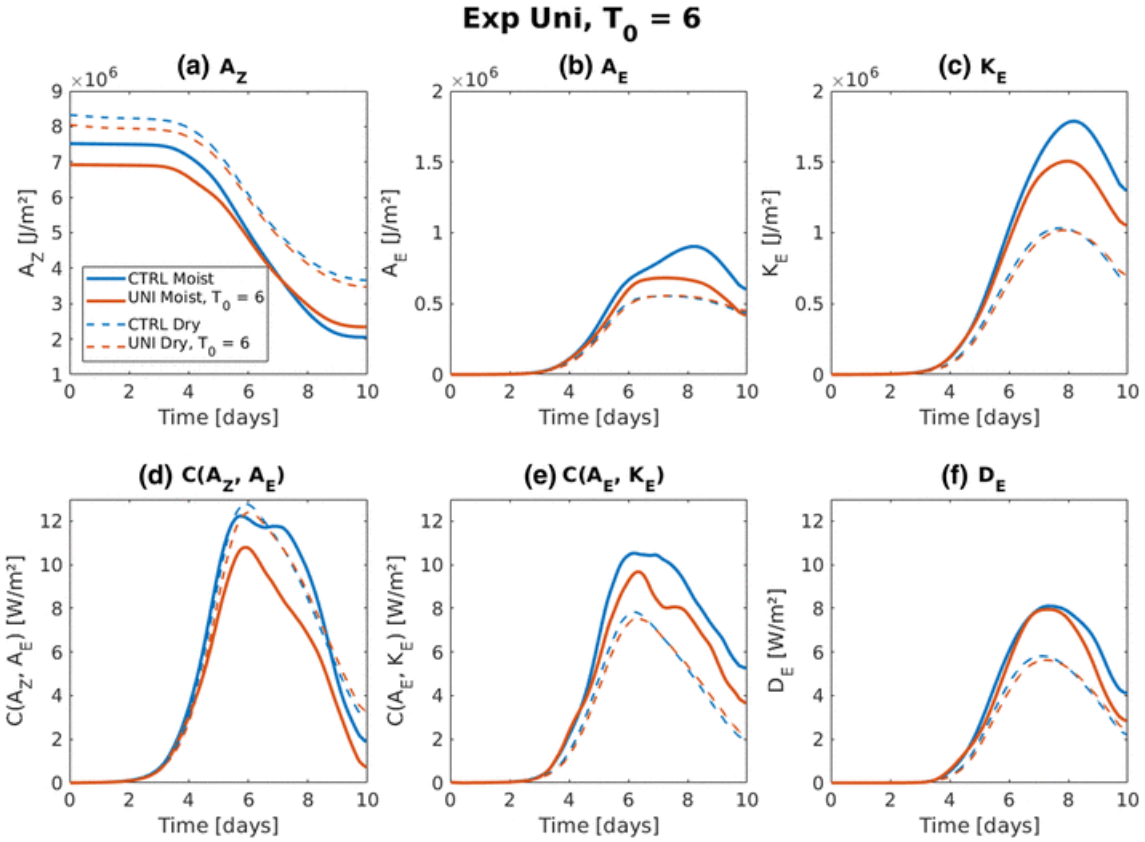

Figure 8: Time evolution of (a) available potential energy of the zonal mean flow (A_Z), (b) available potential energy of the eddy (A_E), (c) kinetic energy of the eddy (K_E), (d) energy conversion from A_Z to A_E, (e) energy conversion from A_E to K_E, and (f) the dissipation rate of K_E. The dashed lines indicate simulations without atmospheric moisture and solid lines with moist environment. The blue lines (both dashed and solid) depict the control runs and the red lines depict the runs where temperature has been increased uniformly by 6 K. Figure adopted from **Paper II**.

Due to the weaker conversion from A_Z to A_E, the maximum of A_E remained about 25% smaller in the warmer environment (red solid line in Fig. 8b) than in the control run (blue solid line). The reason for this behaviour remained slightly unclear, but we suspect that the weakening of the jet stream by 1.5 m s^{-1} with the warming may play a

role, via weaker meridional heat flux which acts to generate A_E in the atmosphere. The weaker jet stream results from the uniform warming: with fixed surface pressure, the geopotential heights increased more in the northern part of the domain where the initial temperature was lower, which then acted to reduce the meridional pressure gradient and caused the deceleration of the initial zonal wind speed.

As expressed earlier, the cyclones in warmer environment are expected to intensify more rapidly and their minimum surface pressure may be lower due to increased diabatic processes. However, despite the fact that they may be deeper, the kinetic energy of these systems (K_E) may be actually lower, as seen from Fig. 8c. We suspect that this behaviour is related to the fact that the pressure minimum caused by diabatic processes can be very localised and small-scale, which does not affect considerably K_E averaged over the whole model domain, and moreover, the major contribution to K_E comes from the upper troposphere where the winds are strongest.

The physical reason for about 15 % lower K_E with the warming originates presumably from the structural changes of the ETC. We found that the core of the rising motion shifted downstream with the warming - a result which was found earlier in other studies (e.g. in Kirshbaum et al., 2018), and was confirmed later in **Paper IV**. Due to the downstream migration of ascent, the warm sector coincided less well with the area of rising motion in the eddy. Since K_E is produced when relatively warm air rises, the worse phasing between temperature and vertical motion decreases effectively the production of K_E. This reduced production of K_E in the warmer environment (red solid line) than in the control simulation (blue solid line) is seen in Fig. 8e.

In **Paper II**, we also performed two additional numerical experiments where we modified the meridional temperature gradient of the environment. Firstly, the main outcome from the experiment with reduced low-level temperature gradient was that the resulting cyclone was weaker in terms of maximum of A_E and K_E in both dry and moist simulations (not shown, see **Paper II**). This highlights the fact the low-level temperature gradient has a substantial control over the ETC intensity which results from the decreased baroclinic processes rather than the diabatics.

Secondly, we discovered that the energy cycle of the idealized ETC responds differently to the changes in the lower and upper level temperature gradient. While modifying the lower level temperature gradient had a clear effect on A_E and K_E in both dry and moist simulations, modifying the upper-level temperature gradient provided slightly weaker

control (not shown, see **Paper II**). Furthermore, the response to increased upper level temperature gradient was different depending on the presence of atmospheric moisture. In the dry environment, the interaction between upper and lower level waves was weaker, and thus the increase of baroclinicity at upper levels was not materialized as higher K_E. In the moist atmosphere, in contrast, the mid-tropospheric latent heating acted as a link between the upper and lower PV anomalies and thus the increased baroclinicity in the upper troposphere was reflected more efficiently in the intensity of the simulated cyclone, increasing thus also K_E.

As a summary of **Paper II**, it can be said that both the uniform warming of the atmosphere and the decrease of the lower-level temperature gradient tend to reduce the energy of ETCs. Because both phenomena are taking place simultaneously in the northern mid-latitudes, it is expected that in the future climate, the kinetic energy associated with ETCs will potentially decrease. However, more research is needed to make further conclusions, especially because in our simulations the temperature changes were conducted one at a time while in the real world they are occurring simultaneously. Given the possible nonlinear responses and also the increase of the upper-level temperature gradient, drawing direct conclusions to the real world must be done with caution.

5 Discussion and conclusions

This thesis contributed to understanding of (1) the role of various synoptic-scale forcing terms to the evolution of ETCs and (2) the effects of warmer climate to the characteristics and structure of ETCs. The point (1) was studied with the diagnostic tools which consisted of the generalized omega equation and either the Zwack-Okossi equation or the traditional vorticity equation. The diagnostic tools were applied to an idealised, text-book type of ETC as well as a real-world, post-tropical ETC. These two cases represented very different examples of ETCs in terms of their synoptic evolution and the used model configuration.

The diagnostic tools performed well in reproducing the total atmospheric vertical motion, geopotential height tendency, and vorticity tendency when those quantities were compared to the corresponding model-simulated fields. The applied decomposition revealed the contributions of different physical processes behind the total fields. While both adiabatic and diabatic processes were important for the development of the idealized ETC, the transitioned ex-hurricane was strongly driven by diabatic processes.

The diagnostic method presented in this thesis has the advantage that vertical motion is partitioned into its causes rather than treated as an independent forcing for weather systems. In many earlier diagnostic studies (e.g. Azad and Sorteberg, 2009; Fu et al., 2018) the adiabatic heating/cooling associated with vertical motions is interpreted as an independent forcing, which is problematic due to the strong tendency of vertical motions to compensate the effect of other physical processes.

Our finding that the simulated cyclone in the warmer environment in **Paper II** was unable to exploit the atmospheric baroclinicity as efficiently as the cyclone in the control simulation was consistent with Tierney et al. (2018) but contrary to Kirshbaum et al. (2018). However, the results obtained from baroclinic wave simulations can be surprisingly sensitive to the initial jet stream configuration, as shown in Kirshbaum et al. (2018). Furthermore, Kirshbaum et al. (2018) also stress the fact that the simulated ETC may start to unphysically interact with itself in the channel mode simulations, which is naturally not a desirable feature. Nevertheless, the decreased conversion from A_E to K_E and, thus, eventually the lower K_E with the uniform warming reported in **Paper II** seems to be a more robust result, which is confirmed by numerous other studies with idealized baroclinic waves (e.g. Booth et al., 2013; Tierney et al., 2018; Kirshbaum et al., 2018) and also with global model simulations (e.g. O'Gorman, 2011;

Pfahl et al., 2015).

The results from the simulations conducted in the warmer climate in **Paper IV** suggest faster deepening rate and larger number of extreme ETCs, in line with Büeler and Pfahl (2019), who also reported that the most intense ETCs could reach higher intensity in warmer climates. However, these results seem to be inconsistent with simulations performed with fully coupled climate models (Bengtsson et al., 2009; Catto et al., 2011; Seiler and Zwiers, 2016). This may be due to the absence of Arctic amplification in our model set-ups, which decreases the lower level meridional temperature gradient and reduces the ETC intensity, as evidenced in **Paper II**. Thus, the results expressed in **Paper IV** may be more applicable to the southern hemisphere in this sense, but they also confirm the impact of Arctic amplification on the intensity of ETCs.

While it is evident that simulating one ETC with baroclinic wave configurations has its limitations when attempting to draw conclusions to real-world changes in ETCs, the aqua-planet configuration used in **Paper IV** serves a useful intermediate step which accounts for example the non-linear interactions between the eddies. However, one interesting step forward from **Paper IV** would be to add the polar amplification to the simulations and see how the intensity and structure of ETCs respond to both warming and the decrease of lower level temperature gradient simultaneously, similarly as in the real world.

In the future, it would be valuable to develop further the diagnostic software to be easier to adopt by different end-users. This would need additional programming to make the tool fit seamlessly for different model outputs, and run with different super-computer environments. As regards scientific future directions, it would be interesting to conduct more comprehensive analysis on the forcing term contributions for ETC development and investigate for example their geographical or seasonal differences, or target the study only to transitioning cyclones and explore whether our findings in the Ophelia case can be generalized for other cyclones undergoing extratropical transition. The tool could also be applied to climate change simulations with OpenIFS, and investigate how much the contributions of different adiabatic and diabatic terms to the intensity of ETCs change with the warming.

6 Review of papers and the author's contribution

This thesis consists of four peer-reviewed publications that aim to increase the general knowledge on the dynamics of ETCs by (1) presenting and applying the diagnostic method for an idealized baroclinic wave (**Paper I**) and a real-world case study (**Paper III**), and (2) studying how ETCs respond to climate change in idealized baroclinic wave simulations (**Paper II**) and global model simulations with intermediate complexity (**Paper IV**).

Paper I acts as a documentation of the diagnostic method which can be used for idealized baroclinic wave simulations by the Weather Research and Forecasting (WRF) model or similar models which employ Cartesian coordinate system. The author contributed to the software development, did the meteorological analysis and wrote most of the manuscript.

Paper II provides insight into how sensitive the different energy quantities and the conversions between them are for the anticipated temperature changes in the future climate. We also made an attempt to identify which structural changes of ETCs are behind the changes of energetics. The author performed the model simulations, analysed the results together with the co-authors, and was responsible of writing the paper.

Paper III extends the method used in **Paper I** for global model output on a spherical grid rather than Cartesian. We demonstrate the method by analysing the synoptic-scale forcing terms affecting the extratropical transition of Hurricane Ophelia (2017). The author contributed to the technical development of the diagnostic method. The application of the tool, most of the analysis, and almost all of the writing were performed by the author.

Paper IV investigates the changes in the characteristics and structure of ETCs with the warming of climate by using 10 year-long aqua-planet simulations. The paper extends the topic of **Paper II** into a global domain and beyond one cyclone to much larger sample size. The author performed the decomposition of the vertical motion with the diagnostic omega equation tool, and contributed to analysing and discussing the results, together with the first author and the other co-authors.

References

Ahmadi-Givi, F., Graig, G., and Plant, R. (2004). The dynamics of a midlatitude cyclone with very strong latent-heat release. *Quarterly Journal of the Royal Meteorological Society*, 130(596):295–323.

Allen, R. J. and Sherwood, S. C. (2008). Warming maximum in the tropical upper troposphere deduced from thermal winds. *Nature Geoscience*, 1(6):399.

Azad, R. and Sorteberg, A. (2009). A diagnosis of warm-core and cold-core extratropical cyclone development using the Zwack–Okossi equation. *Atmospheric Science Letters*, 10(4):220–225.

Azad, R. and Sorteberg, A. (2014a). The vorticity budgets of North Atlantic winter extratropical cyclone life cycles in MERRA reanalysis. Part I: development phase. *Journal of the Atmospheric Sciences*, 71(9):3109–3128.

Azad, R. and Sorteberg, A. (2014b). The vorticity budgets of North Atlantic winter extratropical cyclone life cycles in MERRA reanalysis. Part II: decaying phase. *Journal of the Atmospheric Sciences*, 71(9):3129–3143.

Beare, R. J. (2007). Boundary layer mechanisms in extratropical cyclones. *Quarterly Journal of the Royal Meteorological Society*, 133(623):503–515.

Bengtsson, L., Hodges, K. I., and Keenlyside, N. (2009). Will extratropical storms intensify in a warmer climate? *Journal of Climate*, 22(9):2276–2301.

Boer, G. and Lambert, S. (2008). The energy cycle in atmospheric models. *Climate Dynamics*, 30(4):371–390.

Booth, J. F., Wang, S., and Polvani, L. (2013). Midlatitude storms in a moister world: lessons from idealized baroclinic life cycle experiments. *Climate Dynamics*, 41(3-4):787–802.

Büeler, D. and Pfahl, S. (2017). Potential vorticity diagnostics to quantify effects of latent heating in extratropical cyclones. Part I: methodology. *Journal of the Atmospheric Sciences*, 74(11):3567–3590.

Büeler, D. and Pfahl, S. (2019). Potential vorticity diagnostics to quantify effects of latent heating in extratropical cyclones. Part II: application to idealized climate change simulations. *Journal of the Atmospheric Sciences*, 76(7):1885–1902.

Caron, J.-F., Zwack, P., and Pagé, C. (2006). Dionysos: A diagnostic tool for numerically-simulated weather systems. *Technical related document see http://www.dionysos.uqam.ca/doc/Dionysos.pdf*.

Catto, J. L., Ackerley, D., Booth, J. F., Champion, A. J., Colle, B. A., Pfahl, S., Pinto, J. G., Quinting, J. F., and Seiler, C. (2019). The future of midlatitude cyclones. *Current Climate Change Reports*.

Catto, J. L., Shaffrey, L. C., and Hodges, K. I. (2010). Can climate models capture the structure of extratropical cyclones? *Journal of Climate*, 23(7):1621–1635.

Catto, J. L., Shaffrey, L. C., and Hodges, K. I. (2011). Northern hemisphere extratropical cyclones in a warming climate in the HiGEM high-resolution climate model. *Journal of Climate*, 24(20):5336–5352.

Chagnon, J., Gray, S., and Methven, J. (2013). Diabatic processes modifying potential vorticity in a North Atlantic cyclone. *Quarterly Journal of the Royal Meteorological Society*, 139(674):1270–1282.

Chang, E. K. (2018). CMIP5 projected change in Northern Hemisphere winter cyclones with associated extreme winds. *Journal of Climate*, 31(16):6527–6542.

Chang, E. K., Guo, Y., and Xia, X. (2012). CMIP5 multimodel ensemble projection of storm track change under global warming. *Journal of Geophysical Research: Atmospheres*, 117(D23).

Charney, J. G. (1947). The dynamics of long waves in a baroclinic westerly current. *Journal of Meteorology*, 4(5):136–162.

Collins, M., Knutti, R., Arblaster, J., Dufresne, J.-L., Fichefet, T., Friedlingstein, P., Gao, X., Gutowski, W. J., Johns, T., Krinner, G., et al. (2013). Long-term climate change: projections, commitments and irreversibility. In *Climate Change 2013: The Physical Science Basis. Contribution of Working Group I to the Fifth Assessment Report of the Intergovernmental Panel on Climate Change*, pages 1029–1136. Cambridge University Press.

Dacre, H., Hawcroft, M., Stringer, M., and Hodges, K. (2012). An extratropical cyclone atlas: a tool for illustrating cyclone structure and evolution characteristics. *Bulletin of the American Meteorological Society*, 93(10):1497–1502.

Dacre, H. F., Martinez-Alvarado, O., and Mbengue, C. O. (2019). Linking atmospheric rivers and warm conveyor belt airflows. *Journal of Hydrometeorology*, 20(6):1183–1196.

Davis, C. A. and Emanuel, K. A. (1991). Potential vorticity diagnostics of cyclogenesis. *Monthly Weather Review*, 119(8):1929–1953.

DiMego, G. J. and Bosart, L. F. (1982). The transformation of Tropical Storm Agnes into an extratropical cyclone. Part II: moisture, vorticity and kinetic energy budgets. *Monthly Weather Review*, 110(5):412–433.

Eady, E. T. (1949). Long waves and cyclone waves. *Tellus*, 1(3):33–52.

ECMWF (2014). Documentation–Cy40r1 Part IV: Physical processes. *European Centre for Medium-Range Weather Forecasts: Reading, UK*.

Ertel, H. (1942). Ein neuer hydrodynamischer wirbelsatz. *Meteorologische Zeitschrift*, 59:277–281.

Evans, J. L. and Hart, R. E. (2003). Objective indicators of the life cycle evolution of extratropical transition for Atlantic tropical cyclones. *Monthly Weather Review*, 131(5):909–925.

Fink, A. H., Pohle, S., Pinto, J. G., and Knippertz, P. (2012). Diagnosing the influence of diabatic processes on the explosive deepening of extratropical cyclones. *Geophysical Research Letters*, 39(7).

Fu, S.-M., Sun, J.-H., Li, W.-L., and Zhang, Y.-C. (2018). Investigating the mechanisms associated with the evolutions of twin extratropical cyclones over the northwest Pacific Ocean in mid-January 2011. *Journal of Geophysical Research: Atmospheres*, 123(8):4088–4109.

Grams, C. M. and Archambault, H. M. (2016). The key role of diabatic outflow in amplifying the midlatitude flow: A representative case study of weather systems surrounding western North Pacific extratropical transition. *Monthly Weather Review*, 144(10):3847–3869.

Grams, C. M. and Blumer, S. R. (2015). European high-impact weather caused by the downstream response to the extratropical transition of North Atlantic Hurricane Katia (2011). *Geophysical Research Letters*, 42(20):8738–8748.

Hart, R. E. (2003). A cyclone phase space derived from thermal wind and thermal asymmetry. *Monthly weather review*, 131(4):585–616.

Hartmann, D. L. (2015). *Global physical climatology*, volume 103. Newnes.

Hartmann, D. L., Tank, A. M. K., Rusticucci, M., Alexander, L. V., Brönnimann, S., Charabi, Y. A. R., Dentener, F. J., Dlugokencky, E. J., Easterling, D. R., Kaplan, A., et al. (2013). Observations: Atmosphere and Surface. In *Climate Change 2013: The Physical Science Basis. Contribution of Working Group I to the Fifth Assessment Report of the Intergovernmental Panel on Climate Change*, pages 159–254. Cambridge University Press.

Hawcroft, M., Walsh, E., Hodges, K., and Zappa, G. (2018). Significantly increased extreme precipitation expected in Europe and North America from extratropical cyclones. *Environmental Research Letters*, 13(12):124006.

Hernández-Deckers, D. and von Storch, J.-S. (2011). The energetics response to a warmer climate: relative contributions from the transient and stationary eddies. *Earth System Dynamics*, 2:105–120.

Hodges, K. (1995). Feature tracking on the unit sphere. *Monthly Weather Review*, 123(12):3458–3465.

Hodges, K. I. (1994). A general method for tracking analysis and its application to meteorological data. *Monthly Weather Review*, 122(11):2573–2586.

Hoskins, B. J., McIntyre, M. E., and Robertson, A. W. (1985). On the use and significance of isentropic potential vorticity maps. *Quarterly Journal of the Royal Meteorological Society*, 111(470):877–946.

Kirshbaum, D., Merlis, T., Gyakum, J., and McTaggart-Cowan, R. (2018). Sensitivity of idealized moist baroclinic waves to environmental temperature and moisture content. *Journal of the Atmospheric Sciences*, 75(1):337–360.

Knippertz, P. and Fink, A. H. (2008). Dry-season precipitation in tropical West Africa and its relation to forcing from the extratropics. *Monthly Weather Review*, 136(9):3579–3596.

Knippertz, P., Fink, A. H., and Pohle, S. (2009). Comments on "Dry-season precipitation in tropical West Africa and its relation to forcing from the extratropics" reply. *Monthly Weather Review*, 137(9):3151–3157.

Kuo, Y.-H., Shapiro, M., and Donall, E. G. (1991). The interaction between baroclinic and diabatic processes in a numerical simulation of a rapidly intensifying extratropical marine cyclone. *Monthly Weather Review*, 119(2):368–384.

Kuwano-Yoshida, A. and Enomoto, T. (2013). Predictability of explosive cyclogenesis over the northwestern Pacific region using ensemble reanalysis. *Monthly Weather Review*, 141(11):3769–3785.

Lavers, D. A., Allan, R. P., Wood, E. F., Villarini, G., Brayshaw, D. J., and Wade, A. J. (2011). Winter floods in Britain are connected to atmospheric rivers. *Geophysical Research Letters*, 38(23).

Lee, S. H., Williams, P. D., and Frame, T. H. (2019). Increased shear in the North Atlantic upper-level jet stream over the past four decades. *Nature*, 572(7771):639–642.

Liberato, M., Pinto, J., Trigo, R., Ludwig, P., Ordóñez, P., Yuen, D., and Trigo, I. (2013). Explosive development of winter storm Xynthia over the subtropical North Atlantic ocean. *Natural Hazards and Earth System Sciences*, 13(9):2239–2251.

Liberato, M. L., Pinto, J. G., Trigo, I. F., and Trigo, R. M. (2011). Klaus–an exceptional winter storm over northern Iberia and southern France. *Weather*, 66(12):330–334.

Lorenz, E. N. (1955). Available potential energy and the maintenance of the general circulation. *Tellus*, 7(2):157–167.

Lupo, A. R. and Smith, P. J. (1998). The interactions between a midlatitude blocking anticyclone and synoptic-scale cyclones that occurred during the summer season. *Monthly Weather Review*, 126(2):502–515.

Lupo, A. R., Smith, P. J., and Zwack, P. (1992). A diagnosis of the explosive development of two extratropical cyclones. *Monthly Weather Review*, 120(8):1490–1523.

Martínez-Alvarado, O., Gray, S. L., and Methven, J. (2016). Diabatic processes and the evolution of two contrasting summer extratropical cyclones. *Monthly Weather Review*, 144(9):3251–3276.

O'Gorman, P. A. (2011). The effective static stability experienced by eddies in a moist atmosphere. *Journal of the Atmospheric Sciences*, 68(1):75–90.

O'Gorman, P. A. and Schneider, T. (2008). Energy of midlatitude transient eddies in idealized simulations of changed climates. *Journal of Climate*, 21(22):5797–5806.

Oort, A. H. (1964). On estimates of the atmospheric energy cycle. *Monthly Weather Review*, 92.

Pagé, C., Fillion, L., and Zwack, P. (2007). Diagnosing summertime mesoscale vertical motion: Implications for atmospheric data assimilation. *Monthly Weather Review*, 135(6):2076–2094.

Palmén, E. (1958). Vertical circulation and release of kinetic energy during the development of Hurricane Hazel into an extratropical storm. *Tellus*, 10(1):1–23.

Pauley, P. M. and Nieman, S. J. (1992). A comparison of quasigeostrophic and non-quasigeostrophic vertical motions for a model-simulated rapidly intensifying marine extratropical cyclone. *Monthly Weather Review*, 120(7):1108–1134.

Pfahl, S., O'Gorman, P. A., and Singh, M. S. (2015). Extratropical cyclones in idealized simulations of changed climates. *Journal of Climate*, 28(23):9373–9392.

Pirret, J. S., Knippertz, P., and Trzeciak, T. M. (2017). Drivers for the deepening of severe European windstorms and their impacts on forecast quality. *Quarterly Journal of the Royal Meteorological Society*, 143(702):309–320.

Pithan, F., Shepherd, T. G., Zappa, G., and Sandu, I. (2016). Climate model biases in jet streams, blocking and storm tracks resulting from missing orographic drag. *Geophysical Research Letters*, 43(13):7231–7240.

Räisänen, J. (1995). Factors affecting synoptic-scale vertical motions: a statistical study using a generalized omega equation. *Monthly Weather Review*, 123(8):2447–2460.

Räisänen, J. (1997). Height tendency diagnostics using a generalized omega equation, the vorticity equation, and a nonlinear balance equation. *Monthly Weather Review*, 125(7):1577–1597.

Ralph, F. M., Neiman, P. J., Wick, G. A., Gutman, S. I., Dettinger, M. D., Cayan, D. R., and White, A. B. (2006). Flooding on California's Russian River: Role of atmospheric rivers. *Geophysical Research Letters*, 33(13).

Roebber, P. J. and Schumann, M. R. (2011). Physical processes governing the rapid deepening tail of maritime cyclogenesis. *Monthly Weather Review*, 139(9):2776–2789.

Rolfson, D. M. and Smith, P. J. (1996). A composite diagnosis of synoptic-scale extratropical cyclone development over the United States. *Monthly Weather Review*, 124(6):1084–1099.

Rossby, C. (1939). Planetary flow patterns in the atmosphere. *Quarterly Journal of the Royal Meteorological Society*, 66:68.

Schultz, D. M., Bosart, L. F., Colle, B. A., Davies, H. C., Dearden, C., Keyser, D., Martius, O., Roebber, P. J., Steenburgh, W. J., Volkert, H., et al. (2019). Extratropical cyclones: a century of research on meteorology's centerpiece. *Meteorological Monographs*, 59:16–1.

Seiler, C. and Zwiers, F. W. (2016). How will climate change affect explosive cyclones in the extratropics of the Northern Hemisphere? *Climate Dynamics*, 46(11-12):3633–3644.

Sekioka, M. (1956). A hypothesis on complex of tropical and extratropical cyclones for typhoon in the middle latitudes. *Journal of the Meteorological Society of Japan. Ser. II*, 34(5):276–287.

Serreze, M., Barrett, A., Stroeve, J., Kindig, D., and Holland, M. (2009). The emergence of surface-based Arctic amplification. *The Cryosphere*, 3(1):11–19.

Shamarock, W., Klemp, J., Dudhia, J., Gill, D., Barker, D., Duda, M., Huang, X., Wang, W., and Powers, J. (2008). A description of the advanced research WRF version 3. *NCAR technical note NCAR/TN–475+STR*.

Stepanyuk, O., Räisänen, J., Sinclair, V. A., and Järvinen, H. (2017). Factors affecting atmospheric vertical motions as analyzed with a generalized omega equation and the OpenIFS model. *Tellus A: Dynamic Meteorology and Oceanography*, 69(1):1271563.

Stewart, S. R. (2018). Tropical cyclone report: Hurricane Ophelia, 9–15 October 2017. *National Hurricane Center*.

Stoelinga, M. T. (1996). A potential vorticity-based study of the role of diabatic heating and friction in a numerically simulated baroclinic cyclone. *Monthly Weather Review*, 124(5):849–874.

Thompson, D. W. and Solomon, S. (2005). Recent stratospheric climate trends as evidenced in radiosonde data: global structure and tropospheric linkages. *Journal of Climate*, 18(22):4785–4795.

Tierney, G., Posselt, D. J., and Booth, J. F. (2018). An examination of extratropical cyclone response to changes in baroclinicity and temperature in an idealized environment. *Climate Dynamics*, 51(9-10):3829–3846.

Tracton, M. S. (1973). The role of cumulus convection in the development of extratropical cyclones. *Monthly Weather Review*, 101(7):573–593.

Wernli, H., Dirren, S., Liniger, M. A., and Zillig, M. (2002). Dynamical aspects of the life cycle of the winter storm 'Lothar'(24–26 December 1999). *Quarterly Journal of the Royal Meteorological Society*, 128(580):405–429.

Wernli, H. and Schwierz, C. (2006). Surface cyclones in the ERA-40 dataset (1958–2001). Part I: novel identification method and global climatology. *Journal of the Atmospheric Sciences*, 63(10):2486–2507.

Willison, J., Robinson, W. A., and Lackmann, G. M. (2013). The importance of resolving mesoscale latent heating in the North Atlantic storm track. *Journal of the Atmospheric Sciences*, 70(7):2234–2250.

Willison, J., Robinson, W. A., and Lackmann, G. M. (2015). North Atlantic storm-track sensitivity to warming increases with model resolution. *Journal of Climate*, 28(11):4513–4524.

Yettella, V. and Kay, J. E. (2017). How will precipitation change in extratropical cyclones as the planet warms? Insights from a large initial condition climate model ensemble. *Climate Dynamics*, 49(5-6):1765–1781.

Yoshida, A. and Asuma, Y. (2004). Structures and environment of explosively developing extratropical cyclones in the northwestern Pacific region. *Monthly Weather Review*, 132(5):1121–1142.

Zappa, G., Shaffrey, L. C., and Hodges, K. I. (2013a). The ability of CMIP5 models to simulate North Atlantic extratropical cyclones. *Journal of Climate*, 26(15):5379–5396.

Zappa, G., Shaffrey, L. C., Hodges, K. I., Sansom, P. G., and Stephenson, D. B. (2013b). A multimodel assessment of future projections of North Atlantic and European extratropical cyclones in the CMIP5 climate models. *Journal of Climate*, 26(16):5846–5862.

Zwack, P. and Okossi, B. (1986). A new method for solving the quasi-geostrophic omega equation by incorporating surface pressure tendency data. *Monthly Weather Review*, 114(4):655–666.

Geosci. Model Dev., 10, 827–841, 2017
www.geosci-model-dev.net/10/827/2017/
doi:10.5194/gmd-10-827-2017

Geoscientific Model Development
Open Access
EGU

OZO v.1.0: software for solving a generalised omega equation and the Zwack–Okossi height tendency equation using WRF model output

Mika Rantanen[1], **Jouni Räisänen**[1], **Juha Lento**[2], **Oleg Stepanyuk**[1], **Olle Räty**[1], **Victoria A. Sinclair**[1], **and Heikki Järvinen**[1]

[1]Department of Physics, University Of Helsinki, Helsinki, Finland
[2]CSC – IT Center for Science, Espoo, Finland

Correspondence to: Mika Rantanen (mika.p.rantanen@helsinki.fi)

Received: 19 August 2016 – Discussion started: 29 September 2016
Revised: 3 February 2017 – Accepted: 6 February 2017 – Published: 21 February 2017

Abstract. A software package (OZO, Omega–Zwack–Okossi) was developed to diagnose the processes that affect vertical motions and geopotential height tendencies in weather systems simulated by the Weather Research and Forecasting (WRF) model. First, this software solves a generalised omega equation to calculate the vertical motions associated with different physical forcings: vorticity advection, thermal advection, friction, diabatic heating, and an imbalance term between vorticity and temperature tendencies. After this, the corresponding height tendencies are calculated with the Zwack–Okossi tendency equation. The resulting height tendency components thus contain both the direct effect from the forcing itself and the indirect effects (related to the vertical motion induced by the same forcing) of each physical mechanism. This approach has an advantage compared with previous studies with the Zwack–Okossi equation, in which vertical motions were used as an independent forcing but were typically found to compensate the effects of other forcings.

The software is currently tailored to use input from WRF simulations with Cartesian geometry. As an illustration, results for an idealised 10-day baroclinic wave simulation are presented. An excellent agreement is found between OZO and the direct WRF output for both the vertical motion and the height tendency fields. The individual vertical motion and height tendency components demonstrate the importance of both adiabatic and diabatic processes for the simulated cyclone. OZO is an open-source tool for both research and education, and the distribution of the software will be supported by the authors.

1 Introduction

Today, high-resolution atmospheric reanalyses provide a three-dimensional (3-D) view on the evolution of synoptic-scale weather systems (Dee et al., 2011; Rienecker et al., 2011). On the other hand, simulations by atmospheric models allow for exploring the sensitivity of both real-world and idealised weather systems to factors such as the initial state (e.g. Leutbecher et al., 2002; Hoskins and Coutinho, 2005), lower boundary conditions (e.g. Elguindi et al., 2005; Hirata et al., 2016), and representation of sub-grid scale processes (e.g. Wernli et al., 2002; Liu et al., 2004; Beare, 2007). Nevertheless, the complexity of atmospheric dynamics often makes the physical interpretation of reanalysis data and model output far from simple. Therefore, there is also a need for diagnostic methods that help to separate the effects of individual dynamical and physical processes on the structure and evolution of weather systems.

Two variables that are of special interest in the study of synoptic-scale weather systems are the geopotential height tendency and vertical motion (Holton and Hakim, 2012). Height tendencies are directly related to the movement and intensification or decay of low- and high-pressure systems. Vertical motions affect atmospheric humidity, cloudiness, and precipitation. They also play a crucial role in

atmospheric dynamics by inducing adiabatic temperature changes, by generating cyclonic or anticyclonic vorticity, and by converting available potential energy to kinetic energy (Lorenz, 1955; Holton and Hakim, 2012).

For the need of diagnostic tools, some software packages have been developed to separate the contributions of each forcing to the vertical motion and height tendency. DIONYSOS (Caron et al., 2006), a tool for analysing numerically simulated weather systems, provides currently online daily diagnostics for the output of numerical weather prediction models. RIP4 (Stoelinga, 2009) can calculate Q-vectors (Hoskins et al., 1978; Holton and Hakim, 2012) and a quasi-geostrophic (QG) vertical motion (Holton and Hakim, 2012) from Weather Forecast and Research (WRF) model output, but the division of ω into contributions from various atmospheric processes is not possible in RIP4. Furthermore, many research groups have developed tools for their own needs but do not have resources to distribute the software.

Here, we introduce a software package Omega–Zwack–Okossi (OZO) that can be used for diagnosing the contributions of different dynamical and physical processes to atmospheric vertical motions and height tendencies. OZO calculates vertical motion from a quasi-geostrophic and a generalised omega equation (Räisänen, 1995) while height tendencies are calculated using the Zwack–Okossi tendency equation (Zwack and Okossi, 1986; Lupo and Smith, 1998). The current, first version of OZO has been tailored to use output from the WRF model (Wang et al., 2007; Shamarock et al., 2008) simulations run with idealised Cartesian geometry. Due to the wide use of the WRF model, we expect OZO to be a useful open-source tool for both research and education.

In the following, we first introduce the equations solved by OZO: the two forms of the omega equation in Sect. 2.1 and the Zwack–Okossi height tendency equation in Sect. 2.2. The numerical techniques used in solving these equations are described in Sect. 3. We have tested the software using output from an idealised 25 km resolution WRF simulation described in Sect. 4. Section 5 provides some computational aspects of the software. The next two sections give an overview of the vertical motion (Sect. 6) and height tendency (Sect. 7) calculations for this simulation. Software limitations and plans for future development are presented in Sect. 8, and the conclusions are given in Sect. 9. Finally, information about the data and code availability is given in Sect. 10.

2 Equations

2.1 Omega equation

The omega equation is a diagnostic tool for estimating atmospheric vertical motions and studying their physical and dynamical causes. Its well-known QG form, obtained by combining the QG vorticity and thermodynamic equations, infers vertical motion from geostrophic advection of absolute vorticity and temperature (Holton, 1992):

$$L_{\mathrm{QG}}(\omega) = F_{V(\mathrm{QG})} + F_{T(\mathrm{QG})}, \tag{1}$$

where

$$L_{\mathrm{QG}}(\omega) = \sigma_0(p)\,\nabla^2\omega + f^2\frac{\partial^2\omega}{\partial p^2} \tag{2}$$

and the two right-hand side (RHS) terms are

$$F_{V(\mathrm{QG})} = f\frac{\partial}{\partial p}\left[\boldsymbol{V}_{\mathrm{g}}\cdot\boldsymbol{\nabla}\left(\zeta_g + f\right)\right], \tag{3}$$

$$F_{T(\mathrm{QG})} = \frac{R}{p}\nabla^2\left(\boldsymbol{V}_{\mathrm{g}}\cdot\boldsymbol{\nabla}T\right). \tag{4}$$

(the notation is conventional, see Table 1 for an explanation of the symbols.)

Qualitatively, the QG omega equation indicates that cyclonic (anticyclonic) vorticity advection increasing with height and a maximum of warm (cold) advection should induce rising (sinking) motion in the atmosphere. However, when deriving this equation, ageostrophic winds, diabatic heating, and friction are neglected. In addition, hydrostatic stability is treated as a constant and several terms in the vorticity equation are omitted. Although Eq. (1) often provides a reasonable estimate of synoptic-scale vertical motions at extratropical latitudes (Räisänen, 1995), these approximations inevitably deteriorate the accuracy of the QG omega equation solution.

The omega equation can be generalised by relaxing the QG approximations (e.g. Krishnamurti, 1968; Pauley and Nieman, 1992; Räisänen, 1995). Here we use the formulation

$$L(\omega) = F_V + F_T + F_V + F_Q + F_A, \tag{5}$$

where

$$\begin{aligned} L(\omega) =& \nabla^2(\sigma\omega) + f(\zeta+f)\frac{\partial^2\omega}{\partial p^2} - f\frac{\partial^2\zeta}{\partial p^2}\omega \\ &+ f\frac{\partial}{\partial p}\left[\boldsymbol{k}\cdot\left(\frac{\partial\boldsymbol{V}}{\partial p}\times\boldsymbol{\nabla}\omega\right)\right] \end{aligned} \tag{6}$$

is a generalised form of Eq. (2) and the RHS terms have the expressions

$$F_V = f\frac{\partial}{\partial p}\left[\boldsymbol{V}\cdot\boldsymbol{\nabla}\left(\zeta+f\right)\right], \tag{7}$$

$$F_T = \frac{R}{p}\nabla^2\left(\boldsymbol{V}\cdot\boldsymbol{\nabla}T\right), \tag{8}$$

$$F_F = -f\frac{\partial}{\partial p}\left[\boldsymbol{k}\cdot\left(\boldsymbol{\nabla}\times\boldsymbol{F}\right)\right], \tag{9}$$

$$F_Q = -\frac{R}{c_p p}\nabla^2 Q, \tag{10}$$

Table 1. List of mathematical symbols.

$c_p = 1004\,\mathrm{J\,kg^{-1}}$	specific heat of dry air at constant volume
f	Coriolis parameter
F	forcing in the omega equation
$\boldsymbol{F}$	friction force per unit mass
$g = 9.81\,\mathrm{m\,s^{-2}}$	gravitational acceleration
$\boldsymbol{k}$	unit vector along the vertical axis
L	linear operator in the left-hand side of the omega equation
p	pressure
Q	diabatic heating rate per mass
$R = 287\,\mathrm{J\,kg^{-1}}$	gas constant of dry air
$S = -T\frac{\partial ln\theta}{\partial p}$	stability parameter in pressure coordinates
t	time
T	temperature
$\boldsymbol{V}$	horizontal wind vector
$\boldsymbol{V}_\mathrm{g}$	geostrophic wind vector
α	relaxation coefficient
$\sigma = -\frac{\mathrm{RT}}{p\theta}\frac{\partial\theta}{\partial p}$	hydrostatic stability
σ_0	isobaric mean of hydrostatic stability
ζ	vertical component of relative vorticity
ζ_g	relative vorticity of geostrophic wind
ζ_ag	relative vorticity of ageostrophic wind
$\omega = \frac{\mathrm{d}p}{\mathrm{d}t}$	isobaric vertical motion
$\boldsymbol{\nabla}$	horizontal nabla operator
∇^2	horizontal laplacian operator

$$F_A = f\frac{\partial}{\partial p}\left(\frac{\partial\zeta}{\partial t}\right) + \frac{R}{p}\nabla^2\left(\frac{\partial T}{\partial t}\right). \tag{11}$$

Apart from the reorganisation of the terms in Eq. (6), this generalised omega equation is identical with the one used by Räisänen (1995). It follows directly from the isobaric primitive equations, which assume hydrostatic balance but omit the other approximations in the QG theory. The first four terms on the RHS represent the effects of vorticity advection (F_V), thermal advection (F_T), friction (F_F), and diabating heating (F_Q). The last term (F_A) describes imbalance between the temperature and vorticity tendencies. For constant f and constant R, the imbalance term is directly proportional to the pressure derivative of the ageostrophic vorticity tendency (Räisänen, 1995).

Because the operators L_QG and L are linear, the contributions of the various RHS terms to ω can be calculated separately if homogeneous boundary conditions ($\omega = 0$ at horizontal and vertical boundaries) are used. These contributions will be referred to as ω_X, where X identifies the corresponding forcing term. The contribution of orographic vertical motions could be added by using a non-zero lower boundary condition (Krishnamurti, 1968) but is not included in the current version of OZO.

2.2 Zwack–Okossi height tendency equation

In the Zwack–Okossi method (Zwack and Okossi, 1986; Lupo and Smith, 1998), height tendencies are calculated from the geostrophic vorticity tendency. Neglecting the variation of the Coriolis parameter,

$$\zeta_\mathrm{g} = \frac{g}{f}\nabla^2 Z \tag{12}$$

and hence

$$\frac{\partial Z}{\partial t} = \nabla^{-2}\left(\frac{f}{g}\frac{\partial\zeta_\mathrm{g}}{\partial t}\right). \tag{13}$$

The geostrophic vorticity tendency at level p_L is obtained from the equation

$$\frac{\partial\zeta_\mathrm{g}}{\partial t}(p_\mathrm{L}) = \frac{1}{p_s - p_t}\left[\int_{p_t}^{p_s}\left(\frac{\partial\zeta}{\partial t} - \frac{\partial\zeta_\mathrm{ag}}{\partial t}\right)\mathrm{d}p - \frac{R}{f}\int_{p_t}^{p_s}\left(\int_{p}^{p_\mathrm{L}}\nabla^2\frac{\partial T}{\partial t}\frac{\mathrm{d}p}{p}\right)\mathrm{d}p\right], \tag{14}$$

where p_s (here 1000 hPa) and p_t (here 100 hPa) are the lower and the upper boundaries of the vertical domain. The vorticity tendency $\frac{\partial\zeta}{\partial t}$ is calculated from the vorticity equation (Eq. 2 in Räisänen, 1997) and the temperature tendency $\frac{\partial T}{\partial t}$ from the thermodynamic equation (Eq. 3.6 in Holton and Hakim, 2012). The ageostrophic vorticity tendency $\frac{\partial\zeta_\mathrm{ag}}{\partial t}$ is estimated from time series of vorticity and geostrophic vorticity (Eq. 12) using centred time differences

$$\frac{\partial\zeta_\mathrm{ag}}{\partial t} \approx \frac{\Delta(\zeta - \zeta_\mathrm{g})}{2\Delta t}. \tag{15}$$

For the calculations shown in this paper, $\Delta t = 1800\,\mathrm{s}$ was used.

In Eq. (14), the first integral gives the mass-weighted vertical average of the geostrophic vorticity tendency between the levels p_s and p_t. The difference between the geostrophic vorticity tendency at level p_L and this mass-weighted average is obtained from the second double integral. In this latter integral, hydrostatic balance is assumed to link the pressure derivative of the geostrophic vorticity tendency to the Laplacian of the temperature tendency.

Analogously with the vertical motion, the height tendency is divided in OZO to the contributions of different physical and dynamical processes as

$$\frac{\partial Z}{\partial t} = \left(\frac{\partial Z}{\partial t}\right)_V + \left(\frac{\partial Z}{\partial t}\right)_T + \left(\frac{\partial Z}{\partial t}\right)_F + \left(\frac{\partial Z}{\partial t}\right)_Q + \left(\frac{\partial Z}{\partial t}\right)_A. \quad (16)$$

By substituting the vorticity equation and the thermodynamic equation into Eq. (14), and then combining the result with Eq. (13), the expressions for the RHS components of Eq. (16) are derived as follows:

i. Vorticity advection (V) and friction (F) have a direct effect on the vorticity tendency in Eq. (14).

ii. Thermal advection (T) and diabatic heating (Q) have a direct effect on the temperature tendency in Eq. (14).

iii. The ageostrophic vorticity tendency in Eq. (14) is attributed to the imbalance term (A).

iv. All five terms also affect the vorticity and temperature tendencies indirectly via vertical motions, which are calculated for each of them separately with the generalised omega equation.

This results in the following new expressions:

$$\left(\frac{\partial Z}{\partial t}\right)_V = \frac{f}{g(p_s - p_t)}\nabla^{-2}\Bigg[\int_{p_t}^{p_s}\Big(-\boldsymbol{V}\cdot\boldsymbol{\nabla}(\zeta+f) - \omega_V\frac{\partial\zeta}{\partial p} + (\zeta+f)\frac{\partial\omega_V}{\partial p} + \boldsymbol{k}\cdot\left(\frac{\partial \boldsymbol{V}}{\partial p}\times\boldsymbol{\nabla}\omega_V\right)\Big)\mathrm{d}p - \frac{R}{f}\int_{p_t}^{p_s}\left(\int_p^{p_\mathrm{L}}\nabla^2(S\omega_V)\frac{\mathrm{d}p}{p}\right)\mathrm{d}p\Bigg], \quad (17)$$

$$\left(\frac{\partial Z}{\partial t}\right)_T = \frac{f}{g(p_s - p_t)}\nabla^{-2}\Bigg[\int_{p_t}^{p_s}\Big(-\omega_T\frac{\partial\zeta}{\partial p} + (\zeta+f)\frac{\partial\omega_T}{\partial p} + \boldsymbol{k}\cdot\left(\frac{\partial \boldsymbol{V}}{\partial p}\times\boldsymbol{\nabla}\omega_T\right)\Big)\mathrm{d}p - \frac{R}{f}\int_{p_t}^{p_s}\left(\int_p^{p_\mathrm{L}}\nabla^2(S\omega_T)\frac{\mathrm{d}p}{p}\right)\mathrm{d}p\Bigg], \quad (18)$$

$$\left(\frac{\partial Z}{\partial t}\right)_F = \frac{f}{g(p_s - p_t)}\nabla^{-2}\Bigg[\int_{p_t}^{p_s}\Big(\boldsymbol{k}\cdot\boldsymbol{\nabla}\times\boldsymbol{F} - \omega_F\frac{\partial\zeta}{\partial p} + (\zeta+f)\frac{\partial\omega_F}{\partial p} + \boldsymbol{k}\cdot\left(\frac{\partial \boldsymbol{V}}{\partial p}\times\boldsymbol{\nabla}\omega_F\right)\Big)\mathrm{d}p - \frac{R}{f}\int_{p_t}^{p_s}\left(\int_p^{p_\mathrm{L}}\nabla^2(S\omega_F)\frac{\mathrm{d}p}{p}\right)\mathrm{d}p\Bigg], \quad (19)$$

$$\left(\frac{\partial Z}{\partial t}\right)_Q = \frac{f}{g(p_s - p_t)}\nabla^{-2}\Bigg[\int_{p_t}^{p_s}\Big(-\omega_Q\frac{\partial\zeta}{\partial p} + (\zeta+f)\frac{\partial\omega_Q}{\partial p} + \boldsymbol{k}\cdot\left(\frac{\partial \boldsymbol{V}}{\partial p}\times\boldsymbol{\nabla}\omega_Q\right)\Big)\mathrm{d}p - \frac{R}{f}\int_{p_t}^{p_s}\left(\int_p^{p_\mathrm{L}}\nabla^2\left(\frac{Q}{c_p}+S\omega_T\right)\frac{\mathrm{d}p}{p}\right)\mathrm{d}p\Bigg], \quad (20)$$

$$\left(\frac{\partial Z}{\partial t}\right)_A = \frac{f}{g(p_s - p_t)}\nabla^{-2}\Bigg[\int_{p_t}^{p_s}\Big(-\frac{\partial\zeta_\mathrm{ag}}{\partial t} - \omega_A\frac{\partial\zeta}{\partial p} + (\zeta+f)\frac{\partial\omega_A}{\partial p} + \boldsymbol{k}\cdot\left(\frac{\partial \boldsymbol{V}}{\partial p}\times\boldsymbol{\nabla}\omega_A\right)\Big)\mathrm{d}p - \frac{R}{f}\int_{p_t}^{p_s}\left(\int_p^{p_\mathrm{L}}\nabla^2(S\omega_A)\frac{\mathrm{d}p}{p}\right)\mathrm{d}p\Bigg]. \quad (21)$$

The equation system used in this study has been adopted partly from Räisänen (1997). However, whereas Räisänen (1997) used the vorticity equation and the non-linear balance equation to obtain height tendencies, the Zwack–Okossi equation is used here. The main advantage of this choice is its smaller sensitivity to numerical errors. Our method produces quite smooth vertical profiles of height tendencies because the tendencies at neighbouring levels are bound to each other by the vertical integration in Eq. (14). On the other hand, our method differs from earlier applications of the Zwack–Okossi equation (e.g. Zwack and Okossi, 1986; Lupo and Smith, 1998) because the use of the generalised omega equation eliminates vertical motion as an independent height tendency forcing. This is an important advantage because these earlier studies have shown a tendency of compensation between vertical motions and the other forcing terms.

Earlier diagnostic tools have come close to our technique. The most similar approach is probably used in the DIONYSOS (Caron et al., 2006) tool. Regardless of many similarities, there are still three major differences between DIONYSOS and OZO. First, DIONYSOS eliminates the ageostrophic vorticity tendency as an independent forcing using an iterative procedure. Second, DIONYSOS uses simple

parameterisations of diabatic heating and friction, whereas OZO relies directly on model output. Third, DIONYSOS uses the method of Räisänen (1997) to convert vorticity tendencies to height tendencies, whereas the Zwack–Okossi method is used in OZO.

2.3 Vorticity and temperature advection by non-divergent and divergent winds

Following the Helmholtz theorem, the horizontal wind can be divided to non-divergent ($\boldsymbol{V}_\psi$) and divergent ($\boldsymbol{V}_\chi$) parts. Their contributions to vorticity advection and temperature advection can be separated as

$$-\boldsymbol{V}\cdot\nabla(\zeta+f) = -\boldsymbol{V}_\psi\cdot\nabla(\zeta+f) - \boldsymbol{V}_\chi\cdot\nabla(\zeta+f), \quad (22)$$

$$-\boldsymbol{V}\cdot\nabla T = -\boldsymbol{V}_\psi\cdot\nabla T - \boldsymbol{V}_\chi\cdot\nabla T, \quad (23)$$

and the same applies to the corresponding ω and height tendency contributions. This separation between $\boldsymbol{V}_\psi$ and $\boldsymbol{V}_\chi$ contributions is included in OZO because Räisänen (1997) found it to be important for the height tendencies associated with vorticity advection.

OZO calculates the divergent part of the wind ($\boldsymbol{V}_\chi$) from the gradient of the velocity potential χ (Eq. 24), which is derived from the horizontal divergence by inverting the Laplacian in Eq. (25).

$$\boldsymbol{V}_\chi = \nabla\chi \quad (24)$$

$$\nabla^2\chi = \nabla\cdot\boldsymbol{V} \quad (25)$$

The non-divergent wind is obtained as the difference between $\boldsymbol{V}$ and $\boldsymbol{V}_\chi$. The output of OZO explicitly includes the vorticity advection and temperature advection terms of the ω and height tendency equations due to both the full wind field $\boldsymbol{V}$ and the divergent wind $\boldsymbol{V}_\chi$. The contributions associated with the non-divergent wind $\boldsymbol{V}_\psi$ can be calculated as their residual.

3 Numerical methods

The first version of the OZO software package is tailored to use output from WRF simulations in idealised Cartesian geometry. The computational domain is periodic in the zonal direction, whereas symmetric boundary conditions are used at the northern and southern boundaries. Before the calculation, the WRF data need to be interpolated to pressure coordinates.

3.1 Calculation of right-hand side terms

All of the right-hand side terms of the omega equation (Eq. 5) and the Zwack–Okossi equation (Eq. 16) are calculated in grid point space. Horizontal and vertical derivatives are approximated with two-point central differences with the exception at the meridional and vertical boundaries, where one-sided differences are used. In the calculation of the imbalance term of the omega and Zwack–Okossi equations (Eqs. 11 and 21), also tendencies of T, ζ and Z are needed. These tendencies are approximated by central differences of the corresponding variables.

Because the calculations are done in pressure coordinates, the lower boundary of the domain does not correspond to the actual surface. To mitigate the impact of this, vorticity and temperature advection, friction, diabatic heating, and the ageostrophic vorticity tendency are all attenuated below the actual surface by multiplying them by a factor varying from 0 to 1. The multiplication factor at each level depends on how far down the level is below the ground. For example, for a surface pressure of 950 hPa and vertical mass-centred grid spacing of 50 hPa, the multiplication factor is 0 at 1000 hPa, 0.5 at 950 hPa, and 1 at 900 hPa and all higher levels.

3.2 Inversion of left-hand side operators

The omega equation is solved using a multigrid algorithm (Fulton et al., 1986). Each multigrid cycle starts from the original (finest) grid, denoted below with the superscript (1). A rough solution in this grid ($\widetilde{\omega}^{(1)}$) is found using ν_1 iterations of simultaneous under relaxation, starting either from the previous estimate of ω or (in the first cycle) $\omega = 0$. The residuals,

$$\mathrm{Res}^{(1)} = F - L(\widetilde{\omega}^{(1)}), \quad (26)$$

are then upscaled to a coarser grid (superscript (2)), in which the number of points is halved in all three dimensions. In this grid, the equation

$$L(\omega^{(2)}) = \mathrm{Res}^{(1)} \quad (27)$$

is then roughly solved replicating the method used in the first grid. The residual of this calculation is fed to the next coarser grid, and the procedure is continued until the grid only has five points on its longest (meridional) axis. Thus, for an idealised baroclinic wave simulation with horizontal resolution of 25 km, the meridional axis has 320 grid points. That makes six coarser resolutions (160, 80, 40, 20, 10, and 5 points on the meridional axis) in addition to the original one.

Having obtained the estimate $\widetilde{\omega}^{(N)}$ for the coarsest grid, a new estimate for the second coarsest grid is formed as

$$\widetilde{\omega}^{(N-1)}_{\mathrm{NEW1}} = \widetilde{\omega}^{(N-1)} + \alpha\widetilde{\omega}^{(N)}, \quad (28)$$

where α is a relaxation coefficient. To reduce the effect of regridding errors, this estimate is refined using ν_2 iterations of simultaneous under relaxation. The result, $\widetilde{\omega}^{(N-2)}_{\mathrm{NEW2}}$, is then substituted to the next finer grid

$$\widetilde{\omega}^{(N-2)}_{\mathrm{NEW1}} = \widetilde{\omega}^{(N-2)} + \alpha\widetilde{\omega}^{(N-1)}_{\mathrm{NEW2}} \quad (29)$$

and the sequence is repeated until the original grid is reached.

After each multigrid cycle, the maximum difference between the new and the previous estimate of ω in the original

(finest) grid is computed. If this difference exceeds a user-defined threshold (by default $5 \times 10^{-5}\,\mathrm{Pa\,s^{-1}}$), the multigrid cycle is repeated. Typically, several hundreds of cycles are required to achieve the desired convergence.

OZO has four parameters for governing the multigrid algorithm, with the following default values: the under relaxation coefficient ($\alpha = 0.017$), the number of sub-cycle iterations in the descending ($\nu_1 = 30$) and ascending phases of the multigrid cycle ($\nu_2 = 4$), and the threshold for testing convergence (toler $= 5 \times 10^{-5}$ $\mathrm{Pa\,s^{-1}}$). All these parameters can be adjusted via a name list. The mentioned default values of α, ν_1 and ν_2 have been optimised for a 25 km grid resolution. At lower resolution, α can be increased and ν_1 and ν_2 reduced to speed up the algorithm.

In the Zwack–Okossi equation, geostrophic vorticity tendencies are converted to geopotential height tendencies using Eq. (13), which is a 2-D Poisson's equation. To solve this equation computationally effectively, we utilise Intel's MKL (Math Kernel Library) fast Poisson solver routines, which employ the DFT (discrete Fourier transform) method. Intel's MKL is widely available and free to download, although registration is required.

3.3 Boundary conditions

In the omega equation, homogeneous boundary conditions ($\omega = 0$) at both the meridional and the lower and the upper boundaries are used. For the Zwack–Okossi equation, a slightly more complicated procedure is used to ensure that the area means of the individual height tendency components are consistent with the corresponding temperature tendencies. First, for all of V, T, F, Q and A, the height tendency is initially solved from Eq. (13) using homogenous boundary conditions ($\frac{\partial Z}{\partial t} = 0$) at the northern and southern boundaries. Then, the area mean temperature tendencies for these five terms are calculated, taking into account both the direct effect of temperature advection (for T) and diabatic heating (for Q) and the adiabatic warming–cooling associated with the corresponding omega component. These temperature tendencies are substituted to the hypsometric equation to calculate the corresponding area mean height tendencies. In the vertical integration of the hypsometric equation, the area mean height tendency at the lower boundary (1000 hPa) is set to 0, following the expectation that the total atmospheric mass in the model domain is conserved. Horizontally homogeneous adjustments are then made to the initial height tendencies for V, T, F, Q and A, forcing their area means to agree with those derived from the hypsometric equation.

4 The WRF set-up

WRF is a non-hydrostatic model and can generate atmospheric simulations using real data or idealised configurations (Wang et al., 2007; Shamarock et al., 2008). The calculations presented in this paper used input data from an idealised moist baroclinic wave simulation, which simulates the evolution of a baroclinic wave within a baroclinically unstable jet in the Northern Hemisphere under the f-plane approximation (Blázquez et al., 2013). The value of the Coriolis parameter was set to $10^{-4}\,\mathrm{s^{-1}}$ in the whole model domain.

The simulation presented in Sects. 6–7 was run for 10 days with a 30 min output interval, in a domain of 4000 km × 8000 km × 16 km, with 25 km horizontal grid spacing. The horizontal grid was Cartesian and staggered, and 64σ levels were used in the vertical direction. The boundary conditions were symmetric in the meridional direction and periodic in the zonal direction. Cloud microphysics is parameterised using the WRF single-moment 3-class scheme (Hong et al., 2004). Cumulus convection is treated with the Kain–Fritsch scheme (Kain and Fritsch, 1993) and boundary layer turbulence with the YSU scheme (Hong et al., 2006). The radiation scheme was switched off in our model integration.

After running the simulation, data were interpolated from model levels to 19 evenly spaced pressure levels (1000, 950, ..., 100 hPa). The interpolation was done with WRF utility *wrf_interp*, which is freely available from the WRF website. During the interpolation, the horizontal data grid was unstaggered to mass points, thus having 160 grid points in the zonal and 320 grid points in the meridional direction.

The model output data contained all the variables needed in solving the generalised omega equation and the Zwack–Okossi equation: temperature, wind components, geopotential height, surface pressure, and parameterised diabatic heating and friction components. Diabatic heating and friction in WRF included contributions from various physical processes, such as cumulus convection, boundary layer physics and microphysics. The physical tendencies are not in the default WRF output, and need to be added by modifying the WRF registry file.

To study the performance of OZO at a resolution that is more similar to that used in several earlier diagnostic studies of synoptic-scale dynamics (Räisänen, 1995, 1997; Caron et al., 2006; Stepanyuk et al., 2017), WRF was also run in the same domain at 100 km grid spacing. Results for this simulation are presented in the supplementary material. An intermediate simulation at 50 km resolution was also made to study the resolution dependence of the computational performance.

Table 2. The dependence of computing time on model resolution. Note that the numbers of grid points are per vertical level, whereas the computing times are per the whole 3-D domain.

DX	Number of grid points per vertical level	Average computing time per timestep
100 km	3200	3.1 s
50 km	12 800	1.1 min
25 km	51 200	19 min

5 Computational aspects

OZO can be run on a basic laptop with Linux environment, provided that standard NetCDF library, Intel's MKL and some Fortran compiler, preferably GNU's gfortran, are available. The source code of OZO is written in Fortran 90 standard and can be currently compiled only for a serial version.

The inversion of the left-hand side operator of the omega equation (Eq. 6) is computationally quite a heavy process. Hence, in our previously described test runs, the calculation of the five plus two ω components took almost all of the total computing time. For the height tendencies, the inversion of the horizontal Laplacian (Eq. 13) is much more straightforward to do and, moreover, MKL fast Poisson solver routines are employed. For that reason, only a small fraction of the computing time is spent for the height tendency calculation. Table 2 provides information on the absolute computing times and how they depend on the number of grid points in the model domain. It is our goal to improve the computational performance by utilising better scalable solver routines for the omega equation in a future version of the software.

6 Results – vertical motion

6.1 Comparison between calculated and WRF-simulated vertical motions

Figure 1 compares the solution of the generalised omega equation (ω_{TOT}) with ω as being obtained directly from the WRF output (ω_{WRF}), at the 700 hPa level after 118 h of simulation when the cyclone is approaching its maximum intensity. The agreement is excellent. A strong maximum of rising motion ($\omega \approx -3\,\mathrm{Pa\,s^{-1}}$) occurs near the occlusion point to the east of the surface low in both cases, with a somewhat weaker ascent along the cold frontal zone to the south-west and in the north-eastern sector of the low. Descent prevails further east of the low and behind the cold front. However, lots of mesoscale details are visible in both the simulated and the calculated ω, although with some not perfect agreement between these two. The difference between ω_{TOT} and ω_{WRF} (Fig. 1c) is noisy, although it suggests slightly more discrepancy behind the cold front where shallow convection takes place.

The QG omega equation (Eq. 1) also captures the large-scale patterns of rising and sinking motion reasonably well (Fig. 1d). However, it substantially underestimates the ascent to the east of the low and along the cold front, and there are two bands of strong descent (behind the cold front and to the east of the low) that are much weaker in ω_{WRF} and ω_{TOT}. Furthermore, many of the mesoscale details shared by ω_{WRF} and ω_{TOT} are missing in the QG solution.

The majority of the differences between ω_{TOT} and ω_{WRF} most likely result from numerical errors. One source of these errors is the approximation of the time derivatives in F_A in Eq. (11) with central differences. As shown in Fig. 2, the agreement between ω_{TOT} and ω_{WRF} gradually improves when the half-span of these time differences is reduced from 2 h to 1 min (i.e. the time step in the WRF simulation). The 30 min output interval used for the other calculations shown in this paper is a compromise between accuracy and the need to control the data volume of the WRF output for the 10-day simulation.

A more comprehensive statistical evaluation of the calculated vertical motions is given in Figs. 3 and 4, by using data from the whole model area and the 8 last days of the simulation. The first 2 days, when both the cyclone and the vertical motions are still weak, are neglected. Figure 3 shows the time-averaged spatial correlation between ω_{WRF} and various omega equation solutions. The correlation between ω_{TOT} (line VTFQA) and ω_{WRF} is excellent, reaching 0.95 in the mid-troposphere and exceeding 0.88 at all levels from 250 to 850 hPa. However, leaving out ω_A, which requires non-synoptic information from the time derivatives of temperature and vorticity, deteriorates the correlation substantially (line VTFQ). The solution of the QG omega equation only correlates with ω_{WRF} at $r \sim 0.6$ in the mid-troposphere (line VT(QG)), although the correlation approaches 0.65 at 300 hPa where diabatic heating is less important than at lower levels.

Caron et al. (2006) reported excellent correlations (at most levels, from 0.9 to 0.96) between the vertical motions calculated by the DIONYSOS tool and their original model output (their Figs. 2a and 3a), for two cases and nine synoptic times at 3 h intervals for both. These correlations are similar to or even higher than those shown in Fig. 3. However, in these tests the horizontal resolution of DIONYSOS was 100 km, whereas we used 25 km resolution in our WRF simulation. In fact, the correlations for OZO are also improved and reach 0.97 in the mid-troposphere for a 100 km resolution WRF simulation (see the Supplement, Fig. S3). Naturally, the performance may also depend on the synoptic case studied.

Figure 4 compares the root-mean-square (RMS) amplitudes of ω_{WRF} and ω_{TOT}. RMS(ω_{TOT}) is typically about 5 % smaller than RMS(ω_{WRF}), which is presumably due to the truncation errors that occur when the derivatives in the forcing terms are approximated with second-order central differences. An exception to this is the lower troposphere where vertical motions calculated by OZO(ω_{TOT}) are slightly

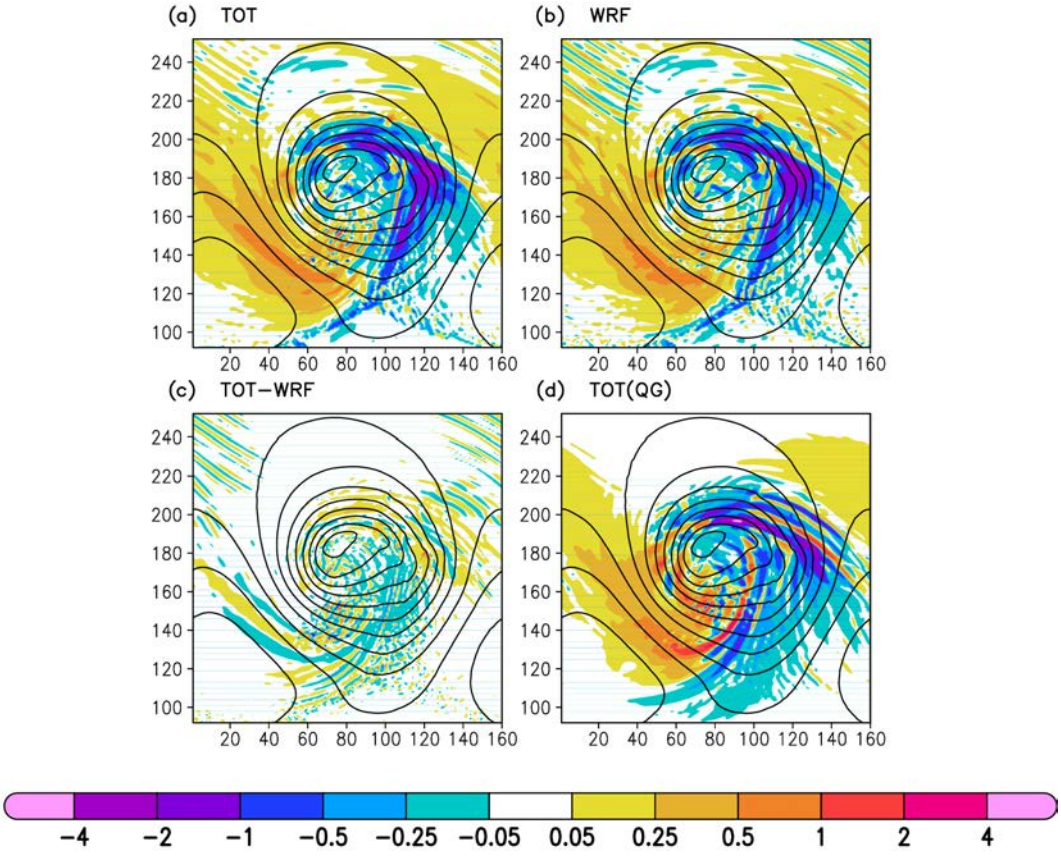

Figure 1. (a) The sum of all ω components from Eq. (5) (ω_{TOT}), **(b)** ω from WRF (ω_{WRF}), **(c)** difference ($\omega_{\mathrm{TOT}} - \omega_{\mathrm{WRF}}$) and **(d)** solution of the QG omega equation ($\omega_{V(\mathrm{QG})} + \omega_{T(\mathrm{QG})}$) at 700 hPa level at time 118 h. Unit is Pa s^{-1}. Contours show geopotential height at 900 hPa level with an interval of 50 m. Labels on x and y axes indicate grid point numbers. Note that the area covers only half of the model domain in the meridional direction.

stronger compared to the direct WRF output (ω_{WRF}). The RMS amplitudes of the individual ω components will be discussed in the next subsection.

6.2 Contributions of individual forcing terms to ω

Figure 5 shows the contributions of the five individual forcing terms to ω(700 hPa) for the situation studied in Fig. 1. Vorticity advection and thermal advection both contribute substantially to the vertical motions (Fig. 5a–b), but the maximum of ascent is further east for ω_T (Fig. 5b) than ω_V (Fig. 5a). Due to this phase shift, there is a cancellation between rising motion from ω_V and sinking motion from ω_T behind the cold front. This cancellation effect is well-known and typically occurs just behind the cold front, where cold advection and increasing cyclonic vorticity advection with height take place (Lackmann, 2011). On the other hand, these two terms both induce rising motion to the south-east of the centre of the low. Diabatic heating, which is dominated by latent heat release, strongly enforces the ascent along the main frontal zones of the cyclone (Fig. 5d). Compensating subsidence prevails in the surrounding areas, except for spots of localised ascent associated with convective precipitation well behind the cold front. The imbalance term ω_A is remarkably large but noisy. Friction induces ascent close to the centre of the low and descent around and to the north-east of the surface high (Fig. 5c), but its contribution is quite weak at the 700 hPa level. Figures S1 and S2 in the Supplement present the actual forcing fields for the vertical motions fields in Fig. 5a–e.

In terms of the RMS amplitudes evaluated over the whole model area and the last 8 days of the simulation, temperature advection makes the largest contribution to the calculated ω (line T in Fig. 4). Vorticity advection (line V), diabatic heating (line Q) and the imbalance term (line A) are all similar in magnitude in the mid- and upper troposphere. Near the surface, the imbalance term has a tendency to compensate the effects of temperature advection, as their RMS values are even larger than the RMS of the total vertical motion (line TOT). RMS(ω_Q) peaks at 850 hPa, which is mostly due to shallow convection behind the cold front (not shown). This peak is visible also in the RMS(ω_{TOT}). Our sensitivity experiments with different output intervals suggest that the half-hour tem-

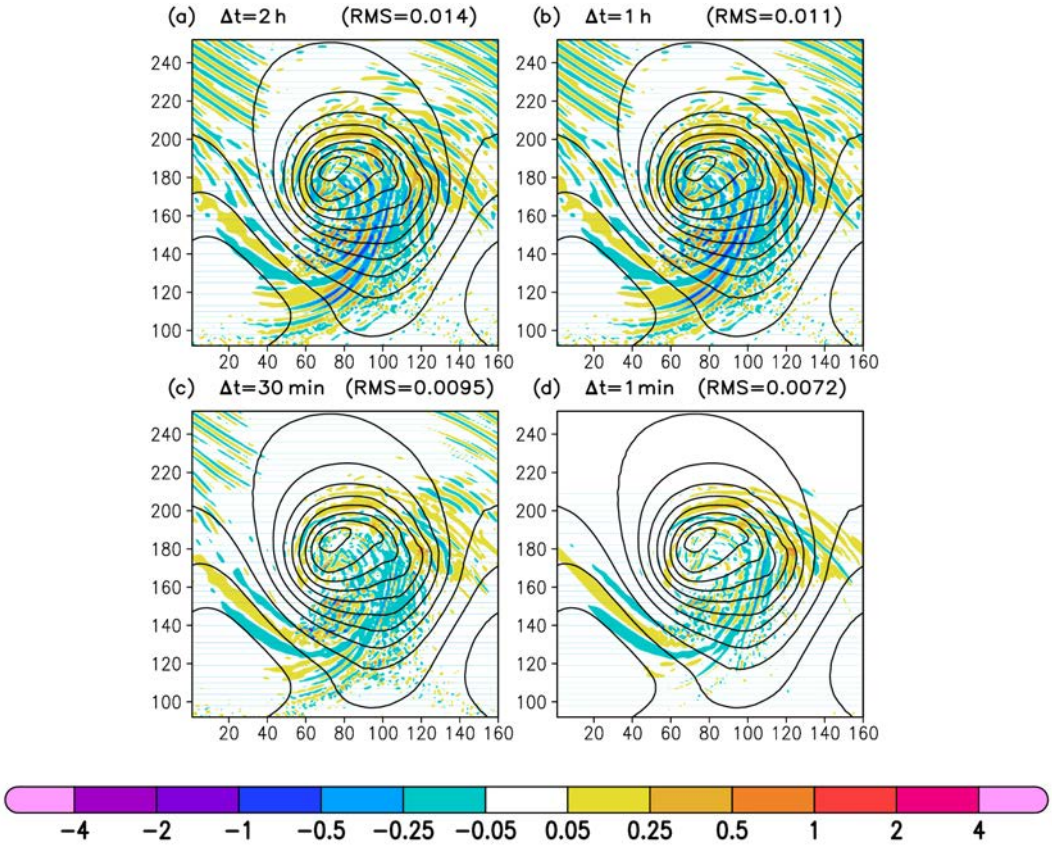

Figure 2. The difference $\omega_{\mathrm{TOT}} - \omega_{\mathrm{WRF}}$ at 700 hPa level at time 118 h at **(a)** 2 h, **(b)** 1 h, **(c)** 30 min and **(d)** 1 min time resolution in the computation of the imbalance term. Unit is $\mathrm{Pa\,s^{-1}}$.

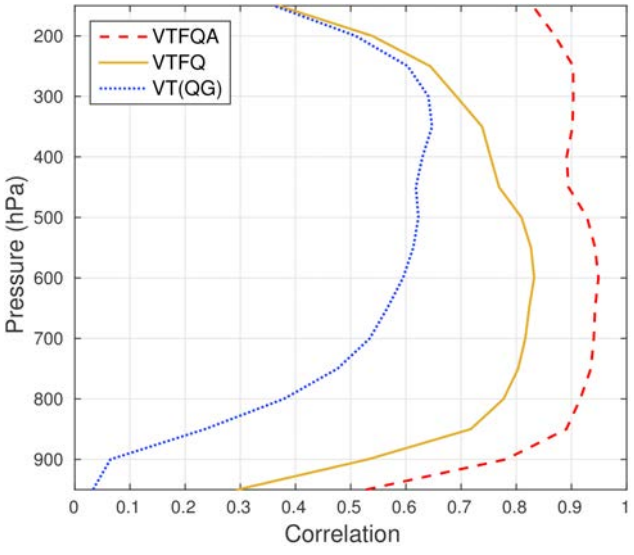

Figure 3. Correlation of the omega equation solutions with ω_{WRF}. VTFQA $= \omega_{\mathrm{TOT}}$, VTFQ $= \omega_{\mathrm{TOT}} - \omega_A$, VT(QG) $= \omega_{V(\mathrm{QG})} + \omega_{T(\mathrm{QG})}$.

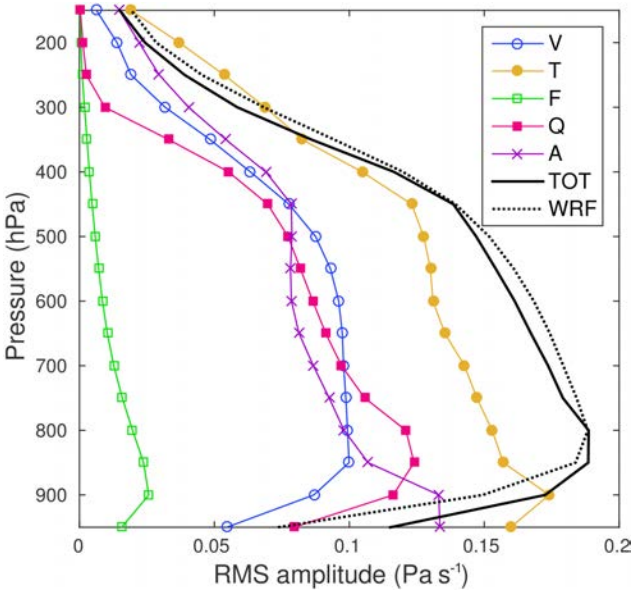

Figure 4. RMS amplitudes of ω_{WRF}, ω_{TOT}, and the individual ω components from Eq. (5).

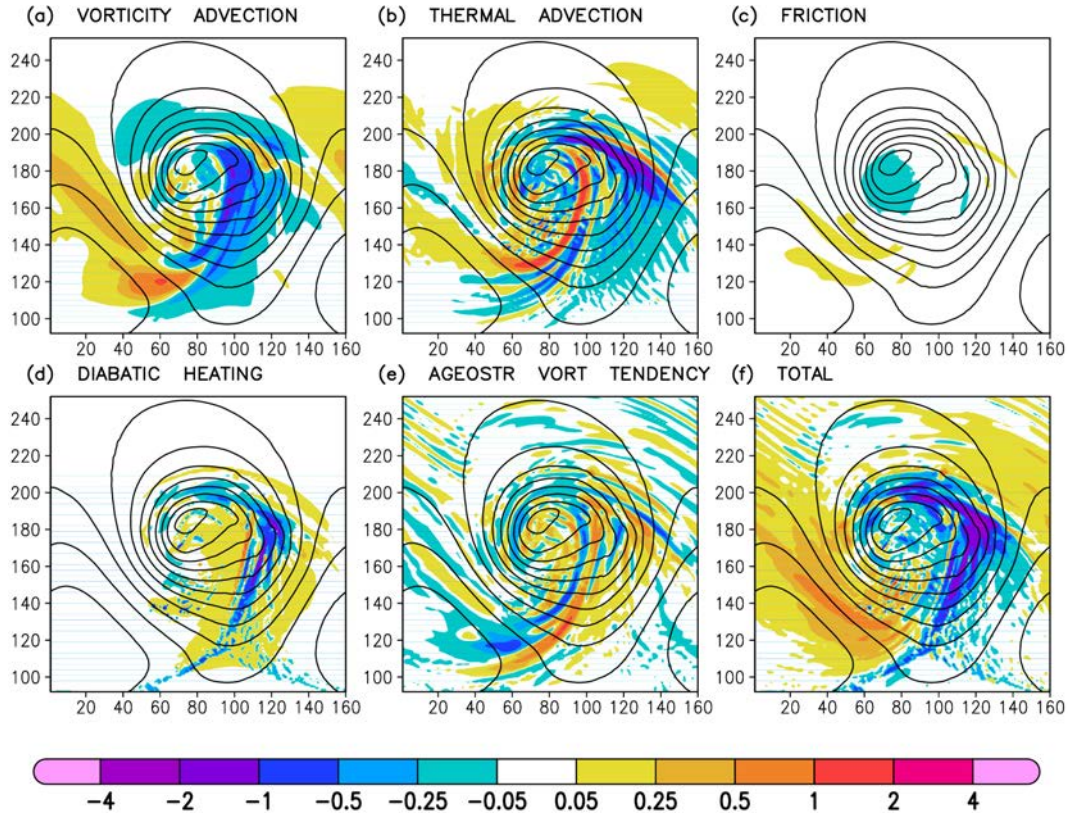

Figure 5. Vertical motions induced by individual forcing terms at level 700 hPa at time 118 h. **(a)** ω_V, **(b)** ω_T, **(c)** ω_F, **(d)** ω_Q, **(e)** ω_A and **(f)** ω_{TOT}. Unit is Pa s^{-1} and contour lines show 900 hPa geopotential height with 50 m interval.

poral resolution is too sparse for proper estimation of the imbalance term in the presence of fast-moving convection cells, which causes the over-estimation of total vertical motion in the lowest troposphere. RMS(ω_F) is at its maximum near the top of the boundary layer at 900 hPa but remains weak even at this level.

These results are partly consistent with similar calculations made for observation-based analysis data (Räisänen, 1995) and for model data (Stepanyuk et al., 2017) at lower spatial resolution. However, the imbalance term was relatively small in the study by Räisänen (1995), because the 6 h time resolution of its input data was not sufficient for a proper estimation of this term. In addition, RMS(ω_T) is more dominant in our study than in Räisänen (1995) and in Stepanyuk et al. (2017). The main reason for this is the improved horizontal resolution. Räisänen (1995) found that the influence of thermal advection compared to vorticity advection increases when the horizontal resolution is improved. This is because vertical motions induced by thermal advection typically have a smaller horizontal scale than those induced by vorticity advection (Räisänen, 1995). In this paper, the horizontal resolution is almost 10 times higher than in the study by Räisänen (1995). Conversely, RMS(ω_F) is smaller in Fig. 4 than found for the midlatitudes in Räisänen (1995) and Stepanyuk et al. (2017). This may be at least in part because Räisänen (1995) and Stepanyuk et al. (2017) included both land and sea areas, whereas our WRF simulation was made for an idealised ocean surface.

A further division of ω_V and ω_T to contributions from advection by rotational and divergent wind reveals that they both are largely dominated by the rotational wind (not shown).

7 Results – height tendency

7.1 Comparison between calculated and WRF-simulated height tendencies

In this subsection, the calculated total height tendencies are compared with height tendencies from the WRF simulation. The latter were estimated as central differences from the 30 min time series of the simulated geopotential heights.

Figure 6 shows the distributions of the calculated height tendency, the WRF height tendency and their difference slightly before the cyclone reaches its maximum intensity ($t = 118$ h). The values are shown at the 900 hPa level, which is sufficiently low to represent the processes affecting the low-level cyclogenesis. Negative (positive) height tendency

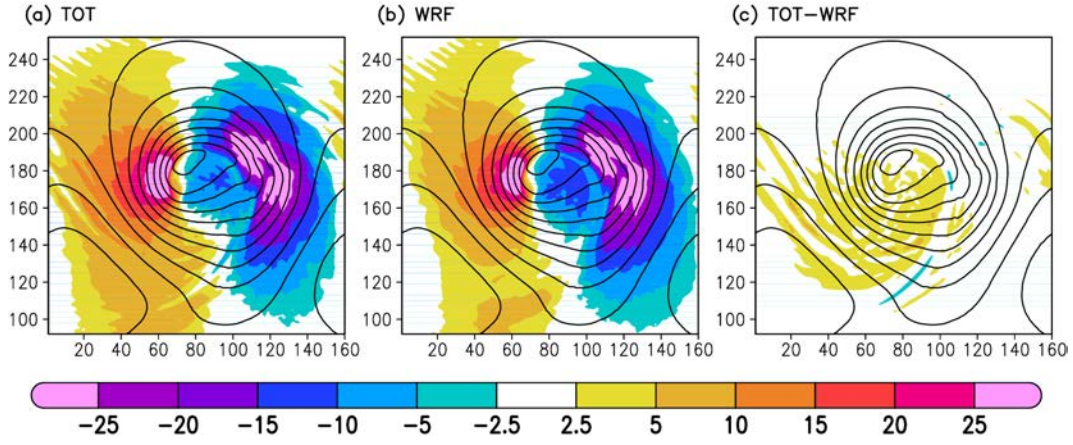

Figure 6. As Fig. 1, but for the height tendency at 900 hPa. Unit is $m\,h^{-1}$.

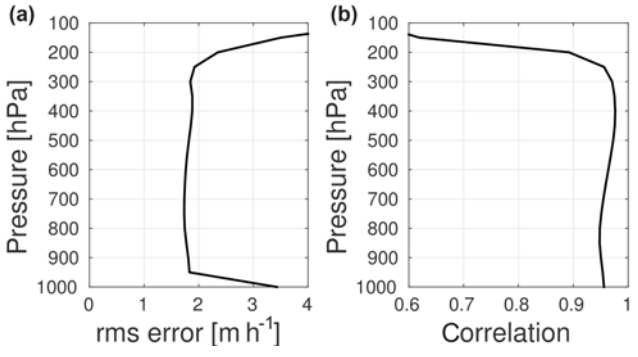

Figure 7. Time mean **(a)** rms error and **(b)** spatial correlation coefficient between the calculated and WRF height tendency over the last 8 days of the 10-day simulation.

over the low centre indicates deepening (weakening) of the low. In general, a very close agreement between the fields is seen, although a somewhat more positive bias is visible behind the cold front.

Figure 7 shows the time-averaged RMS error and correlation coefficient between the calculated and WRF height tendency as a function of height. The RMS error is quite constant from 950 hPa up to the 250 hPa level (Fig. 7a). Above this level, the error grows rapidly towards the stratosphere. This error growth is accompanied by a decrease of correlation coefficient at the same altitude. This deterioration is presumably at least partly due to the 50 hPa vertical resolution in the OZO, which is too coarse for an adequate representation of stratospheric dynamics.

The correlation between the calculated and WRF height tendency is highest in the upper troposphere, which is roughly 0.97. The correlation weakens slightly closer the surface, but still exceeds 0.95. Thus, the calculated height tendency is generally in very good agreement with the tendency diagnosed directly from the WRF output. These correlations are comparable but mostly slightly higher than those reported by Caron et al. (2006) for DIONYSOS (their Fig. 6a).

7.2 Contributions of individual terms during the mature stage

The contributions of the individual height tendency components at the 900 hPa level at 118 h are shown in Fig. 8. Vorticity advection (Fig. 8a) produces a wide and strongly positive height tendency behind the surface low (see Sect. 7.4 for further analysis of this term). Thermal advection (Fig. 8b) causes a positive height tendency in the area behind the surface low and a negative height tendency at the opposite side. This large negative height tendency ahead of the low is caused by warm air advection in the mid- and upper troposphere. In this baroclinic life cycle simulation, thermal advection is the main contributor to the movement of the cyclone, which is in agreement with the study of Räisänen (1997).

Friction (Fig. 8c) always acts to damp synoptic-scale weather systems and is thereby inducing a positive (negative) height tendency over the surface low (high). Diabatic heating (Fig. 8d) is causing uniformly negative lower tropospheric height tendencies in the vicinity of the surface low. The largest negative height tendency due to diabatic heating is located south-east from the low centre, where strong latent heat release occurs in connection with frontal precipitation.

The imbalance term (Fig. 8e) shows more small-scale structure than the other terms. In general, however, it is in phase with the total height tendency near the centre of the low, with negative values to the east and positive values to the west. The reason for this feature is most probably the following. The conversion from geostrophic vorticity tendencies to height tendencies for the other terms was done by assuming a geostrophic balance according to Eq. (13). However, in cyclones the wind is typically sub-geostrophic (e.g. Holton and Hakim, 2012). Therefore, the tendency of geostrophic vorticity exceeds the actual vorticity tendency. This implies that

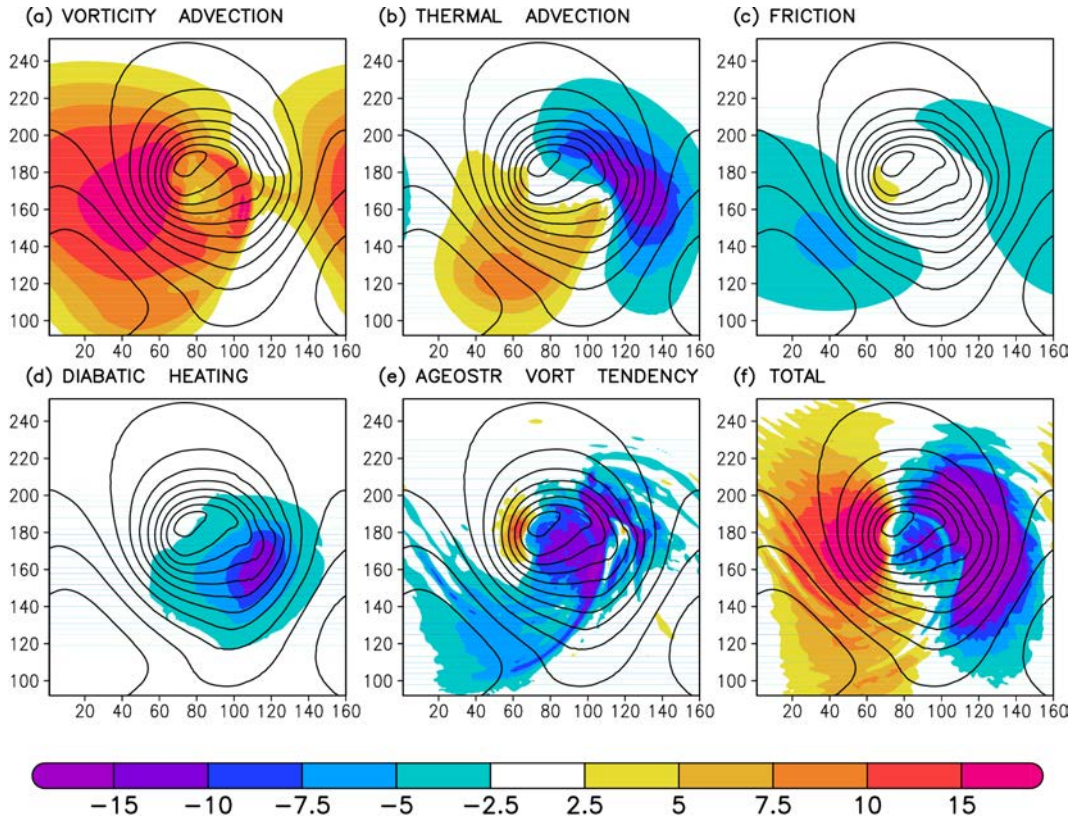

Figure 8. As Fig. 5, but for height tendency components at 900 hPa level. Unit is $\mathrm{m\,h^{-1}}$. Note that the colour scale of **(f)** differs from Fig. 6a.

height tendencies calculated from the actual vorticity tendency under the geostrophic assumption will be too small. The imbalance term takes care of this and makes the calculated total height tendency to correspond better to the actual change of the geopotential height field.

7.3 Height tendencies in the cyclone centre

Figure 9 shows the 900 hPa level height tendencies induced by the five individual terms in the cyclone centre during the deepening period. The low deepens vigorously roughly between 72 and 120 h of simulation, as shown by the negative total height tendency (black line) during this period. The total height tendency is also in a good agreement with the WRF height tendency (dotted line). The deepening is mostly due to vorticity advection (blue line) and the imbalance term (grey line). Later on, roughly from 96 h onward, diabatic heating (red line) and thermal advection (orange line) together with the imbalance term make the largest contributions to maintaining the intensity of the surface low. Friction (green line) systematically destroys cyclonic vorticity over the cyclone centre and thus produces a slightly positive height tendency during the whole life cycle. After circa 96 h, vorticity advection also acts a damping mechanism for the surface low (see also the next subsection).

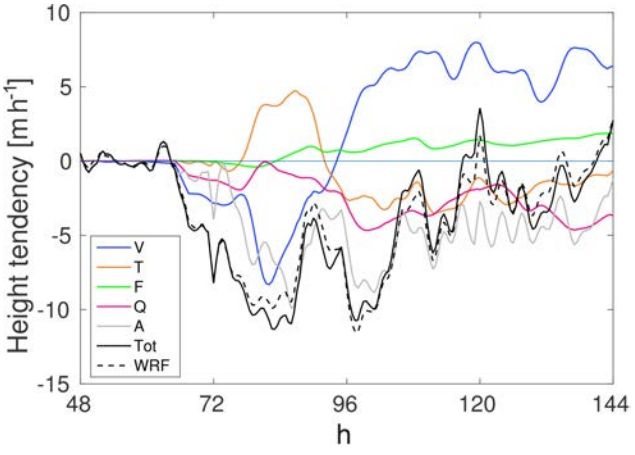

Figure 9. Time series of individual height tendency components at the 900 hPa level from the cyclone centre during the deepening period. V is vorticity advection, T is thermal advection, F is friction, Q is diabatic heating, A is imbalance term, Tot is total and WRF is WRF height tendency. Height tendencies at the cyclone centre were averaged over all grid boxes in which the 900 hPa geopotential height was less than 5 m above its minimum. In addition, the values are 2.5 h moving averages.

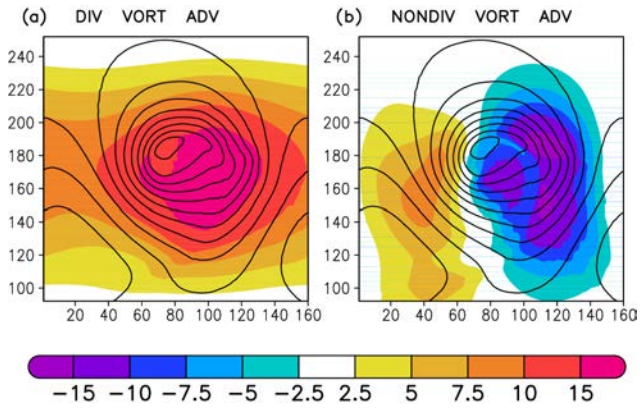

Figure 10. Height tendency associated with vorticity advection by the **(a)** divergent and **(b)** nondivergent winds at 900 hPa at time 118 h. Unit is $\mathrm{m\,h^{-1}}$.

7.4 The effect of vorticity and thermal advection by divergent and non-divergent winds

Figure 10 presents the height tendencies associated with vorticity advection by $\boldsymbol{V}_\chi$ and $\boldsymbol{V}_\psi$ separately. The divergent wind vorticity advection causes widespread and strong positive height tendency over and around the surface low (Fig. 10a). According to Räisänen (1997), the divergent wind transports anticyclonic vorticity from the surroundings of the surface low, and is thus acting to reduce the cyclonic vorticity at the centre of the low. In the case of the non-divergent wind component (Fig. 10b), positive (negative) height tendencies behind (ahead of) the low originate from the upper troposphere, where the non-divergent wind and thereby vorticity advection is the strongest. Cyclonic vorticity advection ahead of the trough produces negative height tendency in the same area, while anticyclonic vorticity advection ahead of the ridge does the opposite. Furthermore, the non-divergent vorticity advection is substantially contributing to the deepening of the cyclone, since the area of the negative height tendency reaches the centre of the low as well.

In contrast to vorticity advection, thermal advection by divergent winds was found to cause a negligible height tendency (not shown).

8 Limitations and plans for future developments

The idealised baroclinic wave simulation provides an effective and widely used tool for studying cyclone dynamics in an easily controlled model environment. For this reason, we chose to begin the development work of OZO from a relatively simple Cartesian implementation. Nevertheless, the idealised Cartesian geometry obviously reduces the number of potential applications of OZO. We aim to extend OZO to more complex spherical grid applications in the future. However, in principle the use of OZO is possible with some limited-area real cases where spherical geometry has been used, if the data are regridded to Cartesian geometry afterwards. However, in this case, one must change the lateral boundary conditions of OZO since they are tailored for periodic model domain by default.

Another limiting factor in the current version of OZO is the weak scalability in the multigrid omega equation solver together with the lack of parallelisation of the source code. For high-resolution runs, this means significant slowing of the calculations (Table 2). To reduce the lengthy computing times, we are currently developing a parallel version of OZO, which uses a different solving method for the omega equation. We aim to release this parallel version by the end of the year 2017.

An issue associated with the physical interpretation of high-resolution simulations should also be noted. In OZO, the vertical motion and height tendency contributions of vorticity advection, thermal advection, friction, and diabatic heating are calculated assuming geostrophic balance between the vorticity and temperature tendencies, while the deviations from this balance are attributed to the imbalance term. As the balance assumption is increasingly violated at higher resolution, the imbalance term grows larger. This complicates the interpretation of the results particularly when the imbalance term opposes the other terms. Such compensation is indeed apparent in our results for vertical motions in the lower troposphere, where the contributions of thermal advection and diabatic heating are strongly opposed by the imbalance term (Fig. 4). At resolutions much higher than 25 km, issues like this are likely to become increasingly problematic.

9 Conclusions

In this paper, a software package called OZO is introduced. OZO is a tool for investigating the physical and dynamical factors that affect atmospheric vertical motions and geopotential height tendencies, tailored for WRF simulations with idealised Cartesian geometry. As input to OZO, the output of the WRF model interpolated to evenly spaced pressure levels is required.

The generalised omega equation diagnoses the contributions of different physical and dynamical processes to vertical motions: vorticity advection, thermal advection, friction, diabatic heating, and imbalance between temperature and vorticity tendencies. Then, analogously with the vertical motion, the height tendencies associated with these forcings are calculated. As an advance over traditional applications of the Zwack–Okossi equation (Zwack and Okossi, 1986; Lupo and Smith, 1998), the use of the generalised omega equation allows OZO to eliminate vertical motion as an independent forcing in the calculation of height tendencies.

The calculated total vertical motions and height tendencies in the test case are generally in excellent agreement with the vertical motions and height tendencies diagnosed directly

from the WRF simulations. The time-averaged correlation between the calculated and the WRF height tendency was 0.95–0.97 in the troposphere. For the vertical motion as well, a correlation of 0.95 was found in the mid-troposphere. Our analysis further illustrates the importance of both adiabatic and diabatic processes to atmospheric vertical motions and the development of the simulated cyclone.

The OZO software is applicable to different types of WRF simulations, as far as Cartesian geometry with periodic boundary conditions in the zonal direction is used. One example of potential applications are simulations with increased sea surface temperatures as the lower boundary condition. Combined with OZO, such simulations provide a simple framework for studying the changes in cyclone dynamics in a warmer climate.

10 Data and code availability

The source code of OZO is freely available under MIT licence in GitHub (https://github.com/mikarant/ozo). OZO v.1.0 described in this manuscript is also archived at http://doi.org/10.5281/zenodo.157188. In addition to the source code, the package also includes a makefile for compiling and running the program, a small sample input dataset for testing the functionality, and two README files containing the instructions for both generating input data with WRF and running the OZO program. The WRF model as well as the interpolation utility (*wrf_interp*) are downloadable from the WRF users page (http://www2.mmm.ucar.edu/wrf/users/downloads.html). Intel's MKL can be downloaded after registration from their web page (https://software.intel.com/en-us/articles/free-mkl). OZO v1.0 is guaranteed to work with WRF version 3.8.1.

The Supplement related to this article is available online at doi:10.5194/gmd-10-827-2017-supplement.

Competing interests. The authors declare that they have no conflict of interest.

Acknowledgements. We thank the Doctoral Programme of Atmospheric Sciences, University of Helsinki for financially supporting the work of M. Rantanen. The work of O. Stepanyuk was supported by the Maj and Thor Nessling foundation (project 201600119) and the work of O. Räty was supported by the Vilho, Yrjö, and Kalle Väisälä Foundation. V. A. Sinclair was supported by the Academy of Finland Centre of Excellence Program (grant 272041).

Edited by: D. Ham
Reviewed by: two anonymous referees

References

Beare, R. J.: Boundary layer mechanisms in extratropical cyclones, Q. J. Roy. Meteor. Soc., 133, 503–515, 2007.

Blázquez, J., Pessacg, N. L., and Gonzalez, P. L.: Simulation of a baroclinic wave with the WRF regional model: sensitivity to the initial conditions in an ideal and a real experiment, Meteorol. Appl., 20, 447–456, 2013.

Caron, J.-F., Zwack, P., and Pagé, C.: DIONYSOS: A diagnostic tool for numerically-simulated weather systems, Atmos.-Ocean, Technical related document available at: http://www.dionysos.uqam.ca/doc/Dionysos.pdf, submitted, 2006.

Dee, D., Uppala, S., Simmons, A., Berrisford, P., Poli, P., Kobayashi, S., Andrae, U., Balmaseda, M., Balsamo, G., Bauer, P., Bechtold, P., Beljaars, A., van de Berg, L., Bidlot, J., Bormann, N., Delsol, C., Dragani, R., Fuentes, M., Geer, A., Haimberger, L., Healy, S., Hersbach, H., Hólm, E., Isaksen, L., Kållberg, P., Köhler, M., Matricardi, M., McNally, A., Monge-Sanz, B., Morcrette, J.-J., Park, B.-K., Peubey, C., de Rosnay, P., Tavolato, C., Thépaut, J.-N., and Vitart, F.: The ERA-Interim reanalysis: configuration and performance of the data assimilation system, Q. J. Roy. Meteor. Soc., 137, 553–597, 2011.

Elguindi, N., Hanson, B., and Leathers, D.: The Effects of Snow Cover on Midlatitude Cyclones in the Great Plains, J. Hydrometeorol., 6, 263–279, 2005.

Fulton, S. R., Ciesielski, P. E., and Schubert, W. H.: Multigrid Methods for Elliptic Problems: A Review, Mon. Weather Rev., 114, 943–959, 1986.

Hirata, H., Kawamura, R., Kato, M., and Shinoda, T.: Response of rapidly developing extratropical cyclones to sea surface temperature variations over the western Kuroshio–Oyashio confluence region, J. Geophys. Res.-Atmos., 121, 3843–3858, 2016.

Holton, J.: An introduction to dynamic meteorology, Academic Press, 1992.

Holton, J. R. and Hakim, G. J.: An introduction to dynamic meteorology, vol. 88, Academic press, 2012.

Hong, S.-Y., Dudhia, J., and Chen, S.-H.: A revised approach to ice microphysical processes for the bulk parameterization of clouds and precipitation, Mon. Weather Rev., 132, 103–120, 2004.

Hong, S.-Y., Noh, Y., and Dudhia, J.: A new vertical diffusion package with an explicit treatment of entrainment processes, Mon. Weather Rev., 134, 2318–2341, 2006.

Hoskins, B., Draghici, I., and Davies, H.: A new look at the ω-equation, Q. J. Roy. Meteor. Soc., 104, 31–38, 1978.

Hoskins, B. J. and Coutinho, M. M.: Moist singular vectors and the predictability of some high impact European cyclones, Q. J. Roy. Meteor. Soc., 131, 581–601, 2005.

Kain, J. S. and Fritsch, J. M.: Convective parameterization for mesoscale models: The Kain-Fritsch scheme, in: The representation of cumulus convection in numerical models, 165–170, Springer, 1993.

Krishnamurti, T.: A diagnostic balance model for studies of weather systems of low and high latitudes, Rossby number less than 1, Mon. Weather Rev., 96, 197–207, 1968.

Lackmann, G.: Midlatitude synoptic meteorology, American Meteorological Society, 2011.

Leutbecher, M., Barkmeijer, J., Palmer, T. N., and Thorpe, A. J.: Potential improvement to forecasts of two severe storms using targeted observations, Q. J. Roy. Meteor. Soc., 128, 1641–1670, 2002.

Liu, Y., Wu, G., and Ren, R.: Relationship between the Subtropical Anticyclone and Diabatic Heating, J. Climate, 17, 682–698, 2004.

Lorenz, E. N.: Available Potential Energy and the Maintenance of the General Circulation, Tellus, 7, 157–167, 1955.

Lupo, A. and Smith, P.: The interactions between a midlatitude blocking anticyclone and synoptic-scale cyclones that occurred during the summer season, Mon. Weather Rev., 126, 502–515, 1998.

Pauley, P. M. and Nieman, S. J.: A comparison of quasigeostrophic and nonquasigeostrophic vertical motions for a model-simulated rapidly intensifying marine extratropical cyclone, Mon. Weather Rev., 120, 1108–1134, 1992.

Räisänen, J.: Factors affecting synoptic-scale vertical motions: A statistical study using a generalized omega equation, Mon. Weather Rev., 123, 2447–2460, 1995.

Räisänen, J.: Height tendency diagnostics using a generalized omega equation, the vorticity equation, and a nonlinear balance equation, Mon. Weather Rev., 125, 1577–1597, 1997.

Rienecker, M. M., Suarez, M. J., Gelaro, R., Todling, R., Bacmeister, J., Liu, E., Bosilovich, M. G., Schubert, S. D., Takacs, L., Kim, G.-K., Bloom, S., Chen, J., Collins, D., Conaty, A., da Silva, A., Gu, W., Joiner, J., Koster, R. D., Lucchesi, R., Molod, A., Owens, T., Pawson, S., Pegion, P., Redder, C. R., Reichle, R., Robertson, F. R., Ruddick, A. G., Sienkiewicz, M., and Woollen, J.: MERRA: NASA's Modern-Era Retrospective Analysis for Research and Applications, J. Climate, 24, 3624–3648, 2011.

Shamarock, W., Klemp, J., Dudhia, J., Gill, D., Barker, D., Duda, M., Huang, X., Wang, W., and Powers, J.: A description of the advanced research WRF version 3, NCAR technical note NCAR/TN/u2013475, 2008.

Stepanyuk, O., Räisänen, J., Sinclair, V. A., and Järvinen, H.: Factors affecting atmospheric vertical motions as analyzed with a generalized omega equation and the OpenIFS model, Tellus A, 69, 1271563, doi:10.1080/16000870.2016.1271563, 2017.

Stoelinga, M. T.: A users' guide to RIP version 4: A program for visualizing mesoscale model output, NCAR, available at: http://www2.mmm.ucar.edu/wrf/users/docs/ripug.htm (last access: 20 February 2017), 2009.

Wang, W., Barker, D., Bray, J., Bruyere, C., Duda, M., Dudhia, J., Gill, D., and Michalakes, J.: User's Guide for Advanced Research WRF (ARW) Modeling System Version 3, Mesoscale and Microscale Meteorology Division–National Center for Atmospheric Research (MMM-NCAR), 2007.

Wernli, H., Dirren, S., Liniger, M. A., and Zillig, M.: Dynamical aspects of the life cycle of the winter storm "Lothar" (24–26 December 1999), Q. J. Roy. Meteor. Soc., 128, 405–429, 2002.

Zwack, P. and Okossi, B.: A new method for solving the quasi-geostrophic omega equation by incorporating surface pressure tendency data, Mon. Weather Rev., 114, 655–666, 1986.

II

Climate Dynamics (2019) 52:2703–2719
https://doi.org/10.1007/s00382-018-4283-3

Sensitivity of idealised baroclinic waves to mean atmospheric temperature and meridional temperature gradient changes

Mika Rantanen[1] · **Jouni Räisänen**[1] · **Victoria A. Sinclair**[1] · **Heikki Järvinen**[1]

Received: 27 November 2017 / Accepted: 29 May 2018 / Published online: 6 June 2018

Abstract
The sensitivity of idealised baroclinic waves to different atmospheric temperature changes is studied. The temperature changes are based on those which are expected to occur in the Northern Hemisphere with climate change: (1) uniform temperature increase, (2) decrease of the lower level meridional temperature gradient, and (3) increase of the upper level temperature gradient. Three sets of experiments are performed, first without atmospheric moisture, thus seeking to identify the underlying adiabatic mechanisms which drive the response of extra-tropical storms to changes in the environmental temperature. Then, similar experiments are performed in a more realistic, moist environment, using fixed initial relative humidity distribution. Warming the atmosphere uniformly tends to decrease the kinetic energy of the cyclone, which is linked both to a weaker capability of the storm to exploit the available potential energy of the zonal mean flow, and less efficient production of eddy kinetic energy in the wave. Unsurprisingly, the decrease of the lower level temperature gradient weakens the resulting cyclone regardless of the presence of moisture. The increase of the temperature gradient in the upper troposphere has a more complicated influence on the storm dynamics: in the dry atmosphere the maximum eddy kinetic energy decreases, whereas in the moist case it increases. Our analysis suggests that the slightly unexpected decrease of eddy kinetic energy in the dry case with an increased upper tropospheric temperature gradient originates from the weakening of the meridional heat flux by the eddy. However, in the more realistic moist case, the diabatic heating enhances the interaction between upper- and low-level potential vorticity anomalies and hence helps the surface cyclone to exploit the increased upper level baroclinicity.

Keywords WRF model · Idealised simulation · Extratropical cyclone · Energy conversion

1 Introduction

Extra-tropical cyclones are ubiquitous in the mid-latitude atmosphere, occurring most frequently during the winter season. They affect our everyday life by inducing variations and extremes of weather, sometimes with severe impacts to the society (e.g., Wernli et al. 2002; Fink et al. 2009). Extra-tropical cyclones also transport large amounts of heat and momentum, and are thus an important component of the atmospheric general circulation.

A large number of previous studies have investigated the changes in the intensity (e.g., Bengtsson et al. 2009), frequency (e.g., Lambert and Fyfe 2006; Zappa et al. 2013), and tracks (e.g., Yin 2005; Bengtsson et al. 2006) of extra-tropical cyclones in a warmer climate. All of these changes in cyclone characteristics partly result from the different atmospheric temperature distribution in the future climate. For example, climate change projections made with General Circulation Models (GCM) suggest that in mid-latitudes, the meridional low-level temperature gradient will decrease whereas the gradient at upper levels will increase (Woollings 2008; Catto et al. 2011).

One widely used method for studying the dynamics of extra-tropical cyclones is idealised simulations (e.g., Fantini 2004; Boutle et al. 2010, 2011; Booth et al. 2013; Blázquez et al. 2013; Kirshbaum et al. 2018). One specific example is the baroclinic lifecycle simulation, in which only one low pressure system is simulated. This technique allows one to explore the changes in extra-tropical cyclone dynamics

Electronic supplementary material The online version of this article (https://doi.org/10.1007/s00382-018-4283-3) contains supplementary material, which is available to authorized users.

✉ Mika Rantanen
mika.p.rantanen@helsinki.fi

[1] Institute for Atmospheric and Earth System Research/Physics, University of Helsinki, P.O. Box 64, Gustaf Hällströmin katu 2a, 00014 Helsinki, Finland

much more easily than the simulations created using e.g. complex Earth System models. Most of the recent studies carried out with idealised baroclinic wave simulations have investigated the effect of atmospheric moisture on cyclone characteristics. For instance, Boutle et al. (2010) studied the dry and moist boundary layer structure and vertical transport of moisture within the idealised cyclone. They found that the kinetic energy of the storm was doubled with the inclusion of moisture. Furthermore, the changes in cyclone dynamics and intensity with increased atmospheric moisture content have been studied in detail by Booth et al. (2013). The robust result in that study was that nearly all the important metrics of storm strength increase when the moisture is increased.

However, less emphasis has been given to studying how changes in the large-scale temperature distribution, as anticipated for the future climate, affect the strength and development of numerically simulated cyclones in idealised cases. Boutle et al. (2011) studied the sensitivity of moisture transport by idealised cyclones to some large-scale environmental variables, such as initial relative humidity, absolute temperature, and the meridional temperature gradient and thus the strength of the zonal jet. They concluded that relative humidity has little impact on the ability of a cyclone to transport moisture, whereas the absolute temperature and its meridional gradient provide much stronger controls. They, however, did not focus on the mechanisms by which the change of temperature and its gradient affect the dynamics and intensity of the storm.

The sensitivity of idealised moist baroclinic waves to environmental temperature and moisture content was studied by Kirshbaum et al. (2018). They initialized the model runs with different mean surface temperatures, varying between 275–290 K, and found that the eddy kinetic energy did not increase at larger temperatures due to unfavourable phasing between vertical motion and buoyancy within the warm sector. Another methodological novelty of their study was that the model domain was much larger in the zonal direction ($L_x = 16{,}000$ km) than typically used in baroclinic life cycle experiments (e.g., Boutle et al. 2010 used $L_x = 4000$ km) and that two types of simulations were performed: one set using a single domain-centered initial perturbation and the second set using three equally spaced perturbations. The simulations initialised with three perturbations show a different response to the environmental temperature than than simulations with a single perturbation as the wave was found to interact negatively with itself. Thus, Kirshbaum et al. (2018) conclude that periodic waves exhibited faster decrease in intensity at larger temperatures compared to isolated waves, which had not been documented previously.

Very recently, Tierney et al. (2018) reported how extra-tropical cyclones respond to changes in baroclinicity and temperature in an idealized environment. This study was an important addition to the existing literature, as the changes in baroclinicity have received relatively little attention amongst recent idealized studies. Tierney et al. (2018) changed simultaneously both the baroclinicity and the bulk temperature of the cyclone environment, and thus discovered the relative effects of these two factors to the cyclone intensity.

In general, the main consensus among the recent studies is an amplification of the storm when the moisture content is increased from zero to typical present-day values (Boutle et al. 2010; Booth et al. 2013; Kirshbaum et al. 2018; Tierney et al. 2018). However, increasing the atmospheric moisture further from the present-day values has led to partly contradictory results in previous idealised experiments. For example, keeping the relative humidity fixed, Boutle et al. (2011) found that the eddy kinetic energy tends to increase with increasing atmospheric temperature. A similar result was found in Whitaker and Davis (1994), who reported more rapid cyclogenesis when the mean surface temperature was increased by 10 K. However, inconsistent with these two studies, the main conclusion of Kirshbaum et al. (2018) was that the increase of temperature with constant relative humidity makes the storm weaker. In addition, Tierney et al. (2018) documented the non-monotonic behavior of the storm intensity with increasing temperature, regardless of the magnitude of baroclinicity. These two outcomes are in agreement with recent idealised aqua-planet GCM studies, where the sensitivity of eddy kinetic energy to global mean atmospheric temperature has been studied: O'Gorman (2011) and Pfahl et al. (2015) show that with present-day temperature values the eddy kinetic energy is very close to its maximum, and tends to decrease with further warming.

Nonetheless, in addition to increased moisture content, changes in the meridional temperature gradient with changing climate are also expected to impact the development of baroclinic eddies. Thus, the main objective of this paper is to study the sensitivity of extra-tropical cyclones to meridional temperature gradient changes. Since opposing changes in the temperature gradient are expected to occur in the Northern Hemisphere at lower and upper levels (Woollings 2008), the effects of the lower and upper level changes are studied separately. Before that, the response of the simulated mid-latitude cyclone to an uniform increase of temperature is reported. This experiment of uniform warming is included in our paper to address the three different temperature forcings predicted to occur in the warmer climate: (1) uniform increase of atmospheric temperature, (2) decreased lower level temperature gradient and (3) increased upper level temperature gradient. Based on earlier, slightly contradictory results, we cannot formulate a clear hypothesis of how the uniform increase of temperature will affect to the intensity of the storm. On the other hand, we would expect that the changes in lower level and upper level temperature gradient will have opposing effects on the intensity of the cyclone, due to their opposing effects on atmospheric baroclinicity.

To assess the changes in the adiabatic dynamics of cyclones, the experiments are first conducted without atmospheric moisture. After that, the experiments are repeated in a moist environment.

First, in Sect. 2, the model set-up, the experiments and the energy metrics used in this paper are described. Then, the results of our experiments are reported in Sect. 3, which is divided to three subsections, according to the three temperature experiments. A brief discussion of some pertinent issues arising from the results is then given in Sect. 4. Finally, in Sect. 5, the main conclusions of the study are reported.

2 Methods

2.1 The model

We used the Weather Research and Forecast (WRF) model v. 3.8.1 (Shamarock et al. 2008), in its idealized mode in a Cartesian geometry. The model configuration was a periodic channel, with symmetric north-south boundaries and periodic east-west boundaries. The simulations were run for 10 days, in a domain of 5000 km × 8000 km × 16 km, in the x, y and z directions, respectively. The horizontal grid spacing in our study was 50 km. We tested different zonal wavelengths, and thus different zonal domain sizes, varying between 3500 and 6000 km. 5000 km was finally chosen because the longest wavelengths were found to generate unwanted secondary lows, whereas wavelengths shorter than 5000 km produced a less deep cyclone. Although Kirshbaum et al. (2018) used a much wider domain in the zonal direction, our choice of domain is more closely comparable with the domains used in other baroclinic wave studies. In the vertical direction, 64 sigma levels were used. The pressure at the model top varied between 125 and 100 hPa, depending on the experiment and location in south-north direction. After running the simulations, the model output data were interpolated to 19 evenly spaced pressure levels, from 1000 to 100 hPa. Thus, a small part of our data at the upper boundary were extrapolated above the model top. The Coriolis parameter was held constant, with value of 10^{-4} s^{-1}, corresponding to the real value at the latitude $\phi = 43°$.

Cloud microphysics were parameterized using the WSM3 scheme (Hong et al. 2004), which has 3-class microphysics (raindrops, cloud droplets and water vapor) for liquid water, but assumes ice processes below the freezing point. The WSM3 scheme assumes immediate cloud formation above water saturation at temperatures above − 40 °C (Dudhia 1989), which may effect the simulations as latent heat release is suppressed until the entire grid box is saturated. For cumulus convection, the Kain–Fritsch scheme (Kain and Fritsch 1993) was used, and the YSU scheme (Hong et al. 2006) was selected to parameterize the boundary layer turbulence. Surface fluxes were calculated using the MM5 similarity scheme (e.g., Paulson 1970). For simplicity, the radiation scheme was switched off in our experiments. Even though this choice of neglecting radiation moves our experiments further from reality, it makes the interpretation of diabatic heating easier, leaving latent heat release as the only major source of diabatic heating in the free atmosphere.

For the model runs, we used the standard initial condition of the baroclinic test case, which is included in the WRF model package. The unperturbed initial states of zonal wind and temperature were zonally symmetric and in thermal wind balance, resembling their distributions in the Northern Hemisphere winter (Fig. 1). The same initial conditions were used e.g. by Sinclair and Keyser (2015), and the zonal jet is described in the paper of Waite and Snyder (2009). To enable others to reproduce our results, we have archived the initial condition files of our experiments, the namelist used in the WRF simulations, and a piece of WRF source code which sets up the initial conditions needed to run the model. These data are available from https://zenodo.org/record/1044980.

The evolution of the baroclinic disturbance was triggered by applying a sinusoidal temperature perturbation to the mid-tropospheric temperature field. The maximum of the initial perturbation was 1 K, located vertically at the level of 8 km and in the middle of the domain in the y-direction. The magnitude of the disturbance decreased to zero when approaching the top and the bottom of the domain. See Sect. S1.1 of the Supplementary material for details.

2.2 Numerical experiments

Three sets of experiments were performed. These are denoted as Experiment UNI, LOW and UP, referring to temperature forcings uniformly in the atmosphere, at lower levels, and at upper levels, respectively. Each of the experiments consisted of three numerical simulations with different amplitudes of the temperature forcing. Technically, the initial atmospheric temperature distribution was first changed. After this, the new pressure distribution was calculated, by integrating the hydrostatic equation from the bottom of the domain to the top, maintaining the surface pressure constant in all the experiments. To keep the initial state in a hydrostatic balance, new density values were calculated with the ideal gas law, using the new temperature and pressure values. Finally, the zonal wind field was adapted to the modified temperature and pressure fields by applying the geostrophic wind law. Thus, in addition to temperature, this procedure yielded slightly different initial conditions also for zonal wind speed and pressure in all three experiments. Nevertheless, the resulting initial states were in a perfect thermal

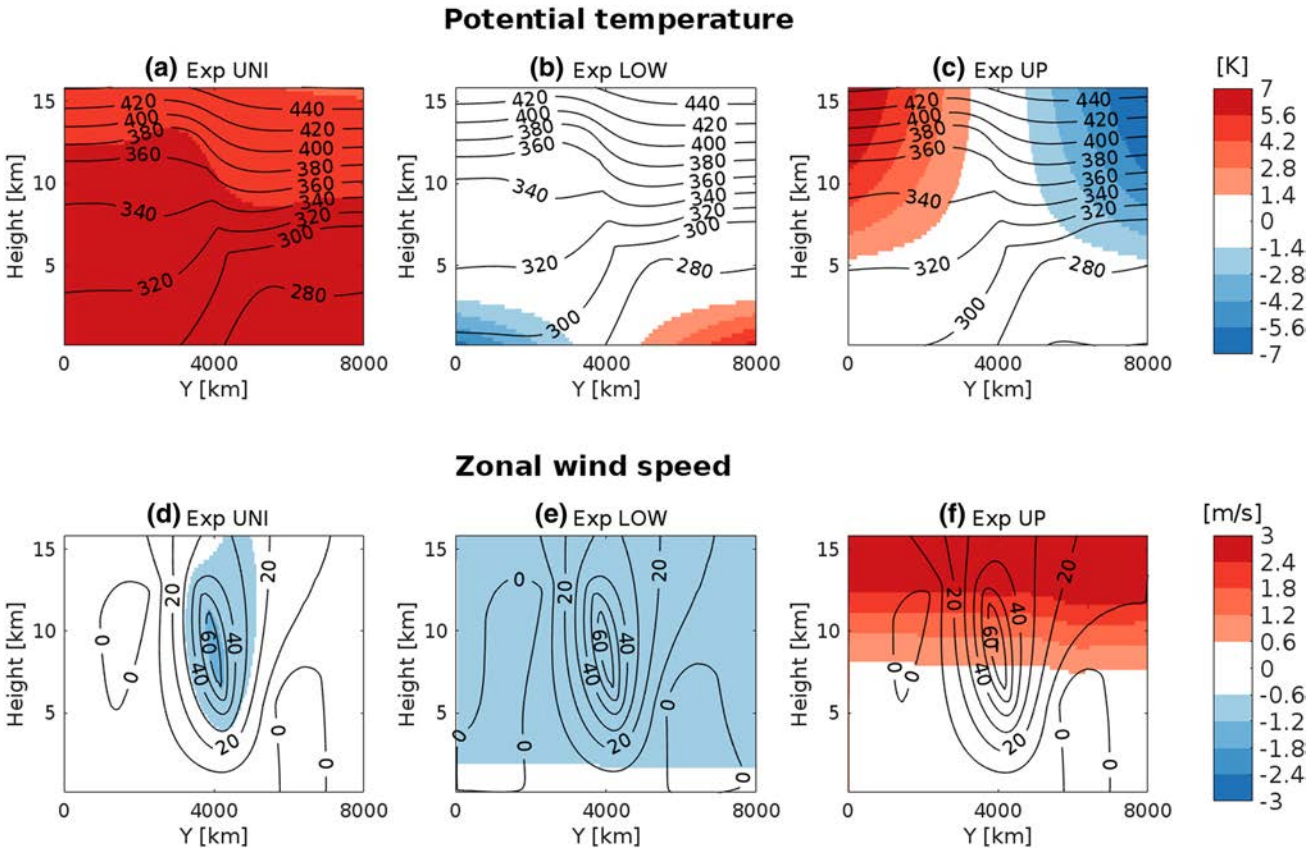

Fig. 1 Zonal mean potential temperature (contours) and differences from the control run (shading) for **a** uniform temperature increase, **b** the decrease of lower level temperature gradient and **c** the increase of upper level temperature gradient. **d**–**f** Same experiments but for the zonal wind speed. The contours show the initial potential temperature or wind speed for the $T_0 = 6$ K runs and the shading shows the difference $T_0 = 6$ minus control

wind balance and did not evolve with time when simulations were performed without the initial disturbance (not shown).

In all the numerical simulations, the same initial distribution of relative humidity was used, meaning that the moisture content of the atmosphere varied based on the temperature change. Keeping relative humidity constant is a reasonable assumption based on global climate model simulations (Solomon 2007).

A control run (hereafter denoted as CTRL) with no temperature change was also performed. The sea surface temperature (SST) in CTRL varied from 298 K (southern boundary) to 259 K (northern boundary), being 279 K in middle of the domain, in the area where the baroclinic wave developed. In CTRL, as well as the other experiments, the SST was uniformly 0.5 K colder than the initial air temperature at the lowest model level. Thus, the SST was changed in all experiments, according to the change of the lowest level air temperature.

First, in Experiment UNI, the mean atmospheric temperature was increased uniformly everywhere in the model domain by $T_0 = 2$, 4 and 6 K. The initial state of the potential temperature in the $T_0 = 6$ K run and the difference from CTRL are shown in Fig. 1a. Note that the uniform increase was imposed to the initial temperature field, whereas Fig. 1 shows the initial potential temperature. The warming of the whole domain by 6 K caused the deceleration of the initial jet stream by up to 1.5 ms^{-1} (Fig. 1d). This was because the uniform warming made pressure increase relatively more in the northern part of the domain, which reduced the meridional pressure gradient and hence decreased the geostrophic wind speed.

In Experiment LOW, the meridional temperature gradient in the lower troposphere was decreased. The northern boundary of the model domain was warmed and the southern boundary cooled by $T_0 = 2$, 4 and 6 K, with a linear interpolation in-between, giving zero change in the middle of the domain. The initial temperature change as a function of the meridional coordinate (y) and pressure (p) was

$$\Delta T(y,p) = T_0 * \frac{2y - (y_n + 1)}{y_n - 1} * \begin{cases} \frac{p - p_{th}}{p_S - p_{th}} & \text{if } p > p_{th} \\ 0 & \text{if } p < p_{th} \end{cases}. \quad (1)$$

Here $T_0 = 2$, 4 or 6 K is the amplitude of the gradient change and $y_N = 160$ is the number of grid points in the meridional direction. The change had its maximum amplitude at the surface (pressure p_S) and was linearly reduced to zero at the level $p_{\text{th}} = 600$ hPa. In the $T_0 = 6$ K run of Experiment LOW, the initial zonal wind speed was roughly 1 ms^{-1} reduced compared to the control run over all of the simulation domain, except at the surface (Fig. 1e), because of the decreased baroclinicity in the lower troposphere.

Thirdly, in Experiment UP, the meridional temperature gradient in the upper troposphere was increased. The implementation was analogous to Experiment LOW except for the sign of the temperature change and the layer in which it was applied:

$$\Delta T(y,p) = T_0 * \frac{(y_n+1)-2y}{y_n-1} * \begin{cases} \frac{p_{th}-p}{p_{th}-p_{TOP}} & \text{if } p < p_{th} \\ 0 & \text{if } p > p_{th} \end{cases} \tag{2}$$

where again $T_0 = 2$, 4 or 6 K. p_{TOP} is the pressure at the model top (at the altitude of 16 km), and $p_{\text{th}} = 600$ hPa. Increasing of the upper level temperature gradient by $T_0 = 6$ K accelerated the zonal wind speed near the top of the model domain by over 3 ms^{-1} (Fig. 1f).

In Experiment LOW at the surface and Experiment UP at the model top, the changes $T_0 = 2$, 4 and 6 K correspond to changes of 4, 8 and 12 K in the meridional temperature difference across the model domain. In the vertical direction, the gradient changes in both experiments were gradually attenuated to zero at the level of 600 hPa. Note that even though the thicknesses of the modified temperature layers in Experiment LOW and UP are almost equal in terms of the pressure interval, the zonal wind speed change in Experiment UP was notably larger, due to the lower density in the upper troposphere.

In order to better understand the adiabatic dynamics in our numerical experiments, we first conducted the experiments in a dry mode. The absence of moisture in the dry experiments simplifies the dynamics of the simulated weather system, and in that way helps to elucidate the consequences of the environmental temperature changes without the effect of latent heat release. Dry integrations are used in idealized simulations, for example when studying the boundary-layer characteristics of mid-latitude cyclones (Sinclair et al. 2010; Boutle et al. 2010). Some studies have also been done with dry initial conditions, but allowing moisture to enter the atmosphere through the surface fluxes during the simulation (e.g., Boutle et al. 2011; Booth et al. 2013). In our dry cases, however, the atmosphere was kept dry throughout the whole integration. This was done by turning off the cloud microphysics and cumulus convection, and switching off the surface moisture fluxes. After that, similar experiments were performed with moisture. These moisture-including simulations are hereafter called "MOIST", and "DRY" refers to simulations done without moisture. Note that in both dry and moist simulations, the surface sensible heat and momentum fluxes were on all the time.

2.3 Cyclone energetics

To shed light on the mechanisms by which the changes in temperature affect the cyclone development, more in-depth analysis of the cyclone energetics was conducted. To this end, time series of different energy quantities for each experiment, and for both dry and moist simulations were calculated. The values of the energy quantities are area-averaged and integrated over the whole air column, thus representing the state of the whole model domain. Furthermore, only the most important parts of the atmospheric energy cycle in terms of mid-latitude cyclone dynamics are analysed in this paper. A complete list of atmospheric energy components and conversion terms can be found from Boer and Lambert (2008). The equations were derived originally by Lorenz (1955) and Oort (1964). The notation in the following equations is conventional and the symbols are listed in Table 1.

The available potential energy of the zonal mean flow (A_Z) is calculated as follows:

$$\langle A_Z \rangle = \int_{p_T}^{p_0} \frac{1}{2} c_p \gamma \left\langle [T]''^2 \right\rangle \frac{dp}{g}. \tag{3}$$

A_Z acts as a source of energy for the baroclinic wave, and therefore decreases with time. The corresponding eddy available potential energy A_E

Table 1 Notation in the energy metrics

[ ]	Zonal mean
*	Deviation from the zonal mean
⟨ ⟩	Area mean
"	Deviation from the area mean
$c_p = 1004$ J kg^{-1}	Specific heat of dry air at constant volume
$\mathbf{F}$	Friction force per unit mass
$g = 9.81$ m s^{-2}	Gravitational acceleration
p	Pressure
p_{TOP}	Upper boundary of the model domain
$p_0 = 1000$ hPa	Lower boundary of the analysis domain
$p_T = 100$ hPa	Upper boundary of the analysis domain
$R = 287$ J kg^{-1}	Gas constant of dry air
T	Temperature
$\mathbf{V}$	Horizontal wind vector
α	Specific volume
$\gamma = \frac{R}{c_p p}(\frac{p_0}{p})^{\kappa}(-\frac{\partial\langle\theta\rangle}{\partial p})^{-1}$	Stability parameter
$\kappa = R/c_p$	Kappa parameter
θ	Potential temperature
$\omega = \frac{dp}{dt}$	Isobaric vertical motion

$$\langle A_E \rangle = \int_{p_T}^{p_0} \frac{1}{2} c_p \gamma \left\langle T^{*2} \right\rangle \frac{dp}{g} \tag{4}$$

represents the potential energy that can be further converted to eddy kinetic energy K_E:

$$\langle K_E \rangle = \int_{p_T}^{p_0} \frac{1}{2} \left\langle \left| \mathbf{V}^* \right|^2 \right\rangle \frac{dp}{g}. \tag{5}$$

The conversion terms between the mentioned energy quantities are also calculated. The conversion between A_Z and A_E ($C(A_Z, A_E)$), which is usually positive in the atmosphere, is given by:

$$C\Big(\langle A_Z \rangle, \langle A_E \rangle\Big) = -\int_{p_T}^{p_0} c_p \gamma \left\langle \left[T^* v^*\right] \frac{\partial T}{\partial y} \right\rangle \frac{dp}{g} - \int_{p_T}^{p_0} c_p \gamma \left(\frac{p}{p_0}\right)^{\kappa} \left\langle \left[T^* \omega^*\right]'' \frac{\partial [\theta]''}{\partial p} \right\rangle \frac{dp}{g}. \tag{6}$$

This means that the eddy is receiving potential energy from the zonal mean flow, which occurs when the meridional heat flux is directed towards lower temperatures, i.e. the cyclone acts to reduce temperature differences in the meridional direction but increase them in the zonal direction. Furthermore, A_E can be converted to K_E through the sinking of relatively cold air and the rising of warm air in the eddy:

$$C\Big(\langle A_E \rangle, \langle K_E \rangle\Big) = -\int_{p_T}^{p_0} \left\langle \alpha^* \omega^* \right\rangle \frac{dp}{g}. \tag{7}$$

Finally, the dissipation of K_E by friction and turbulence is calculated as follows:

$$\langle D_E \rangle = -\int_{p_T}^{p_0} \left\langle \mathbf{V}^* \cdot \mathbf{F}^* \right\rangle \frac{dp}{g}. \tag{8}$$

Before going to the results of our experiments, we need to pay attention to one technicality of A_Z. As will be discussed in Sect. 3, the inclusion of moisture reduces A_Z. This is because we held the air density the same between the corresponding dry and moist simulations. Thus, with the same density, the run with moisture needs to be slightly colder, particularly in the southern part of the model domain where the moisture content is larger. Consequently, the meridional temperature gradient at lower levels is slightly stronger in dry simulations. Note that although the air density was fixed between dry and moist simulations, it was changed between CTRL and the different temperature experiments.

The energy equations used in our analyses are all for a dry atmosphere, which means that they are not fully accurate for the moist waves. In particular, the amount of A_Z may differ largely between moist and dry atmospheres, and can also show opposite sensitivity to increased atmospheric temperature (Kirshbaum et al. 2018). However, as the calculation of A_Z for moist flows is not a straightforward task (Stansifer et al. 2017), we acknowledge this limitation of our analyses and leave it for a potential further investigation.

As a last note, only the results of the $T_0 = 6$ K runs are shown in Sect. 3. The differences in the responses between the $T_0 = 2$, 4 and 6 K runs are in most cases sufficiently linear, and thus showing only the $T_0 = 6$ K run serves the purpose. These $T_0 = 6$ K runs of Experiments UNI, LOW and UP are denoted in the text as UNI6, LOW6 and UP6. However, the corresponding figures for the $T_0 = 2$ and 4 K runs are included in Sect. S1.2 of the supplementary material.

3 Results

Figure 2 gives a snapshot of the structure of the cyclone in DRY-CTRL and MOIST-CTRL, 5 days after the start of the simulation. The cyclone without moisture (Fig. 2a) has 1.3 hPa higher central surface pressure compared to the one with moisture (Fig. 2b). This difference in their intensities is still growing, reaching 7.4 hPa at their deepest stage (see Table 2 for the numerical values). This is because diabatic heating, dominated by latent heat release, acts as a deepening mechanism in this idealized baroclinic wave simulation, which was diagnosed with height tendency equation in Rantanen et al. (2017). However, in both simulations the initial disturbance develops eventually to a very typical, text-book type extratropical cyclone.

Figure 3 shows the time evolution of minimum surface pressure (hereafter SP_{min}) and K_E for both DRY-CTRL

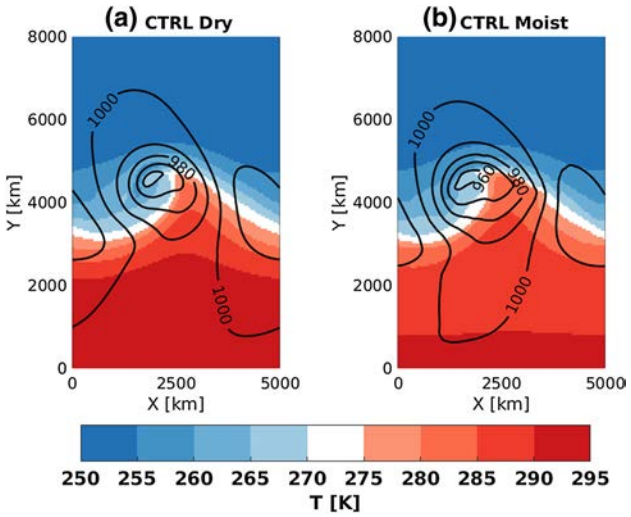

Fig. 2 Surface pressure (contours) and 850 hPa temperature (colors) in **a** DRY-CTRL and **b** MOIST-CTRL at t = 5 days

Table 2 SP_{min} and K_E at $t = 5$ days and the minimum of SP_{min} and maximum of K_E during the 10-day simulations

Run	SP (5 days)	SP (min)	K_E (5 days)	K_E (max)
Dry CTRL	957.5	947.5	3.2	10.3
Dry UNI6-CTRL	2.4	1.5	− 0.33	− 0.15
Dry LOW6-CTRL	2.8	1.9	− 0.48	− 0.58
Dry UP6-CTRL	− 1.7	− 0.6	0.39	− 0.19
Moist CTRL	956.2	940.1	4.5	18
Moist UNI6-CTRL	4.8	− 6.8	− 0.25	− 2.8
Moist LOW6-CTRL	1.9	3.1	− 0.64	− 1.2
Moist UP6-CTRL	− 3.4	− 3.1	0.66	1.2

The results for the $T_0 = 6$ K runs of the three experiments are shown as differences from the control run values. The values at $t = 5$ days can be used as a proxy for the initial growth rate whereas the minimum/maximum values reflect the maximum intensity of the cyclone. The unit for SP_{min} is hPa and that for K_E 10^5 Jm^{-2}

and MOIST-CTRL, and for the $T_0 = 6$ runs of the experiments. Firstly, besides being deeper (compare Fig. 3a and b), the cyclones formed in a moist environment clearly have also more kinetic energy (compare Fig. 3c and d) than the ones formed in a dry environment. Furthermore, the response to the temperature forcings is greater in the moist simulations, as there is more variation in minimum of SP_{min} and maximum of K_E.

The numerical values of SP_{min} and K_E at two different times are given in Table 2. The values for the three temperature experiments are given as differences relative to the relevant CTRL run (e.g. DRY-CTRL or MOIST-CTRL). In the table, the SP_{min} and K_E values at $t = 5$ days are used as a proxy for the initial deepening rate and the K_E growth rate of the cyclone, respectively. In addition, the minimum of SP_{min} and maximum of K_E are given. It is important to consider both the rate of change and the peak values when studying the intensity of cyclones.

The uniform increase of temperature by 6 K in the dry atmosphere slows down the deepening of the cyclone by 2.4 hPa during the first 5 days (Table 2). This difference in the depth is slightly reduced when the deepest stage of the low is reached, being then only 1.5 hPa. In line with these SP_{min} values, DRY-UNI6 has less K_E than DRY-CTRL both during the deepening stage and at the mature stage of the cyclone.

In DRY-LOW6, the response is similar to but slightly larger than that in DRY-UNI6: both the deepening rate and the maximum intensity are reduced when the lower level temperature gradient is decreased (see Table 2). Finally, in DRY-UP6, the upper level temperature gradient was

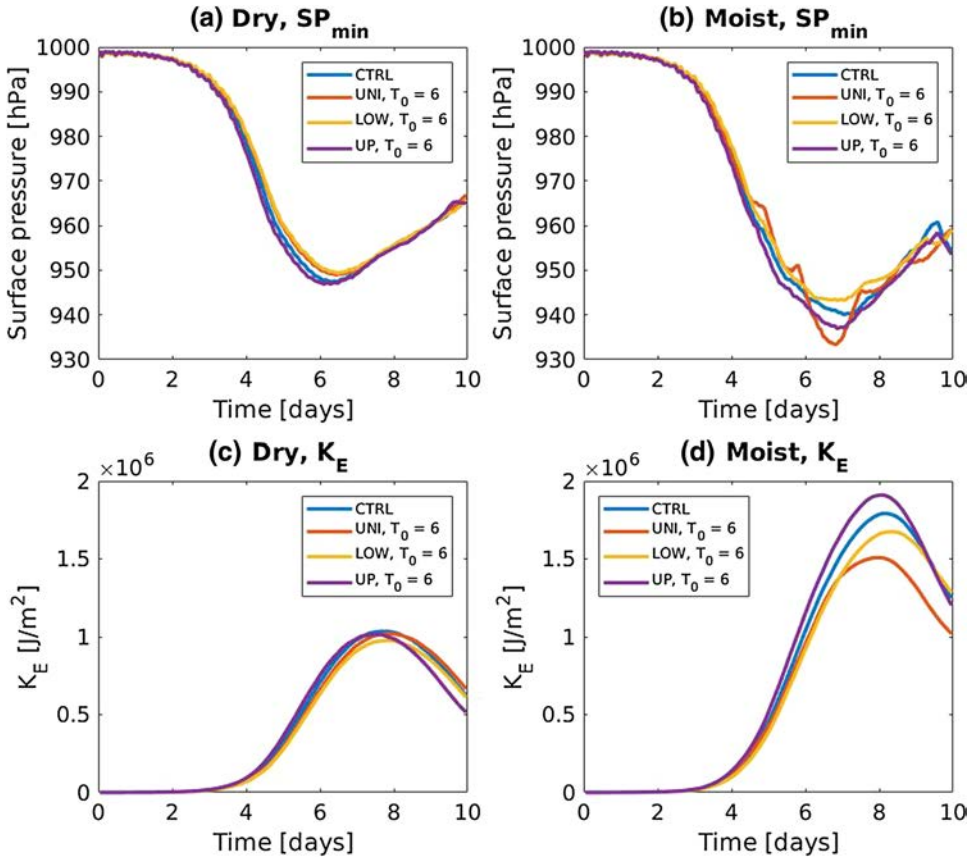

Fig. 3 Time evolution of **a** the minimum surface pressure in the dry experiments, **b** the minimum surface pressure in the moist experiments, **c** eddy kinetic energy in the dry experiments and **d** eddy kinetic energy in the moist experiments. In addition to CTRL, only the $T_0 = 6$ K runs from each experiment are included

increased, which slightly accelerates the deepening and the K_E growth rate of the cyclone during the first 5 days (Table 2). However, even though the cyclone remains marginally (by 0.6 hPa) deeper than in DRY-CTRL at the deepest stage, it actually contains less kinetic energy when its maximum intensity is reached. We will analyze the causes of this unintuitive behaviour later, in Sect. 3.3.

In MOIST-UNI6, the surface low is 4.8 hPa shallower than in MOIST-CTRL at $t = 5$ days, but still reaches a 6.8 hPa lower minimum pressure at the mature stage. This is due to enhanced diabatic processes, as will be discussed in Sect. 3.1. Furthermore, the kinetic energy of MOIST-UNI6 stays constantly below MOIST-CTRL, as also seen from Fig. 3d (red line). Similarly as in the dry simulation, the cyclone in MOIST-LOW6 is weaker than the cyclone in MOIST-CTRL. This is a direct consequence of the weakened baroclinicity and holds true with all the SP_{min} and K_E measures in Table 2. Lastly, the increase of upper tropospheric temperature gradient in the moist atmosphere induces 3.4 hPa/5 days faster cyclogenesis, with the eventual minimum value being 3.1 hPa below MOIST-CTRL. In contrast with the dry simulation, the maximum value of K_E in MOIST-UP6 exceeds that in MOIST-CTRL (see also Fig. 3d, violet line).

3.1 Experiment UNI: uniform temperature increase (dry + moist)

In DRY-UNI6, the cyclone formed in a 6 K warmer environment is slightly weaker than in DRY-CTRL (see Table 2 and the red lines in Fig. 3a and c). This modest weakening of the cyclone with the warming is related to the weakening of the jet stream and thus baroclinicity with the warming (Fig. 1d). This is because the uniform warming of the atmosphere increased pressure relatively more in the northern side of the domain, which weakened the meridional pressure gradient and thus also decelerated the geostrophic wind speed. The reduction of the baroclinicity is visible also in Fig. 4a where the $T_0 = 6$ run (red dashed line) has less A_Z compared to the control run (blue dashed line).

Diabatic processes become important when moisture enters the simulations. The warming of the whole domain by 6 K raises the atmospheric moisture content, which then materializes as an increased latent heat release in the vicinity

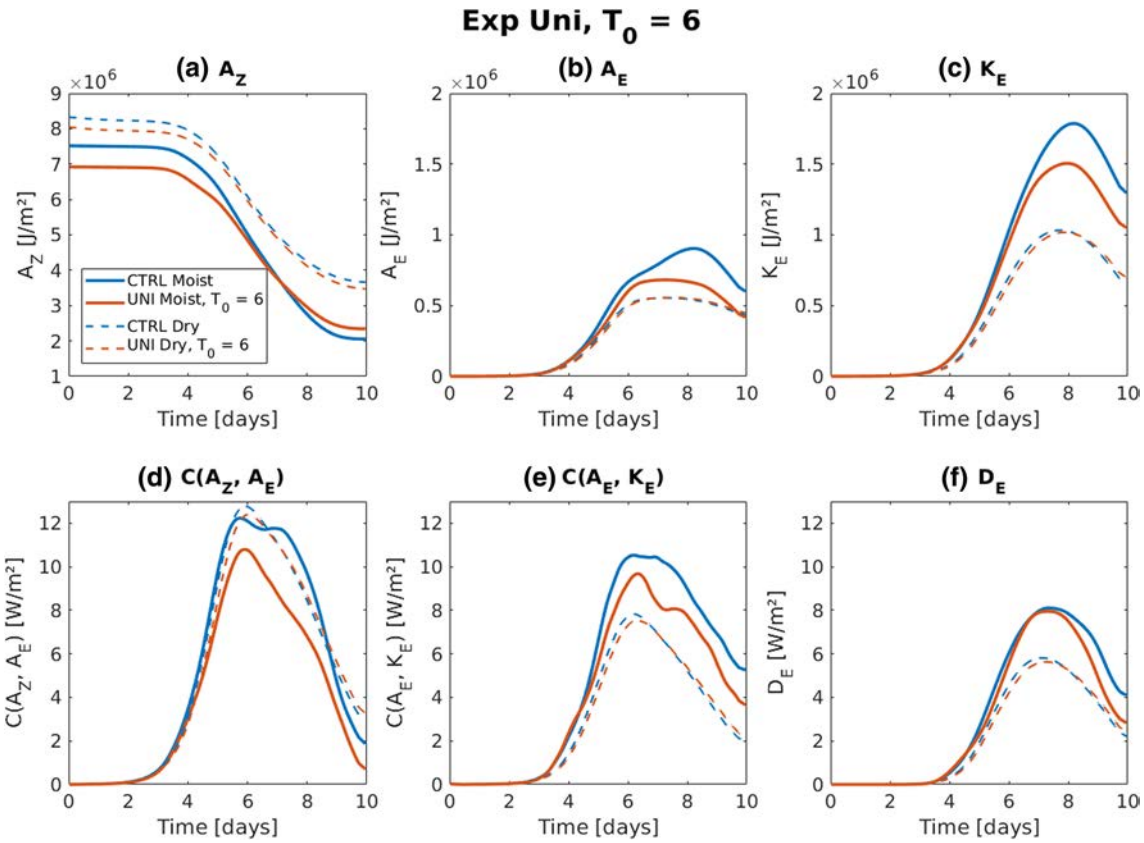

Fig. 4 Time evolution of **a** available potential energy of the zonal mean flow (A_Z), **b** available potential energy of the eddy (A_E), **c** kinetic energy of the eddy (K_E), **d** energy conversion from A_Z to A_E, **e** energy conversion from A_E to K_E and **f** eddy kinetic energy dissipation. In all of the panels, blue dashed line is DRY-CTRL and red dashed line is DRY-UNI6. The solid lines are the same, but for moist simulations. Unit for the energy terms (**a**–**c**) is Jm^{-2} and that for the conversion terms (**d**–**f**) Wm^{-2}

of the surface low. This enhanced diabatic heating results in the surface low reaching a lower minimum pressure than in MOIST-CTRL (Fig. 5). However, the deepening does not occur steadily. Figure 5 shows that the rapid deepening periods starting on days 5 and 6 coincide with increased diabatic heating above the surface low (Fig. 5, red line). During the last deepening period, on day 6, the centre of surface low in MOIST-UNI6 is located near the occlusion point of the cyclone (Fig. 6d), which differs noticeably from MOIST-CTRL (Fig. 6c). Thus, these separate deepening periods are due to localized, small-scale features which intensified consecutively within the surface low. Similar type of rapid re-intensification of the surface low was found in Boutle et al. (2010). They attribute this to a localized spin-up near the surface caused by the latent heat release.

Nevertheless, even though the uniform warming of the environment by 6 K in the moist case produces the deepest surface low in our experiments, this cyclone actually has the lowest maximum K_E of all the moist experiments, including MOIST-CTRL (Table 1; Fig. 3d). This is because the localized minima of surface pressure, induced by latent heat release, are so small scale features that they have very little effect on the domain-averaged K_E (Boutle et al. 2010). Figure 4a shows that MOIST-UNI6 has less A_Z (red solid line) than MOIST-CTRL (blue solid line) in the beginning of the simulation. Moreover, the cyclone in MOIST-UNI6 also does not exploit A_Z as efficiently as the one in MOIST-CTRL, due to weaker $C(A_Z, A_E)$ (Fig. 4d). For this reason, MOIST-UNI6 has more A_Z left in the end of the simulation than MOIST-CTRL.

Kirshbaum et al. (2018) studied closely the production of K_E in their warmed and moistened simulations, and found

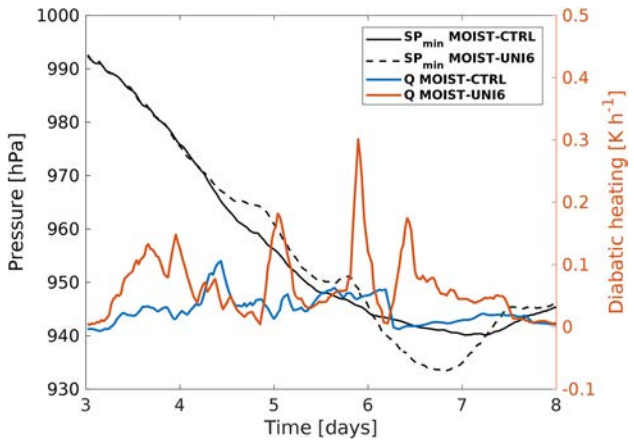

Fig. 5 Time evolution of the minimum surface pressure in MOIST-CTRL (black solid line) and MOIST-UNI6 (black dashed line), and vertically averaged diabatic heating in MOIST-CTRL (blue line) and MOIST-UNI6 (red line) from an area of 350 km × 350 km centered at the surface pressure minimum. The time series of diabatic heating are smoothed by 2-h moving average

that the warm-frontal updraft strengthens and migrates progressively eastwards when temperature is increased. For this reason, the area of updraft coincides less well with the warm sector, and thereby the baroclinic production of K_E can be hindered. Although they increased the temperature more (from 275 to 290 K in the middle of the domain) than what is done in our simulations (from 279 to 285 K), our results seem to confirm this outcome. This can be seen from Fig. 6. On day 5, MOIST-UNI6 has two separate ascent maximums (Fig. 6b), while in MOIST-CTRL, the frontal ascent is located more evenly along the warm front. For this reason, less rising motion is taking place within the warm sector (indicated as red lines in Fig 6) in MOIST-UNI. Moreover, and consistent with the findings of Kirshbaum et al. (2018), the ascent in MOIST-UNI6 on day 5 and 6 extends further east, occurring more outside of the warm sector. Therefore, the phasing between ω^* and $\alpha^*(= RT^*/p^*)$ weakens, which indicates reduced $C(A_E, K_E)$ according to Eq. (7).

The reason why A_E in MOIST-UNI6 also experiences such a major reduction (−25 % in maximum value compared to MOIST-CTRL, solid lines in Fig. 4b) remains partially unclear for us. However, similar results were shown by Tierney et al. (2018) who found that eddy available potential energy decreased when surface temperature in the middle of the domain increased above 276.5 K. Based on their results, the reduction of A_E with the warming originated from decreased $C(A_Z, A_E)$, which is consistent with our results. By contrast, the findings of Kirshbaum et al. (2018) are somewhat inconsistent: in their study, the tendency of A_E is not noticeably dependent on temperature (Fig. 17a in their paper), which differs from Fig. 4b of our study, and Fig. 8a of Tierney et al. (2018). In any case, one explanation for this reduction of A_E could be that the weakening of winds associated with the weaker production of K_E reduces the meridional heat flux induced by the eddy, which then appears as a lower maximum of A_E later on, at day 8. Nevertheless, the decreased $C(A_Z, A_E)$ combined with the fact that the cyclone in MOIST-UNI6 has initially less A_Z leads to the situation where the cyclone in MOIST-UNI6 has less A_E compared to MOIST-CTRL.

Booth et al. (2013) and Tierney et al. (2018) found that the horizontal scale of the cyclone also tends to decrease with increased moisture content in the atmosphere. Thus, they suggest that this contraction of the storm is intimately related to the decrease of K_E. In our simulations, when raising the temperature 6 K from MOIST-CTRL, the meridional extent of the storm seems to decrease slightly (compare potential vorticity (hereafter PV) anomalies in Fig. 6e and f). In addition, Booth et al. (2013) and Tierney et al. (2018) found that the maximum of K_E responds non-monotonically to increasing atmospheric moisture. Their results indicate that the amount of K_E increases significantly when moisture is added from dry to normal conditions. Beyond that, the

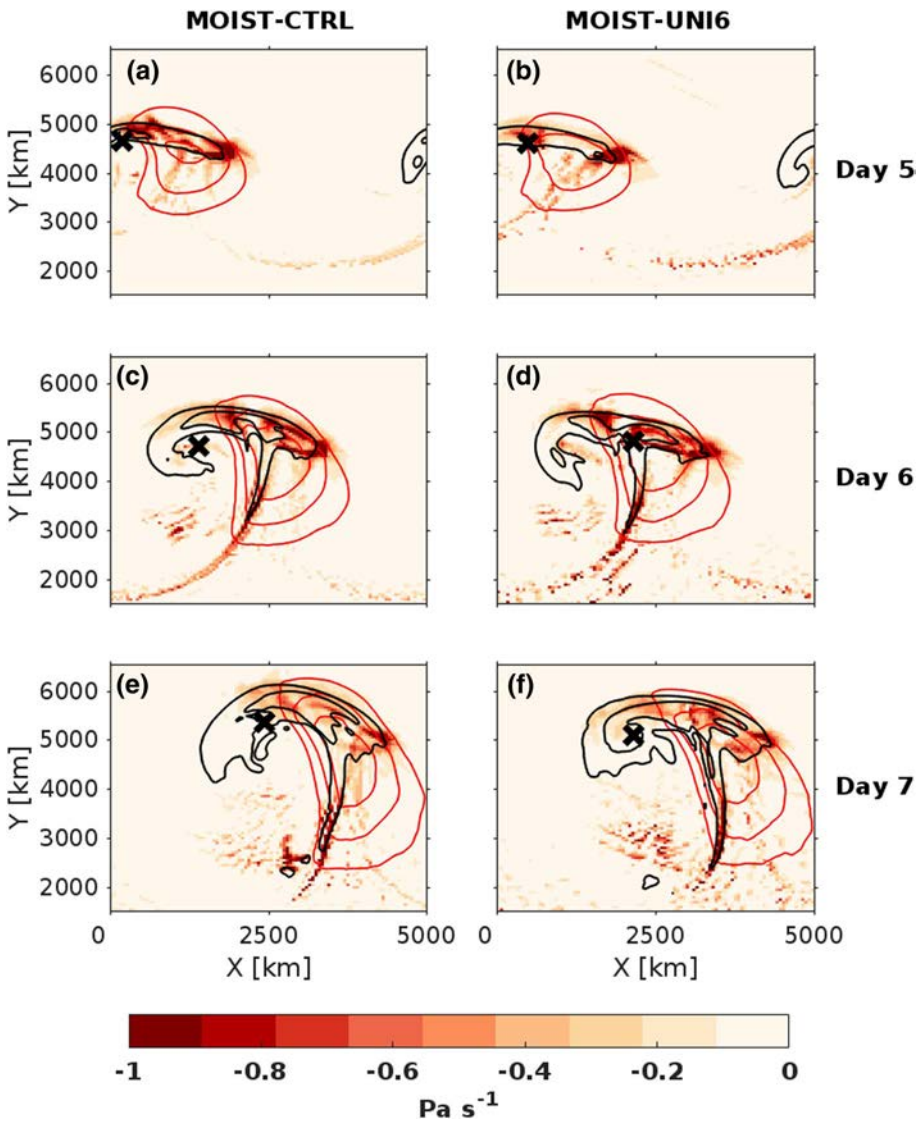

Fig. 6 500–900 hPa mean ω (colours, only negative values shown), 500–900 hPa mean T^* (red contours for 5, 9 and 13 K values) and 700–900 hPa Ertel PV (black contours for 1 and 2 PVU) for MOIST-CTRL (left) and MOIST-UNI6 (right) on day 5, 6 and 7. The cross marks the location of the surface low

increase of absolute moisture actually starts to reduce the maximum K_E. This is consistent with our results (Fig. 4c) as well; K_E increases considerably when the moisture is included (cf. blue dashed and solid lines in Fig. 4c), but then decreases when the moisture is further increased (blue solid and red solid lines in Fig. 4c).

3.2 Experiment LOW: decrease of lower level temperature gradient (dry + moist)

The time series of SP_{min} and K_E of Experiment LOW are presented with yellow lines in Fig. 3. In this experiment, the low level meridional temperature gradient was decreased. The results are largely as expected: the cyclone remains weaker, regardless if moisture is present or not. The decrease in baroclinicity is explicit in Fig. 7a: both simulations show $\sim$ 10 % a reduction of the initial A_Z. Why the modification of the lower tropospheric temperature gradient has such a clear impact on A_Z and consequently the development of the cyclone is partly explained by the vertical distribution of A_Z. The northward decrease in temperature (and therefore A_Z) in these experiments, and in the Northern Hemisphere in general, is strongest near the surface; this makes the reduction of the initial temperature gradient to occur at the levels where A_Z reaches its maximum. For this reason, even a small change in the temperature gradient in the lower troposphere can have a large impact on the total amount of A_Z.

The mechanisms of the weakening can be traced further by studying the energetics of the cyclone: Fig. 7 shows that the maximum values of all energy components and conversion terms are systematically smaller in the $T_0 = 6$ K run than in the control runs. Although the changes in the moist simulations (solid lines) are somewhat larger, the sign of the $T_0 = 6$ K runs relative to the control runs are qualitatively similar in both dry and moist simulations, which increases the robustness of the result.

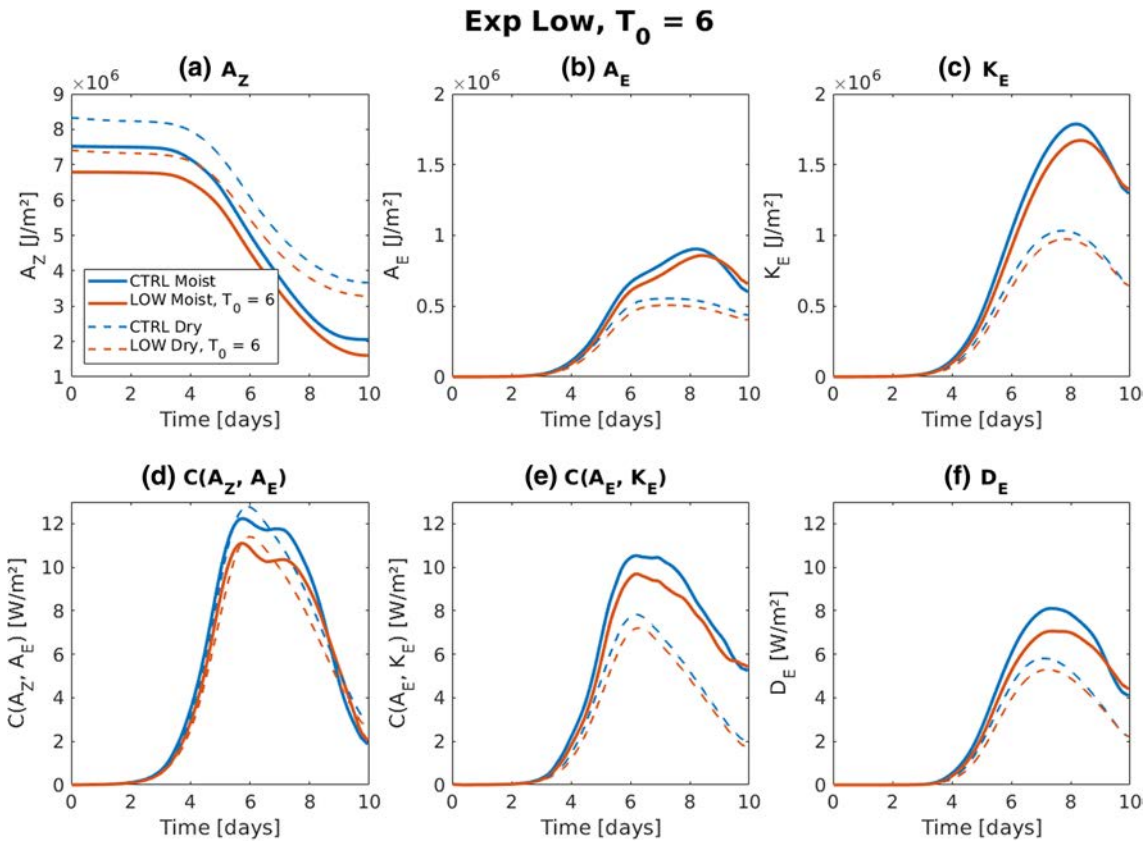

Fig. 7 As Fig. 4, but for Experiment LOW

3.3 Experiment UP: increase of upper level temperature gradient (dry + moist)

As Table 2 reveals, the increase of baroclinicity in the upper troposphere does not increase the maximum K_E in DRY-UP6. In fact, K_E in DRY-UP6 exceeds DRY-CTRL at $t = 5$ days (Table 2), but the maximum of K_E remains actually lower (see also Fig. 8c, dashed lines). In other words, the kinetic energy starts to increase faster, but the cyclone decays earlier. However, the situation changes when moisture is present: the kinetic energy increases (Figs. 3d and 8c, solid lines) and the surface low also becomes notably deeper (Fig. 3b). Thus, in the more realistic case where the moisture is included, increasing the upper level temperature gradient leads to a more intense life cycle.

Because the results of the DRY-UP simulations were somewhat against our initial hypothesis, we studied in more detail the energetics of this experiment. To shed light on the changes in the dynamics of the cyclone, we first need to consider the dashed lines in Fig. 8a. Naturally, A_Z is greater in DRY-UP6 than in DRY-CTRL due to the increase in the upper level temperature gradient. Despite the larger storage of A_Z, however, the maximum of A_E (Fig. 8b, dashed lines) and the maximum of K_E (Fig. 8c, dashed lines) remain lower compared to DRY-CTRL. In other words, the cyclone in DRY-UP6 has seemingly more favourable initial conditions, but it cannot exploit as much of the potential energy in theory available from the zonal mean flow and thus stays weaker.

One reason for the weaker ability of the cyclone to exploit the increased baroclinicity is related to the fact that the temperature gradient was only increased in the upper troposphere. There, the acceleration of zonal wind speed (Fig. 1f) induces faster development of the surface low, which is also seen as slightly lower values of SP_{min} during the deepening phase at $t = 5$ days (Table 2). This marginally stronger cyclogenesis, due to the positive anomaly of A_Z in the upper troposphere, leads to a faster consumption of A_Z also in the lower troposphere (not shown). However, since DRY-UP6 does not have a larger storage of A_Z to be utilized in the lower troposphere, this faster conversion makes the amount of lower tropospheric A_Z in DRY-UP6 decrease faster compared to DRY-CTRL.

Figure 8d (dashed lines) shows the time evolution of $C(A_Z, A_E)$ in DRY-UP6. Beginning from day 6, the conversion is weaker than in DRY-CTRL, because a larger part of the lower tropospheric storage of A_Z has already been consumed by that time DRY-UP6. Although the difference is quite small,

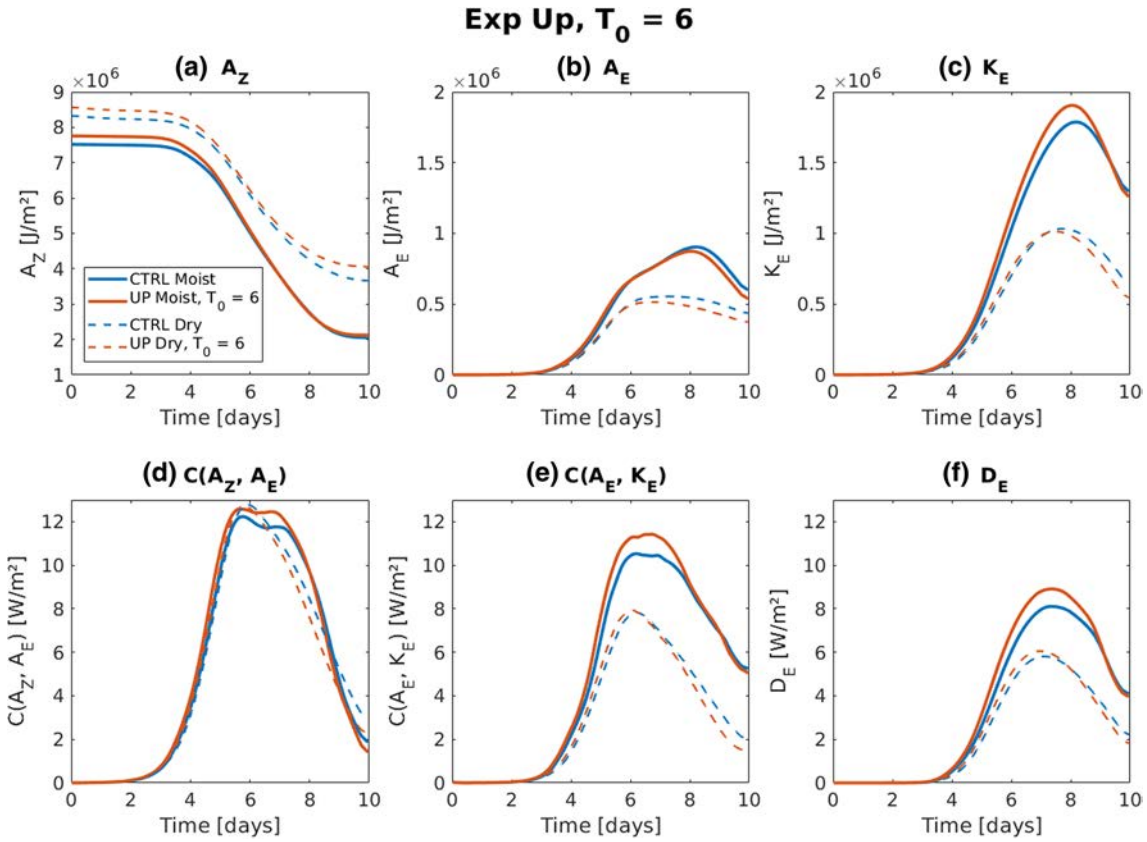

Fig. 8 As Fig. 4, but for Experiment UP

the reduced energy conversion after day 6 is most likely the main reason behind the lower maximum of A_E and K_E in DRY-UP6 compared to DRY-CTRL.

$C(A_Z, A_E)$ in the atmosphere is largely dominated by the meridional heat flux in the eddy (the first term on the right-hand side of Eq. 6). By only taking into account this first term of the conversion equation, and using the fact that the correlation between T^* and v^* is defined as

$$r(T^*v^*) = \frac{[T^*v^*]}{\sigma_{T^*}\sigma_{v^*}}, \tag{9}$$

we can rewrite the conversion as follows:

$$C_{xyz}\Big(\langle A_Z\rangle, \langle A_E\rangle\Big) \approx -\int_0^{p_0} c_p\gamma\left\langle r(T^*v^*)_x(\sigma_{T^*}\sigma_{v^*})_y\frac{\partial T}{\partial y}_z\right\rangle\frac{dp}{g}. \tag{10}$$

Here the covariance $[T^*v^*]$ has been substituted with the product of the correlation $r(T^*v^*)$ and standard deviations $(\sigma_{T^*}\sigma_{v^*})$ of the named variables. The subscript x, y or z refers either to the DRY-CTRL $(x, y, z = 0)$ or DRY-UP6 $(x, y, z = 1)$. Thus, Eq. (10) can be used for investigating the conversion in more detail: we can calculate how $C(A_Z, A_E)$ changes when only some factors from DRY-UP6 are present in the calculation of $C(A_Z, A_E)$. The value of γ in Eqs. (10)–(13) is from DRY-CTRL.

The blue line in Fig. 9a presents the conversion which has been calculated by using the values of DRY-CTRL $(x, y, z = 0$):

$$C_{000}\Big(\langle A_Z\rangle, \langle A_E\rangle\Big) \approx -\int_0^{p_0} c_p\gamma\left\langle r(T^*v^*)_0(\sigma_{T^*}\sigma_{v^*})_0\frac{\partial T}{\partial y}_0\right\rangle\frac{dp}{g}. \tag{11}$$

To study how much the intensity of the cyclone alone affects the conversion, the standard deviations of temperature and meridional wind speed in Eq. (11) have been replaced by the values from DRY-UP6 $(y = 1, x, z = 0)$, while keeping the stability, the correlation between temperature and meridional wind speed, and the meridional temperature gradient at their values in DRY-CTRL:

$$C_{010}\Big(\langle A_Z\rangle, \langle A_E\rangle\Big) \approx -\int_0^{p_0} c_p\gamma\left\langle r(T^*v^*)_0(\sigma_{T^*}\sigma_{v^*})_1\frac{\partial T}{\partial y}_0\right\rangle\frac{dp}{g}. \tag{12}$$

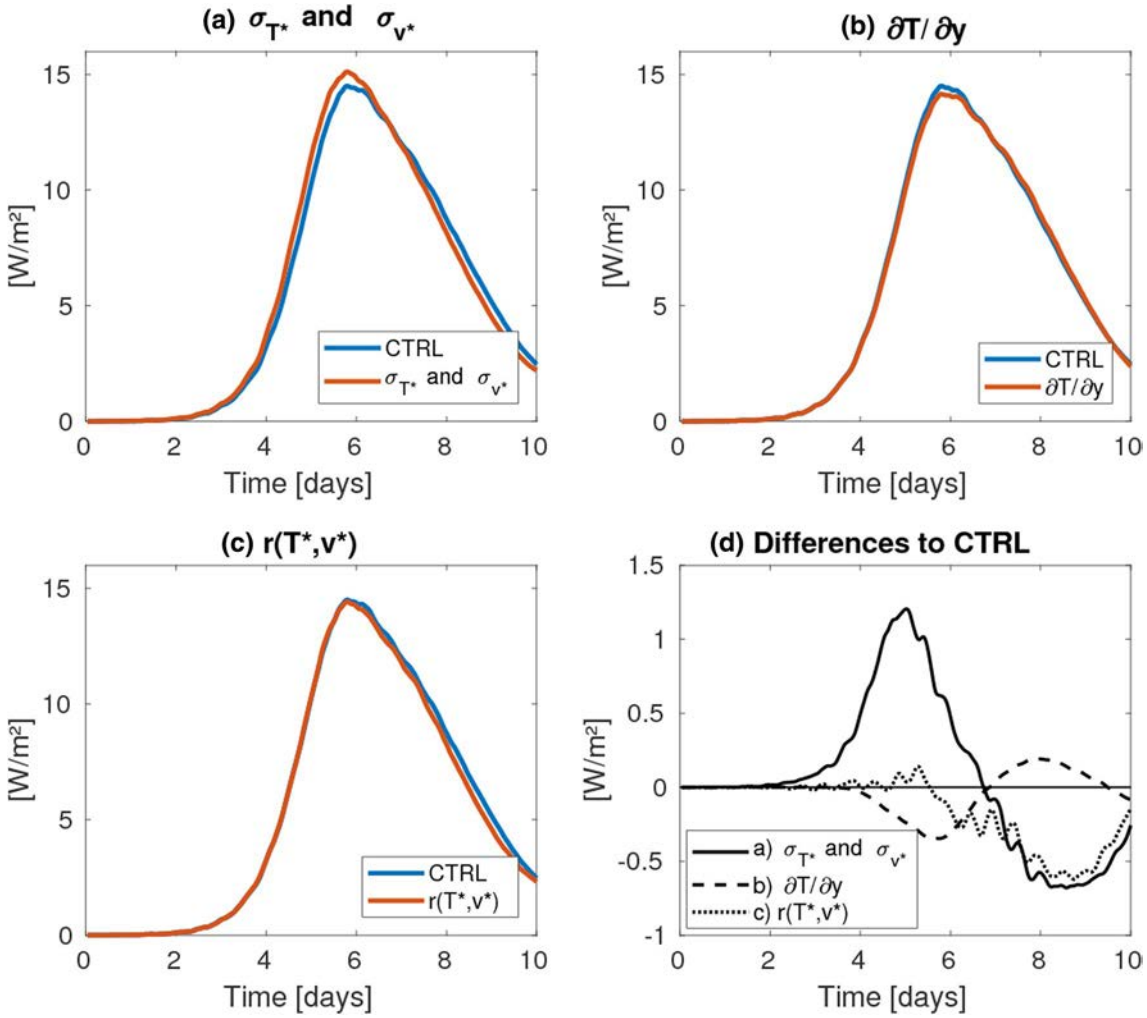

Fig. 9 The effect of different factors on energy conversion from A_Z to A_E. In the calculation of the conversion term in Eq. (10) (red line), only the named factors have been taken from DRY-UP6: **a** standard deviations of temperature and meridional wind speed, **b** meridional temperature gradient, and **c** correlation between temperature and meridional wind speed. The other factors are from DRY-CTRL. For full explanation of the method, see Sect. 3.3. Finally, in **d**, the anomalies of **a**–**c** relative to the control run (blue line) are shown

This conversion C_{010} is shown with the red line in Fig. 9a. By comparing this with C_{000} (blue line), we can see that C_{010} at its maximum is ~ 9 % more efficient, on day 5. Hence, if the temperature gradient was unchanged, the conversion by the cyclone in DRY-UP6 would be initially larger simply because the cyclone develops faster and becomes stronger earlier. See also the anomaly relative to DRY-CTRL in Fig. 9d (solid line).

In Fig. 9b, the conversion depicted with the red line has been calculated in the same manner as in Fig. 9a, but now the meridional temperature gradient has been taken from DRY-UP6 and the other parameters from DRY-CTRL ($z = 1$, $x, y = 0$):

$$C_{001}\Big(\langle A_Z\rangle, \langle A_E\rangle\Big) \approx -\int_0^{p_0} c_p\gamma\left\langle r(T^*v^*)_0(\sigma_{T^*}\sigma_{v^*})_0\frac{\partial T}{\partial y}_1\right\rangle\frac{dp}{g} \tag{13}$$

Surprisingly, the conversion C_{001} would be weaker on days 4–7 (Fig. 9d, dashed line) regardless of the increased upper tropospheric temperature gradient. This weakened conversion originates from the lower troposphere. The temperature gradients at lower levels are initially similar in both runs, but due to the more rapid cyclogenesis in DRY-UP6 the low-level baroclinicity is consumed faster. This is the reason for the weakened conversion during days 4–7 in Fig. 9b (see also the dashed line in Fig. 9d).

The final factor affecting $C(A_Z, A_E)$ is the phasing between the temperature and wind fields. This reflects the structure of the disturbance: the more closely the area of relatively warm (cold) air matches with the area of southerly (northerly) wind, the more effective the meridional heat flux and thus the conversion is. This factor is represented by the correlation $r(T^*, v^*)$ in Eq. (6). Thus, the

conversion with the red line in Fig. 9c has been calculated by taking $r(T^*, v^*)$ from DRY-UP6 but the other parameters from DRY-CTRL. Clearly, the effect of $r(T^*, v^*)$ on the conversion remains very small until day 6, but after that the weakening of the correlation starts to decrease the energy conversion.

As a summary of Fig. 9, the retardation of the fast development in DRY-UP6 originates from the weakened $C(A_Z, A_E)$. This reduced energy transfer is first due to a loss of baroclinicity in the lower troposphere (Fig. 9b), and slightly later also due to unfavorable phasing between temperature and wind fields (Fig. 9c). The unfavorable phasing is ultimately because of the increased wind speed in the upper troposphere (Fig. 1f), which disturbs the vertical structure of the cyclone. Furthermore, the trough axis is more vertically aligned in DRY-UP6 than in DRY-CTRL after day 4 (not shown). According to Hoskins et al. (1985), too strong upper-level winds can disrupt the phase-locking and sustained growth of a synoptic-scale disturbance whose amplitude is initially small. This also seems to be the case in the DRY-UP6. Finally, after day 7, the weakening of the disturbance itself starts to decrease its energy production (Fig. 9a). As the net effect of all these three factors, the decrease in K_E starts earlier in DRY-UP6 than in DRY-CTRL and the maximum of K_E is slightly lower.

To get a more concrete understanding of the weakening $C(A_Z, A_E)$ in DRY-UP6, T^*v^* maps of the $T_0 = 6$ K run and their differences to DRY-CTRL at 600 hPa are shown in Fig. 10 for four different times. Furthermore, the zonal means of the differences are depicted to the right of each map. On day 5, the meridional heat flux T^*v^* is generally larger in DRY-UP6 (map of Fig. 10a) than in DRY-CTRL, which is mostly due to higher v^* in DRY-UP6. This makes the conversion stronger (sum of Fig. 9a and c). However, on day 6, the meridional heat flux starts to become weaker than in DRY-CTRL, decreasing first around the centre of the surface low (Fig. 10b). After that, on days 7 and 8, the zonal mean of the meridional heat flux ($[T^*v^*]$) becomes ~ 5–10 K ms^{-1} weaker than in DRY-CTRL (Fig. 10c and d, blue lines), which means a ~ 15–20 % reduction in relative terms (not shown). This reduction in $[T^*v^*]$ originates from the narrow area on the western edge of the warm sector (map of Fig. 10c). Another visible feature in the maps is the reduction of the positive (red) $[T^*v^*]$ anomaly within the warm sector, which ends up being negative (blue) on day 8 (Fig. 10d). The decrease in the warm-sector heat flux is

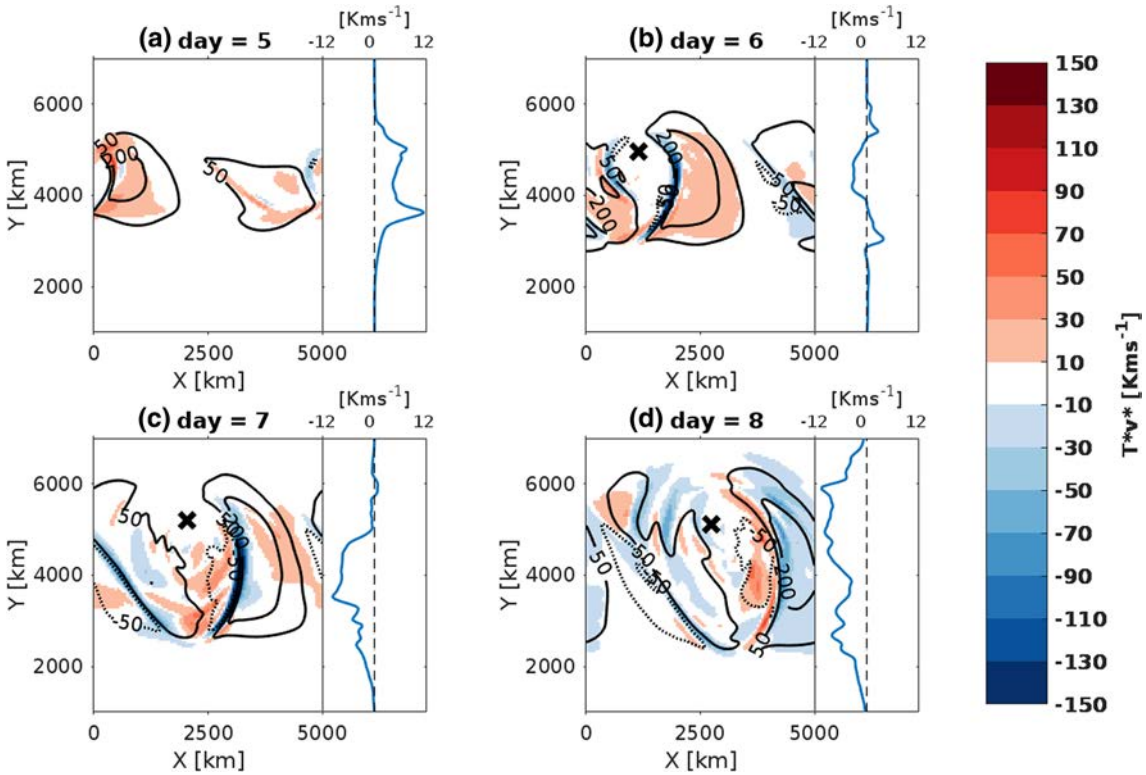

Fig. 10 T^*v^* (contours) and its difference to the control run (colours) at the 600 hPa level in DRY-UP6, at **a** day 5, **b** day 6, **c** day 7 and **d** day 8. Zonal means of the T^*v^* differences are shown next to each map with blue line. In the maps, solid lines depict positive T^*v^* values (contours for 50, 200 and 400 km s^{-1}) while negative values are shown with dashed lines (− 50 km s^{-1} contour). The cross marks the location of the surface low. When calculating the difference between DRY-UP6 and DRY-CTRL, the T^*v^* fields have been shifted so that the surface lows from both runs are aligned in x-direction

consistent with the overall weakening of the cyclone relative to DRY-CTRL, and starts to weaken $C(A_Z, A_E)$ compared to DRY-CTRL after day 6.

In MOIST-UP6, the maximum of A_E (Fig. 8b, solid lines) remains lower than in MOIST-CTRL, whereas K_E (Fig. 8c, solid lines) peaks notably higher. The higher maximum of K_E is due to more effective conversion from A_E to K_E (Fig. 8e, solid lines). Figure 11 shows the meridional averages (from 2000 to 6000 km in y-direction) of diabatic heating and PV* in DRY-UP6 and MOIST-UP6. DRY-UP6 does not contain moisture, thus the only contribution to diabatic heating comes from the boundary-layer dissipation and surface heat fluxes. In any case, the upper level winds in both DRY-UP6 and MOIST-UP6 are increased relative to corresponding CTRL runs, hence implying faster eastward propagation of the upper level PV anomalies. We suggest the following explanation for why the increased upper-level baroclinicity leads to an increase in K_E in MOIST-UP6 despite a decrease in DRY-UP6. In MOIST-UP6, diabatic heating extends up to the height of upper level PV anomalies (~ 300 hPa level) (Fig. 11d, f). Thus, the heating helps to connect the upper- and low-level PV anomalies via the generation of low-level PV below the heating maximum. For example, in MOIST-UP6, as the upper level wind speeds are increased, the propagation speed of the heating maximums and thus the propagation speed of low-level PV generation increase accordingly. In addition, the heating enhances the negative PV anomaly and divergence aloft, which restricts the forward propagation of the positive PV anomaly associated with the upper trough. This whole process allows the cyclone to exploit more effectively the increased baroclinicity in the upper troposphere, which is seen as higher maximums of $C(A_Z, A_E)$ (Fig. 8d) and $C(A_E, K_E)$ (Fig. 8e) compared to MOIST-CTRL. However, this mechanism is not

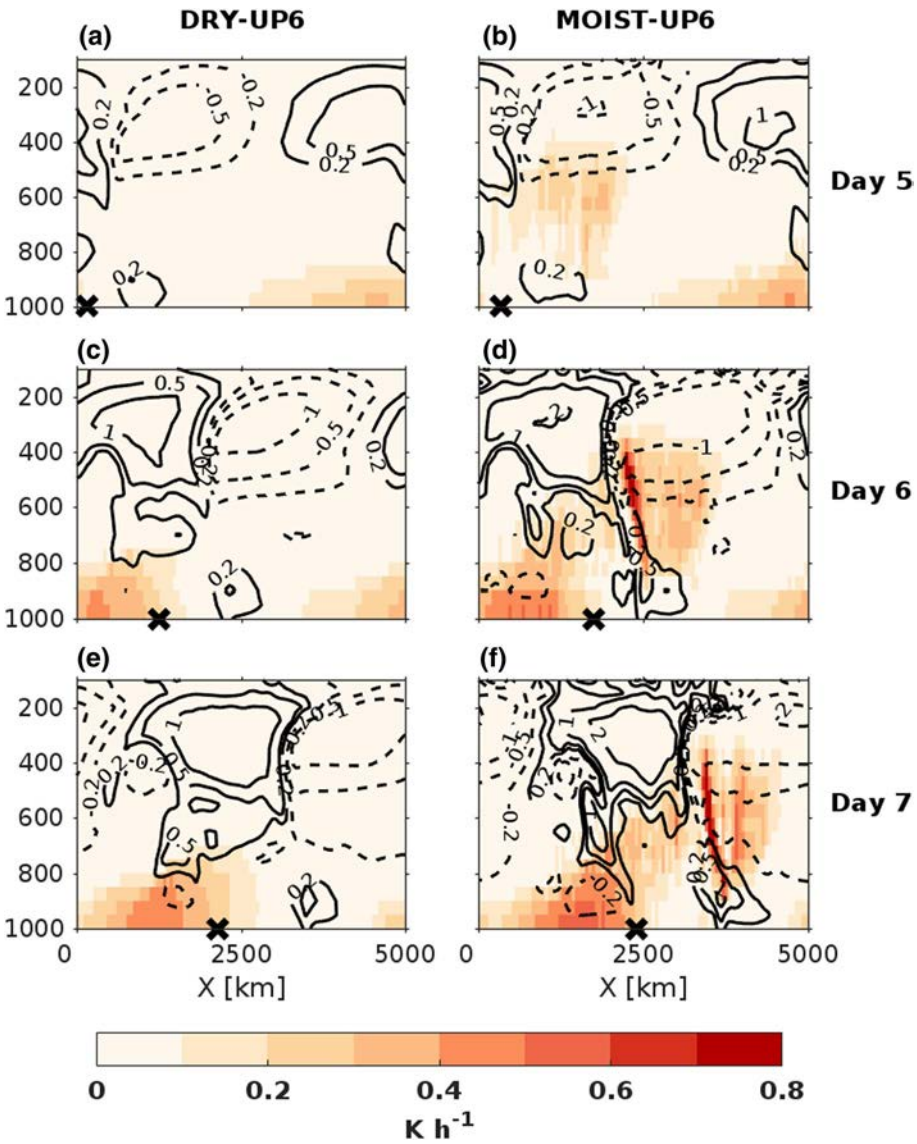

Fig. 11 Meridionally averaged cross sections of diabatic heating (colours) and Ertel PV departure from the zonal mean (contours, positive values in solid lines, negative values in dashed lines) in DRY-UP6 (left) and MOIST-UP6 (right) on day 5, 6 and 7. The meridional average has been taken over 2000–6000 km in y-direction of the domain. The cross marks the location of the surface low

present in DRY-UP6 (Fig. 11c, e), where the phase-locking between upper and lower levels can break more easily if the upper level winds are increased too much.

4 Discussion

In order to identify the changes in adiabatic dynamics of the cyclones, all experiments were conducted first in a dry atmosphere. Naturally, this can raise a reasonable question: why focus on the effects in a dry atmosphere, as the results are not directly applicable to the real, moist atmosphere? Our answer is that the scope of this study is to identify the mechanisms by which modified temperature distributions affect the dynamics of mid-latitude cyclones. In this context, idealized dry simulations provide a valuable benchmark, although they clearly must be complemented by more realistic moist simulations.

Our results do not necessarily apply to all baroclinic waves. As found in Kirshbaum et al. (2018), the sensitivity of K_E to larger temperatures can be reversed using a different jet stream in the model initialization. In addition, the surface type and the wavelength may also affect the sensitivity. However, as these caveats found by Kirshbaum et al. (2018) affect the production of K_E, which is strongly dependent on the distribution of diabatic heating in the eddy, they are only directly applicable to the MOIST-UNI experiment. In the LOW and UP experiments instead, where the magnitude of diabatic heating was not changed significantly compared to corresponding CTRL runs, the changes in cyclone intensity are mainly related to the changed baroclinicity. Therefore, the results of the LOW and UP experiments might be more universal amongst various baroclinic waves, but of course more experiments are needed to confirm this.

Finally, although the temperature changes investigated in this study will occur simultaneously in the real atmosphere, investigating their effects on mid-latitude cyclogenesis separately will help to understand and interpret e.g. the results of climate change projections made with GCMs. Nevertheless, one topic for additional studies would be to apply all three temperature modifications together, like they will occur in the real world. That would help to assess the linearity of the cyclone dynamics to the performed temperature changes. This is an important issue when drawing conclusions from our results to real-world changes in mid-latitude cyclones in a changing climate.

5 Conclusions

We investigated the response of extra-tropical cyclones to different atmospheric temperature changes: (1) uniform temperature increase, (2) decrease of the lower level meridional temperature gradient and (3) increase of the upper level temperature gradient. These temperature forcings are incorporated to the initial state of the idealised model experiments one at a time. Hence, this method allows one to identify how extra-tropical cyclones respond to changes in the environmental temperature distribution and ascertain the underlying responsible physical mechanisms. The main tool for identifying the changes in the simulated weather systems is an energy cycle analysis, which is carried out for each model experiment.

Increasing the temperature and thus moisture content in the atmosphere from typical present-day values induces deeper cyclones with less amplified upper-level dynamic properties, such as eddy kinetic energy. This decrease of eddy kinetic energy with the warming is in line with recent studies by Kirshbaum et al. (2018) and Tierney et al. (2018), but contrary to Boutle et al. (2011). In addition, Kirshbaum et al. (2018) did not observe the decrease of minimum surface pressure, which can be partly explained by the coarser horizontal grid spacing ($\Delta x = 100$ km) used in their simulations. According to Kirshbaum et al. (2018), the reduction of eddy kinetic energy with warming can be traced further to be a consequence from unfavourable phasing between rising motion and buoyancy within the warm sector. This is also confirmed by our results. Furthermore, and similarly to Kirshbaum et al. (2018), the warming of the cyclone environment uniformly decreases the capability of the cyclone to utilize the available potential energy from the zonal mean flow.

The main outcome emerging from our temperature gradient experiments is that the cyclone responds differently to the changes in lower and upper level gradients. The decrease of lower level meridional temperature gradient, a scenario expected with climate change in Northern mid-latitudes, is found to decrease the strength of the storm in a straightforward way: all the energy quantities used in this paper remain lower regardless whether moisture is present in the simulation or not. This is a direct outcome from the decreased baroclinicity.

The increase of the upper level temperature gradient, also a scenario expected in a warmer climate, however, is found to affect the development of the cyclone in a more complex way. In the dry atmosphere, increasing the upper level temperature gradient decreases the eddy kinetic energy, whereas in the moist atmosphere the kinetic energy of the cyclone increases. The increase of baroclinicity in the upper troposphere boosts the jet stream considerably, which induces stronger cyclogenesis and thereby faster consumption of the potential energy in the lower troposphere. This leads eventually to a loss of conversion from the available potential energy of the zonal mean flow to eddy potential energy during the mature stage, and consequently a premature decay of the storm. However, due to latent heat release,

the response in the moist atmosphere is different: diabatic heating enhances the interaction between upper- and low-level PV anomalies, and hence helps the surface cyclone to exploit the increased upper level baroclinicity. As a result, the kinetic energy of the cyclone increases at larger meridional temperature gradients in the upper troposphere, when moisture is present.

Acknowledgements MR acknowledges the Doctoral Programme in Atmospheric Sciences (ATM-DP, University of Helsinki) for financial support. This work was partially funded by the Academy of Finland Center of Excellence programme (project no. 307331). The authors wish to acknowledge CSC—IT Center for Science, Finland, for computational resources. The authors thank also Daniel Kirshbaum and three other anonymous reviewers for their insightful and constructive comments.

References

Bengtsson L, Hodges KI, Roeckner E (2006) Storm tracks and climate change. J Clim 19:3518–3543

Bengtsson L, Hodges KI, Keenlyside N (2009) Will extratropical storms intensify in a warmer climate? J Clim 22:2276–2301

Blázquez J, Pessacg NL, Gonzalez PL (2013) Simulation of a baroclinic wave with the wrf regional model: sensitivity to the initial conditions in an ideal and a real experiment. Meteorol Appl 20:447–456

Boer G, Lambert S (2008) The energy cycle in atmospheric models. Clim Dyn 30:371–390

Booth JF, Wang S, Polvani L (2013) Midlatitude storms in a moister world: lessons from idealized baroclinic life cycle experiments. Clim Dyn 41:787–802

Boutle I, Beare R, Belcher SE, Brown A, Plant RS (2010) The moist boundary layer under a mid-latitude weather system. Bound-Lay Meteorol 134:367–386

Boutle I, Belcher S, Plant R (2011) Moisture transport in midlatitude cyclones. Q J R Meteor Soc 137:360–373

Catto JL, Shaffrey LC, Hodges KI (2011) Northern Hemisphere extratropical cyclones in a warming climate in the HiGEM high-resolution climate model. J Clim 24:5336–5352

Dudhia J (1989) Numerical study of convection observed during the winter monsoon experiment using a mesoscale two-dimensional model. J Atmos Sci 46:3077–3107

Fantini M (2004) Baroclinic instability of a zero-PVE jet: Enhanced effects of moisture on the life cycle of midlatitude cyclones. J Atmos Sci 61:1296–1307

Fink AH, Brücher T, Ermert V, Krüger A, Pinto JG (2009) The European storm Kyrill in January 2007: synoptic evolution, meteorological impacts and some considerations with respect to climate change. Nat Hazard Earth Sys 9:405–423

Hong SY, Dudhia J, Chen SH (2004) A revised approach to ice microphysical processes for the bulk parameterization of clouds and precipitation. Mon Weather Rev 132:103–120

Hong SY, Noh Y, Dudhia J (2006) A new vertical diffusion package with an explicit treatment of entrainment processes. Mon Weather Rev 134:2318–2341

Hoskins BJ, McIntyre M, Robertson AW (1985) On the use and significance of isentropic potential vorticity maps. Q J R Meteor Soc 111:877–946

Kain JS, Fritsch JM (1993) Convective parameterization for mesoscale models: the Kain–Fritsch scheme. In: The representation of cumulus convection in numerical models, Springer, pp 165–170

Kirshbaum DJ, Merlis T, Gyakum J, McTaggart-Cowan R (2018) Sensitivity of idealized moist baroclinic waves to environmental temperature and moisture content. J Atmos Sci 75:337–360

Lambert SJ, Fyfe JC (2006) Changes in winter cyclone frequencies and strengths simulated in enhanced greenhouse warming experiments: results from the models participating in the IPCC diagnostic exercise. Clim Dyn 26:713–728

Lorenz EN (1955) Available potential energy and the maintenance of the general circulation. Tellus 7:157–167

O'Gorman PA (2011) The effective static stability experienced by eddies in a moist atmosphere. J Atmos Sci 68:75–90

Oort AH (1964) On estimates of the atmospheric energy cycle. Mon Weather Rev 92:483–493

Paulson CA (1970) The mathematical representation of wind speed and temperature profiles in the unstable atmospheric surface layer. J Appl Meteorol 9:857–861

Pfahl S, Ogorman PA, Singh MS (2015) Extratropical cyclones in idealized simulations of changed climates. J Clim 28:9373–9392

Rantanen M, Räisänen J, Lento J, Stepanyuk O, Räty O, Sinclair VA, Järvinen H (2017) OZO v. 1.0: software for solving a generalised omega equation and the Zwack-Okossi height tendency equation using WRF model output. Geosci Model Dev 10:827–841

Shamarock W, Klemp J, Dudhia J, Gill D, Barker D, Duda M, Huang X, Wang W, Powers J (2008) A description of the advanced research WRF version 3. NCAR technical note NCAR/TN/u2013475

Sinclair VA, Keyser D (2015) Force balances and dynamical regimes of numerically simulated cold fronts within the boundary layer. Q J R Meteor Soc 141:2148–2164

Sinclair VA, Belcher SE, Gray SL (2010) Synoptic controls on boundary-layer characteristics. Bound-Lay Meteorol 134:387–409

Solomon S (2007) Climate change 2007 - the physical science basis: Working group I contribution to the fourth assessment report of the IPCC, vol 4. Cambridge University Press, Cambridge

Stansifer EM, O'Gorman PA, Holt JI (2017) Accurate computation of moist available potential energy with the Munkres algorithm. Q J R Meteor Soc 143:288–292

Tierney G, Posselt DJ, Booth JF (2018) An examination of extratropical cyclone response to changes in baroclinicity and temperature in an idealized environment. Clim Dyn 1–18

Waite ML, Snyder C (2009) The mesoscale kinetic energy spectrum of a baroclinic life cycle. J Atmos Sci 66:883–901

Wernli H, Dirren S, Liniger MA, Zillig M (2002) Dynamical aspects of the life cycle of the winter storm Lothar (24–26 December 1999). Q J R Meteor Soc 128:405–429

Whitaker JS, Davis CA (1994) Cyclogenesis in a saturated environment. J Atmos Sci 51:889–908

Woollings T (2008) Vertical structure of anthropogenic zonal-mean atmospheric circulation change. Geophys Res Lett 35(19)

Yin JH (2005) A consistent poleward shift of the storm tracks in simulations of 21st century climate. Geophys Res Lett 32(18)

Zappa G, Shaffrey LC, Hodges KI, Sansom PG, Stephenson DB (2013) A multimodel assessment of future projections of North Atlantic and European extratropical cyclones in the CMIP5 climate models. J Clim 26:5846–5862

Tellus SERIES A DYANAMIC METEOROLOGY AND OCEANOGRAPHY
PUBLISHED BY THE INTERNATIONAL METEOROLOGICAL INSTITUTE IN STOCKHOLM

The extratropical transition of Hurricane Ophelia (2017) as diagnosed with a generalized omega equation and vorticity equation

By MIKA RANTANEN[1]*, JOUNI RÄISÄNEN[1], VICTORIA A. SINCLAIR[1], JUHA LENTO[2], and HEIKKI JÄRVINEN[1], [1]*Institute for Atmospheric and Earth System Research/Physics, Faculty of Science, University of Helsinki, Helsinki, Finland;* [2]*CSC–IT Center for Science, Espoo, Finland*

(Manuscript Received 14 June 2019; in final form 20 November 2019)

ABSTRACT

Hurricane Ophelia was a category 3 hurricane which underwent extratropical transition and made landfall in Europe as an exceptionally strong post-tropical cyclone in October 2017. In Ireland, Ophelia was the worst storm in 50 years and resulted in significant damage and even loss of life. In this study, the different physical processes affecting Ophelia's transformation from a hurricane to a mid-latitude cyclone are studied. For this purpose, we have developed software that uses OpenIFS model output and a system consisting of a generalized omega equation and vorticity equation. By using these two equations, the atmospheric vertical motion and vorticity tendency are separated into the contributions from different physical processes: vorticity advection, thermal advection, friction, diabatic heating, and the imbalance between the temperature and vorticity tendencies. Vorticity advection, which is often considered an important forcing for the development of mid-latitude cyclones, is shown to play a small role in the re-intensification of the low-level cyclone. Instead, our results show that the adiabatic upper-level forcing was strongly amplified by moist processes, and thus, the diabatic heating was the dominant forcing in both the tropical and extratropical phases of Ophelia. Furthermore, we calculated in more detail the diabatic heating contributions from different model parameterizations. We find that the temperature tendency due to the convection scheme was the dominant forcing for the vorticity tendency during the hurricane phase, but as Ophelia transformed into a mid-latitude cyclone, the microphysics temperature tendency, presumably dominated by large-scale condensation, gradually increased becoming the dominant forcing once the transition was complete. Temperature tendencies caused by other diabatic processes, such as radiation, surface processes, vertical diffusion, and gravity wave drag, were found to be negligible in the development of the storm.

Keywords: extratropical transition, hurricane, omega equation, vorticity tendency

1. Introduction

Tropical cyclones which curve poleward and enter mid-latitudes often lose their tropical characteristics and transform into mid-latitude cyclones through a process called extratropical transition (ET; Sekioka, 1956; Palmén, 1958). The ET does not occur instantly, but is rather defined as a time period during which the tropical characteristics of the cyclone are replaced by the features typical for mid-latitude cyclones, such as a cold core and fronts (e.g. Evans et al., 2017). An objective and widely used methodology to characterize the transformation process is the cyclone phase space diagram (Hart, 2003). The diagram describes both the thermal wind ($-V_T^L$-parameter) and frontal asymmetry (B-parameter) during the cyclone's life cycle. Evans and Hart (2003) defined the onset of ET when the cyclone becomes asymmetric ($B > 10$ m) and the completion of ET when the cold core develops ($-V_T^L < 0$ m).

In the North Atlantic, up to half of all tropical cyclones undergo ET and become mid-latitude cyclones (Hart and Evans, 2001; Bieli et al., 2019). Furthermore, out of the tropical cyclones that undergo extratropical transition in the North Atlantic, 51% undergo post-ET intensification (Hart and Evans, 2001). This result is based on a dataset covering 61 cases between 1979 and 1993. Thus, according to the climatology, western Europe is impacted

*Corresponding author. e-mail: mika.p.rantanen@helsinki.fi

Citation: Tellus A: 2020, **72**, 1721215, https://doi.org/10.1080/16000870.2020.1721215

by a transitioning tropical cyclone once every 1–2 years (Hart and Evans, 2001). These post-tropical storms can cause severe damage by themselves (e.g. Browning et al., 1998; Thorncroft and Jones, 2000; Feser et al., 2015), or downstream via amplification of the mid-latitude flow (Grams and Blumer, 2015; Keller et al., 2018). Moreover, due to the warming of climate, post-tropical storms impacting Europe are projected to become more frequent (Haarsma et al., 2013; Baatsen et al., 2015; Liu et al., 2017).

For this reason, understanding the atmospheric forcing mechanisms that cause tropical cyclones to intensify as post-tropical cyclones is of great importance. The energy source of tropical cyclones is the warm sea surface temperatures, which allow latent heat release via deep, moist convection. Extratropical cyclones are, in contrast, primarily driven by baroclinic processes due to meridional temperature and moisture gradients at mid-latitudes. Therefore, the ET of tropical cyclones involves often complex dynamics as the tropical storm enters the mid-latitudes and starts to experience the baroclinic environment.

The complexity of dynamics and the strong involvement of both thermodynamic and dynamic processes in the transitioning cyclones raises a relevant question: What is the relative importance of different forcing mechanisms for the cyclone during its transition process? This paper is a case study that attempts to answer this question by examining the contributions of different synoptic-scale forcing terms to the evolution of Hurricane Ophelia, which hit Ireland as a strong post-tropical storm in October 2017.

Earlier diagnostic case studies about extratropical cyclones have discovered the equal importance of diabatic heating and thermal advection to the Presidents' Day cyclone in 1979 (Räisänen, 1997), the primary contribution from cyclonic vorticity advection to continental cool-season extratropical cyclones over the U.S. (Rolfson and Smith, 1996), and warm-air advection (diabatic heating) having the largest influence on explosive development in cold-core (warm-core) cyclones over the North Atlantic (Azad and Sorteberg, 2009). Bentley et al. (2019) studied the extratropical cyclones leading to extreme weather events over Central and Eastern North America. They concluded that both baroclinic and diabatic processes are important during the life cycles of the cyclones that lead to extreme weather. However, the study did not make an attempt to directly quantify the magnitude of the baroclinic and diabatic processes affecting the evolution of the cyclones. A very recent study (Seiler, 2019), performed with an inversion of potential vorticity, suggests that in about half of the extreme extratropical cyclones in the Northern Hemisphere the largest contribution to the maximum intensity is associated with condensational heating in the lower-level atmosphere.

There are numerous diagnostic studies about tropical cyclones that undergo extratropical transition in the literature. Milrad et al. (2009) studied poleward-moving tropical cyclones occurring in Eastern Canada during 1979–2005. According to their results, the differential vorticity advection above the surface cyclone played a major role in the post-ET intensification. The vorticity advection was associated with a decrease of the trough-ridge wavelength, which, in turn, led to a stronger circulation and larger values of warm-air advection. Consistently, the advection of vorticity by the non-divergent wind in the upper-troposphere was found to be a considerable forcing also for the reintensification of Tropical Storm Agnes along the East Coast of United States (DiMego and Bosart, 1982) and the extratropical cyclone developed from the remnants of Typhoon Bart in the Western North Pacific (Klein et al., 2002). Conversely, one reason for the post-tropical decay of Typhoon Jangmi in 2008 was its weak phasing with upper-level forcing for broad-scale ascending motion (Grams et al., 2013). Ritchie and Elsberry (2007) reported significantly stronger midtropospheric cyclonic vorticity advection and lower-tropospheric thermal advection above intensifying transitioning cyclones compared to the decaying ones. In summary, based on both real world examples and idealized simulations, there is clear evidence that baroclinic forcing terms can act substantially in the post-ET intensification.

We expect that diabatic processes were dominant in the tropical phase of Ophelia. We hypothesize also that that baroclinic processes became approximately as important as diabatic heating for the cyclone development when it moved to mid-latitudes and strengthened after the ET. In this study, the contributions of different forcing mechanisms to Ophelia's evolution are assessed using a generalized omega equation and the vorticity equation. This equation system was adapted from Räisänen (1997), and the first version of the diagnostic software used in this paper was documented in Rantanen et al. (2017) (hereafter R17). The equations, the model simulation, and the diagnostic software are presented in Section 2. Section 3 provides the synoptic overview of Ophelia's life cycle, and the performance of the model simulation is evaluated in Section 4. The main results, namely the contributions of different forcing terms to the atmospheric vertical motion and vorticity tendency of the cyclone, are presented in Section 5. Some aspects of the results are further discussed in Section 6, and finally, the main conclusions are given in Section 7.

2. Equations and model simulation

2.1. OpenIFS model and simulations

The life cycle of Ophelia was simulated with the Open Integrated Forecast System (OpenIFS) model, which is

the open version of the Integrated Forecast System (IFS) model by the European Centre for Medium-Range Weather Forecasts (ECMWF). OpenIFS is not an open-source model, but available to academic and research institutions under licence.

IFS is a state-of-the-art global forecast model, which includes a data assimilation system and forecast systems for the atmosphere, ocean, waves, and sea ice. OpenIFS has only the atmospheric and wave model parts of the IFS, but contains exactly the same dynamics and physical parametrizations as IFS. OpenIFS does not have the data assimilation, so it can be used only for research purposes with externally generated initial conditions. The version of OpenIFS used in this study is cycle 40r1, which was in operational use at ECMWF from November 2013 to May 2015.

The initial conditions for the model simulations were generated from the ECMWF operational analyses. The model was run at a spectral resolution of T639, corresponding to 0.28125° × 0.28125° grid spacing, and with 137 model levels. One-hourly output was generated for 20 evenly spaced pressure levels, from 1000 hPa to 50 hPa. Some variables were also archived on constant potential vorticity and potential temperature levels. Coarser-resolution simulations with T159 and T255 spectral truncation were found to not capture the ET of Ophelia with sufficient accuracy (not shown).

The initialization time of the OpenIFS simulation was 12 UTC 13 October 2017. Ophelia developed into a hurricane at 18 UTC 11 October (Stewart, 2018). Model simulations with different initialization times, starting from 6 October to 16 October, were also examined. The runs with earlier initialization times, however, had larger errors in the track of Ophelia, and they also simulated the ET less accurately. The model simulations with later initialization times were mostly more accurate, but the length of the cyclone's tropical phase in the simulation was shorter. Hence, the selected initialization time was a compromise between the skill of the forecast and the length of the simulation. The length of our simulation was six days, from which the first four days are examined in this paper.

2.2. ERA5 reanalysis

To verify that the transition of Ophelia was simulated correctly by OpenIFS, we compare the model output to reanalysis data. Reanalysis datasets are useful for analysing synoptic-scale weather systems, because reanalyses combine the available observational data with the model analysis, resulting in a consistent dataset over the years. For this study, we used ERA5 reanalysis from ECMWF. ERA5 covers the period from 1979 to present and has one-hourly temporal resolution with 31-km spatial grid spacing (T639 in spectral space). There are 137 levels from the surface up to a height of 80 km. ERA5 has been produced with a four-dimensional variational (4 D-Var) data assimilation system by the cycle 41r2 of ECMWF's IFS model. ERA5 reanalysis data was downloaded from Copernicus Climate Data Store (cds.climate.copernicus.eu) for both pressure levels and the 2.0 potential vorticity unit (PVU) level for October 2017. The horizontal grid spacing of the ERA5 data was the same as in the OpenIFS model simulation. ERA5 alone is not used for this study as temperature and wind tendencies due to diabatic and frictional processes are not available for ERA5. These variables are required for our analysis and can be output from OpenIFS.

2.3. Equations

The equation system in this study consists of a generalized omega equation and the vorticity equation. The combination of these equations is adapted from Räisänen (1997).

2.3.1. Generalized omega equation and vorticity equation. The generalized omega equation is a diagnostic equation for analysing the causes of atmospheric vertical motions (Stepanyuk et al., 2017), which can be derived directly from the primitive equations in isobaric coordinates (Räisänen, 1995). The equation's better-known form, the quasi-geostrophic (QG) omega equation, applies many assumptions such as use of geostrophic winds and omission of diabatic heating and friction. These simplifications in the QG omega equation markedly deteriorate its accuracy, and thus make it less useful for a detailed analysis of atmospheric vertical motions. By contrast, the generalized omega equation used in this study does not include any of the simplifications used in the QG theory, except for hydrostatic balance, which is always implicitly assumed when isobaric coordinates are used (Räisänen, 1995).

The generalized omega equation used here is the same as in R17:

$$L(\omega) = F_V + F_T + F_F + F_Q + F_A \tag{1}$$

where

$$L(\omega) = \nabla^2(\sigma\omega) + f(\zeta + f)\frac{\partial^2\omega}{\partial p^2} - f\frac{\partial^2\zeta}{\partial p^2}\omega + f\frac{\partial}{\partial p}\left[\boldsymbol{k}\cdot\left(\frac{\partial \boldsymbol{V}}{\partial p}\times\boldsymbol{\nabla}\omega\right)\right] \tag{2}$$

and the right-hand side (RHS) terms have the expressions

$$F_V = f\frac{\partial}{\partial p}[\boldsymbol{V}\cdot\boldsymbol{\nabla}(\zeta + f)], \tag{3}$$

$$F_T = \frac{R}{p}\nabla^2(\boldsymbol{V}\cdot\boldsymbol{\nabla}T), \tag{4}$$

$$F_F = -f\frac{\partial}{\partial p}[\boldsymbol{k}\cdot(\nabla\times\boldsymbol{F})], \tag{5}$$

$$F_Q = -\frac{R}{c_p p}\nabla^2 Q, \tag{6}$$

$$F_A = f\frac{\partial}{\partial p}\left(\frac{\partial\zeta}{\partial t}\right) + \frac{R}{p}\nabla^2\left(\frac{\partial T}{\partial t}\right). \tag{7}$$

The symbols used in all the equations are listed in Table 1. The RHS terms of the equation represent the effects of different forcing mechanisms on vertical motion: differential vorticity advection (Eq. 3), the Laplacian of thermal advection (Eq. 4), the curl of friction (Eq. 5), and the Laplacian of diabatic heating (Eq. 6). The last term (Eq. 7) describes the imbalance between temperature tendencies and vorticity tendencies. At mid-latitudes, and with constant R, the imbalance term (Eq. 7) is proportional to the pressure derivative of ageostrophic vorticity tendency (Räisänen, 1995). The left-hand side (LHS) operator of the generalized omega equation (Eq. 2) is linear with respect to ω. Hence, the contributions of the five RHS terms (Eqs. 3–7) can be solved separately provided that homogeneous boundary conditions ($\omega = 0$ at the upper ($p = 50$ hPa) and lower ($p = 1000$ hPa) boundaries of the atmosphere) are used.

By solving the generalized omega equation, and then using the vorticity equation

$$\frac{\partial\zeta}{\partial t} = -\boldsymbol{V}\cdot\nabla(\zeta+f) - \omega\frac{\partial\zeta}{\partial p} + (\zeta+f)\frac{\partial\omega}{\partial p} + \boldsymbol{k}\cdot\left(\frac{\partial\boldsymbol{V}}{\partial p}\times\nabla\omega\right) + \boldsymbol{k}\cdot\nabla\times\boldsymbol{F} \tag{8}$$

we can separate the atmospheric vertical motion (Eq. 9) and vorticity tendency (Eq. 10) fields into components caused by the five forcing terms:

$$\omega = \omega_V + \omega_T + \omega_F + \omega_Q + \omega_A \tag{9}$$

$$\frac{\partial\zeta}{\partial t} = \left(\frac{\partial\zeta}{\partial t}\right)_V + \left(\frac{\partial\zeta}{\partial t}\right)_T + \left(\frac{\partial\zeta}{\partial t}\right)_F + \left(\frac{\partial\zeta}{\partial t}\right)_Q + \left(\frac{\partial\zeta}{\partial t}\right)_A. \tag{10}$$

Here the subscripts follow Eqs. 3–7. In Eq. 10, the components are defined as follows:

$$\left(\frac{\partial\zeta}{\partial t}\right)_V = -\boldsymbol{V}\cdot\nabla(\zeta+f) - \omega_V\frac{\partial\zeta}{\partial p} + (\zeta+f)\frac{\partial\omega_V}{\partial p} + \boldsymbol{k}\cdot\left(\frac{\partial\boldsymbol{V}}{\partial p}\times\nabla\omega_V\right) \tag{11}$$

$$\left(\frac{\partial\zeta}{\partial t}\right)_F = \boldsymbol{k}\cdot\nabla\times\boldsymbol{F} - \omega_F\frac{\partial\zeta}{\partial p} + (\zeta+f)\frac{\partial\omega_F}{\partial p} + \boldsymbol{k}\cdot\left(\frac{\partial\boldsymbol{V}}{\partial p}\times\nabla\omega_F\right) \tag{12}$$

$$\left(\frac{\partial\zeta}{\partial t}\right)_X = -\omega_X\frac{\partial\zeta}{\partial p} + (\zeta+f)\frac{\partial\omega_X}{\partial p} + \boldsymbol{k}\cdot\left(\frac{\partial\boldsymbol{V}}{\partial p}\times\nabla\omega_X\right), X = T, Q, A \tag{13}$$

Table 1. List of mathematical symbols.

$c_p = 1004$ J kg^{-1}	Specific heat of dry air at constant volume
f	Coriolis parameter
F	Forcing in the omega equation
$\boldsymbol{F}$	Friction force per unit mass
$\boldsymbol{k}$	Unit vector along the vertical axis
L	Linear operator on the left-hand-side of the omega equation
p	Pressure
p_s	Surface pressure
Q	Diabatic heating rate per unit mass
$R = 287$ J kg^{-1}	Gas constant of dry air
t	Time
T	Temperature
$\boldsymbol{V}$	Horizontal wind vector
$\boldsymbol{V}_\chi$	Divergent wind vector
$\boldsymbol{V}_\psi$	Rotational wind vector
χ	Velocity potential
ψ	Stream function
$\sigma = -\frac{RT}{p\theta}\frac{\partial\theta}{\partial p}$	Hydrostatic stability
ζ	Vertical component of relative vorticity
$\omega = \frac{dp}{dt}$	Isobaric vertical motion
∇	Horizontal nabla operator
∇^2	Horizontal Laplacian operator

Hereafter, the RHS terms of Eqs. 9 and 10 are called omega and vorticity tendency due to vorticity advection, thermal advection, friction, diabatic heating, and the imbalance term, respectively. Vorticity advection and friction have both their direct effect on vorticity tendency (RHS term 1 in Eqs. 11 and 12), and indirect effects that come from the vertical motions induced by them (RHS terms 2–4 in Eqs. 11 and 12). The thermal advection, diabatic heating, and imbalance term only contain the indirect contributions (RHS terms 1–3 in Eq. 13).

It is important to note that some of the five forcing terms cannot be considered to be totally independent forcings for vertical motion as they can be affected by vertical motions themselves. For example, a large proportion of the total diabatic heating is due to latent heat release, however, latent heat release primarily occurs in regions of ascent forced by adiabatic processes (RHS terms 1 and 2 in Eq. 1). Thus, latent heating acts to enhance, rather than cause, ascent. Furthermore, based on the continuity equation, divergent winds and hence vorticity and temperature advection by divergent winds depend largely on the field of existing vertical motions (Räisänen, 1997). The importance of the divergent circulation for the vorticity advection term is explained in the next subsection.

In many previous diagnostic studies in which the vorticity tendency budget has been studied, the atmospheric

vertical motion is treated as an independent forcing for weather systems (e.g. Rolfson and Smith, 1996; Azad and Sorteberg, 2009). This treatment is problematic, since the vertical motion should be considered to be a result of other processes rather than an independent forcing. For example, the vorticity advection increases vorticity directly by the advection itself. But vorticity advection also affects vertical motions and thus can generate vorticity via the stretching term. Another example is warm-air advection, which causes rising motion. The rising air adiabatically cools the atmosphere and compensates partly the warming caused by the advection itself. The novel part of our methodology is that the vertical motion is decomposed into contributions from various forcing terms and thus the vorticity tendency terms include also the indirect effects coming from the vertical circulation.

Another benefit of our methodology is that it is free from the geostrophic assumptions used e.g. in Rolfson and Smith (1996) and Azad and Sorteberg (2009). A very similar method was used in Azad and Sorteberg (2014) for investigating the vorticity budgets of North Atlantic winter extratropical cyclones. However, in their study the effect of diabatic heating was estimated with the thermodynamic equation, and the effect of friction was estimated assuming balance between the pressure gradient, frictional, and Coriolis forces in the boundary layer. In our study, the temperature and wind tendencies due to diabatic heating and friction are parametrized and come directly from the OpenIFS model.

2.3.2. Vorticity advection by rotational and divergent winds. Räisänen (1997) identified negative low-level vorticity advection by divergent winds as an equally important damping mechanism for extratropical cyclone evolution as surface friction. Consistent with that, R17 also found the divergent vorticity advection to cause a substantial positive geopotential height tendency at the centre of their idealized cyclone. By contrast, the rotational (non-divergent) vorticity advection was found to strongly deepen the extratropical cyclone in both studies.

As the effects of divergent and rotational vorticity advections on the evolution of cyclones are fundamentally different, it is useful to study their contributions separately. Thus, following Räisänen (1997) and R17, vorticity advection is divided into contributions from rotational ($\boldsymbol{V}_\psi$) and divergent ($\boldsymbol{V}_\chi$) winds as follows:

$$-\boldsymbol{V}\cdot\nabla(\zeta+f) = -\boldsymbol{V}_\psi\cdot\nabla(\zeta+f) - \boldsymbol{V}_\chi\cdot\nabla(\zeta+f). \qquad (14)$$

This division can also be applied to thermal advection, but because both R17 and Räisänen (1997) found the divergent part of thermal advection to be usually negligible compared to the rotational part, this division is not made here.

Note that in many traditional forms of the omega equation (e.g. in the QG omega equation) the vorticity advection is calculated using only the non-divergent part of the wind. In our method, however, the vorticity and thermal advection terms account also for the divergent circulation, which can have quite a substantial effect on the evolution of the surface low.

2.3.3. Diabatic heating components. The total diabatic heating rate Q in Eq. 6 is the net effect of many different processes, such as radiation, latent heat release, and surface heat fluxes. In numerical weather prediction models, these processes need to be parametrized. For example, in OpenIFS, the total heating rate Q consists of five different temperature tendencies

$$Q = Q_r + Q_d + Q_g + Q_c + Q_{mp} \qquad (15)$$

which all come from different model parametrization schemes and are explained in Table 2. Substituting Eq. 15 into Eq. 6, we solved the generalized omega equation and vorticity equation for these diabatic heating components separately. This decomposition provides new insight especially in systems that involve both convective and large-scale precipitation during their life cycle. Tropical cyclones undergoing ET, such as Ophelia, are good examples of such a system.

2.4. Solving the equations with OZO diagnostic software

The equations described in Section 2.3 are solved with the diagnostic software OZO. The first version of OZO (v1.0), tailored for Weather Research and Forecasting (WRF) model output, was documented in R17. The version used in this study, OZO v2.0, is tailored for OpenIFS output, and is freely available from GitHub: https://github.com/mikarant/cozoc2.0. For this study, OZO was substantially advanced from v1.0. The main difference is that the software is now suitable to global model data with spherical geometry, while OZO v1.0 only works with an idealized Cartesian coordinate channel domain. Furthermore, the software is now parallelized and employs a faster solving algorithm by the Portable, Extensible Toolkit for Scientific Computation (PETSc) library. Parallelization and the use of PETSc reduce the computation time markedly when running the software on a supercomputer or cluster.

As input for OZO, temperature (T), wind ($\boldsymbol{V}$), relative vorticity (ζ), surface pressure (p_s), stream function (ψ), velocity potential (χ), and temperature and wind tendencies associated with diabatic heating (Q) and friction ($\boldsymbol{F}$) are required. In R17, geopotential height tendencies were calculated using the Zwack–Okossi tendency equation.

Table 2. Temperature tendencies in OpenIFS model.

Q_r	Temperature tendency from radiation
Q_d	Temperature tendency from vertical diffusion, orographic drag, and surface processes
Q_g	Temperature tendency from gravity wave drag
Q_c	Temperature tendency from convection
Q_{mp}	Temperature tendency from cloud and semi-Lagrangian physics

This functionality does not yet exist in OZO v2.0, but is planned for a future version of the software.

2.5. Cyclone tracking algorithm

After running the OpenIFS model, the location of Ophelia at each time step was determined by using the feature-tracking algorithm called TRACK (Hodges, 1994, 1995), which has been widely used in previous studies (e.g. Zappa et al., 2013; Hawcroft et al., 2018; Sinclair and Dacre, 2019). As an input for TRACK, the fields of relative vorticity averaged over the 900–800-hPa layer and mean sea level pressure were given. TRACK smooths the vorticity field with T63 spectral truncation and then identifies the maxima (minima) of the smoothed vorticity field in the Northern (Southern) Hemisphere. Ophelia is identified by objectively comparing the tracks to Ophelia's best track data by National Hurricane Center (NHC). After identifying Ophelia's track using the vorticity maximum, the minimum of sea level pressure within a 5° radius around the vorticity maximum is obtained at each time step. Furthermore, area-averages of all the vorticity tendency components (Eq. 10) centred on the cyclone centre are calculated. This area is defined as a circle with 1.5° radius centred on the location of the vorticity maximum at each time step. The sensitivity of our results for smaller and larger radii, ranging from 0.5° to 5°, was also examined. The main conclusions of this study were found to be insensitive to this choice of radius (not shown).

3. Synoptic overview

This section gives a synoptic overview of Ophelia's evolution based on the post-season NHC report (Stewart, 2018) and ERA5 reanalysis data, focusing primarily on the transition and extratropical phase of the storm.

Ophelia was the farthest-east major hurricane observed in the satellite era (Stewart, 2018). At its peak intensity at 12 UTC 14 October Ophelia was classified as a category 3 hurricane, with minimum surface pressure of 959 hPa and maximum 1-minute sustained winds of 51 m s^{-1} (Stewart, 2018). Ophelia's formation was strongly influenced by anticyclonic wave breaking in the western North Atlantic, which caused high potential vorticity air from mid-latitudes to fold south towards the subtropics. This high potential vorticity air was thinned and detached from the westerly flow, and turned into an isolated upper-level positive potential vorticity anomaly above the central sub-tropical Atlantic on 6 October (not shown).

The upper-level potential vorticity anomaly above a warm sea surface destabilized the atmosphere, which induced shallow convection and, eventually, the formation of a surface low. As the sea beneath the low was warm (T = 27 °C), the convection gradually became deeper. On 9 October, a tropical storm had formed. Based on NOAA Optimum Interpolation Sea Surface Temperature (OISST) v2 data (Reynolds et al., 2007), the sea surface temperatures were close to 1971–2000 average on the area where the storm formed (not shown).

The storm, which was named as Ophelia, was located between two ridges: one to the north over the mid-latitude North Atlantic, and another to the south, over the subtropical Atlantic. Due to this synoptic configuration, the steering currents in the central and eastern North Atlantic were weak. Ophelia stayed almost in the same place during the next few days (note the crosses close to each other in the lower left corner of Fig. 1). Even though the sea surface temperatures beneath Ophelia were only moderately warm (T = 26 °C, see Fig. 1), the relatively cold mid- and upper-troposphere, associated with the positive potential vorticity anomaly resulted in steep lapse rates and vigorous deep convection in the vicinity of the storm's centre (not shown), which eventually led to the strengthening of Ophelia to a category 1 hurricane on 11 October (Stewart, 2018).

The tropical, transition, and extratropical phases of the storm are estimated using both the phase space diagram of Ophelia (Fig. 2; Hart, 2018) and the NHC report (Stewart, 2018). The phase space diagram is based on ERA5 reanalysis. The storm became asymmetric (B > 10 m) at 12 UTC 14 October, which indicates the onset of the ET. The completion of ET is defined as $-V_T^L$ < 0 m, which in Ophelia's case took place at 18 UTC 16 October. In the NHC report, however, Ophelia is classified as a hurricane until 18 UTC 15 October, and then as an extratropical storm onwards from 00 UTC 16 October.

The spatial fields of 900–800-hPa relative vorticity and tropopause level (2.0-PVU) potential temperature based on ERA5 reanalysis are depicted in Fig. 3a, d and g. The figures are from three different times with a 24-hour interval: 9 UTC 14 October, 9 UTC 15 October, and 9 UTC 16 October. At the first time (9 UTC 14 October) the storm has just started ET (Fig. 2), but was still classified as a category 3 hurricane based on the NHC report (Stewart, 2018). The second time (9 UTC 15 October)

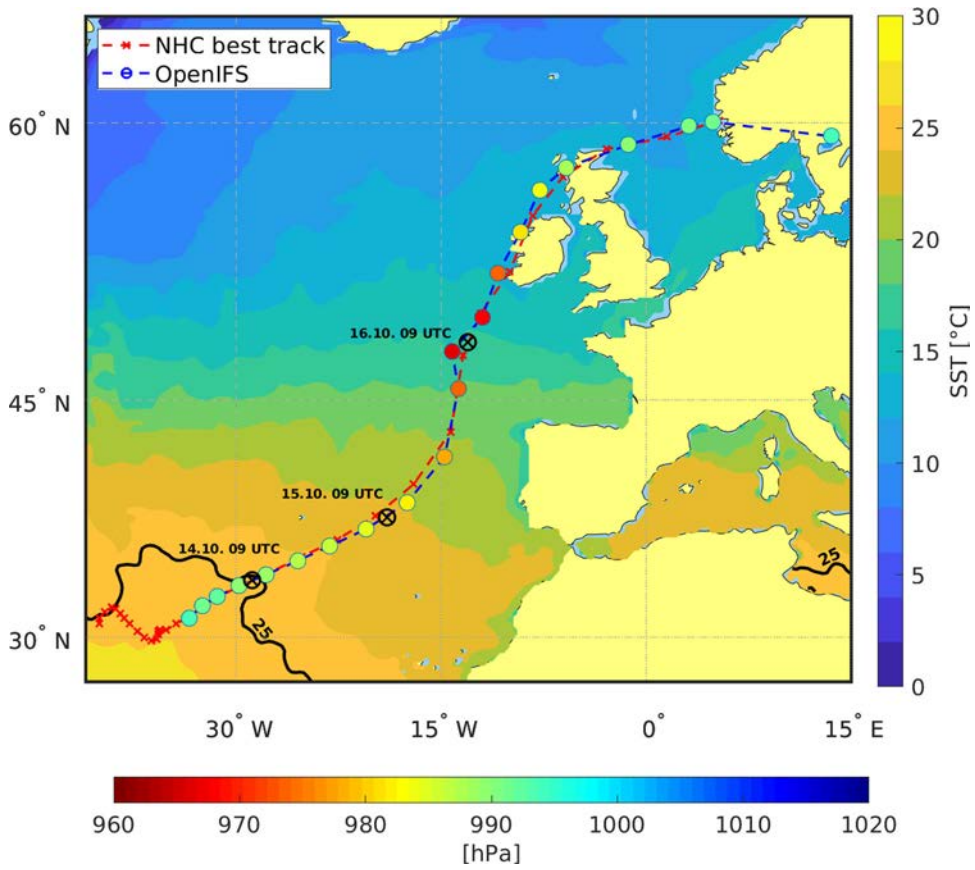

Fig. 1. National Hurricane Center best track for Hurricane Ophelia (red) and OpenIFS track based on minimum sea level pressure (blue). The colours in the OpenIFS track denote minimum sea level pressure in the OpenIFS simulation. The background colours show the sea surface temperatures at 12 UTC 14 October, with 25 °C isotherm contoured. The locations of Ophelia at its peak intensity as a hurricane (9 UTC 14 October), and 24 (9 UTC 15 October) and 48 hours later (9 UTC 16 October) are also indicated.

represents the transition phase of the storm, and the latest time (9 UTC 16 October) corresponds with the time of Ophelia's maximum intensity as an extratropical storm, which falls between the classified extratropical phases of the diagram and the NHC report. Hereafter, these three times represent the tropical, transition, and extratropical phases of the storm. The location of Ophelia at these three times is also marked in Fig. 1 with black crosses.

From Fig. 3a, Ophelia can be identified as a circular area of low-level vorticity roughly at the location of 35°N and 30°W. To the north and northeast of Ophelia, there is a long vorticity maximum associated with a frontal zone. On 12 October, Ophelia was steered by increased upper-level winds due to a large long-wave trough, which had propagated from North America to the North Atlantic (not shown). Two days later, on 14 October, the trough is visible in Fig. 3a with blue colours (lower potential temperature on the dynamic tropopause). Ophelia is experiencing south-westerly upper-level flow (arrows in Fig. 3a). The trough started to direct Ophelia towards Europe, and at 12 UTC 14 October, regardless of relatively cool sea surface temperatures (T = 25 °C, Fig. 1), Ophelia reached its peak intensity as a category 3 hurricane (roughly at the time of Fig. 3a). The strengthening was possible because of strong deep convection near the storm centre allowed by steep lapse rates due to cooler than average ambient temperatures in the mid- and upper troposphere (Stewart, 2018).

Later, on 15 October, Ophelia started losing its tropical characteristics due to the increased wind shear caused by the jet stream associated with the upper-level trough (Fig. 3d). The low-level vorticity maximum was no longer circular, but slightly stretched meridionally towards the frontal zone (Fig. 3d). Although this behaviour led to a decrease of surface wind speeds (Stewart, 2018), the favorable interaction with the upper-level trough ensured that the minimum surface pressure did not start to increase (Fig. 4, red dashed line). The decrease of maximum wind speeds with steady surface pressure can be

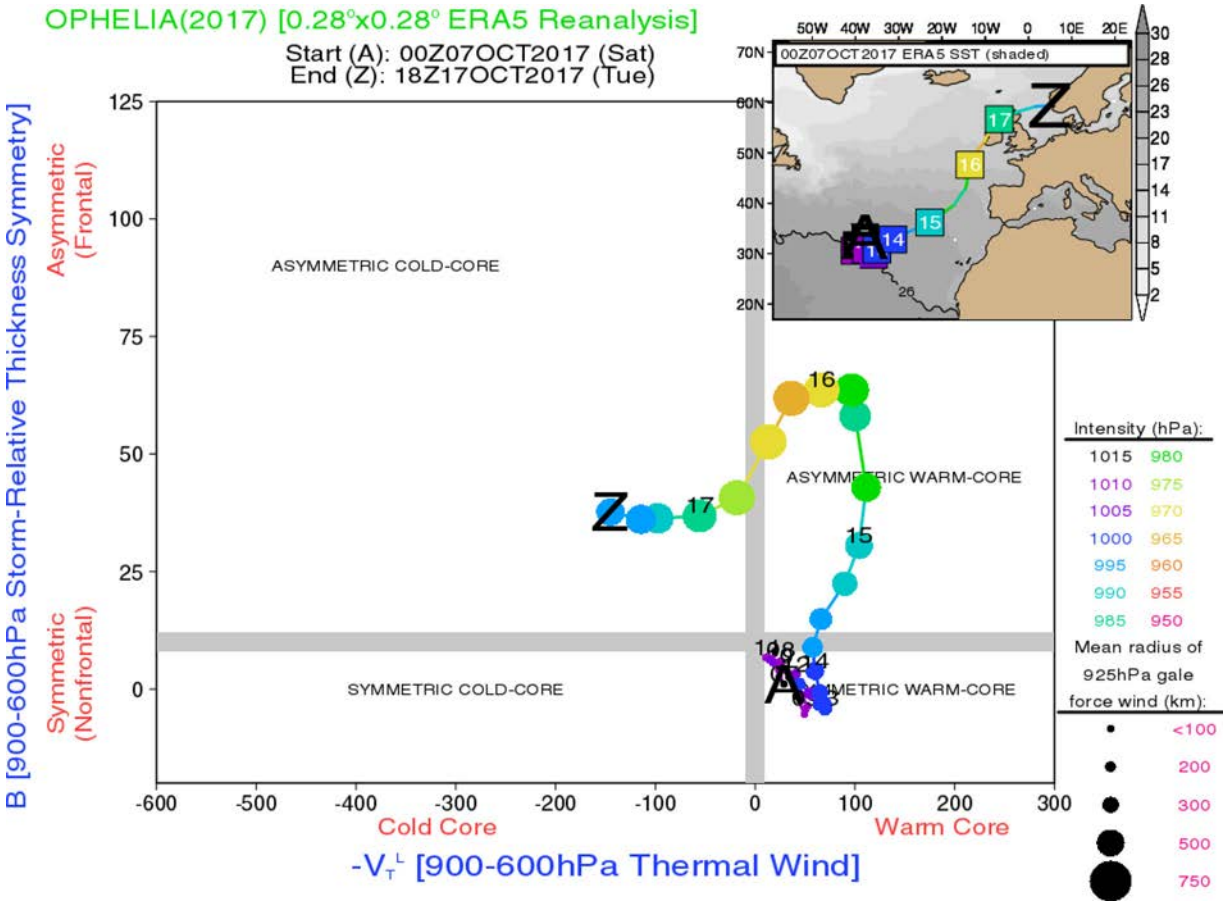

Fig. 2. Phase space diagram of Ophelia based on ERA5 reanalysis. The dots are plotted every six hours and the numbers labeled in the dots indicate the days of October 2017. The figure is from Hart (2018) and is used with permission.

explained with the growing horizontal size of the storm. This can be seen from Fig. 2 as growing size of the circles, indicating larger radius of 925-hPa gale-force winds when the storm is approaching the extratropical phase.

The favorable interaction with the upper-level trough is consistent with the results of Hart et al. (2006). They showed that tropical cyclones interacting closely with negatively tilted large-scale troughs are more likely to undergo post-ET intensification than cyclones interacting further apart and with positively tilted troughs. Investigation of ERA5 reanalysis data revealed that the 500-hPa trough preceding Ophelia's transition was indeed slightly negatively tilted, and the location of Ophelia relative to the trough (not shown) was very similar to fig. 12b in Hart et al. (2006). In addition, the enhanced upper-level divergence caused by the right entrance region of the jet stream (see Fig. 3a and d) most likely enhanced Ophelia's vertical mass flux during the ET, and, thus, helped Ophelia to remain as an intense storm during the transition phase. The fact that Ophelia remained its intensity is in line with the results of Davis et al (2008) and Leroux et al. (2013), who both showed tropical cyclones intensifying in a presence of vertical wind shear caused by the upper-level trough.

Based on the ERA5 reanalysis, at 9 UTC 15 October the circular area of high vorticity associated with Ophelia had almost merged with the more linear frontal vorticity (Fig. 3d). The presence of both areas of vorticity indicates that the system had both tropical and extratropical characteristics and, thus, Ophelia is undergoing extratropical transition at this time. Based on Stewart (2018), the ET of Ophelia was completed at 00 UTC 16 October, which falls in between the times in Fig. 3d and 3g.

Favourable interaction with the upper-level trough helped Ophelia still deepen slightly as a powerful post-tropical cyclone. NHC analysis suggests a pressure minimum of 957 hPa at 9 UTC 16 October (Fig. 4), when Ophelia was just about to make landfall to Ireland (Fig. 3g). Soon after hitting Ireland, Ophelia started to weaken quite rapidly (Fig. 4). The storm further moved across northern Scotland on 17 October, and finally dissipated over Norway on 18 October (Fig. 1).

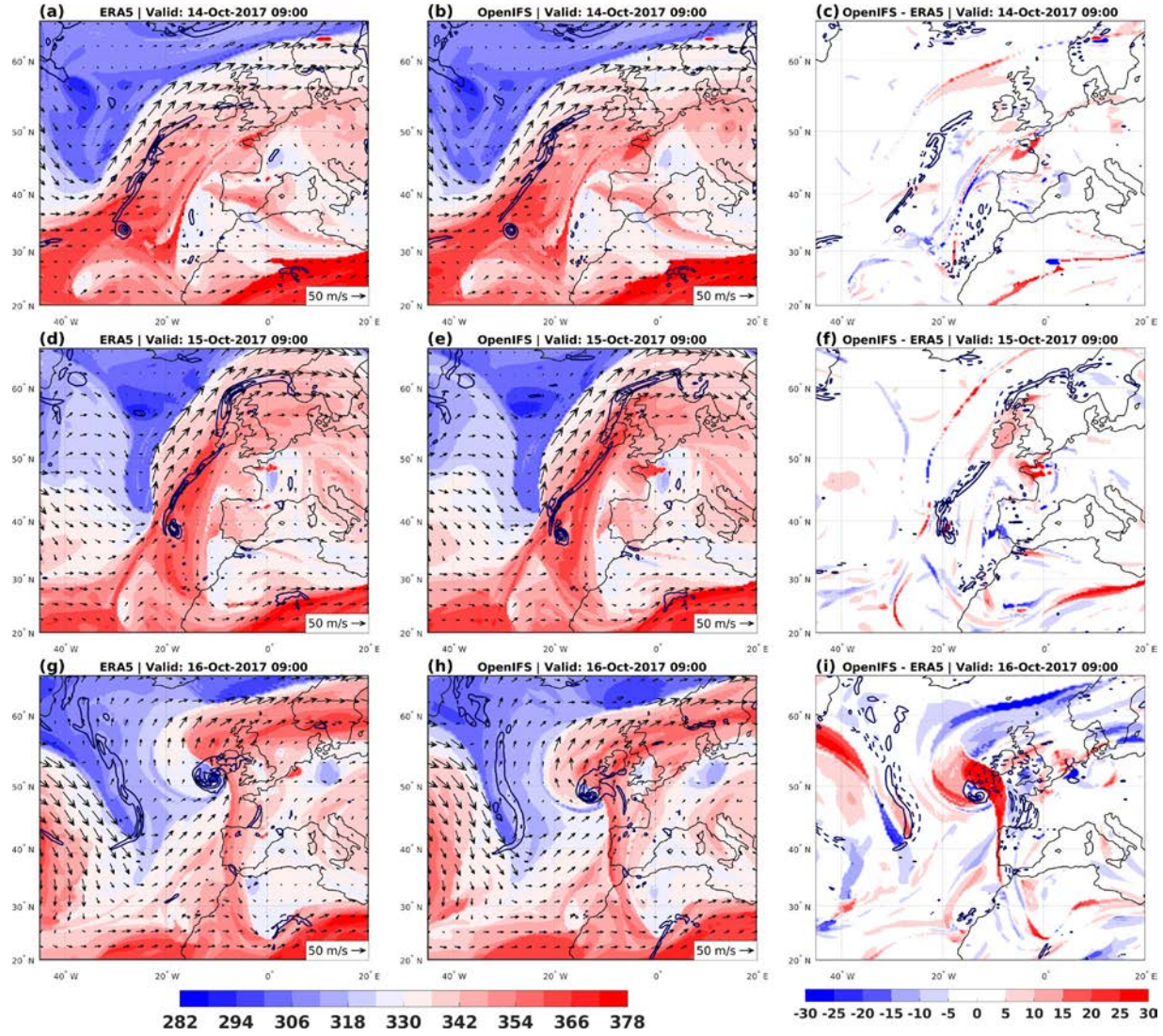

Fig. 3. Potential temperature (colours, K) and wind (arrows, reference arrow in the lower-right corner) on dynamic tropopause (2.0 PVU), and relative vorticity averaged over 950–850-hPa layer (contours, with 2×10^{-4} s^{-1} interval starting from 10^{-4} s^{-1}) from ERA5 (left column) and OpenIFS (middle column) at 9 UTC 14 October (upper row), 9 UTC 15 October (middle row), and 9 UTC 16 October (bottom row). The difference OpenIFS - ERA5 of potential temperature on 2.0 PVU (colours, with a separate colourbar) and relative vorticity averaged over 950–850-hPa layer (contours) are shown in the right column. In panels (c), (f) and (i), the solid lines show areas where the relative vorticity is higher in OpenIFS than in ERA5, and the dashed lines show the opposite.

4. Comparison of OpenIFS simulation to ERA5 data

Figure 1 shows the track of Ophelia based on minimum sea level pressure in the OpenIFS simulation and the analysed track according to NHC. The agreement between the tracks is very good, and shows only slight difference in the area west and southwest from the British isles. This is the area where Ophelia was located when it underwent ET, a process known to be challenging to simulate correctly by numerical weather prediction models (e.g. Evans et al., 2017).

Figure 3 compares the spatial fields of low-level vorticity and upper-level potential temperature between ERA5 (left column) and OpenIFS (middle column). Their differences (OpenIFS - ERA5) at the three time steps are shown in the right column. The fields are very similar to each other during the tropical phase at 9 UTC 14 October (Fig. 3a–c). This agreement continues the next day, when the storm was in the middle of its transition process (Fig. 3d–f). On 16 October, however, there is a slight timing discrepancy between the ERA5 and OpenIFS fields (Fig. 3g–i). While in ERA5 the storm

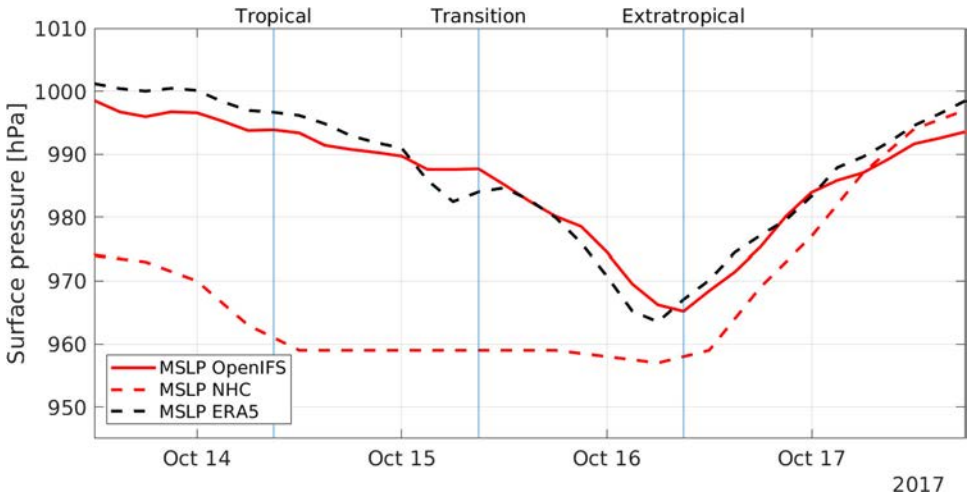

Fig. 4. Time series of mean sea level pressure at the cyclone centre based on OpenIFS (solid red line), ERA5 reanalysis (dashed black line), and National Hurricane Center best track data (dashed red line). The vertical lines mark the tropical, transition, and extratropical phases of the cyclone.

had already passed 50°N latitude by 9 UTC 16 October (Fig. 3g), in our model simulation the storm propagates slightly slower, and remains south of 50°N at this time (Fig. 3h). For this reason, the amplified downstream ridge is also located somewhat further south in OpenIFS, which can be seen particularly from Fig. 3i as an area of large positive difference in upper-level potential temperatures west from the British isles.

Figure 4 depicts the minimum surface pressure of the storm based on the OpenIFS simulation (red solid line) compared to the analysed minimum surface pressure by NHC (red dashed line) and ERA5 reanalysis (black dashed line). During the tropical phase of the storm, both OpenIFS and ERA5 greatly overestimated the central surface pressure. The difference OpenIFS - NHC exceeds 30 hPa at maximum, but was reduced as the storm transformed to a mid-latitude cyclone. OpenIFS also deepened Ophelia more steadily from 13 Oct to 16 Oct, while the NHC best track data shows a clear deepening period on 13–14 October without substantial changes in intensity during the following two days (Fig. 4). Regardless of the large difference between OpenIFS and NHC, the agreement between OpenIFS and ERA5 is generally very good during the whole life cycle of the storm. The implications of the large underestimation of intensity by OpenIFS are discussed further in Section 6.

5. Vertical motion and vorticity tendency diagnostics

5.1. Comparison between calculated and model-simulated vertical motions and vorticity tendencies

In this subsection, the solution of the omega equation (ω_{TOT}) and the vorticity equation ($\frac{\partial \zeta}{\partial t_{TOT}}$) are compared to vertical motion and vorticity tendency from the OpenIFS output (ω_{OIFS} and $\frac{\partial \zeta}{\partial t_{OIFS}}$, respectively). The latter is estimated as a central difference from the one-hour time series of the simulated relative vorticity fields.

Figure 5a and b shows ω_{TOT} and ω_{OIFS} at 700 hPa at 21 UTC 15 October. Their difference is depicted in Fig. 5c. The similarity between the fields is striking. There are some small differences, for example, in the area of descent to the west of the storm.

Vorticity and particularly its tendency fields are often very noisy and contain lots of small-scale variation. For this reason, finding a signal related to synoptic-scale weather systems from the vorticity tendency fields can be challenging. To make the interpretation easier, the vorticity tendencies presented in this paper are smoothed by setting the coefficients for total wave numbers more than 127 to zero. This T127 spectral truncation, which corresponds approximately to 165-km grid spacing, was performed after solving the vorticity equation with OZO, using data with full model truncation. The vorticity and its tendency fields in full T639 resolution are attached in the supplementary material of this study. For vertical motion fields, no smoothing is applied because vertical motion fields at T639 resolution are much smoother than the corresponding vorticity tendency fields.

Figure 5d, e and f shows $\frac{\partial \zeta}{\partial t_{TOT}}$, $\frac{\partial \zeta}{\partial t_{OIFS}}$, and their difference at 21 UTC 15 October, respectively. The agreement between the vorticity tendency fields is very good. However, the $\frac{\partial \zeta}{\partial t_{OIFS}}$ field is overall slightly smoother, which comes from the approximation of the time derivative with the central difference method using one-hour time intervals. There is also a moderate positive bias in the centre of the cyclone, which may result from the relatively rough estimation of the imbalance term with one-

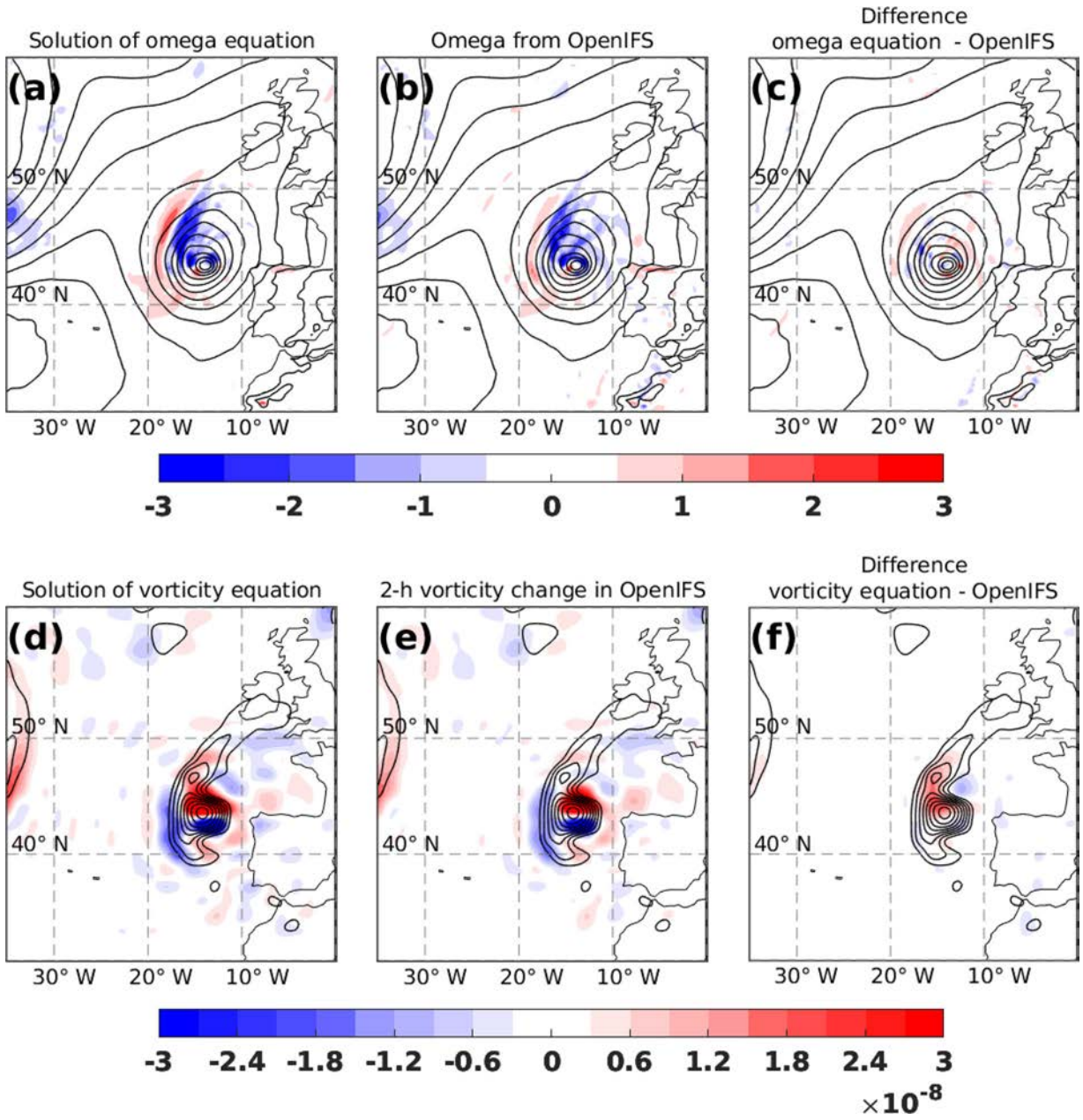

Fig. 5. The solution of the omega equation (ω_{TOT}) (a), omega directly from OpenIFS output (ω_{OIFS}) (b), and the difference ω_{TOT} - ω_{OIFS} at 700 hPa. The same but for vorticity tendencies at the 900–800-hPa layer is shown in panels (d)–(f). Time is at 21 UTC 15 October 2017. Unit in (a)–(c) is Pa s^{-1}, and in (d)–(f) s^{-2}. Contours in (a)–(c) show mean sea level pressure with 4-hPa interval, and in (d)–(f) relative vorticity averaged over 900–800 hPa starting from 5×10^{-5} s^{-1}, with 5×10^{-5} s^{-1} interval.

hour time resolution, which will be discussed further in Section 6.

Spatial correlations between ω_{TOT} and ω_{OIFS}, and between $\frac{\partial \zeta}{\partial t_{TOT}}$ and $\frac{\partial \zeta}{\partial t_{OIFS}}$ as a function of pressure are presented in Fig. 6. The correlations have been calculated from a 10° × 10° moving box which followed the centre of Ophelia, and averaged over the time period 15 UTC 13 October - 12 UTC 18 October. In addition, the correlations of vorticity tendencies are given for both T127 and T639 spectral resolutions.

The correlation of vorticity tendencies at T127 resolution clearly exceeds the correlation at T639 resolution. T127 shows correlations of up to 0.97 in the mid-troposphere, while T639 barely exceeds 0.85. The correlation for vertical motions is between those for the vorticity tendencies at the T127 and T639 resolutions. This order of performance

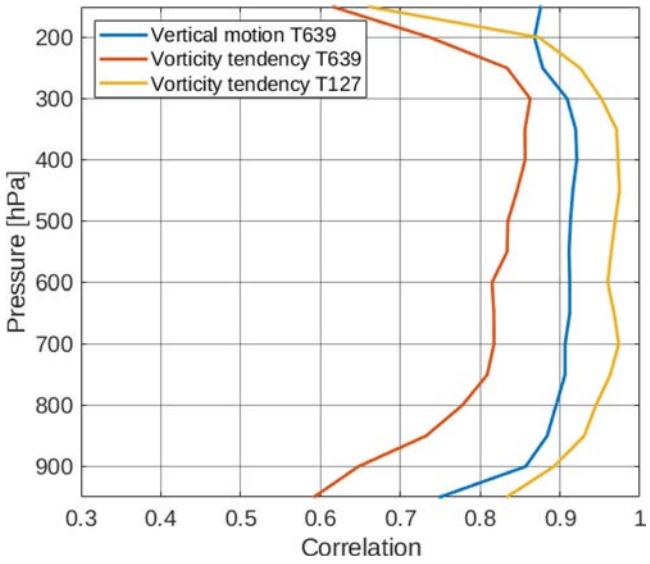

Fig. 6. Correlation between ω_{OIFS} and the solution of the omega equation (blue), and correlation between $\frac{\partial \zeta}{\partial t_{OIFS}}$ and the solution of the vorticity equation (red) as a function of pressure. The values have been calculated from a 10° × 10° moving box centred to the centre of Ophelia, and averaged over the time period 15 UTC 13 October–12 UTC 18 October.

reflects the horizontal scale of the fields: the smaller the scale, the worse the correlation. Nevertheless, the key point from Fig. 6 is that the correlations are high, which means that the method of solving the equations is valid.

5.2. Tropical phase

Figure 7 shows the 700-hPa vertical motion induced by the individual forcing components (Fig. 7b–f) and their sum (Fig. 7a) at 9 UTC 14 October, i.e. two days before the maximum intensity of the storm. ω_{TOT} in Fig. 7a shows strong ascent concentrated on the downshear (eastern) half of the storm, which is mainly caused by diabatic heating (Fig. 7e). This is a typical place for convective cells in tropical cyclones: previous studies have shown that convection usually initiates downshear right and intensifies downshear left of the storm (e.g. Foerster et al., 2014; DeHart et al., 2014).

In addition to diabatic heating, a minor contribution to vertical motion comes from thermal advection (Fig. 7c), which is due to advection of warm air from the subtropics towards mid-latitudes. In contrast, vorticity advection (Fig. 7b) contributes negligibly to the vertical motion at 700 hPa during the tropical phase of the storm. Similarly, the vertical motion caused by friction is near zero (Fig 7d). Note, however, that the vertical motion due to friction reaches its maximum at levels lower than 700 hPa (Stepanyuk et al., 2017).

Examination of vertical velocity fields from 500 hPa and 300 hPa (not shown) revealed that the pattern does not change substantially with height. In particular, the vertical motion due to diabatic heating (ω_Q) is equally strong higher up in the atmosphere, while vertical motion due to thermal advection (ω_T) shows some signs of weakening with height. Vertical motion due to vorticity advection (ω_V) is still negligible at 500 hPa, but has some weak ascent at 300 hPa, located on the western half of the cyclone centre.

Vorticity tendencies due to the different forcing mechanisms at the same time are presented in Fig. 8. The total vorticity tendency field (Fig. 8a) shows a typical positive-negative dipole, which moves the storm eastward. Almost all of this vorticity tendency is caused by vorticity advection (Fig. 8b). Note also that even though vorticity advection is important for the movement of the cyclone, it does not cause significant vertical motion (Fig. 7b).

A small part of the vorticity tendency originates also from diabatic heating (Fig. 8e). This field has some positive values at the centre of the storm, which means that the system is intensifying due to diabatic heating. The latent heat release in the convective clouds enhances rising motion, which, in turn, causes low-level convergence to the lower troposphere. The convergence increases vorticity at the cyclone centre via stretching term (RHS term 2 in Eq. 13).

5.3. Transition phase

At 9 UTC 15 October, when Ophelia is in the middle of its transition to a mid-latitude cyclone, baroclinic processes start to be more important for the cyclone development. The sea level pressure field presented in Fig. 9

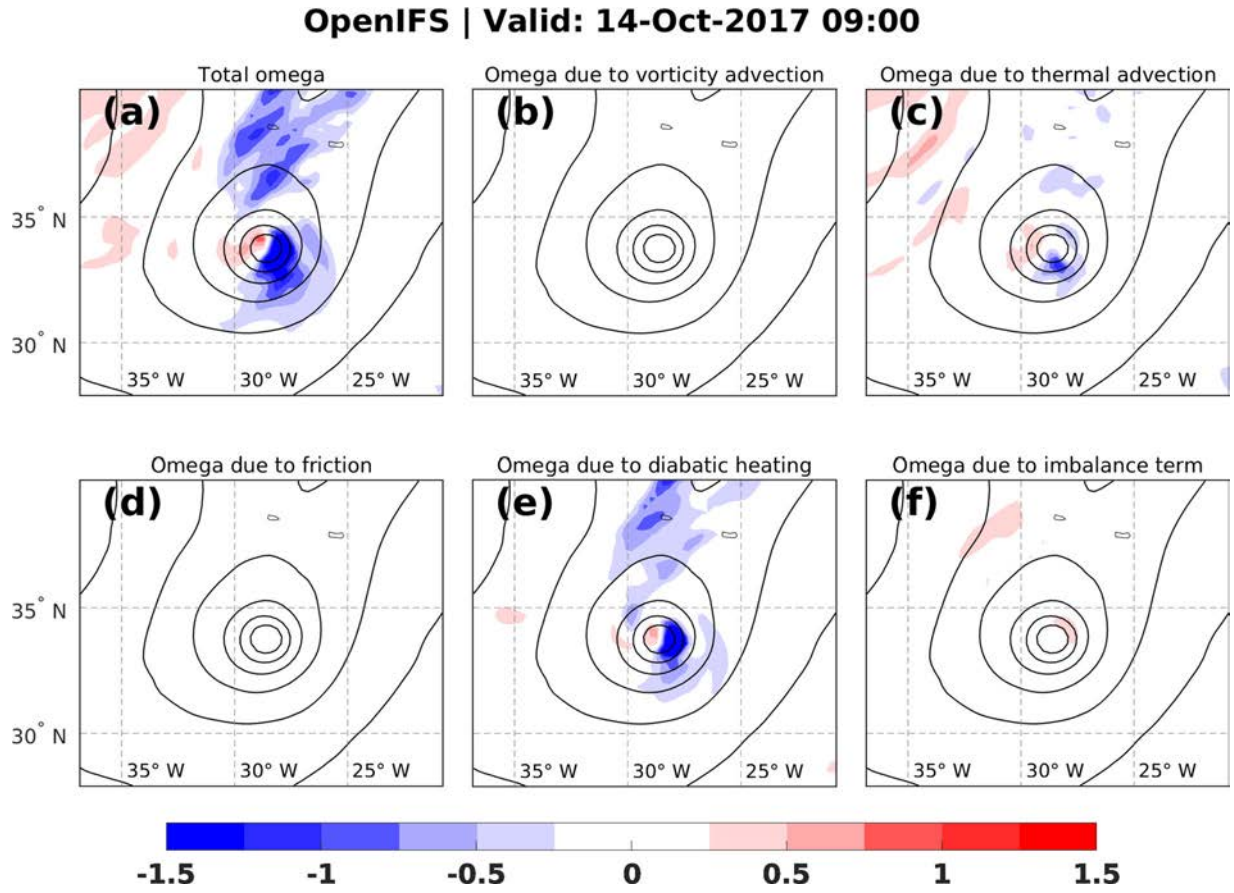

Fig. 7. Vertical motion (shading, Pa s^{-1}) at 700 hPa at 9 UTC 14 October (tropical phase). The panel (a) shows the total vertical motion due to all five forcing terms [the sum of terms (b)–(f)]. Panels (b)–(f) show the contributions from individual forcing terms: vertical motion due to (b) vorticity advection, (c) thermal advection, (d) friction, (e) diabatic heating, and (f) the imbalance term. The contours show sea level pressure with 4-hPa interval.

shows a trough-like feature to the north of the storm, indicating the presence of a frontal zone (see also Fig. 3e). This area also features large-scale ascent induced by vorticity advection (Fig. 9b). The area of ascent north of Ophelia is caused by the upper-level forcing by the approaching mid-latitude trough.

The vertical motion associated with thermal advection (ω_T, Fig. 9c) has more small-scale structures compared to the vertical motion associated with vorticity advection (ω_V). Consistent with the studies of Räisänen (1995) and R17, ω_V tends to have larger scale but lower magnitude compared to ω_T. The rising motion caused by thermal advection is concentrated on the eastern side of the storm, in the area of warm air advection, while the cold air advection on the western side the storm is causing some sinking motion.

The largest contribution to ω_{TOT} (Fig. 9a) comes still from diabatic heating (Fig. 9e), with very strong convective ascent on the downshear side of the storm, which is starting to extend north, towards the frontal zone. One notable difference compared to the situation during the tropical phase (Fig. 7a) is the increased compensating sinking motion west of the rising motion, which is caused by diabatic cooling (Fig. 7e). As this descent due to ω_Q coincides partly with the sinking motion caused by the cold air advection (especially 6–9 hours after the time in Fig. 9, not shown), we suspect that the cooling caused by evaporation/melting of cloud droplets is enhancing the sinking motion caused by the cold air advection in this area.

The imbalance term (Fig. 9f) also shows some vertical motion in the vicinity of the storm centre. The areas of descent coincide with areas of ascent in ω_T (Fig. 9c) and vice versa. This tendency of the imbalance term to compensate the effect of thermal advection has been documented earlier in R17, and the physical reason for this compensating effect is explained next. In the real atmosphere, the temperature tendencies caused by thermal

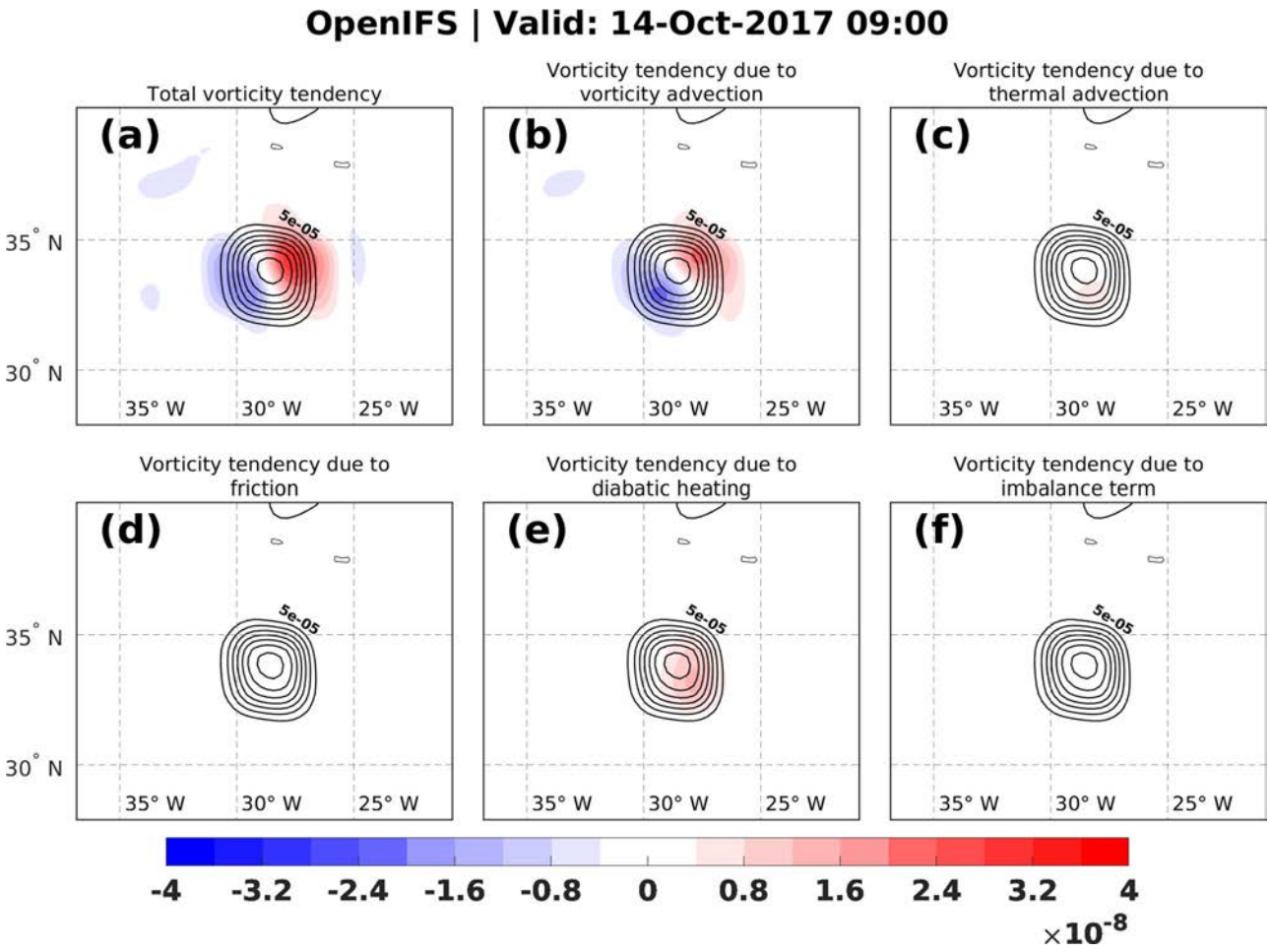

Fig. 8. Vorticity tendency (shading, s^{-2}) averaged over the 900–800-hPa layer at 9 UTC 14 October (tropical phase). The panel (a) shows the total vorticity tendency due to all five forcing terms [the sum of terms (b)–(f)]. Panels (b)–(f) show the contributions from individual forcing terms: vorticity tendency due to (b) vorticity advection, (c) thermal advection, (d) friction, (e) diabatic heating, and (f) the imbalance term. The contours show relative vorticity, starting from 5×10^{-5} s^{-1}, with 5×10^{-5} s^{-1} interval.

advection are often small by their temporal and spatial scales, particularly at low levels. For this reason, the atmosphere usually does not have time to adjust to the new situation and thus compensating vertical motion does not take place. These situations are taken into account by the imbalance term, which often cancels out the effect of thermal advection.

In the transition phase, the low-level vorticity field associated with Ophelia is no longer a symmetric, circular blob, but is extended meridionally towards the frontal zone (Fig. 10, and the full-resolution vorticity in Fig. 3c). This extension of vorticity is mainly caused by diabatic heating, which shows positive vorticity tendency both in the frontal zone and in the vicinity of the storm's centre (Fig. 10e). Vorticity advection is still mainly contributing to the motion of the storm, as the tendency at the storm's centre is close to zero. Vorticity tendencies caused by the other processes (thermal advection, friction, and the imbalance term) are very small. Only thermal advection (Fig. 10c) contributes slightly to the eastward movement of the storm by inducing a similar, but much weaker dipole pattern as the vorticity advection.

5.4. Extratropical phase

Figure 11a presents the potential temperature at 850 hPa at the extratropical phase of Ophelia (9 UTC 16 October). This is the time when Ophelia reaches its maximum intensity as an extratropical storm (Fig. 4) and when fronts are evident. Based on Fig. 11a, the cold front is approximately perpendicular to the warm front (so called T-bone structure). The warm and cold fronts are however not connected. This gap between the fronts is filled by the warm air mass, which extends all the way to the core of the cyclone, forming a classic warm seclusion. The structure resembles the Shapiro–Keyser conceptual

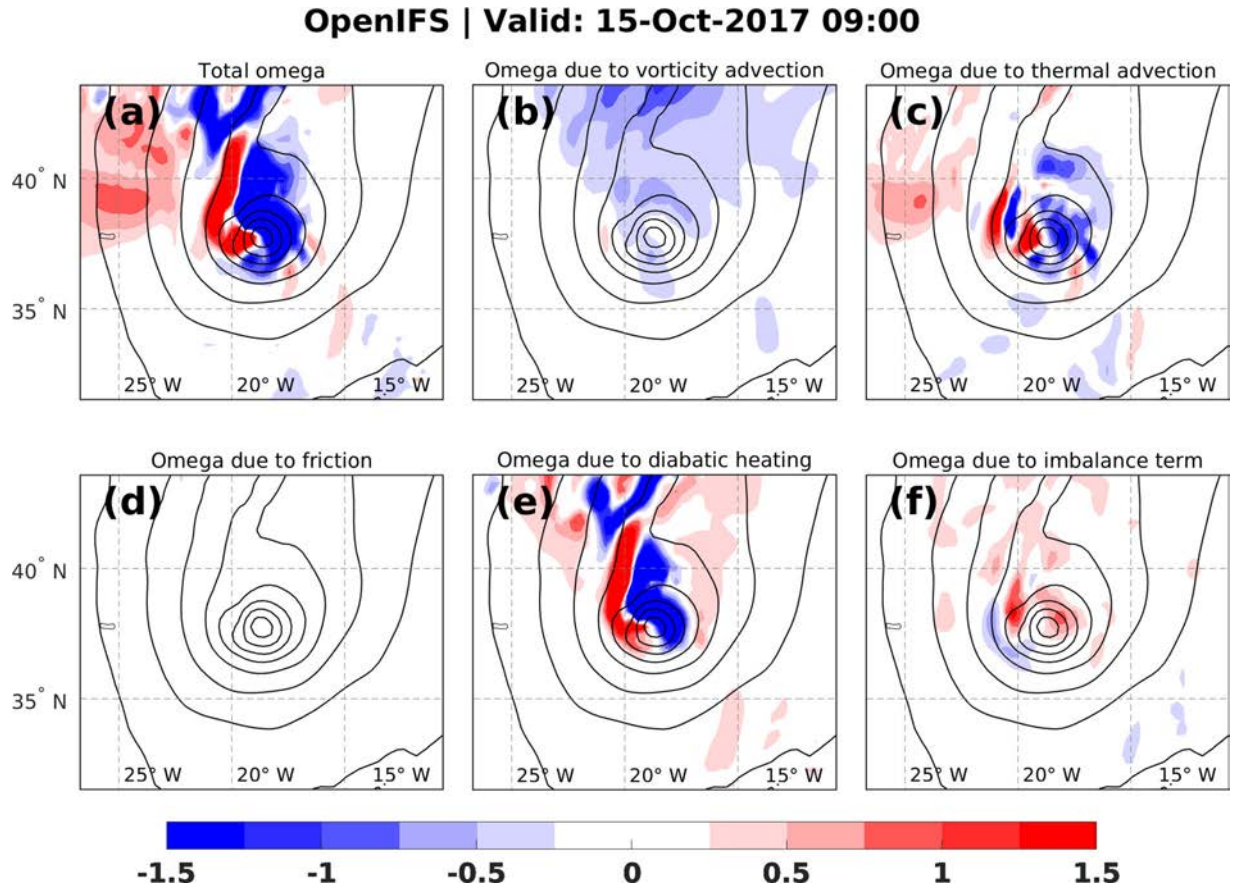

Fig. 9. As Fig. 7, but at 9 UTC 15 October (transition phase).

model of extratropical cyclones (Shapiro and Keyser, 1990). Figure 11b shows the satellite image at 1243 UTC 16 October. The bent back warm front and the long cold front are clearly visible.

Figure 12 represents the vertical motion induced by the different forcing terms at the same time as Fig. 11a. There is a notable expansion of the wind field of the storm, which can be seen from the larger area of strong pressure gradient compared to the situations 24 hours (Fig. 9) and 48 hours (Fig. 7) earlier. The expansion of wind field is a typical behaviour of cyclones undergoing ET (Evans et al., 2017).

From Fig. 12a it can be seen that the ascent is concentrated on the edges of the warm sector. The ascent on the western edge, namely within the warm front, is dominated by diabatic heating (Fig. 12e). The ascent on the eastern edge of the sector is more due to thermal advection (Fig. 12c). In addition, almost all of the sinking motion within the storm is caused by thermal advection, particularly on the southern side of the centre, due to cold air advection as polar maritime air flows eastward behind the cold front. This area of cold-air advection is also visible in the satellite image as mostly cloud-free (Fig. 11b).

Vorticity advection (Fig. 12b) generates ascent nearly everywhere within the storm, and this ascent is more evenly distributed in the warm sector of the storm than the ascent caused by other forcings. In addition, ω_T tends to compensate ω_V within the warm sector and near the cold front.

Although the T127 truncation used in the low-level vorticity fields in Fig. 13 hides partly the frontal structures, the vorticity field shows weak vorticity maxima north and east of the storm centre, which are associated with the warm and cold fronts of the system. The vorticity tendency caused by vorticity advection (Fig. 13b) is still close to zero at the storm centre and hence not contributing to the strengthening of the storm. Compared to the situation 24 hours earlier (Fig. 10b), the field shows now more smaller-scale structures. The most notable addition to the positive-negative dipole centred at the storm centre (Fig. 10b) is a similar dipole around the cold front.

Thermal advection, which only made a very small contribution to Ophelia's intensity in earlier stages (Figs. 8c

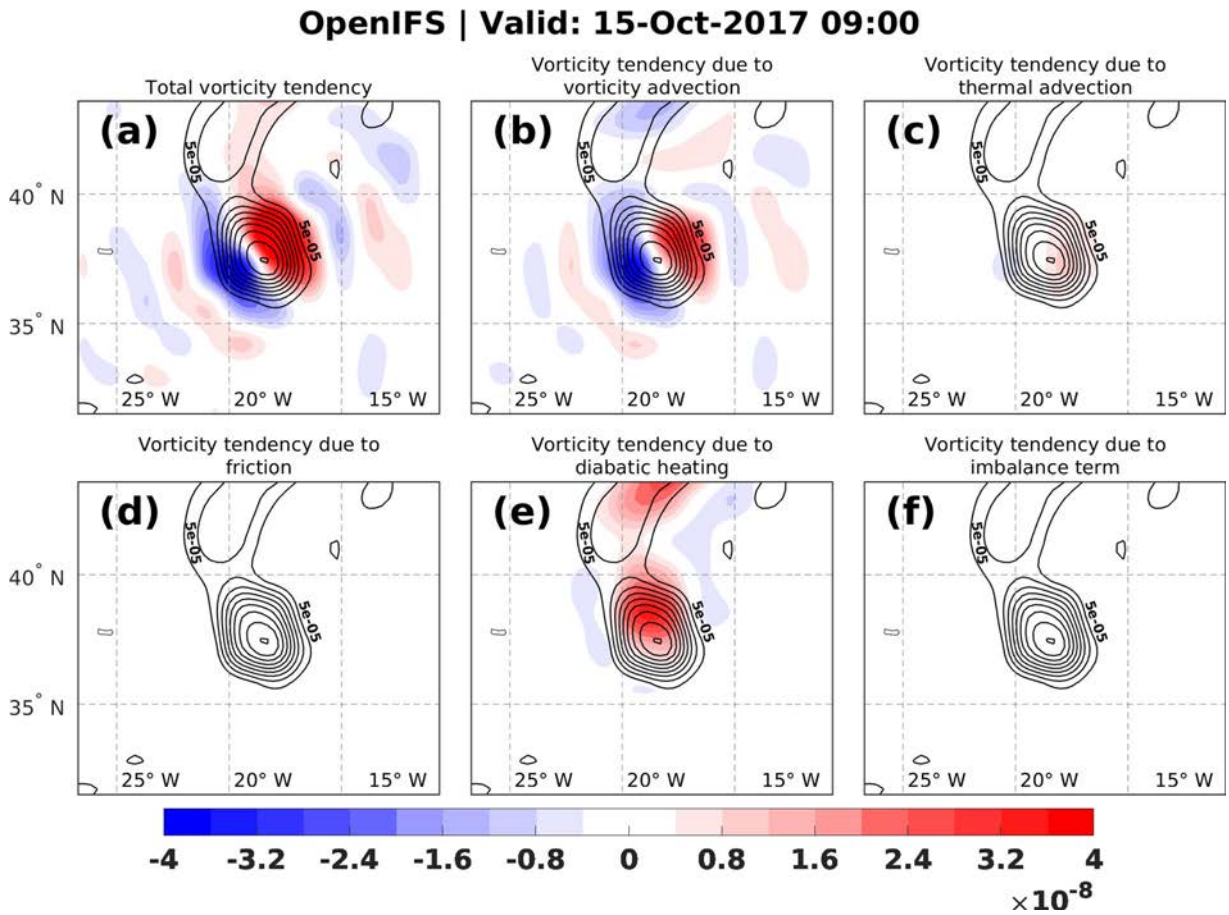

Fig. 10. As Fig. 8, but at 9 UTC 15 October (transition phase).

and 10c), shows now a negative vorticity tendency on the centre and the southern side of the storm (Fig. 13c). The negative vorticity tendency is due to sinking motion caused by the cold-air advection. Sinking motion leads to divergence in the lower troposphere, which vertically compresses the air column and, thus, decreases the vorticity.

Unlike during the tropical and transition phases, friction is now considerably damping the development of the cyclone by inducing a negative vorticity tendency at the cyclone centre (Fig. 13d). One reason for this behaviour is because the maximum of ω_F (the ascent associated with the Ekman pumping) rises from 950 hPa during the tropical phase to 850 hPa during the extratropical phase (not shown), consistently with the growth of the horizontal scale of the storm. The ascent spreads the effect of the surface friction upwards via the indirect terms (RHS terms 2–4 in Eq. 12). For this reason, the vorticity tendency due to friction at 900–800-hPa layer is quite weak in the tropical and transition phases, but increases in the extratropical phase. We also suspect the effect of friction could be slightly underestimated in the tropical phase. This issue is further discussed in Section 6.

The intense vorticity production by diabatic heating within the bent back warm front to the west of the surface low (Fig. 13e) probably contributes to the decay of Ophelia. The reason is that diabatic heating in the mid-troposphere leads to negative vorticity tendency higher up in the atmosphere, to the west of the upper-level trough (not shown). As the generation of vorticity due to diabatic heating slows down the northeastward movement of the surface low (Fig. 13e), the destruction of vorticity does the opposite at the upper levels. As a consequence, the diabatic heating acts to make Ophelia's trough axis vertically stacked faster which is unfavorable for further intensification, because the area of positive upper-level vorticity advection is not situated above the surface low (not shown). As a result, the vorticity tendency caused by the non-divergent vorticity advection at the centre of low-level cyclone remains very modest on 16 October (Fig. 14d).

5.5. *Vorticity tendencies at the cyclone centre*

Figure 15a shows the time evolution of the low-level vorticity tendencies caused by the various forcing terms,

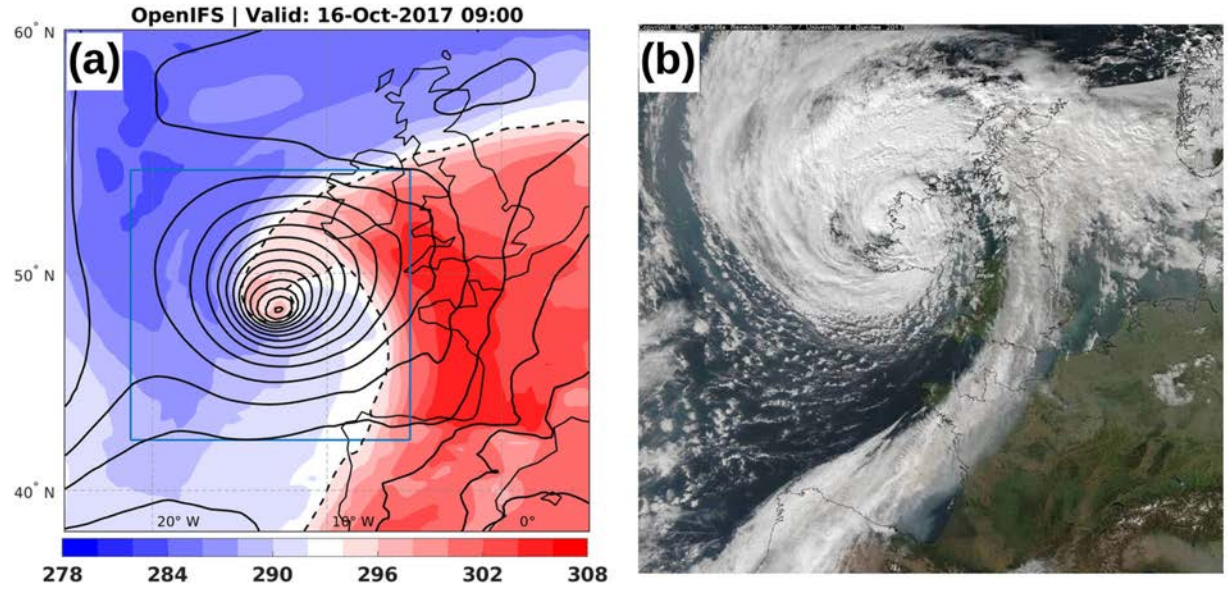

Fig. 11. Potential temperature at 850 hPa (colours, 294 K isentrope contoured with dashed line) at 9 UTC 16 October (extratropical phase) in the OpenIFS simulation (a), and a visible satellite image captured at 1243 UTC 16 October 2017 (b). Contours in (a) represent mean sea level pressure with 4-hPa intervals, and the blue rectangle in (a) marks the area shown in Figs. 12 and 13. Satellite image copyright NERC Satellite Receiving Station, Dundee University, Scotland (http://www.sat.dundee.ac.uk).

averaged within 1.5° radius from the cyclone centre, as identified from the low-level vorticity maximum. The values have been smoothed by a 12-hour moving average, and are, thus, not exactly comparable with vorticity tendencies at the cyclone centre in Figs. 8, 10 and 13. The reason for the 12-hour smoothing is the fact that the amplitudes of the vorticity tendencies are very sensitive to the location of the circle from which the tendencies have been calculated. The sensitivity is especially true for terms which feature a strong positive-negative vorticity tendency dipole, such as the vorticity advection term. In moving systems, the circle is located just in the middle of the dipole, so a small displacement of the circle drastically affects the tendency averaged over the circular area. For this reason, the raw time series has some small time-scale variation which we wanted to eliminate with the moving averaging.

In general, diabatic heating (Fig. 15a, purple line) dominates the generation of cyclonic vorticity during the whole life cycle of Ophelia. The contribution of diabatic heating increases towards the transition period, and peaks just before the deepest stage of the storm, at 3 UTC 16 October. We suspect that the major part of the vorticity increase due to diabatic heating comes from the stretching term (RHS term 2 in Eq. 13). The contributions of different model parametrization schemes to the diabatic heating and the associated vorticity tendencies are studied in more detail in subsection 5.7.

Vorticity advection (Fig. 15a, blue line) is often considered a very important forcing for the development of mid-latitude cyclones, but is found to have neutral or even negative influence for the evolution of Ophelia at 900–800 hPa, varying around zero with the largest negative vorticity tendency right at the deepest stage of the storm. As discussed in the next subsection, the large negative vorticity tendency at the deepest stage is associated with the divergent-wind contribution to vorticity advection.

Thermal advection (Fig. 15a, red line) has the second largest effect on the development of Ophelia during its tropical phase. For the atmosphere, the effect of warm air advection is similar to the effect of diabatic heating; both induce mid-tropospheric rising motion, and hence by mass continuity horizontal convergence in the lower troposphere, which acts to increase cyclonic vorticity. After the transition, the cold-air advection behind the cold front has the opposite influence on the cyclone.

The vorticity tendency caused by friction (Fig. 15a, yellow line) is continuously negative, and its effect grows when Ophelia reaches the extratropical phase. As explained in the earlier subsection, this is mostly due to the increase of ω_F in the extratropical phase.

5.6. Effect of vorticity advection by divergent and rotational winds

As shown in Fig 15a, vorticity advection causes a predominantly negative vorticity tendency near the cyclone

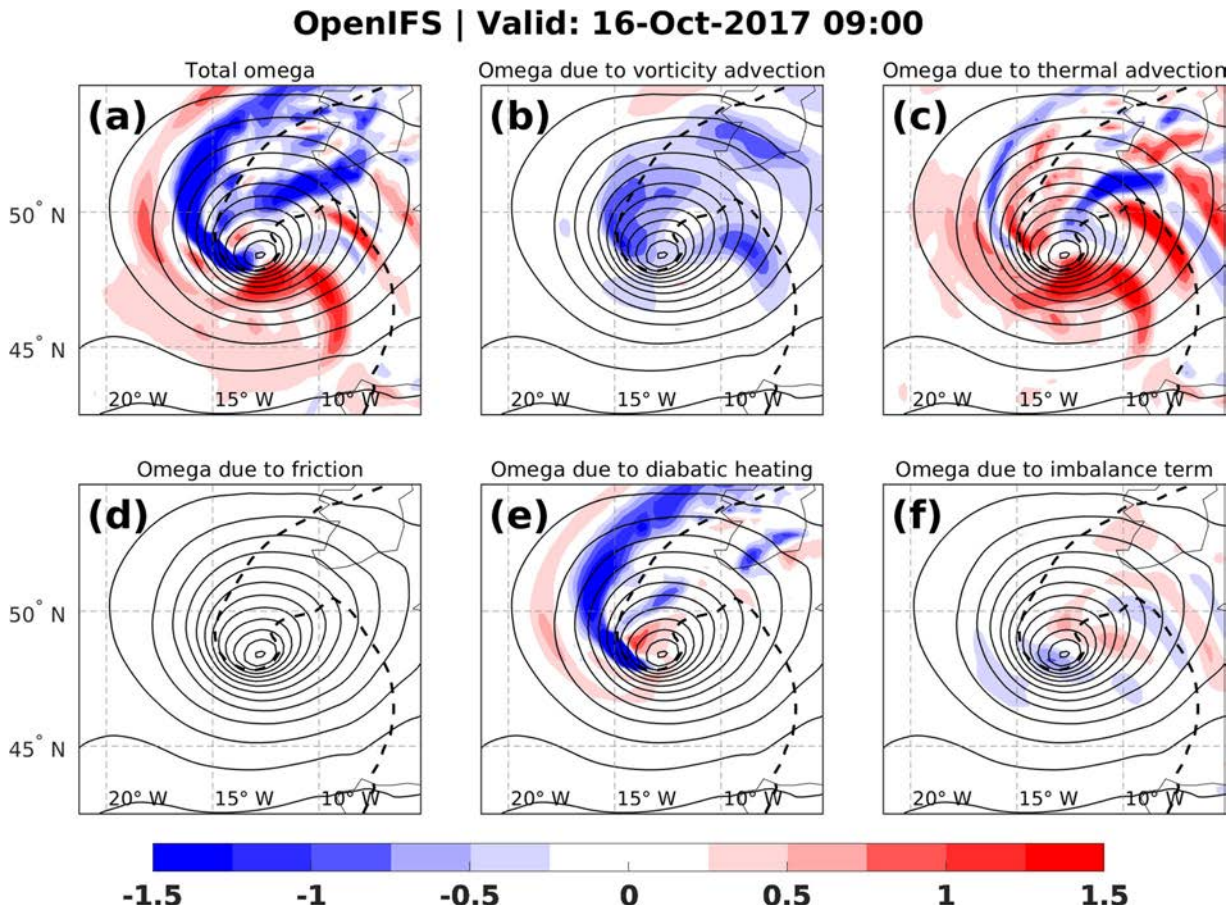

Fig. 12. As Fig. 7, but at 9 UTC 16 October (extratropical phase). The dashed line shows the 294 K isentrope at 850 hPa.

centre during the life cycle of Ophelia. This negative vorticity tendency peaks at 3 UTC 16 October, at the moment when the total vorticity tendency is at its highest (Fig. 15a, dashed line). To understand this behaviour, the vorticity tendencies caused by $\boldsymbol{V}_\psi$ and $\boldsymbol{V}_\chi$ together with their sum are presented in Fig. 14a–c. Figure 14d shows the corresponding time series at the cyclone centre.

When looking at the spatial fields, there is notable similarity between the vorticity tendency by total vorticity advection (Fig. 14a, same as Fig. 13b) and the vorticity tendency due to rotational wind vorticity advection (Fig. 14b). Thus, the major part of the total vorticity advection is caused by the rotational wind.

However, the crucial issue for the cyclone intensity are the vorticity tendencies at the vicinity of the cyclone centre (Fig. 14d). It can be clearly seen that the increase in negative vorticity tendency due to total vorticity advection on 16 October is solely due to vorticity advection by $\boldsymbol{V}_\chi$. Instead, vorticity advection by $\boldsymbol{V}_\psi$ induces weak, but mainly positive vorticity tendency during the transition period. The negative vorticity tendency due to vorticity advection by $\boldsymbol{V}_\chi$ can be seen also from Fig. 14c, where the negative values are spread over the cyclone centre.

The physical reason for the negative vorticity tendency caused by $\boldsymbol{V}_\chi$ at the transition time is the secondary circulation of the cyclone. When the hurricane transforms into a mid-latitude cyclone, its wind field expands and the convergent flow towards the cyclone centre near the surface increases, in part due to friction but also due to other processes that cause lower-tropospheric vertical motion above the cyclone centre. The divergent component of the wind transports air with lower cyclonic vorticity into the area of high cyclonic vorticity. This negative vorticity advection produces negative vorticity tendency, which peaks when the cyclone intensity and its secondary circulation is at its highest. These results align well with R17 and Räisänen (1997).

The divergent flow causing the anticyclonic vorticity advection is due to all processes which causes convergence towards the centre of the storm, including diabatic heating. However, note that the vorticity tendency caused by $\boldsymbol{V}_\chi$ accounts also for the stretching due to vorticity

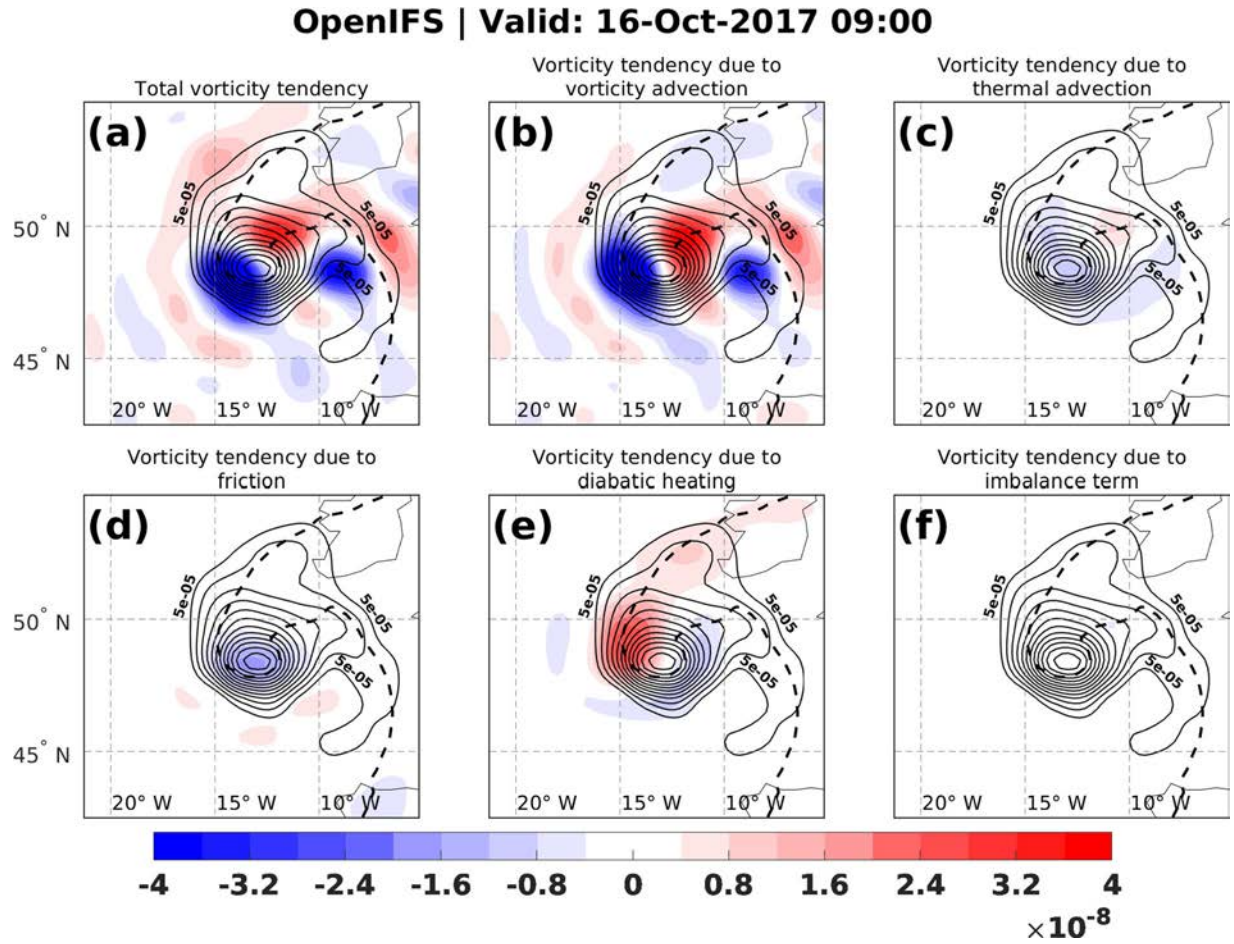

Fig. 13. As Fig. 8, but at 9 UTC 16 October (extratropical phase). The dashed line shows the 294 K isentrope at 850 hPa.

advection (RHS term 3 in Eq. 11). Nevertheless, we suspect that the stretching due to vorticity advection is actually quite modest during the tropical and transition phases of the storm, because of the weak ω_V at the cyclone centre (Figs. 7b and 9b).

5.7. The contributions from different model parametrizations to diabatic heating

Diabatic processes were the dominant forcing in the ET of Ophelia (Fig. 15a). But which diabatic processes were the most important?

In OpenIFS, the total temperature tendency by diabatic heating consists of five parts (Eq. 15 and Table 2). Figure 15b shows the contributions of these five components to the vorticity tendency in the centre of the storm. The vorticity tendencies induced by radiation (blue), vertical diffusion + orographic drag + surface processes (red), and gravity wave drag (yellow) are negligible within 1.5° radius of the storm centre and also elsewhere in the vicinity of the storm (not shown). The vorticity tendencies due to convection (purple) and cloud microphysics (green) were much more important.

The vorticity tendency caused by convection (purple) is the dominant forcing in the beginning of the simulation, during the hurricane phase of Ophelia. From 15 October onwards, the cloud microphysics scheme (green) becomes more important. Finally, in the extratropical phase (at 9 UTC 16 October), the convection scheme does not anymore enhance the cyclone development. At this point, the heating generated by the cloud microphysics scheme is the only diabatic process that produces positive vorticity within 1.5° radius of the cyclone centre.

More information on the different sources of model-simulated diabatic heating can be obtained from the maps. Figure 16 shows the vertical motion induced by the convection scheme (Fig. 16a) and the cloud microphysics scheme (Fig. 16b) at the tropical phase of the storm (9 UTC 14 October). The convection scheme produces ascent which extends horizontally over a large area around the storm, whereas the vertical motions generated by the cloud microphysics scheme are more localized,

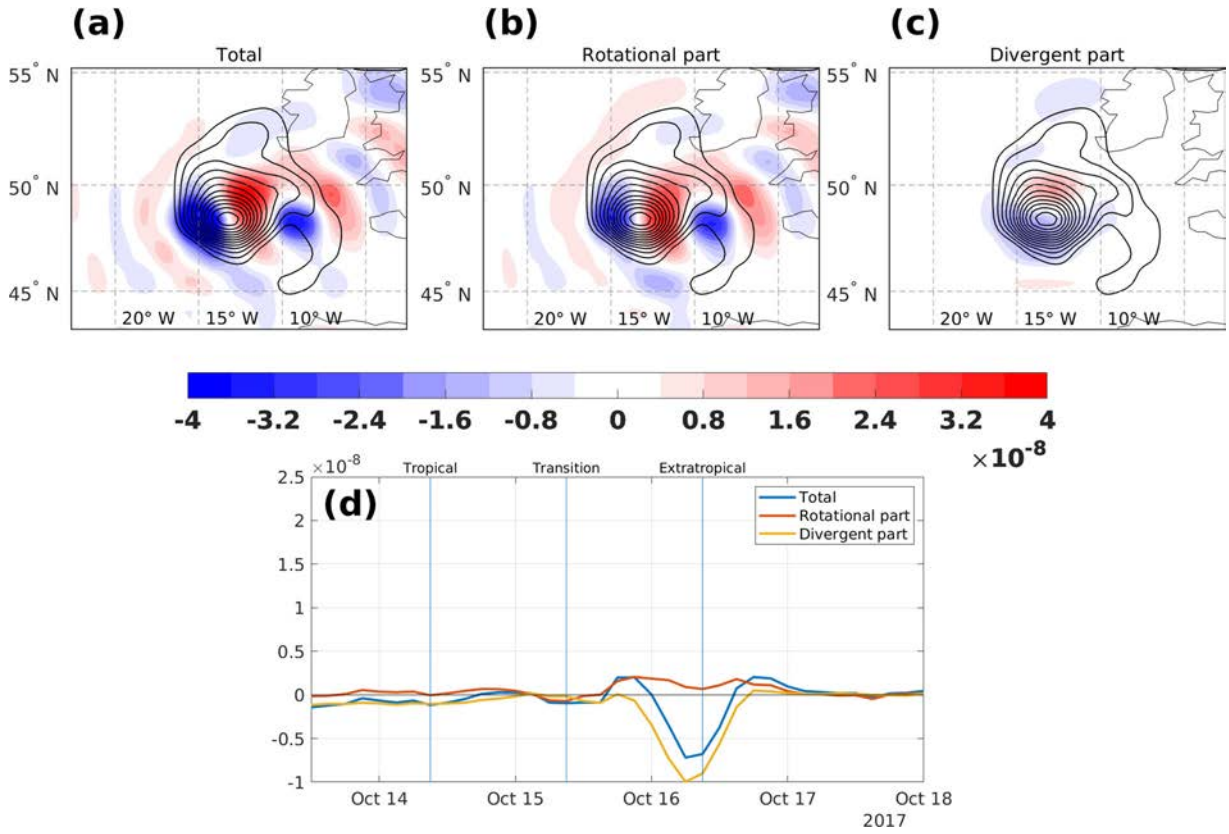

Fig. 14. Vorticity tendency induced by (a) total vorticity advection, (b) vorticity advection by rotational winds, and (c) vorticity advection by divergent winds at 9 UTC 16 October (extratropical phase). In d), time series of vorticity advection by rotational winds (red), divergent winds (yellow), and total winds (blue) averaged over 1.5° circle are shown. The times of tropical, transition, and extratropical phases have been marked with vertical lines in (d).

mainly near the cyclone centre. Figure 16e and f represents the same situation but for the vorticity tendencies. The convection scheme (Fig. 16e) produces cyclonic vorticity in the area of ascent, in the south-east quadrant of the storm. The cloud microphysics scheme (Fig. 16f) generates negligible vorticity tendency, in agreement with Fig. 15b.

Vertical motions and vorticity tendencies due to convection and cloud microphysics schemes at the extratropical phase of the storm (9 UTC 16 October) are presented in Fig. 16c, d, g and h. The convection scheme produces ascent in localised spots within the warm sector and cold front of the storm (Fig. 16c). In particular, there is strong convective lifting occurring over southern Ireland. However, the large-scale rising motion in the warm front is enhanced by the diabatic heating generated by the cloud microphysics scheme (Fig. 16d). Furthermore, there are areas of cancellation between these two schemes. One example is along the part of the cold front closest to the cyclone centre, to the northeast of the storm, where the compensating sinking motion from the cloud microphysics scheme coincides with rising motion associated with the convection scheme. We suspect that convection produces heating via condensation and freezing of water, but part of the rain is evaporated before reaching the surface. Although the convective parametrization produces ascent within the warm sector of the storm, the vorticity tendency caused by it is very weak (Fig. 16g). Instead, the cloud microphysics parametrization generates notably more cyclonic vorticity (Fig. 16h), which is co-located with the frontal ascent.

This analysis illustrates how the emphasis of diabatic heating, and more specifically the latent heat release from the condensation/freezing of water vapour, changes from the convective parametrization to the cloud microphysics parametrization during the ET of the storm. This change in the importance of parametrization schemes is particularly notable in vorticity tendencies near the cyclone centre (Fig. 15b), which effectively affect the strength of the storm. The reason for this change is firstly the shift of convective ascent further away from the storm centre to the area of the warm sector, and secondly the

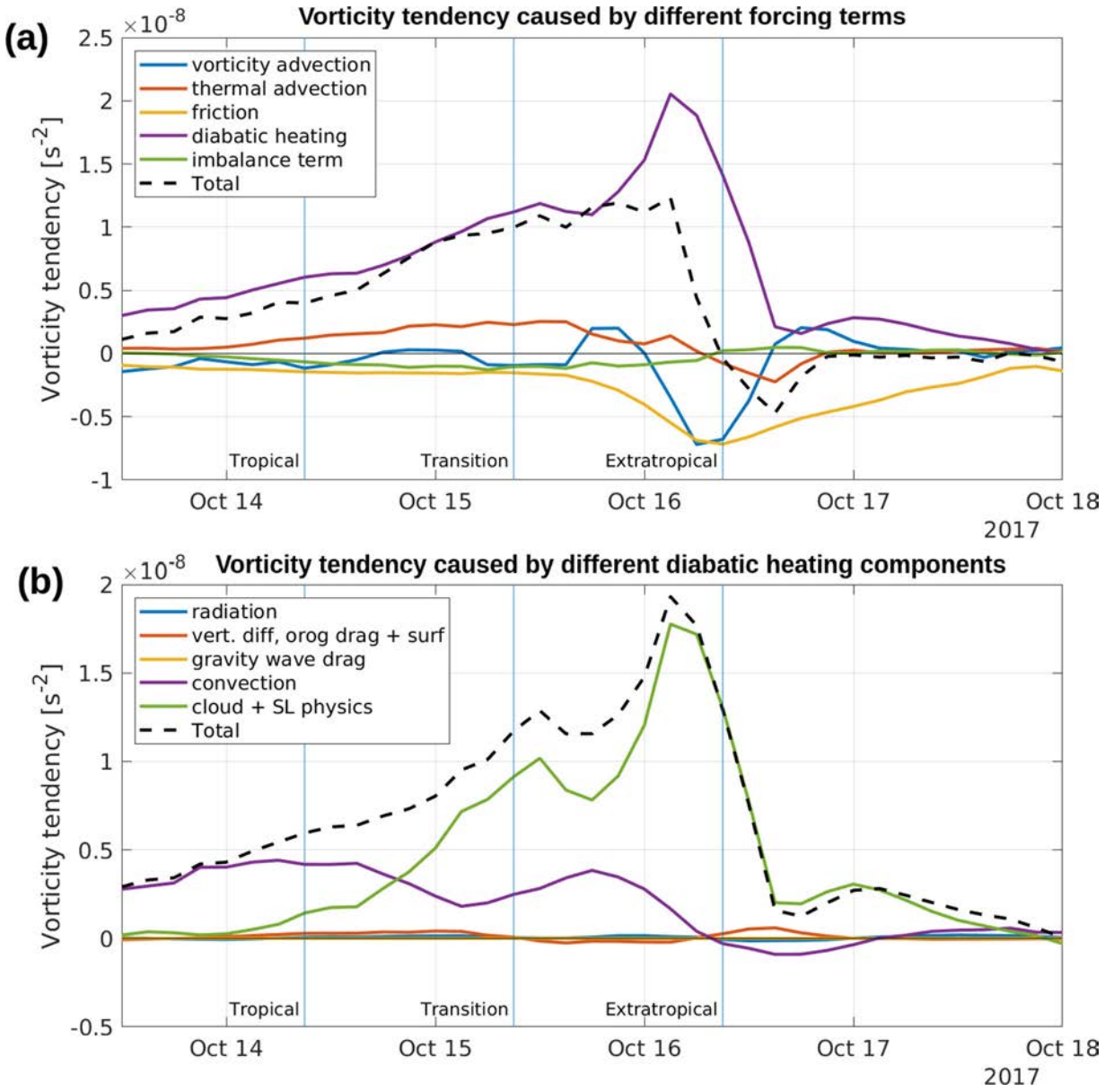

Fig. 15. Time series of vorticity tendencies caused by (a) different forcing terms and (b) different diabatic heating components. The values have been averaged over the 900–800-hPa layer and over a circular area with a 1.5° radius centred on the maximum of the T127 vorticity field. All values are 12-hour moving averages. The times of tropical, transition, and extratropical phases have been marked with vertical lines.

formation of the warm front in which the cloud microphysics scheme in the model is activated.

The diabatic heating components used in this analysis (Table 2) are naturally OpenIFS-specific. In other numerical models, the partitioning of Q into contributions from different heating processes may be done differently. Nevertheless, we would still expect that the shift from convective heating towards latent heat release associated with larger-scale ascent (which is represented by the cloud microphysics scheme) is a typical characteristic of the ET process.

6. Discussion

Although the re-intensification of Hurricane Ophelia when it struck Ireland as a post-tropical storm occurred during favorable interaction with an upper-level trough, we found the direct effect of the adiabatic upper-level

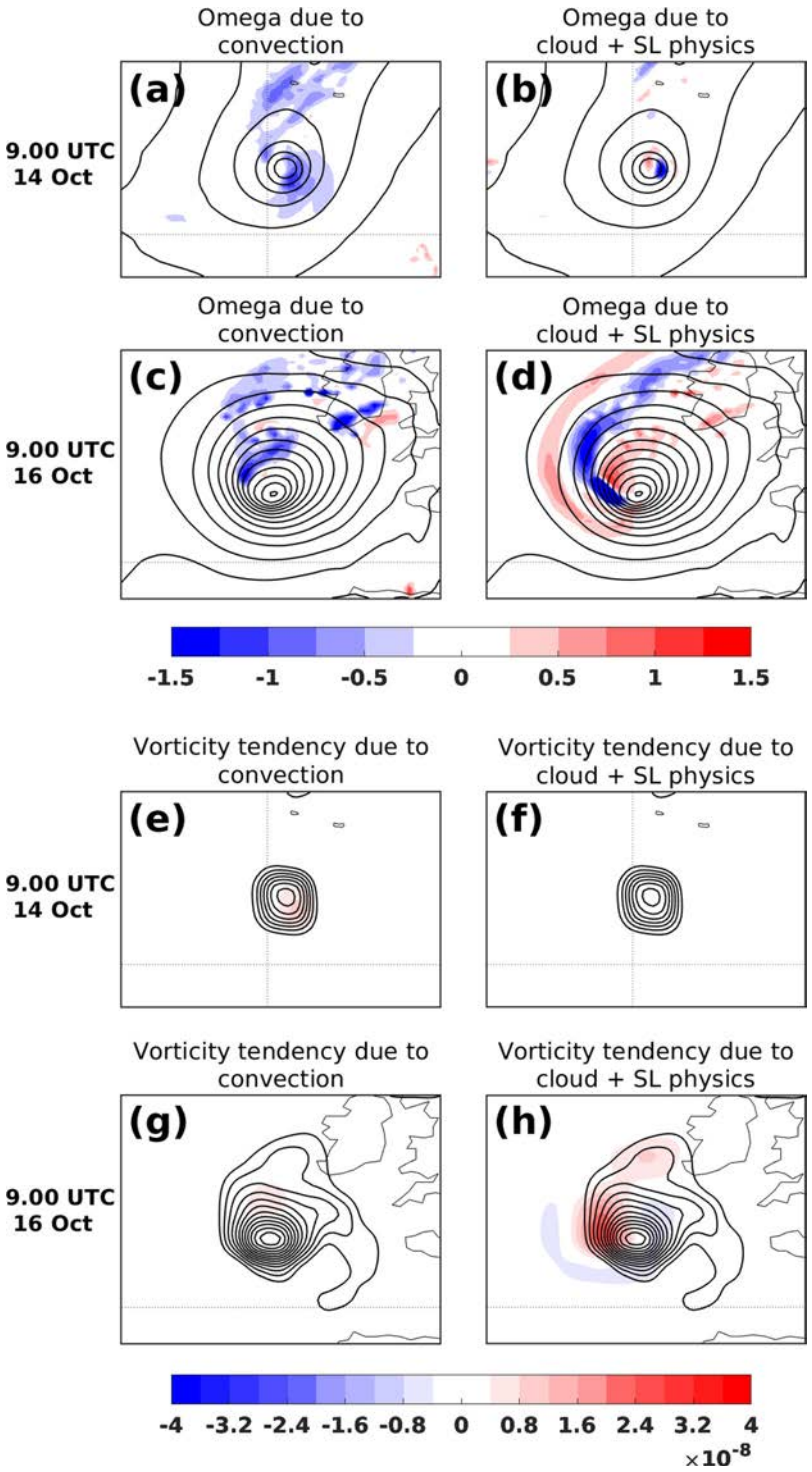

Fig. 16. Panels (a) – (d) show vertical motion (shading, Pa s^{-1}) at 700 hPa and sea level pressure (contours, with 4-hPa interval), and panels (e) – (h) show vorticity tendency (shading, s^{-2}) and relative vorticity (contours, starting from 5×10^{-5} s^{-1}, with 5×10^{-5} s^{-1} interval) averaged over the 900–800-hPa layer. The left-hand panels [(a), (c), (e), and (g)] show vertical motion and vorticity tendency due to the convection parametrization, and the right-hand panels [(b), (d), (f) and (h)] show vertical motion and vorticity tendency due to the microphysics parametrization. The upper panels in both vertical motion [(a) and (b)] and in vorticity tendency [(e) and (f)] show the situation at 9 UTC 14 October (tropical phase), and the lower panels [(c), (d), (g) and (h)] at 9 UTC 16 October (extratropical phase). The size of the panels is 16° longitude by 12° latitude, centred on the cyclone vorticity maximum.

forcing on the lower tropospheric storm to be relatively modest. Rather, our results suggest that the effect of the upper-level forcing was strongly amplified by diabatic processes. This outcome emphasizes the importance of resolving diabatic processes correctly in climate models. Since the effect of diabatic heating on the intensity of extratropical cyclones is quite sensitive to the model resolution (Willison et al., 2013), high-resolution simulations are required to investigate the future projections of post-tropical storms. Fortunately, this is already the case in some recent studies (e.g. Haarsma et al., 2013; Baatsen et al., 2015).

OpenIFS underestimated the intensity of Ophelia during its tropical phase, seen as higher minimum sea level pressure in OpenIFS than in the NHC analysis (Fig. 4). Yamaguchi et al. (2017) reported that all the major global numerical weather prediction models tend to underestimate tropical cyclone intensity, especially when the minimum sea level pressure is 940 hPa or below. They found this systematic error to be present even at the initialization time of the forecasts, which implies that the resolution of the models may be the biggest culprit for the error. Hodges and Klingaman (2019) reported approximately 8 hPa intensity error of tropical cyclones in the Western North Pacific at the initial time of the IFS model forecasts. As our model resolution was coarser than what is typically used in operational weather prediction models, we suspect that the overestimation of sea level pressure (Fig. 4) was primarily due to the coarse resolution. Examination of initial states from the forecast used in this study, and a forecast initialized 24 hours later (at 12 UTC 14 October) revealed that the large overestimation of Ophelia's minimum surface pressure was present already in the initial conditions. Furthermore, the operational analyses by Climate Forecast System Version 2 (CFSv2), Global Forecast System (GFS) and the Japanese 55-year Reanalysis (JRA-55) also underestimated the minimum pressure of Ophelia approximately 30 hPa during the tropical phase (not shown). The fact that the underestimation of intensity was clearly reduced when the ET was completed and the horizontal scale of the storm was increased, supports our conclusion about low resolution of OpenIFS to capture the small-scale pressure minimum during the tropical phase.

As the intensity of the storm during the tropical phase was clearly underestimated, one can also question the reliability of the magnitude of vorticity tendencies calculated in the centre of the storm during the tropical phase (Fig. 15). This is a relevant aspect which needs to be taken into account when interpreting the results. Firstly, the scale of the storm relative to the size of the moving circle from which the vorticity tendencies (1.5° radius) were calculated is smaller in the tropical phase than in the extratropical phase. This means that the averaging smooths the tendencies more when the storm is small relative to the area of the circle, and this has probably had some effect on the smallness of the vorticity tendency terms in the beginning of our simulation in Fig. 15. Secondly, the model resolution also smooths the local vorticity and its tendency structures close to the eye of the hurricane. For these two reasons, the magnitude of vorticity tendencies during the tropical phase are probably underestimated. A simple solution for this would be to run OpenIFS with higher resolution. However, our diagnostic software has some limitations regarding to the high-resolution runs: the imbalance term grows larger and thus the interpretation of the results becomes increasingly problematic. This issue has been explained in detail in Section 8 of R17. Nevertheless, as the main aim of this study was to focus on the transition and extratropical phases of the storm, we acknowledge the weakness of our results in the tropical phase and leave it for a topic of a possible follow-up study.

In our technical framework, we divided only the atmospheric vertical motion and vorticity tendency into contributions from different forcing terms. For consistency, the division of divergent wind into the same contributions could provide new interesting information on the physical processes affecting the secondary circulation of Ophelia. However, as far as we see, the realization of this decomposition is technically complicated, and would lead in an iterative solution that would significantly complicate the solution of the omega equation. For this reason, the implementation of this functionality is not included to the current version of OZO, but it is something which could be worth of carrying out in the future.

Regarding the performance of OZO, the correlations for vertical motion (Fig. 6) are somewhat worse than in the idealized case in R17. The largest source of numerical errors is the calculation of time derivatives of vorticity and temperature in Eq. 7. Because these time derivatives cannot be output directly from OpenIFS, they are approximated with the central difference method with one-hour time interval. By decreasing the time interval, particularly the accuracy of the imbalance term could be improved, which would decrease the difference between ω_{TOT} and ω_{OIFS} as shown in Fig. 2 in R17. This would however affect only the magnitude of the imbalance term, which plays a rather small role for the development of Ophelia.

The diabatic heating rate Q and friction F are not available from OpenIFS as instantaneous values, but rather need to be calculated from time-accumulated tendencies over each output interval. Here, we used a one-hour output interval and evaluated these terms as time-averages over a two-hour time span. This averaging had to be done because otherwise the tendencies would have contained information

only from the past one hour and, therefore, have featured a 30-minute phase shift compared to other variables. For this reason, a decrease of the output time interval could slightly increase the accuracy of the diabatic heating and friction terms. We do not expect this to affect significantly the main results of this study, as the magnitude of the diabatic heating and friction terms would rather increase than decrease when using a smaller time interval for the averaging.

Our main conclusion is that the diabatic heating was the dominant forcing for the intensity of the low-level cyclone. In the extratropical phase, the diabatic heating came mainly from the microphysics scheme, but we did not have information about the contributions of individual microphysical processes (such as condensation, evaporation, freezing) to the heating. The reason for this is that currently OpenIFS does not have a functionality to output the temperature tendencies associated with these various microphysical processes.

In many previous studies the effect of vorticity advection for the development of post-tropical storms has been estimated using the mid- or upper-level winds (e.g. Klein et al., 2002; Ritchie and Elsberry, 2007) or geostrophic winds (e.g. Milrad et al., 2009; Azad and Sorteberg, 2009). As we calculated the forcing terms at the lower troposphere and accounted also for the divergent circulation and the indirect contributions from vertical motion, our results are naturally not comparable with those listed. DiMego and Bosart (1982), who studied the transformation of Tropical Storm Agnes into an extratropical cyclone, stated that" Differential advection by the divergent part of the wind, although generally weaker, act as a sink of vorticity." This statement is consistent with our results. Azad and Sorteberg (2014) used a very similar method for the examination of vorticity tendency budgets in regular North Atlantic winter extratropical cyclones. They reported vorticity advection being the most influential low-level forcing for the composite cyclone. Our results with Ophelia do not agree with this, but on the other hand we studied a post-tropical storm, which is somewhat different by its dynamics than the pure extratropical cyclones used in the study by Azad and Sorteberg (2014).

As a final note, this analysis was purposely performed only for the surface cyclone, since we wanted to study the forcing mechanisms responsible for the surface impacts. This was the main motivation why the vorticity tendencies were calculated for the 900–800-hPa layer, and the choice of 700 hPa for the vertical motion analysis. Hence, the main outcome of our study - the importance of diabatic heating for the strength of the surface cyclone - does not apply at higher levels. In fact, the examination of vorticity tendencies at 500 and 250 hPa levels revealed thermal advection being the main contributor to the strength of the upper trough (not shown).

7. Conclusions

This study investigated the extratropical transition of Hurricane Ophelia with the generalized omega equation and vorticity equation. The main aim was to determine the contributions of different adiabatic and diabatic forcing terms for the life cycle of the storm, and identify which of them led to the strengthening of the storm into a powerful post-tropical cyclone when it made landfall in Ireland in October 2017. Our initial hypothesis was that diabatic processes would be dominant in the tropical phase of the cyclone, but baroclinic processes (vorticity advection and thermal advection) would become more important for the cyclone development after its extratropical transition.

The first part of our hypothesis was correct: diabatic heating, and more specifically the release of latent heat, was indeed the dominant forcing during Ophelia's tropical phase. Latent heat release, ascending motion, and positive low-level vorticity tendency were first produced via the convection scheme, but smoothly changed to the cloud microphysics scheme later, during the transition and the extratropical phases of the storm. Other diabatic heating processes were found to be negligible for the cyclone evolution.

Unlike what we hypothesized, the low-level relative vorticity at the storm centre during the extratropical phase was largely produced by diabatic heating rather than adiabatic processes (vorticity advection or thermal advection). In fact, the net-effect of vorticity advection was actually detrimental for the surface cyclone because the divergent winds within the secondary circulation of the cyclone transported air with less cyclonic vorticity to the centre of the storm, thus reducing the vorticity maximum at the centre. Vorticity advection by the rotational winds did contribute to the intensification of the storm in its extratropical phase, but its contribution was much smaller than that of diabatic heating. Thermal advection, which made a moderate contribution during the tropical phase due to warm-air advection from the subtropics, no longer enhanced the development of the storm during its extratropical phase. The reason for this was the occlusion process, which led cold air advection to wrap from the southwest around the storm and, consequently, to a negative vorticity tendency at the vicinity of the storm centre. The effect of friction was found to increase soon after the extratropical transition, presumably due to the expansion of the wind field. Together with the lack of baroclinic forcings, the effect of friction led to the weakening of the storm after the landfall.

Our results are valid for the surface cyclone, and, thus, not applicable at higher levels. However, it is important to note that diabatic heating, which is largely dominated

by the latent heat release in the clouds, requires usually existing rising motion to occur. Thus, although our analysis suggests a very modest direct role for the upper-level forcing, it may still have been important in triggering the large-scale rising motion that generated the latent heat release above the low-level vortex. Based on one case study it is not possible to conclude whether our outcome is typical in post-tropical storms. Therefore, it would be interesting to conduct a statistical study of cyclones undergoing extratropical transition and investigate what is the average role of different adiabatic and diabatic forcing terms for the evolution of post-tropical storms.

Acknowledgements

The authors wish to acknowledge CSC–IT Center for Science, Finland, for computational resources. ECMWF is acknowledged for making the OpenIFS model available and for generating the ERA5 reanalysis. Copernicus Climate Change Service (C3S) is acknowledged for providing access to the ERA5 data. We thank Kevin Hodges for providing the TRACK code and for his advice with the algorithm. Robert Hart is acknowledged for the cyclone phase space diagram, and NERC Satellite Receiving Station, Dundee University, Scotland for the satellite image. Finally, we would like to also thank the three anonymous reviewers for their constructive feedback.

Disclosure statement

No potential conflict of interest was reported by the authors.

Funding

MR acknowledges the Doctoral Programme in Atmospheric Sciences (ATM-DP, University of Helsinki) for financial support. VAS is funded by the Academy of Finland Center of Excellence programme (project no. 307331).

References

Azad, R. and Sorteberg, A. 2009. A diagnosis of warm-core and cold-core extratropical cyclone development using the Zwack–Okossi equation. *Atmos. Sci. Lett.* **10**, 220–225.

Azad, R. and Sorteberg, A. 2014. The vorticity budgets of North Atlantic winter extratropical cyclone life cycles in MERRA reanalysis. Part I: development phase. *J. Atmos. Sci.* **71**, 3109–3128. doi:10.1175/JAS-D-13-0267.1

Baatsen, M., Haarsma, R. J., Van Delden, A. J. and De Vries, H. 2015. Severe autumn storms in future western Europe with a warmer Atlantic ocean. *Clim. Dyn.* **45**, 949–964. doi:10.1007/s00382-014-2329-8

Bentley, A. M., Bosart, L. F. and Keyser, D. 2019. A climatology of extratropical cyclones leading to extreme weather events over central and eastern North America. *Mon. Wea. Rev.* **147**, 1471–1490. doi:10.1175/MWR-D-18-0453.1

Bieli, M., Camargo, S. J., Sobel, A. H., Evans, J. L. and Hall, T. 2019. A global climatology of extratropical transition part I: characteristics across basins. *J. Climate.* **32**, 3557–3582. doi:10.1175/JCLI-D-17-0518.1

Browning, K., Panagi, P. and Vaughan, G. 1998. Analysis of an ex-tropical cyclone after its reintensification as a warm-core extratropical cyclone. *Q. J. R. Meteorol. Soc.* **124**, 2329–2356. doi:10.1002/qj.49712455108

Davis, C. A., Jones, S. C. and Riemer, M. 2008. Hurricane vortex dynamics during Atlantic extratropical transition. *J. Atmos. Sci.* **65**, 714–736. doi:10.1175/2007JAS2488.1

DeHart, J. C., Houze, R. A. Jr. and Rogers, R. F. 2014. Quadrant distribution of tropical cyclone inner-core kinematics in relation to environmental shear. *J. Atmos. Sci.* **71**, 2713–2732. doi:10.1175/JAS-D-13-0298.1

DiMego, G. J. and Bosart, L. F. 1982. The transformation of Tropical Storm Agnes into an extratropical cyclone. Part II: moisture, vorticity and kinetic energy budgets. *Mon. Wea. Rev.* **110**, 412–433. doi:10.1175/1520-0493(1982)110<0412:TTOTSA>2.0.CO;2

Evans, C., Wood, K. M., Aberson, S. D., Archambault, H. M., Milrad, S. M. and co-authors. 2017. The extratropical transition of tropical cyclones. Part I: cyclone evolution and direct impacts. *Mon. Wea. Rev.* **145**, 4317–4344. doi:10.1175/MWR-D-17-0027.1

Evans, J. L. and Hart, R. E. 2003. Objective indicators of the life cycle evolution of extratropical transition for Atlantic tropical cyclones. *Mon. Wea. Rev.* **131**, 909–925. doi:10.1175/1520-0493(2003)131<0909:OIOTLC>2.0.CO;2

Feser, F., Schubert-Frisius, M., von Storch, H., Zahn, M., Barcikowska, M. and co-authors. 2015. Hurricane Gonzalo and its extratropical transition to a strong European storm. *Bull. Amer. Meteor. Soc.* **96**, S51–S55. doi:10.1175/BAMS-D-15-00122.1

Foerster, A. M., Bell, M. M., Harr, P. A. and Jones, S. C. 2014. Observations of the eyewall structure of Typhoon Sinlaku (2008) during the transformation stage of extratropical transition. *Mon. Wea. Rev.* **142**, 3372–3392. doi:10.1175/MWR-D-13-00313.1

Grams, C. M. and Blumer, S. R. 2015. European high-impact weather caused by the downstream response to the extratropical transition of North Atlantic Hurricane Katia (2011). *Geophys. Res. Lett.* **42**, 8738–8748. doi:10.1002/2015GL066253

Grams, C. M., Jones, S. C., Davis, C. A., Harr, P. A. and Weissmann, M. 2013. The impact of Typhoon Jangmi (2008) on the midlatitude flow. Part I: upper-level ridgebuilding and modification of the jet. *Q. J. R. Meteorol. Soc.* **139**, 2148–2164. doi:10.1002/qj.2091

Haarsma, R. J., Hazeleger, W., Severijns, C., De Vries, H., Sterl, A. and co-authors. 2013. More hurricanes to hit western Europe due to global warming. *Geophys. Res. Lett.* **40**, 1783–1788. doi:10.1002/grl.50360

Hart, R. 2018. Cyclone phase evolution: analyses & forecasts. Online at: http://moe.met.fsu.edu/cyclonephase/archive/2017/gifs/ophelia2017 [accessed 20 May 2019]

Hart, R. E. 2003. A cyclone phase space derived from thermal wind and thermal asymmetry. *Mon. Wea. Rev.* **131**, 585–616. doi:10.1175/1520-0493(2003)131<0585:ACPSDF>2.0.CO;2

Hart, R. E. and Evans, J. L. 2001. A climatology of the extratropical transition of Atlantic tropical cyclones. *J. Climate* **14**, 546–564. doi:10.1175/1520-0442(2001)014<0546:ACOTET>2.0.CO;2

Hart, R. E., Evans, J. L. and Evans, C. 2006. Synoptic composites of the extratropical transition life cycle of North Atlantic tropical cyclones: factors determining posttransition evolution. *Mon. Wea. Rev.* **134**, 553–578. doi:10.1175/MWR3082.1

Hawcroft, M., Walsh, E., Hodges, K. and Zappa, G. 2018. Significantly increased extreme precipitation expected in Europe and North America from extratropical cyclones. *Environ. Res. Lett.* **13**, 124006. doi:10.1088/1748-9326/aaed59

Hodges, K. 1995. Feature tracking on the unit sphere. *Mon. Wea. Rev.* **123**, 3458–3465. doi:10.1175/1520-0493(1995)123<3458:FTOTUS>2.0.CO;2

Hodges, K. and Klingaman, N. 2019. Prediction errors of tropical cyclones in the Western North Pacific in the met office global forecast model. *Wea. Forecasting* **34**, 1189–1209. doi:10.1175/WAF-D-19-0005.1

Hodges, K. I. 1994. A general method for tracking analysis and its application to meteorological data. *Mon. Wea. Rev.* **122**, 2573–2586. doi:10.1175/1520-0493(1994)122<2573:AGMFTA>2.0.CO;2

Keller, J. H., Grams, C. M., Riemer, M., Archambault, H. M., Bosart, L. and co-authors. 2018. The Extratropical Transition of Tropical Cyclones Part II: interaction with the midlatitude flow, downstream impacts, and implications for predictability. *Mon. Wea. Rev.* **147**, 1077–1106. doi:10.1175/MWR-D-17-0329.1

Klein, P. M., Harr, P. A. and Elsberry, R. L. 2002. Extratropical transition of western North Pacific tropical cyclones: midlatitude and tropical cyclone contributions to reintensification. *Mon. Wea. Rev.* **130**, 2240–2259. doi:10.1175/1520-0493(2002)130<2240:ETOWNP>2.0.CO;2

Leroux, M.-D., Plu, M., Barbary, D., Roux, F. and Arbogast, P. 2013. Dynamical and physical processes leading to tropical cyclone intensification under upper-level trough forcing. *J. Atmos. Sci.* **70**, 2547–2565. doi:10.1175/JAS-D-12-0293.1

Liu, M., Vecchi, G. A., Smith, J. A. and Murakami, H. 2017. The present-day simulation and twenty-first-century projection of the climatology of extratropical transition in the North Atlantic. *J. Climate* **30**, 2739–2756. doi:10.1175/JCLI-D-16-0352.1

Milrad, S. M., Atallah, E. H. and Gyakum, J. R. 2009. Dynamical and precipitation structures of poleward-moving tropical cyclones in eastern Canada, 1979–2005. *Mon. Wea. Rev.* **137**, 836–851. doi:10.1175/2008MWR2578.1

Palmén, E. 1958. Vertical circulation and release of kinetic energy during the development of Hurricane Hazel into an extratropical storm. *Tellus* **10**, 1–23.

Räisänen, J. 1995. Factors affecting synoptic-scale vertical motions: a statistical study using a generalized omega equation. *Mon. Wea. Rev.* **123**, 2447–2460. doi:10.1175/1520-0493(1995)123<2447:FASSVM>2.0.CO;2

Räisänen, J. 1997. Height tendency diagnostics using a generalized omega equation, the vorticity equation, and a nonlinear balance equation. *Mon. Wea. Rev.* **125**, 1577–1597. doi:10.1175/1520-0493(1997)125<1577:HTDUAG>2.0.CO;2

Rantanen, M., Räisänen, J., Lento, J., Stepanyuk, O., Räty, O. and co-authors. 2017. OZO v. 1.0: software for solving a generalised omega equation and the Zwack–Okossi height tendency equation using WRF model output. *Geosci. Model Dev.* **10**, 827–841. doi:10.5194/gmd-10-827-2017

Reynolds, R. W., Smith, T. M., Liu, C., Chelton, D. B., Casey, K. S. and co-authors. 2007. Daily high-resolution-blended analyses for sea surface temperature. *J. Climate* **20**, 5473–5496. doi:10.1175/2007JCLI1824.1

Ritchie, E. A. and Elsberry, R. L. 2007. Simulations of the extratropical transition of tropical cyclones: phasing between the upper-level trough and tropical cyclones. *Mon. Wea. Rev.* **135**, 862–876. doi:10.1175/MWR3303.1

Rolfson, D. M. and Smith, P. J. 1996. A composite diagnosis of synoptic-scale extratropical cyclone development over the United States. *Mon. Wea. Rev.* **124**, 1084–1099. doi:10.1175/1520-0493(1996)124<1084:ACDOSS>2.0.CO;2

Seiler, C. 2019. A Climatological Assessment of Intense Extratropical Cyclones from the Potential Vorticity Perspective. *J. Climate* **32**, 2369–2380. doi:10.1175/JCLI-D-18-0461.1

Sekioka, M. 1956. A hypothesis on complex of tropical and extratropical cyclones for typhoon in the middle latitudes. *J. Meteorol. Soc.* **34**, 276–287. doi:10.2151/jmsj1923.34.5_276

Shapiro, M. A. and Keyser, D. 1990. Fronts, jet streams and the tropopause, in: *Extratropical Cyclones*. Springer, New York, pp. 167–191.

Sinclair, V. A. and Dacre, H. F. 2019. Which extra-tropical cyclones contribute most to the transport of moisture in the Southern Hemisphere? *J. Geophys. Res. Atmos.* **124**, 2525–2545. doi:10.1029/2018JD028766

Stepanyuk, O., Räisänen, J., Sinclair, V. A. and Järvinen, H. 2017. Factors affecting atmospheric vertical motions as analyzed with a generalized omega equation and the OpenIFS model. *Tellus A: Dynamic Meteorology and Oceanography* **69**, 1271563. doi:10.1080/16000870.2016.1271563

Stewart, S. R. 2018. *Tropical Cyclone Report: Hurricane Ophelia*, 9–15 October 2017, National Hurricane Center.

Thorncroft, C. and Jones, S. C. 2000. The extratropical transitions of Hurricanes Felix and Iris in 1995. *Mon. Wea. Rev.* **128**, 947–972. doi:10.1175/1520-0493(2000)128<0947:TETOHF>2.0.CO;2

Willison, J., Robinson, W. A. and Lackmann, G. M. 2013. The importance of resolving mesoscale latent heating in the North Atlantic storm track. *J. Atmos. Sci.* **70**, 2234–2250. doi:10.1175/JAS-D-12-0226.1

Yamaguchi, M., Ishida, J., Sato, H. and Nakagawa, M. 2017. WGNE intercomparison of tropical cyclone forecasts by operational NWP models: a quarter century and beyond. *Bull. Amer. Meteor. Soc.* **98**, 2337–2349. doi:10.1175/BAMS-D-16-0133.1

Zappa, G., Shaffrey, L. C. and Hodges, K. I. 2013. The ability of CMIP5 models to simulate North Atlantic extratropical cyclones. *J. Climate* **26**, 5379–5396. doi:10.1175/JCLI-D-12-00501.1

Weather Clim. Dynam., 1, 1–25, 2020
https://doi.org/10.5194/wcd-1-1-2020

Weather and Climate Dynamics
Open Access
EGU

The characteristics and structure of extra-tropical cyclones in a warmer climate

Victoria A. Sinclair, Mika Rantanen, Päivi Haapanala, Jouni Räisänen, and Heikki Järvinen

Institute for Atmospheric and Earth System Research/Physics, Faculty of Science,
P.O. Box 64, University of Helsinki, 00014 Helsinki, Finland

Correspondence: Victoria A. Sinclair (victoria.sinclair@helsinki.fi)

Received: 23 August 2019 – Discussion started: 27 August 2019
Revised: 6 November 2019 – Accepted: 22 November 2019 – Published: 3 January 2020

Abstract. Little is known about how the structure of extra-tropical cyclones will change in the future. In this study aqua-planet simulations are performed with a full-complexity atmospheric model. These experiments can be considered an intermediate step towards increasing knowledge of how, and why, extra-tropical cyclones respond to warming. A control simulation and a warm simulation in which the sea surface temperatures are increased uniformly by 4 K are run for 11 years. Extra-tropical cyclones are tracked, cyclone composites created, and the omega equation applied to assess causes of changes in vertical motion. Warming leads to a 3.3 % decrease in the number of extra-tropical cyclones, with no change to the median intensity or lifetime of extra-tropical cyclones but to a broadening of the intensity distribution resulting in both more stronger and more weaker storms. Composites of the strongest extra-tropical cyclones show that total column water vapour increases everywhere relative to the cyclone centre and that precipitation increases by up to 50 % with the 4 K warming. The spatial structure of the composite cyclone changes with warming: the 900–700 hPa layer averaged potential vorticity, 700 hPa ascent, and precipitation maximums associated with the warm front all move polewards and downstream, and the area of ascent expands in the downstream direction. Increases in ascent forced by diabatic heating and thermal advection are responsible for the displacement, whereas increases in ascent due to vorticity advection lead to the downstream expansion. Finally, maximum values of ascent due to vorticity advection and thermal advection weaken slightly with warming, whereas those attributed to diabatic heating increase. Thus, cyclones in warmer climates are more diabatically driven.

1 Introduction

Extra-tropical cyclones (also referred to as mid-latitude cyclones) are a fundamental part of the atmospheric circulation in the mid-latitudes due to their ability to transport large amounts of heat, moisture, and momentum. Climatologically, extra-tropical cyclones are responsible for most of the precipitation in the mid-latitudes, with over 70 % of precipitation in large parts of Europe and North America due to the passage of an extra-tropical cyclone (Hawcroft et al., 2012). Extra-tropical cyclones are also the primary cause of mid-latitude weather variability and can lead to strong winds. For example, a severe extra-tropical cyclone Kyrill moved over large parts of northern Europe in 2007, bringing strong winds that resulted in 43 deaths and USD 6.7 billion of insured damages (Fink et al., 2009). Intense extra-tropical cyclones can also be associated with heavy rain or snow, which can result in floods and travel disruption. Thus, given the large social and economic impacts that extra-tropical cyclones can cause, there is considerable research devoted to understanding the climatology and governing dynamics of these systems.

Many studies have investigated the spatial distribution and frequency of extra-tropical cyclones in the current climate by analysing reanalysis data sets (e.g. Simmonds and Keay, 2000; Hoskins and Hodges, 2002; Wernli and Schwierz,

2006) and consequently the location of the climatological mean storm tracks, in both hemispheres, in the current climate is well known. Climatologies of cyclone number and intensity in the current climate have also been created based on reanalysis data sets and numerous different objective cyclone tracking algorithms (Neu et al., 2013). Globally there is good agreement between methods for inter-annual variability of cyclone numbers and the shape of the cyclone intensity distribution but less agreement in terms of the total cyclone numbers, particularly in terms of weak cyclones.

The spatial structure of extra-tropical cyclones in the current climate has also been extensively examined (see Schultz et al., 2019, for an overview). The starting point was the development of the Norwegian cyclone model (Bjerknes, 1919), a conceptual framework describing the spatial and temporal evolution of an extra-tropical cyclone. As considerable variability was noted in cyclone structures, Shapiro and Keyser (1990) subsequently developed a sister conceptual model. In a different theme, Harrold (1973), Browning et al. (1973), and Carlson (1980) studied three-dimensional movement of airstreams within extra-tropical cyclones, thus developing the conveyor belt model of extra-tropical cyclones. This model incorporates warm and cold conveyor belts, which are now accepted and well-studied aspects of extra-tropical cyclones (e.g. Thorncroft et al., 1993; Wernli and Davies, 1997; Eckhardt et al., 2004; Binder et al., 2016). Recently, the structure of intense extra-tropical cyclones in reanalysis data sets has been examined in a quantitative manner by creating cyclone composites (e.g. Bengtsson et al., 2009; Catto et al., 2010; Dacre et al., 2012). Cyclone composites have also been created using satellite observations of cloud fraction and precipitation (Field and Wood, 2007; Naud et al., 2010; Govekar et al., 2014; Naud et al., 2018), which enables cyclone structure in both reanalysis and model simulations to be systematically evaluated. Thus, considerable knowledge now exists of the spatial structure, dynamics, and variability of the major precipitation-producing airstreams within extra-tropical cyclones.

A key question is then how the intensity, number, structure, and weather, for example precipitation, associated with extra-tropical cyclones will change in the future as the climate warms. To answer this question, projections from climate models can be analysed. However, how the circulation responds to warming, which includes the characteristics of extra-tropical cyclones, is notably less clear and more uncertain than the bulk, global mean thermodynamic response (Shepherd, 2014). Champion et al. (2011) investigated the impact of warming on extra-tropical cyclone properties with one global climate model by comparing historical (1980–2000) simulations to future (2080–2100) simulations forced by the IPCC A1B scenario. They found small, yet statistically significant, changes to the 850 hPa maximum vorticity, with the number of extreme cyclones increasing slightly in the future and the number of average-intensity cyclones decreasing. Zappa et al. (2013b) analysed output from 19 models that participated in Phase 5 of the Coupled Model Intercomparison Project (CMIP5) and compared 30-year periods of the historical (1976–2005) present-day simulations and the future climate simulations (2070–2099) forced by the Representative Concentration Pathway 4.5 (RCP4.5) and 8.5 (RCP8.5) scenarios. In the RCP4.5 scenario, Zappa et al. (2013b) found a 3.6 % reduction in the total number of extra-tropical cyclones in winter, a reduction in the number of extra-tropical cyclones associated with strong 850 hPa wind speeds, and an increase in cyclone-related precipitation. In addition, they also note that considerable variability in the response was found between different CMIP5 models. In a similar study, Chang et al. (2012) show that CMIP5 models predict a significant increase in the frequency of extreme extra-tropical cyclones during the winter in the Southern Hemisphere but a significant decrease in the most intense extra-tropical cyclones in winter in the Northern Hemisphere. A similar result was obtained by Michaelis et al. (2017), who used a mesoscale model to perform pseudo–global warming simulations over the North Atlantic where the initial and boundary condition temperatures were warmed to a degree consistent with predictions from climate models forced with RCP8.5. They find a reduction in the number of strong storms with warming and an increase in cyclone precipitation.

Models participating in CMIP5 have systematic biases in the location of the climatological storm tracks in historical simulations, particularly in the North Atlantic where the storm track tends to be either too zonal or displaced southward (Zappa et al., 2013a). In addition, the response of the storm track to warming has been found to be correlated to the characteristics of the storm track in historical simulations. Chang et al. (2012) show that in the Northern Hemisphere individual models with stronger storm tracks in historical simulations project weaker changes with warming compared to individual models with weaker historical storm tracks. Moreover, the same study shows that in the Southern Hemisphere individual models with large equatorward biases in storm track latitude predict larger poleward shifts with warming.

In order to increase confidence in climate model projections of the number and intensity of extra-tropical cyclones, there is a clear need to better understand the physical mechanisms causing changes to these weather systems. This is difficult to do based on climate model output alone as fully coupled climate models are very complex, include numerous feedbacks and non-linear interactions, and due to computational and data storage limitations offer somewhat limited model output fields with limited temporal frequency. Therefore in this study we undertake an idealized "climate change" experiment using a state-of-the-art model but configured as an aqua planet.

Idealized studies have been used extensively in the past to understand the dynamics of extra-tropical cyclones. For example, baroclinic wave simulations have been performed to understand the dynamics of extra-tropical cyclones and

fronts in the current climate (e.g. Simmons and Hoskins, 1978; Thorncroft et al., 1993; Schemm et al., 2013; Sinclair and Keyser, 2015). More recently baroclinic life cycle experiments have also been used to assess, in a highly controlled simulation environment, how the dynamics and structure of extra-tropical cyclones may respond to climate change. Given that diabatic processes, and in particular latent heating due to condensation of water vapour, play a large role in the evolution of extra-tropical cyclones (e.g. Stoelinga, 1996), many idealized studies have focused on how the intensity and structure of extra-tropical cyclones change as temperature and moisture content are varied (e.g Boutle et al., 2011; Booth et al., 2013, 2015; Kirshbaum et al., 2018). These studies show that when moisture is increased from low levels to values typical of today's climate, extra-tropical cyclones become more intense. This is a relatively robust result across many studies and can be understood to be a consequence of an induced low-level cyclonic vorticity anomaly beneath a localized maximum in diabatic heating (Hoskins et al., 1985). However, when temperatures and moisture content are increased to values higher than in the current climate, baroclinic life cycle experiments show divergent results. For example, Rantanen et al. (2019) found that uniform warming acts to decrease both the eddy kinetic energy and the minimum surface pressure of the cyclone, whereas Kirshbaum et al. (2018) showed that for large temperature increases with constant relative humidity the eddy kinetic energy decreases whereas the minimum surface pressure increases. Furthermore, Tierney et al. (2018) documented non-monotonic behaviour of the cyclone intensity in terms of both maximum eddy kinetic energy and minimum mean surface pressure with increasing temperature.

A disadvantage of baroclinic life cycle experiments is that often only one cyclone and its response to environmental changes are considered, whereas in reality there is considerable variability in the structure, intensity, size, and lifetime of extra-tropical cyclones. Recent baroclinic life cycle studies have suggested that the response of cyclones to warming in these types of simulations may depend on how the simulation is configured (Kirshbaum et al., 2018). An alternative, yet still idealized approach, is to perform multi-year aqua-planet simulations in which thousands of extra-tropical cyclones develop and can be analysed. A benefit of this approach compared to baroclinic life cycle experiments is that experimental set-up and initial conditions have a much weaker influence on the evolution of the model state and thus on the structure and size of the simulated extra-tropical cyclones. Pfahl et al. (2015) used a simplified general circulation model in an aqua-planet configuration with a slab ocean to assess how the intensity, size, deepening rates, lifetime, and spatial structure of extra-tropical cyclones respond when the longwave optical thickness is varied in such a way that the global mean near-surface air temperature varies from 270 to 316 K. Their main result was that changes in cyclone characteristics are relatively small except for the intensity of the strongest cyclones, which considerably increased in strength with warming. However, this study was based on an idealized general circulation model, which contained simplified physics parameterizations; for example, the large-scale microphysical parameterization only considers the vapour–liquid phase transition.

The first aim of this study is to determine how the number, intensity, and structure of extra-tropical cyclones change in response to horizontally uniform warming. The second aim is to identify the physical mechanisms which lead to changes in vertical motion and precipitation patterns associated with extra-tropical cyclones. These aims are addressed in an idealized modelling context as it is anticipated that mechanisms will be easier to identify than in complex, fully coupled climate model simulations. In particular, a full complexity atmospheric model is used to perform two aqua-planet simulations: a control simulation and an experiment where the sea surface temperatures are uniformly warmed. Extra-tropical cyclones are then tracked and cyclone centred composites are created. The omega equation is used to determine the forcing mechanisms for vertical motion at different locations relative to the cyclone centre and at different points in the cyclone life cycle for extra-tropical cyclones in both the control and warm experiments.

The remainder of this paper is set out as follows. In Sect. 2, the full-complexity numerical model, OpenIFS, which is used in this study, is described along with the numerical experiments that are performed. In Sect. 3, the cyclone tracking scheme and the omega equation diagnostic tool, which are applied to the model output to assist with analysis, are described. The results are presented in Sects. 4 to 7. The large-scale zonal mean state and its response to warming are given briefly in Sect. 4, and the results concerning changes to bulk cyclone statistics are discussed in Sect. 5. The results concerning changes to cyclone structure as ascertained from the cyclone composites are presented in Sect. 6 and the impact of warming on the asymmetry of vertical motion in extra-tropical cyclones is considered in Sect. 7. The conclusions are presented and discussed in Sect. 8.

2 OpenIFS and numerical simulations

2.1 Numerical model: OpenIFS

The numerical simulations are performed with OpenIFS, which is a portable version of the Integrated Forecast System (IFS) developed and used for operational forecasting at the European Centre for Medium Range Forecasting (ECMWF). Since 2013, OpenIFS has been available under license for use by academic and research institutions. The dynamical core and physical parameterizations in OpenIFS are identical to those in the full IFS as are the land surface model and wave model. However, unlike the full IFS, OpenIFS does not have any data assimilation capacity. The

version of OpenIFS used here (Cy40r1) was operational at ECMWF between November 2013 and May 2015. The full documentation of Cy40r1 is available online (ECMWF, 2015).

2.2 Experiments

Numerical simulations are performed with OpenIFS configured as an aqua planet. The surface of the Earth is therefore all ocean, and the sea surface temperatures (SSTs) are specified at the start of the simulation and held constant throughout the simulation. There is no ocean model included. However, the dynamics and physical parameterizations are exactly the same as in the full IFS and the wave model is also active in the aqua-planet simulations.

The control simulation (CNTL) is set up similarly to the experiments proposed by Neale and Hoskins (2000), and their QObs sea surface temperature distribution is used. This SST distribution is specified by a simple geometric function and is intended to resemble observed SSTs more so than the other distributions specified by Neale and Hoskins (2000). The resulting SST pattern is zonally uniform and symmetric about the Equator. The maximum SST is 27 °C in the tropics, and poleward of 60° N in both hemispheres the SSTs are set to 0 °C. There is no sea ice in the simulation. The atmospheric state is initialized from a randomly selected real analysis produced at ECMWF. First the real analysis is modified by changing the land–sea mask and setting the surface geopotential to zero everywhere. The atmospheric fields are then interpolated to the new flat surface in regions where there is topography on Earth. The perturbed experiment (hereinafter referred to as SST4) is identical to CNTL except that the SSTs are uniformly warmed by 4 K everywhere. Both experiments have a diurnal cycle in incoming solar radiation but no annual cycle; throughout the simulations the incoming solar radiation is fixed at the equinoctial value and is thus symmetric about the Equator.

Both aqua-planet simulations are run at T159 resolution (approximate grid spacing of 1.125° equivalent to 125 km) and with 60 model levels. The model top is located at 0.1 hPa. Both simulations are run for a total of 11 years and the first year of each simulation is discarded to ensure that the model has reached a balanced state. Analysis of global precipitation from the first year of simulation (not shown) reveals that a steady state is achieved after 3–4 months. Model output, including temperature tendencies from all physical parameterization schemes, is saved every 3 h.

3 Analysis methods

3.1 Cyclone tracking and compositing

In both numerical experiments, extra-tropical cyclones are tracked using an objective cyclone identification and tracking algorithm, TRACK (Hodges, 1994, 1995). Extra-tropical cyclones are identified as localized maxima in the 850 hPa relative vorticity truncated to T42 spectral resolution based on 6-hourly output from OpenIFS. All cyclones in the Northern Hemisphere are initially tracked; however to ensure that no tropical cyclones are included in the analysis, tracks which do not have at least one point north of 20° N are excluded. Furthermore, to ensure that only synoptic-scale, mobile systems are considered, it is required that a cyclone track last for at least 2 d and travel at least 1000 km. Finally cyclones which have a maximum vorticity of less than $1 \times 10^{-5}\,\mathrm{s}^{-1}$ are also excluded from the analysis. The output from TRACK consists of the longitude, latitude, and relative vorticity value of each point (every 6 h) along each individual extra-tropical cyclone track from which statistics such as genesis and lysis regions may be determined.

The cyclone tracks are then used as the basis to create composites of extra-tropical cyclones following the same method as Catto et al. (2010) and Dacre et al. (2012). Rather than creating a composite of all identified extra-tropical cyclones, only the 200 strongest cyclones in terms of their maximum 850 hPa relative vorticity are selected from the CNTL and SST4 experiments, and composites of a range of meteorological variables are created for these extreme cyclones at different offset times relative to the time of maximum intensity ($t = 0$ h). Each composite is created by first determining the values of the relevant meteorological variable, at each offset time, and for each individual cyclone to be included in the composite, on a spherical grid centred on the cyclone centre. The meteorological values are thus interpolated from the native model longitude–latitude grid to this spherical grid, which has a radius of 12° and is decomposed into 40 grid points in the radial direction and 360 grid points in the angular direction. To reduce smoothing errors, the cyclones are rotated so that all travel due east. To obtain the cyclone composite, the meteorological values on the radial grid are averaged at each offset time. Thus, the composite extra-tropical cyclone is the simple arithmetic mean of the 200 individual, rotated cyclones.

In addition to composites of the 200 strongest extra-tropical cyclones, composites of the 200 "most average" cyclones were also created for both the CNTL and SST4 experiments. These cyclones were identified as the 100 cyclones with maximum vorticity values lower than but closest to the median relative vorticity and the 100 cyclones with maximum vorticity values higher than but closest to the median relative vorticity. The results from these median composites are shown in the Supplement as although uniformly warming the SSTs led to increases in the total column water vapour and precipitation, it had little coherent impact on the spatial structure of the median extra-tropical cyclone.

3.2 Omega equation

The omega equation is a diagnostic equation from which the vertical motion (ω) resulting from different physical pro-

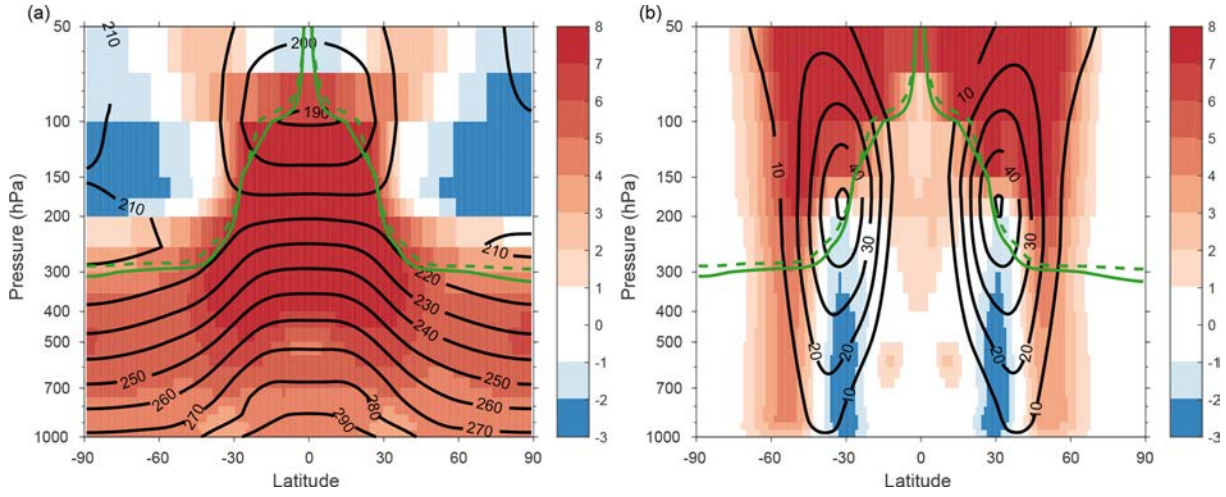

Figure 1. Zonal mean **(a)** temperature (K) and **(b)** zonal winds ($m\,s^{-1}$) averaged over 10 years of simulation. Black contours show the CNTL simulation and shading the difference between the SST4 and control simulations (SST4 − CNTL). The green solid line shows the dynamic tropopause (the 2 PVU surface) in CNTL and the dashed line in SST4.

cesses can be calculated. Different forms of the omega equation with differing degrees of complexity exist and range from the simplest "standard" quasi-geostrophic (QG) form with friction and diabatic heating neglected (Holton and Hakim, 2012) to the complex generalized omega equation (Räisänen, 1995; Rantanen et al., 2017). Here we solve the following version of the QG omega equation in pressure (p) coordinates:

$$\sigma_0(p)\nabla^2\omega + f^2\frac{\partial^2\omega}{\partial p^2} = f\frac{\partial}{\partial p}(\boldsymbol{v}\cdot\nabla(\zeta+f)) + \frac{R}{p}\nabla^2(\boldsymbol{v}\cdot\nabla T) - \frac{R}{c_p p}\nabla^2 Q. \quad (1)$$

The static stability parameter, σ_0, is only a function of pressure and time and is given by

$$\sigma_0(p) = \frac{-RT_0}{p}\frac{1}{\theta_0}\frac{\partial\theta_0}{\partial p}, \quad (2)$$

where $\theta_0(T_0)$ is the horizontally averaged potential temperature (temperature) profile over the global domain calculated at every time step. The left-hand side operator of Eq. (1) is identical to the standard QG omega equation. The terms on the right-hand side of Eq. (1) represent forcing for vertical motion due to differential vorticity advection, thermal advection, and diabatic heating. The right-hand side differs from the standard QG omega equation in that diabatic heating (Q) is retained, the advection terms are calculated using the full horizontal winds (v) rather than the geostrophic winds, and the full relative vorticity (ζ) is advected rather than the geostrophic vorticity. Friction is neglected as on an aqua planet this is expected to be small.

Overall good agreement is found between the model calculated vertical motion and the vertical motion diagnosed by Eq. (1). Correlation coefficients between the model calculated vertical motion and the diagnosed vertical motion were calculated at each grid box and pressure level and averaged over latitude bands (not shown). In the latitude band 30–60° N the correlation coefficients were 0.84 at 700 hPa and exceeded 0.9 at 500 hPa.

4 Climatology and large-scale response to warming

In this section the zonal mean climatology of CNTL is described along with the response to the uniform warming. Figure 1 shows that the control simulation produces a realistic distribution of temperature and of zonal winds. The dynamic tropopause varies from 300 hPa in the polar regions to about 100 hPa in the tropics, similar to what is observed on Earth. The zonal mean jet streams have maximum wind speeds of $45\,m\,s^{-1}$ and are located on the tropopause at 35° N/S. As expected from the aqua-planet model set-up the two hemispheres are almost symmetrically identical.

The response to the uniform 4 K warming is shown by the shading in Fig. 1. The temperature increases everywhere in the troposphere with the largest warming in the tropical upper troposphere, where temperature increases by up to 7 K. Cooling takes place in the polar stratosphere, which acts to increase the upper-level meridional temperature gradient. The tropopause height increases at most latitudes with warming. The spatial pattern of these changes in zonal mean temperature is similar to those found in more complex climate models (e.g. Fig. 12.12, Collins et al., 2013). However, the warming in the low to mid-troposphere is relatively uniform with latitude. The lack of enhanced warming in the Northern Hemisphere polar regions (polar amplification) and hence no decrease in low-level baroclinicity is the most notable differ-

ence in the atmosphere's response to warming in these aqua-planet experiments compared to in complex climate model simulations.

At low levels, the increase in temperature in the SST4 experiment relative to CNTL is typically of the order of 4 K, which is of similar magnitude to the enforced increase in SSTs. This temperature increase can be put into context by comparison with predictions from CMIP5 models. Under the RCP8.5 scenario, CMIP5 models predict that global mean near-surface temperatures will increase by 2.6 to 4.8 K by the end of the 21st century relative to the 1986–2005 mean. Hence, the aqua-planet simulations performed here have a degree of warming that could be expected to occur by the end of the 21st century under large greenhouse gas emissions.

The response of the zonal mean zonal wind shows that the subtropical jet intensifies and moves vertically upwards. The eddy-driven jet, evident at low levels, displays a dipole structure indicative of a poleward shift. This is confirmed when the latitude of the maximum 700 hPa zonal mean zonal wind speed is considered: this moves polewards by 3.3° in the SST4 experiment compared to in CNTL. These responses of the zonal mean jet streams to uniform warming are similar to those found in more complex climate models (e.g. Collins et al., 2013), particularly in the Southern Hemisphere, demonstrating that the OpenIFS aqua planet can realistically simulate an Earth-like atmosphere.

The zonal mean precipitation in both CNTL and SST4 experiments are shown in Fig. 2a. Again strong similarities exist with real Earth observations and CMIP5 model projections (e.g. Lau et al., 2013). The largest rainfall is observed in the tropics and a secondary peak occurs in the mid-latitudes, which is associated with the mid-latitude storm track. The effect of warming the SSTs is to increase the mean precipitation at almost all latitudes. The largest absolute increase occurs in the tropics. In the Northern Hemisphere mid-latitudes the maximum precipitation rate increases from 3.9 to 4.2 mm d^{-1} and the location of the maximum moves polewards by 2.2°. This is in agreement with the poleward shift in the eddy-driven jet and strongly suggests that, on average, extra-tropical cyclones move poleward with warming. This will be confirmed in Sect. 5.

Figure 2b shows the zonal mean mean sea level pressure (MSLP). The highest zonal mean MSLP in the CNTL experiment occurs in the subtropics and moves poleward with warming. The lowest values of MSLP occur on the poleward side of the jet stream and again move poleward with warming. A notable difference between these MSLP distributions and the MSLP distribution on Earth is the absolute magnitude of the values. The mean MSLP on Earth is 1013 hPa, whereas in both the CNTL and SST4 experiments, the global mean MSLP is 985.4 hPa. This difference is solely due to the initialization method (see Sect. 2.2), and the average surface pressure of 985.4 hPa results, as it is the average pressure at the actual surface height in the randomly selected analysis used for the initialization. Figure 2c shows the zonal

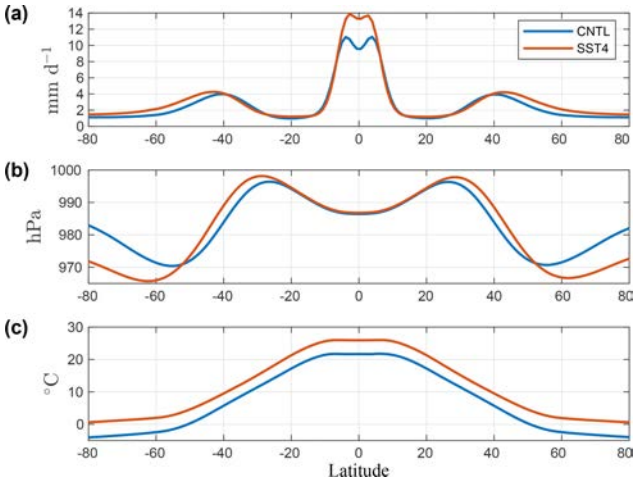

Figure 2. Zonal mean **(a)** total precipitation (mm d^{-1}), **(b)** mean sea level pressure (hPa), and **(c)** 950 hPa temperature (°C) averaged over 10 years of simulation. Blue line shows CNTL and red SST4.

mean 950 hPa temperature, which indicates that the low-level temperature increase is almost constant with latitude and implies that the low-level baroclinicity does not change.

The impact of uniformly warming the SSTs on the baroclinicity can be quantified via the maximum (dry) Eady growth rate, σ, which is given by

$$\sigma = 0.31 \frac{|f|}{N} \left| \frac{\partial u}{\partial z} \right|, \tag{3}$$

where f is the Coriolis parameter, N is the Brunt–Väisälä frequency, and u is the zonal wind component. In the CNTL simulation (Fig. 3a) the Eady growth rate has maximum values of 0.75 day^{-1} in the mid-latitude middle to upper troposphere. A secondary maximum is evident in the stratosphere; however, this most likely has little significance for the growth of extra-tropical cyclones. The response of the Eady growth rate to warming includes an increase just above the dynamical tropopause and a decrease co-located with the secondary maximum in the stratosphere. With the mid-troposphere, the Eady growth rate decreases slightly with warming; for example, at 700 hPa the maximum value decreases from 0.54 d^{-1} in CNTL to 0.50 d^{-1} in SST4. Close to the surface, at 900 hPa, the maximum value of the Eady growth rate also experiences a small decrease with warming, from 0.92 to 0.89 d^{-1}. The most notable impact of warming on the Eady growth rate at 900 hPa is a poleward shift of 5.4° in the position of the maximum. Equatorward of 45° N the 900 hPa Eady growth rate decreases with warming, whereas poleward of 45° N it increases.

Figure 3b and c show the vertical shear of the zonal wind and the Brunt–Väisälä frequency respectively. There is little change in the vertical wind shear with warming in the mid-troposphere, which via thermal wind balance is consistent with the lack of any large changes to the horizontal

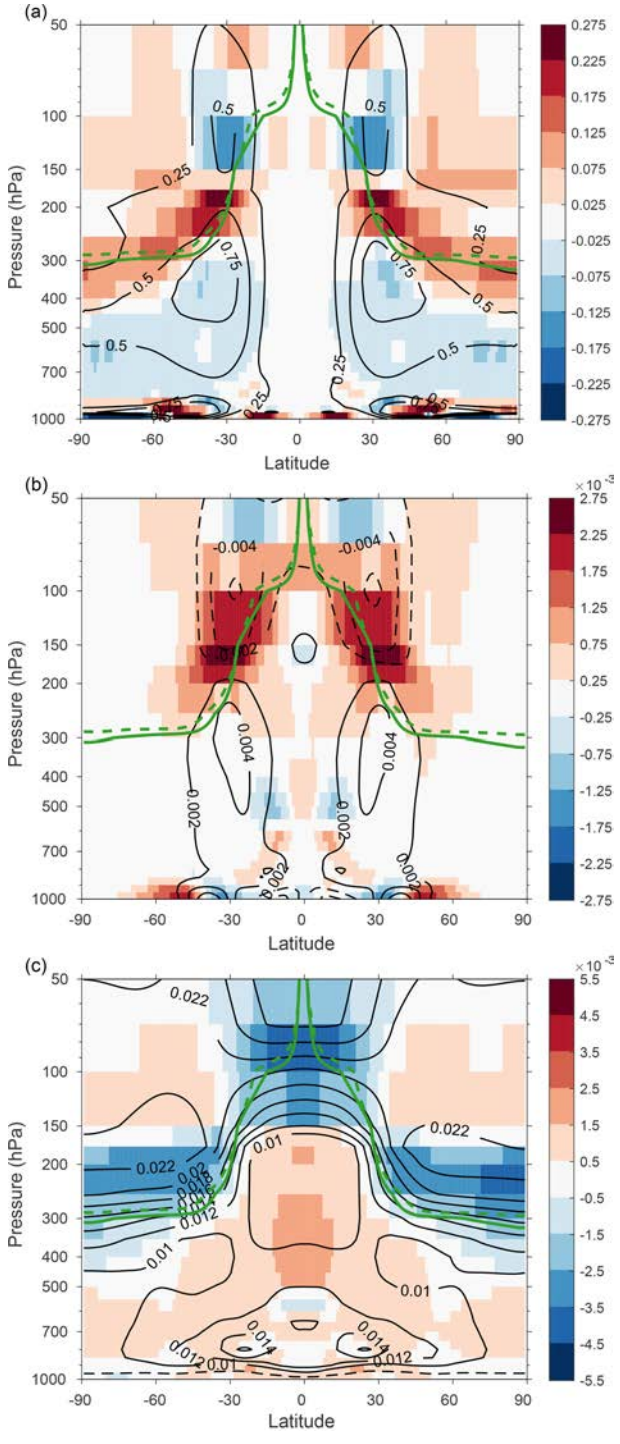

Figure 3. Zonal mean **(a)** maximum Eady growth rate (d^{-1}), **(b)** vertical shear of the zonal wind (s^{-1}), and **(c)** Brunt–Väisälä frequency (s^{-1}) averaged over 10 years of simulation. Black contours show the CNTL simulation, and shading shows the difference between the SST4 and control simulations (SST4 − CNTL). In **(c)** contours are every $0.002\,s^{-1}$ for values greater than $0.01\,s^{-1}$, and the dashed line shows the $0.005\,s^{-1}$ contour. The green solid line shows the dynamic tropopause (the 2 PVU surface) in CNTL and the green dashed line in SST4.

temperature gradient in the troposphere (Fig. 1a). Near the surface, there is a dipole pattern showing that the maximum in wind shear moves polewards. This is consistent with the poleward shift of the eddy-driven jet and also explains the poleward shift in the 900 hPa Eady growth rates. The Brunt–Väisälä frequency increases in the troposphere, which indicates that the decrease in the Eady growth rates at 700 hPa, and at lower latitudes higher up in the troposphere, is due primarily to changes in the static stability. Near the tropopause the decrease in the stability associated with an increase in the tropopause height increases the Eady growth rate. In contrast, the decrease in the secondary maximum in the stratosphere is due to changes in the vertical wind shear.

5 Cyclone statistics

In this section bulk cyclone statistics are presented from both the CNTL and SST4 simulations. All cyclone tracks that meet the criteria described in Sect. 3.1 are included in this analysis, and their mean and median characteristics are summarized in Table 1. In the control simulation there are 3581 extra-tropical cyclones which have a median lifetime of 108 h (4.5 d) and a median maximum vorticity of $5.94 \times 10^{-5}\,s^{-1}$ (Table 1). The uniform warming acts to decrease the total number of cyclone tracks by 3.3 % but does not alter the median duration (lifetime) of extra-tropical cyclones (Table 1). The inter-annual variability in the number of cyclone tracks, quantified by calculating the number of cyclone tracks each year and then obtaining the standard deviation of these 10 values, is small (13.5 in CNTL and 10.1 in SST4) relative to the absolute decrease in the number of cyclone tracks (119). This, and a two-sided Student's t test, shows that the decrease in the number of tracks is statistically significant.

Figure 4a shows histograms of maximum 850 hPa vorticity (also referred to hereinafter as maximum intensity). There are more stronger cyclones, for example with intensities exceeding $10 \times 10^{-5}\,s^{-1}$, in the SST4 experiment than in the CNTL experiment. However, the mean intensity does not change considerably and there is a 3.2 % decrease (equivalent to $0.19 \times 10^{-5}\,s^{-1}$) in the median maximum vorticity. This change (i.e. the signal) is very small compared to the variation between individual cyclones quantified by the standard deviation of the maximum relative vorticity of all storms ($2.55 \times 10^{-5}\,s^{-1}$ in CNTL). Furthermore, the mean maximum vorticity for all cyclones occurring in each individual year can be obtained and the standard deviation of these 10 values calculated to obtain the inter-annual standard deviation of the maximum relative vorticity. For CNTL this is 0.14×10^{-5} and $0.10 \times 10^{-5}\,s^{-1}$ in SST4, which are both larger than the absolute change in the mean maximum relative vorticity ($-0.04 \times 10^{-5}\,s^{-1}$, Table 1). A two-sided Student's t test further confirms that the mean intensity does not differ in a statistically significant way between CNTL

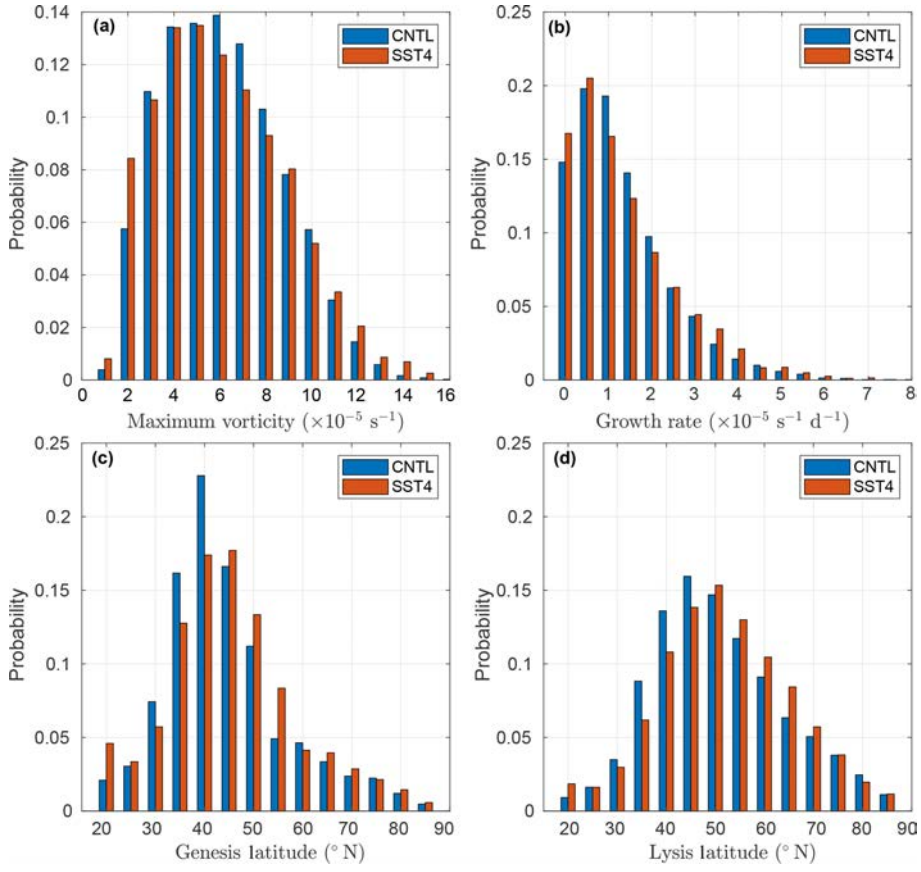

Figure 4. Normalized histograms of the extra-tropical cyclone's **(a)** maximum 850 hPa relative vorticity, **(b)** average deepening rate between time of genesis and time of maximum vorticity, **(c)** genesis latitude, and **(d)** lysis latitude. Blue shows CNTL and red shows SST4.

and SST4, and a Wilcoxon rank-sum test shows that the median maximum intensities are not statistically significantly different between the CNTL and SST4 experiments. However, as evident from Fig. 4a, and confirmed by a one-tailed F test applied to the maximum vorticity distributions, the maximum vorticity distribution in the SST4 experiment has a larger variance than in the CNTL experiment. Thus, it can be concluded that the average population of all cyclones does not change with warming but that there are more stronger and more weak cyclones in the SST4 experiment than in CNTL.

Table 1 also includes the median deepening rates of all extra-tropical cyclones. The deepening rate is the temporal rate of change of the 850 hPa relative vorticity so that positive values indicate a strengthening, or deepening, of the extra-tropical cyclone. In CNTL, the relative vorticity increases by $1.31 \times 10^{-5}\,\mathrm{s}^{-1}$ every 24 h when evaluated from genesis time to time of maximum intensity. In SST4, the corresponding value is $1.28 \times 10^{-5}\,\mathrm{s}^{-1}$ per 24 h. The change is very small in comparison to the standard deviation of the deepening rates (Table 1). Distributions of the deepening rates of all identified extra-tropical cyclones calculated between the time of genesis and time of maximum intensity are shown in Fig. 4b. A rank-sum test performed on the deepening rates between the time of genesis and time of maximum intensity confirms that the median values are not statistically different. The same test applied to the deepening rates calculated over the 24 h before the time of maximum intensity also shows that the control and SST4 experiments do not differ significantly. However, similar to what is found with the maximum vorticity distributions, the variance of the deepening rates is statistically significantly larger in the SST4 experiment compared to in CNTL. The lack of any notable change in the median deepening rate of all extra-tropical cyclones differs somewhat from the zonal mean calculations of the Eady growth rate (Fig. 3a), which indicate a 5 %–10 % decrease. This difference likely arises because the Eady growth rate is a measure of dry baroclinicity whereas moist processes are acting in these simulations.

Distributions of the genesis and lysis latitudes for all extra-tropical cyclones are shown in Fig. 4c and d. As hypothesized in Sect. 4, both genesis and lysis regions move poleward with warming. The median genesis region moves 2° polewards from 44.2 to 46.2° N, and the median lysis region moves poleward by 1.9° from 51.4 to 53.3° N (Table 1). The interannual standard deviation of the genesis latitude is 0.27° in CNTL and 0.69° in SST4, suggesting that the 2° poleward

Table 1. Cyclone statistics from CNTL and SST4. Relative vorticity values have units of $\times 10^{-5}\,s^{-1}$. Duration (lifetime) is given in units of hours. Deepening rates (units of $\times 10^{-5}\,s^{-1}\,(24\,h)^{-1}$) are the temporal rate of change of the 850 hPa relative vorticity. Positive deepening rate values indicate a strengthening, or deepening, of the extra-tropical cyclone. For vorticity, duration, and deepening rates, change is the relative change ((SST4 − CNTL)/CNTL) given as a percentage. For genesis and lysis latitude, change is the absolute change.

	All cyclones			Strongest 200 cyclones		
Diagnostic	CNTL	SST4	Change	CNTL	SST4	Change
Number of tracks/cyclones	3581	3462	−3.3 %	200	200	0 %
Mean maximum 850 hPa vorticity	6.11	6.07	−0.7 %	11.55	11.87	+2.8 %
Median maximum 850 hPa vorticity	5.94	5.75	−3.2 %	11.24	11.56	+2.8 %
Standard deviation of maximum 850 hPa vorticity	2.55	2.80	+9.8 %	1.00	1.22	+22 %
Mean track duration	132.3	127.8	−3.4 %	209.7	190.8	−9.9 %
Median track duration	108.0	108.1	0 %	192.0	180.0	−6.25 %
Standard deviation of track duration	77.3	73.5	−4.9 %	83.0	83.2	+0.24 %
Median deepening rate (genesis to $t = 0$ h)	1.31	1.28	−2.3 %	2.63	3.36	+27.7 %
Standard deviation of deepening rate (genesis to $t = 0$ h)	1.13	1.25	+10.6 %	1.43	1.65	+15.4 %
Median deepening rate (−24 h to $t = 0$ h)	1.42	1.43	+0.7 %	3.57	4.41	+23.5 %
Standard deviation of deepening rate (−24 h to $t = 0$ h)	1.25	1.42	+13.6 %	1.53	1.75	+14.37 %
Median genesis latitude	44.2° N	46.2° N	+2.0°	37.8° N	38.2° N	+0.4°
Median lysis latitude	51.4° N	53.3° N	+1.9°	51.2° N	55.0° N	+3.8°
Standard deviation of genesis latitude	12.8°	13.7°	+0.9°	8.6°	8.9°	+0.3°
Standard deviation of lysis latitude	13.8°	14.7°	+0.9°	11.3°	11.0°	−0.3°
Median dlat (lysis–genesis latitude)	6.2°	6.0°	−0.2°	13.7°	16.7°	+3.0°
Median dlat (max vort lat–genesis latitude)	2.9°	2.9°	0°	9.0°	9.3°	+0.3°
850 hPa relative vorticity threshold for strongest 200 cyclones	–	–	–	10.44	10.88	+4.2 %
Vorticity of the strongest cyclone	–	–	–	15.55	16.80	+8.1 %
Maximum deepening (genesis to time of max)	–	–	–	7.05	9.10	+29.0 %

shift in genesis latitude is significant. Likewise, the inter-annual standard deviation of the lysis latitude is 0.52 and 0.72° in CNTL and SST4 respectively and therefore also smaller than the response to warming. Two-sided Student's t tests show that the mean genesis latitude differs between the CNTL and SST4 experiments at the 95 % confidence level and that both the median genesis and lysis latitudes differ significantly at the 0.05 significance level. The standard deviation of both the genesis latitude (12.8° in CNTL, Table 1) and lysis latitude (13.7° in CNTL, Table 1) of all cyclones is larger than the mean change in genesis and lysis latitudes, indicating that the change is small compared to the variation between individual cyclones.

Table 1 also includes statistics for the strongest 200 extra-tropical cyclones in each experiment as the structure of these intense extra-tropical cyclones will be investigated in detail in Sect. 6. Firstly, the median genesis latitudes of the strongest extra-tropical cyclones are 6 to 8° farther equatorward than for all extra-tropical cyclones in both the CNTL and SST4 experiments, which means that the strongest storms form in climatologically warmer and more moist environments than average-intensity storms. The more equatorward genesis region, combined with similar (CNTL) or more poleward (SST4) lysis regions, means that the strongest extra-tropical cyclones have much larger latitudinal displacements than extra-tropical cyclones do on average. Secondly, the median genesis latitude of the 200 strongest extra-tropical cyclones only moves 0.4° poleward with warming, which is notably less than the 2.0° poleward shift found when all extra-tropical cyclones are considered. Thirdly, deepening rates increase much more with warming for the strongest 200 extra-tropical cyclones than for all extra-tropical cyclones. Finally, the mean, median, and maximum intensity of the 200 strongest extra-tropical cyclones in the SST4 experiment are larger than in the CNTL experiment.

6 Cyclone structure

6.1 Evolution of the composite cyclone in CNTL

The cyclone composite of the strongest 200 extra-tropical cyclones in the CNTL experiment is now discussed. The temporal evolution of the composite mean cyclone in the CNTL simulation, in terms of mean sea level pressure and total column water vapour (TCWV) is shown in Fig. 5. A total of 48 h before the time of maximum intensity ($t = -48$ h, Fig. 5a) the composite cyclone has a closed low-pressure centre with a minimum MSLP of 978 hPa. The location of the cold and warm fronts is evident as enhanced gradients in the TCWV and the warm sector, located between the cold front and warm front, are well defined and have values of

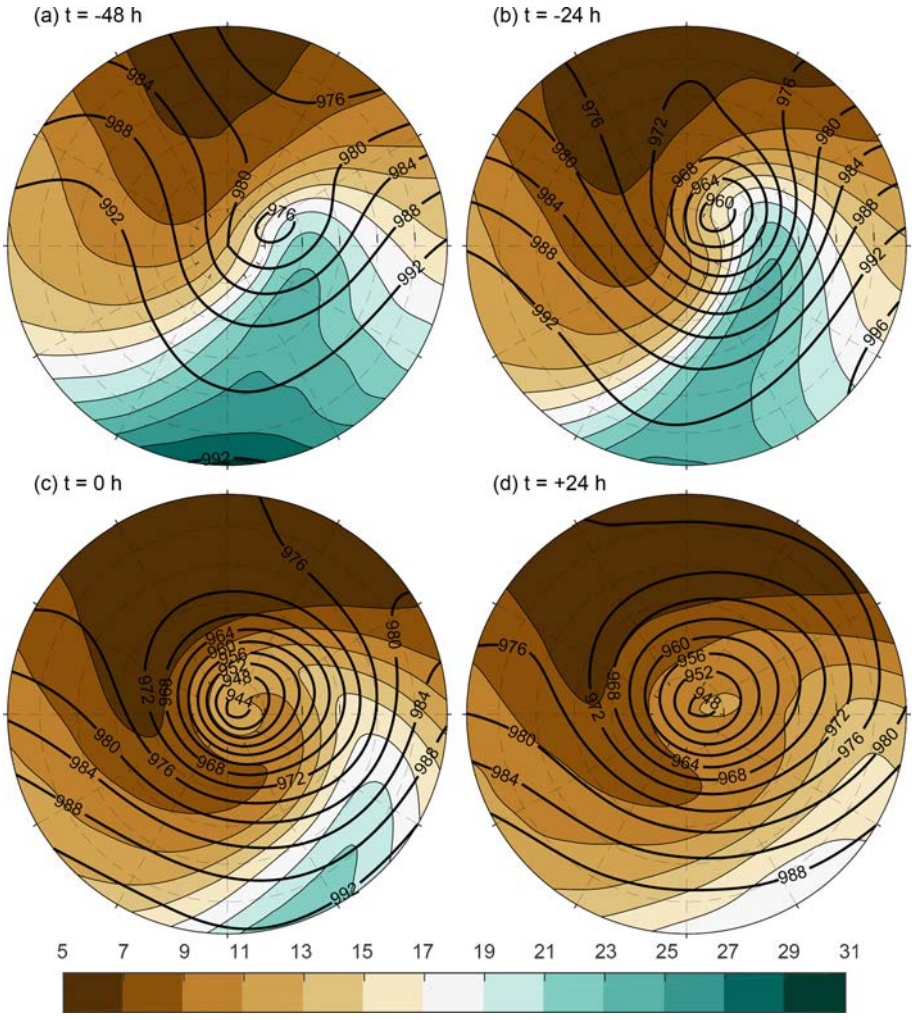

Figure 5. Composite cyclone of the strongest 200 extra-tropical cyclones in the CNTL simulation at **(a)** 48 h before time of maximum vorticity, **(b)** 24 h before time of maximum vorticity, **(c)** time of maximum vorticity, and **(d)** 24 h after the time of maximum vorticity. Shading shows the total column water vapour (g kg^{-1}), and black contours show the mean sea level pressure (hPa). The plotted radius is 12°.

TCWV exceeding 25 g kg^{-1}. At 24 h before the time of maximum intensity ($t = -24$ h, Fig. 5b) the low-pressure centre has become deeper (minimum MSLP of 960 hPa), the warm sector has become narrow and the gradients in TCWV across both the warm and cold fronts have become larger. The dry air moving cyclonically behind the cold front now extends farther south relative to the cyclone centre than it did 24 h earlier. By the time of maximum relative vorticity ($t = 0$ h, Fig. 5c), the MSLP shows a mature, very deep cyclone which has a minimum pressure of 944 hPa. The TCWV over the whole cyclone composite area is now considerably lower than at earlier stages most likely because as the cyclones included in the composite intensify they move poleward to climatologically drier areas. The TCWV pattern also shows that the composite cyclone starts to occlude by this point ($t = 0$ h) as the warm sector does not connect directly to the centre of the cyclone – instead it is displaced downstream. Finally 24 h after the time of maximum intensity ($t = +24$ h, Fig. 5d), the cyclone resembles a barotropic low and has weak frontal gradients associated with it. The evolution of the composite cyclone in the CNTL experiment is, however, qualitatively very similar to real extra-tropical cyclones observed on Earth.

6.2 Low-level potential and relative vorticity

The response of the cyclone structure to warming is now considered primarily using changes to the mean values (i.e. SST4 − CNTL). First the temporal evolution of the low-level potential vorticity (PV) and the changes to this variable with warming are considered (Fig. 6). Before the composite cyclone reaches it maximum intensity (Fig. 6a and b), the maximum in the 900–700 hPa layer-averaged PV in the control simulation is poleward and downstream of the cyclone centre. By the time of maximum intensity (Fig. 6c), the maximum PV is co-located with the cyclone centre and there is

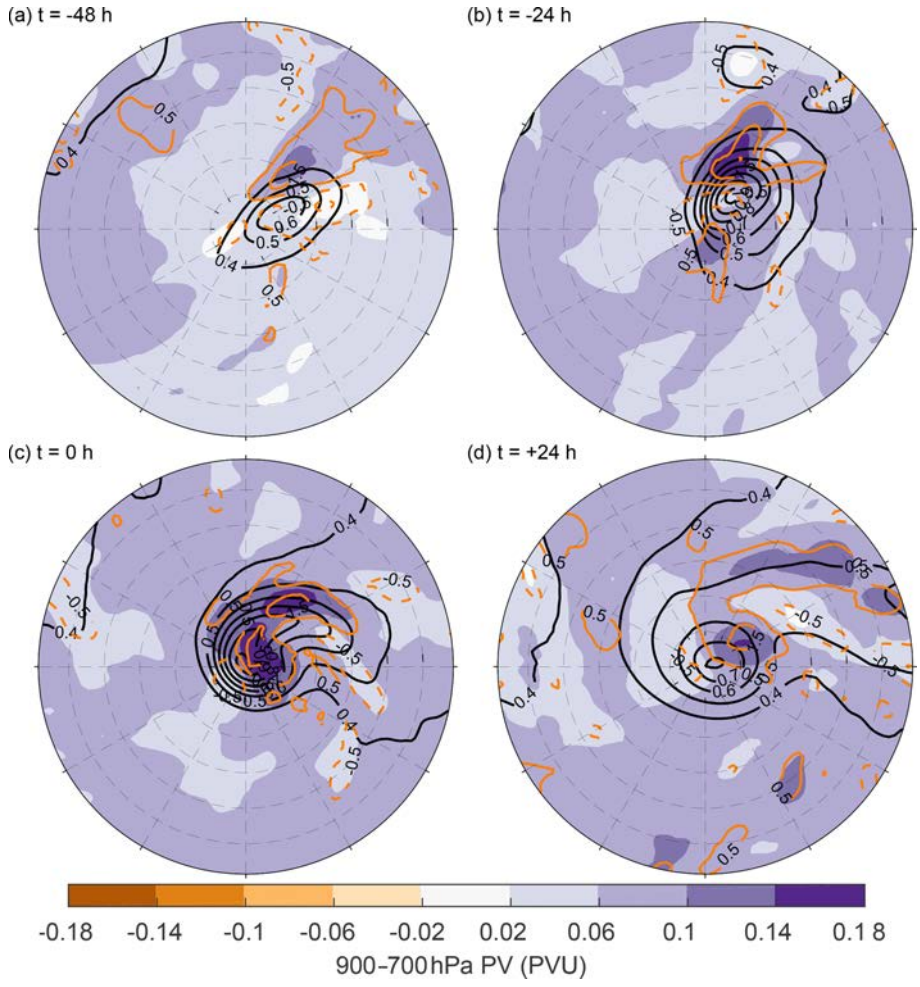

Figure 6. Composite mean of the strongest 200 extra-tropical cyclones at **(a)** 48 h before time of maximum vorticity, **(b)** 24 h before time of maximum vorticity, **(c)** time of maximum vorticity, and **(d)** 24 h after the time of maximum vorticity. Black contours show the 900–700 hPa layer mean potential vorticity in CNTL (contour interval 0.1 PVU, starting at 0.4 PVU). Shading shows the difference in the 900–700 hPa layer mean potential vorticity between SST4 and CNTL. Orange contours show the difference in the 850 hPa relative vorticity between SST4 and CNTL (contour interval 0.5×10^{-5} s^{-1}, the 0 contour is omitted). Solid orange contours show positive differences and dashed contours negative differences.

a secondary maximum which extends downstream of the cyclone centre and is co-located with the warm front.

At $t = -48$ and $t = -24$ h, the largest absolute increases in the 900–700 hPa PV occur poleward of the warm front location (Fig. 6a and b). This low-level PV anomaly is primarily caused by a diabatic heating maximum above this layer and therefore the poleward movement of the maximum indicates that the maximum in diabatic heating has also moved polewards with warming. The increase in PV is co-located with an increase in relative vorticity (orange contours in Fig. 6), which is consistent with an intensified cyclonic circulation beneath a region of localized heating. It can therefore be concluded that the relative vorticity associated the warm front increases with warming. At $t = 0$ and $t = +24$ h (Fig. 6c and d), two distinct regions of increased low-level PV are evident. The first is poleward of the warm front, as found at the earlier stages of development, and the second is almost co-located with the cyclone centre yet displaced slightly downstream. Both localized increases in low-level PV are also associated with increases in relative vorticity. In relative terms (not shown) the low-level potential vorticity poleward of the warm front increases by 25 %–30 %, whereas near the cyclone centre the low-level PV only increases by 15 %–20 %.

The response to warming also shows that almost everywhere within a 12° radius of the cyclone centre, at all offset times, there is an increase in low-level PV. The absolute values of increase are smaller, mostly less than 0.1 PVU, but in relative terms the increase is similar in magnitude to that found near the warm front and cyclone centre. Away from the cyclone centre, where there is no significant relative vorticity, this increase in low-level PV is primarily caused by an

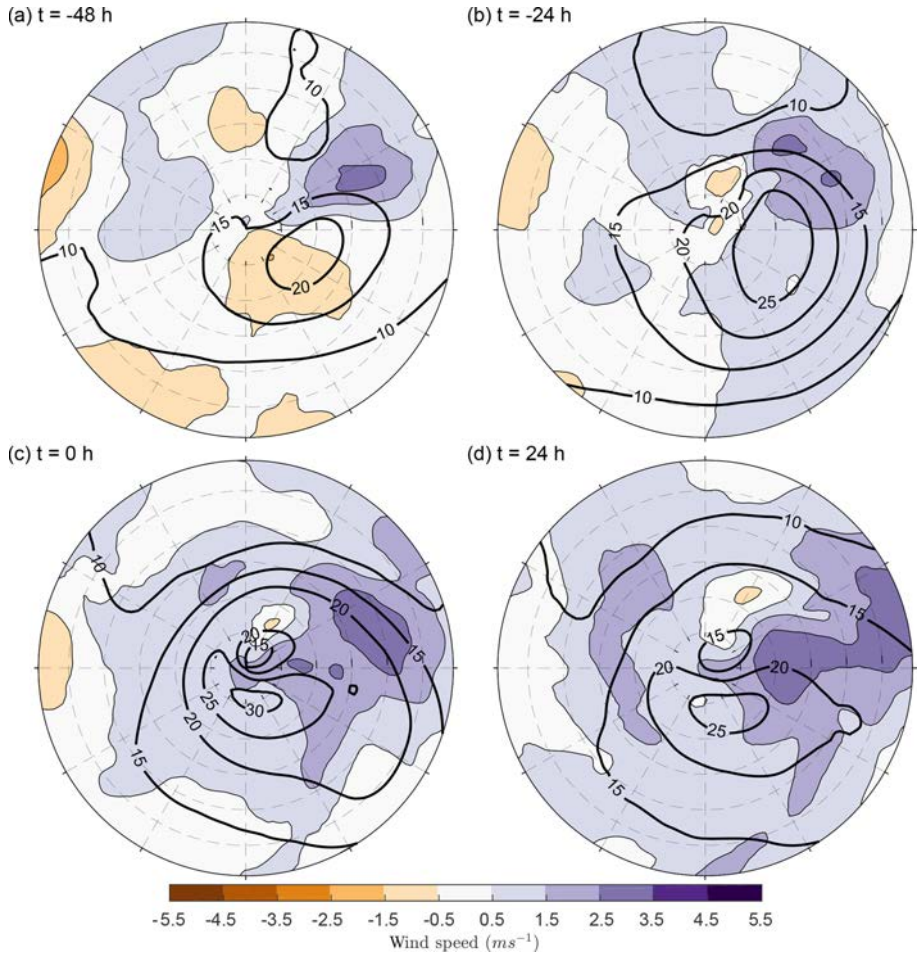

Figure 7. Composite mean of the 900 hPa wind speed of the strongest 200 extra-tropical cyclones in the CNTL simulation (black contours, every 5 m s^{-1}) and the difference between SST4 and CNTL (shading) at **(a)** 48 h before time of maximum intensity, **(b)** 24 h before time of maximum intensity, **(c)** time of maximum intensity, and **(d)** 24 h after the time of maximum intensity.

increase in stratification. However, given that the cyclones are more poleward in the SST4 experiment, the increase in planetary vorticity also plays a small role.

6.3 Low-level wind speed

Figure 6 highlights that the relative vorticity increases with warming at all offset times. Associated with this increase in relative vorticity is an increase in low-level horizontal wind speeds. In the composite from the CNTL experiment, at $t = -48$ and $t = -24$ h (Fig. 7a and b), the strongest 900 hPa wind speeds exceed 20 and 25 m s^{-1} respectively and occur in the warm sector. At the time of maximum intensity (Fig. 7c), the strongest 900 hPa winds in CNTL are located equatorward of the cyclone centre, behind the cold front in a very dry area, and exceed 30 m s^{-1}. By $t = 24$ h (Fig. 7d) the wind speeds have started to weaken. At $t = -48$ h, a dipole structure in the change in wind speed due to warming is evident, indicating that the maximum wind speeds move poleward and downstream relative to those in CNTL (Fig. 7a). However, the positive values are greater in magnitude than the negative values, thus indicating an overall increase in wind speed. At $t = -24$, 0, and 24 h (Fig. 7b–d) the 900 hPa winds speeds of the composite cyclone increase with warming by ~ 1.5 m s^{-1} in a large area surrounding the cyclone and by up to 3.5 m s^{-1} in the warm front area. Consequently, the size of the area affected by wind speeds over a fixed threshold value increases, indicating greater wind risk in warmer climates. As the increase at all offset times is not co-located with maximum wind speed in CNTL, this suggests that the spatial structure of the composite extra-tropical cyclone changes with warming.

6.4 Total column water vapour

The response of the TCWV is now considered (Fig. 8). The uniform warming leads to an increase in TCWV everywhere in the cyclone composite at all offset times. The largest absolute increases occur at $t = -48$ and $t = -24$ h (Fig. 8a and b). At both of these offset times, the largest absolute in-

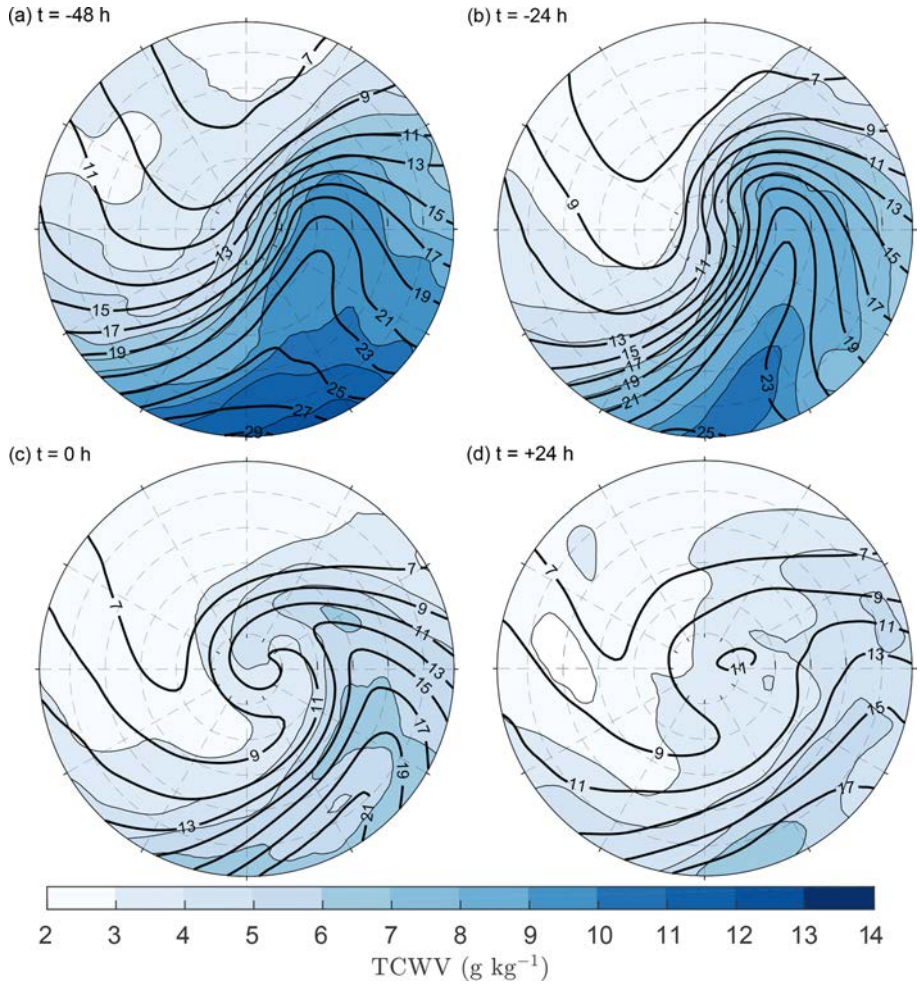

Figure 8. Composite mean of the total column water vapour (TCWV) of the strongest 200 extra-tropical cyclones in the CNTL simulation (black contours, every 2 g kg^{-1}) and the difference between SST4 and CNTL (shading) at **(a)** 48 h before time of maximum intensity, **(b)** 24 h before time of maximum intensity, **(c)** time of maximum intensity, and **(d)** 24 h after the time of maximum intensity.

crease occurs in the warm sector where the mean values are largest in the control simulation. In terms of percentage increase (not shown), at $t = -24$ h, the TCWV increases the least, approximately 25 %, in the cold sector upstream of the cyclone centre and the most ahead of the warm front where the increase exceeds 50 %. At the time of maximum intensity (Fig. 8c), absolute increases of up to 6 g kg^{-1} are still evident in the warm sector and in a localized region northeast of the cyclone centre, whereas at $t = +24$ h (Fig. 8d) increases of this magnitude are constrained to the most southern part of the cyclone composite. The composites also show the meridional moisture gradient across the composite cyclone increases notably with warming since the absolute increase is much larger in the most equatorward regions (e.g. 12 g kg^{-1} at $t = -48$ h) than in the most poleward regions (e.g. an increase of 2 g kg^{-1}).

6.5 Precipitation

The response of the total, convective, and large-scale precipitation to warming is now considered. Composites of total, large-scale, and convective precipitation are shown in Fig. 9 valid 48, 24, and 0 h before the time of maximum intensity. Precipitation is calculated as the 6 h accumulated value centred on the valid time in units of millimetres per 6 h. In the CNTL simulation the maximum total precipitation is downstream and poleward of the cyclone centre at all offset times. At $t = -48$ h, the total precipitation has maximum values of 6 mm (6 h)$^{-1}$ and is mainly located in the warm sector of the cyclone and near the warm front (Fig. 9a). At $t = -24$ h, the total precipitation in the CNTL simulation is slightly larger, covers a greater area, and has a more distinct comma shape than 24 h earlier (Fig. 9d). Also at this time, large values of total precipitation are evident along the cold front to the south of the cyclone centre. By the time of maximum intensity the total precipitation in the CNTL experiment has started to de-

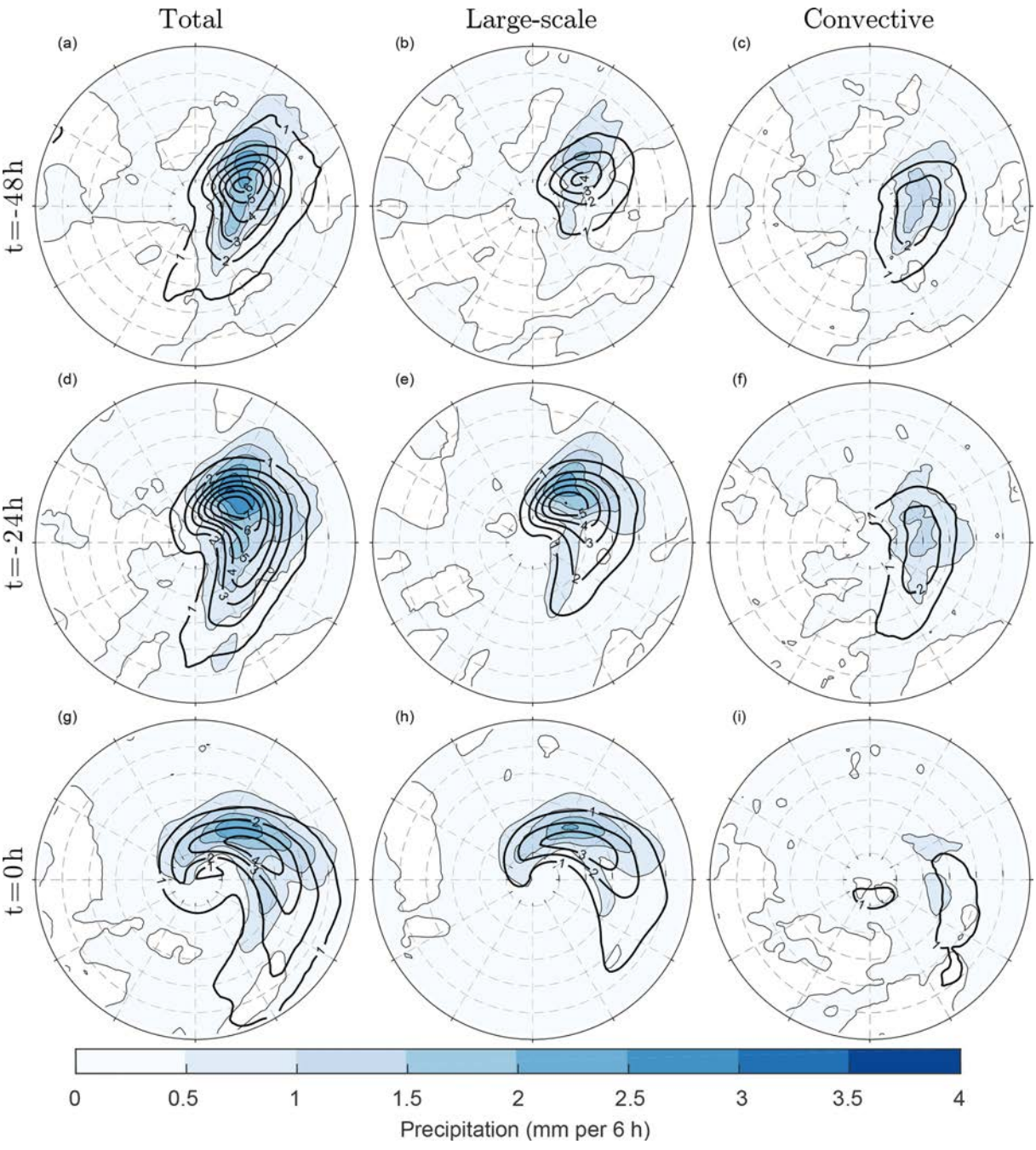

Figure 9. Composites of total precipitation **(a, d, g)**, large-scale precipitation **(b, e, h)**, and convective precipitation **(c, f, i)** in the CNTL simulation (black contours) and the difference between SST4 and control (shading). Panels **(a)–(c)** are valid 48 h before the time of maximum intensity, panels **(d)–(f)** are valid 24 h before the time of maximum intensity, and panels **(g)–(i)** are valid at the time of maximum intensity. All composites are of the strongest 200 extra-tropical cyclones in each experiment.

crease, with maximum values of $4\,\mathrm{mm}\,(6\,\mathrm{h})^{-1}$, and the location of the precipitation has rotated cyclonically around the cyclone centre (Fig. 9g).

The response to warming of the total precipitation is a large absolute and relative increase at all offset times. The maximum absolute increases are of the order of 2.5, 3.5, and $2.0\,\mathrm{mm}\,(6\,\mathrm{h})^{-1}$ at $t = -48$, $t = -24\,\mathrm{h}$, and the time of maximum vorticity ($t = 0\,\mathrm{h}$) respectively. These values correspond to relative increases of up to almost 50 %. The maximum increase in the total precipitation is not co-located with the maximum in the CNTL simulation, indicating that the spatial structure of the composite cyclone has changed with

warming. The largest increases in total precipitation occur in the warm front region, poleward and downstream of the maximum in the CNTL simulation at all offset times. This spatial change is largely similar to that found when the 900–700 hPa potential vorticity response to warming was considered (Fig. 6). This is consistent in the sense that more precipitation, and particularly more condensation, results in more latent heating and thus a stronger positive PV anomaly beneath the localized heating. However at $t = 0$ h, it is interesting to note that while there is only one localized area where precipitation increases in SST4 compared to in CNTL (Fig. 9g), which is ahead of the warm front, there are two regions where the low-level PV increases (Fig. 6c). One of these regions is co-located with the increase in precipitation but the second region is closer to the cyclone centre. While this may be due to the larger mean relative vorticity of the strongest 200 cyclones in SST4 compared to CNTL (Table 1), it is also possible that this second area of enhanced PV may be due to enhanced advection by the cold conveyor belt of PV produced diabatically in the warm front region, beneath the ascending warm conveyor belt. Schemm and Wernli (2014) noted such a mechanism in their study linking warm and cold conveyor belts.

The contribution of the large-scale stratiform precipitation calculated from the cloud scheme and the convective precipitation produced by the convection scheme to the total precipitation is now considered. In CNTL, the large-scale precipitation (Fig. 9b, e, and h) contributes more to the total precipitation than the convective precipitation (Fig. 9c, f, and i), particularly at $t = -24$ h and the time of maximum intensity. However, the convective precipitation is larger and of equal magnitude to the large-scale precipitation in the more equatorward parts of the warm sector of the CNTL composite cyclone where the temperature and moisture content are higher. The large-scale precipitation increases in SST4 compared to CNTL in the warm frontal region, poleward of the maximum in the CNTL simulation, at all offset times. This spatial shift is very similar to that observed for the total precipitation, meaning that the resolved precipitation is leading to the poleward shift in the total precipitation with warming. However, the large-scale precipitation also has a smaller increase (1–1.5 mm per 6 h) in a narrow band along the cold front, upstream of the maximum in the control simulation, which is most evident at $t = -24$ h. In contrast, the convective precipitation, which increases by almost 50 %, has the largest increases co-located with the maximum in the control simulation, meaning that the position of convective precipitation relative to the cyclone centre does not change with warming.

6.6 Vertical velocity

The mean cyclone composite of vertical velocity at 700 hPa (given in pressure coordinates, Pa s^{-1}) obtained directly from the model simulations and the response to warming is shown in Fig. 10a, c, and e. In the CNTL simulation at $t = -48$ and $t = -24$ h, there is large coherent area of ascent downstream of the cyclone centre largely co-located with the warm sector indicative of the warm conveyor belt, an ascending airstream associated with extra-tropical cyclones. At $t = 0$ h (Fig. 10e), the area of ascent is still maximized in the warm sector region but is further downstream relative to the cyclone centre than at earlier times. The ascent at $t = 0$ h has also started to wrap cyclonically around the poleward and upstream side of the cyclone, meaning that the cyclone has formed a bent-back warm front and likely has started to occlude. The absolute magnitude of the largest values of ascent occur at $t = -24$ h and exceed 0.6 Pa s^{-1} (Fig. 10c), approximately 6 cm s^{-1}. A region of weak descent is evident behind the cold front in the drier air mass at all offset times.

Uniform warming changes the vertical motion in a complex manner. The largest increases in ascent are not co-located with the strongest ascent in the CNTL simulation and instead occur poleward and downstream of the maximum. This pattern is present at all offset times and suggests that the warm front and the warm conveyor belt are located farther poleward relative to the cyclone centre in the SST4 simulation. This is consistent with the response of the total and large-scale precipitation, and the low-level potential vorticity, which also showed a poleward shift in the warm frontal region. A tri-pole structure is also evident in Fig. 10a, c, and e, which show that the area of ascent either weakens in the centre and broadens with warming or the ascent associated with the warm and cold fronts becomes more spatially separate with warming. The first of these two options will prove to be correct.

To further understand the spatial pattern of the response of the vertical velocity to warming, the contribution to the total vertical velocity from vorticity advection, thermal advection, and diabatic processes as diagnosed by the omega equation (Eq. 1) is examined. The sum of these three terms (Fig. 10b, d, and f) at 700 hPa is first compared to the total model calculated vertical motion (Fig. 10a, c, and e). At $t = -48$ h, the diagnosed ascent in CNTL is slightly weaker than the model-calculated (i.e. direct from OpenIFS) ascent, particularly in the cold front region. The response of the diagnosed vertical motion to warming is however spatially similar to that of the model-calculated vertical motion. At $t = -24$ h, the diagnosed ascent is slightly stronger than the model-calculated ascent and covers a larger area, especially in the zonal direction. In addition, the descent diagnosed from Eq. (1) covers a smaller area than descent in the model-calculated vertical motion field. Similar differences between the model-calculated and diagnosed vertical motion occur at $t = 0$ h. There is, however, broad agreement between the model-calculated vertical motion and the vertical motion diagnosed using Eq. (1) in CNTL at all offset times, and the response to warming in the diagnosed vertical motion field is very similar to that in the model-calculated field. Thus, the individual contributions to the diagnosed ascent will provide

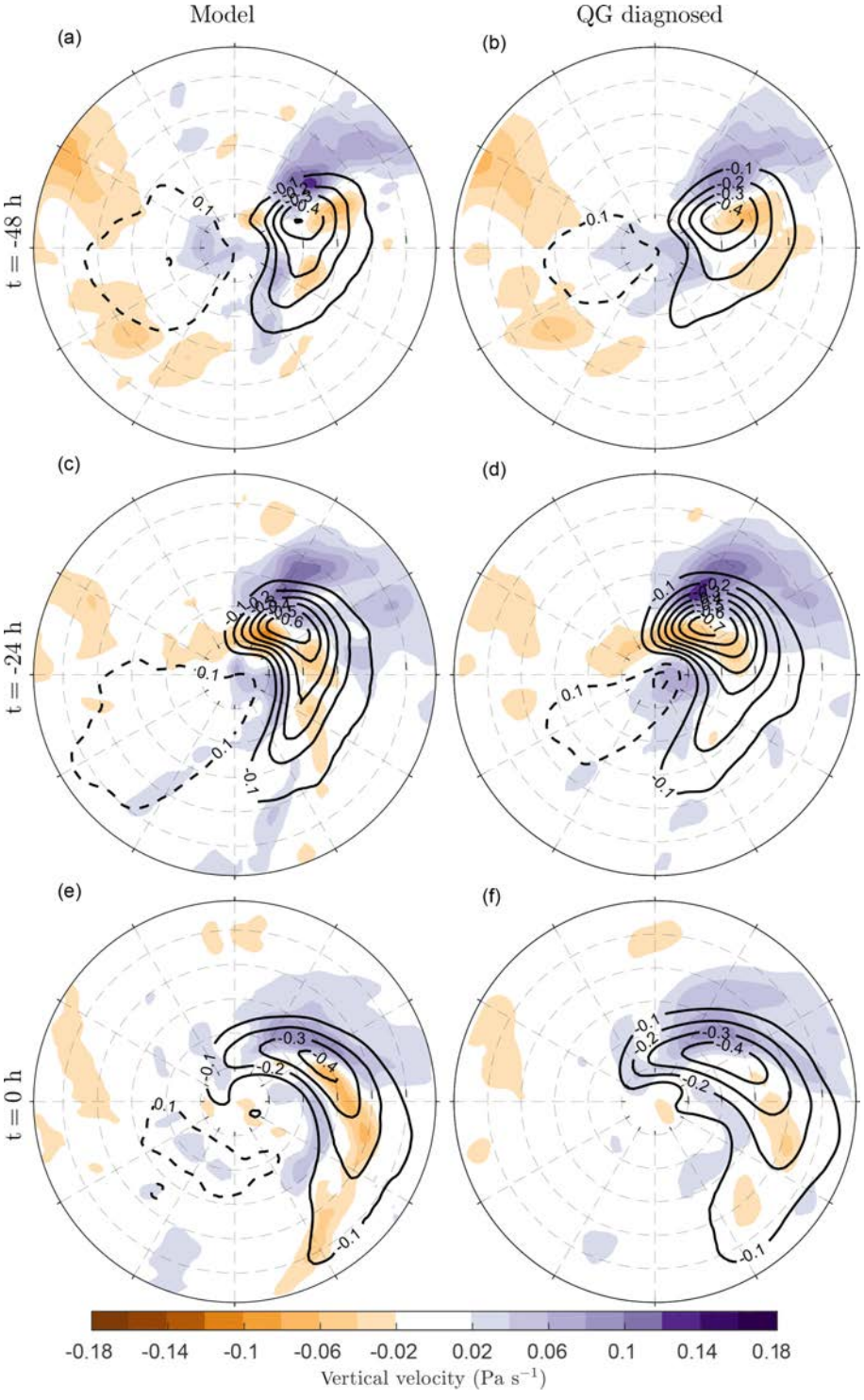

Figure 10. Composite mean and change in 700 hPa vertical velocity in pressure coordinates for **(a, c, e)** total model calculated vertical velocity and **(b, d, f)** vertical velocity calculated from the modified quasi-geostrophic omega equation (Eq. 1). Panels **(a)** and **(b)** are valid 48 h before the time of maximum intensity, panels **(c)** and **(d)** are valid 24 h before the time of maximum intensity, and panels **(e)** and **(f)** are valid at the time of maximum intensity. All composites are of the strongest 200 extra-tropical cyclones in each experiment.

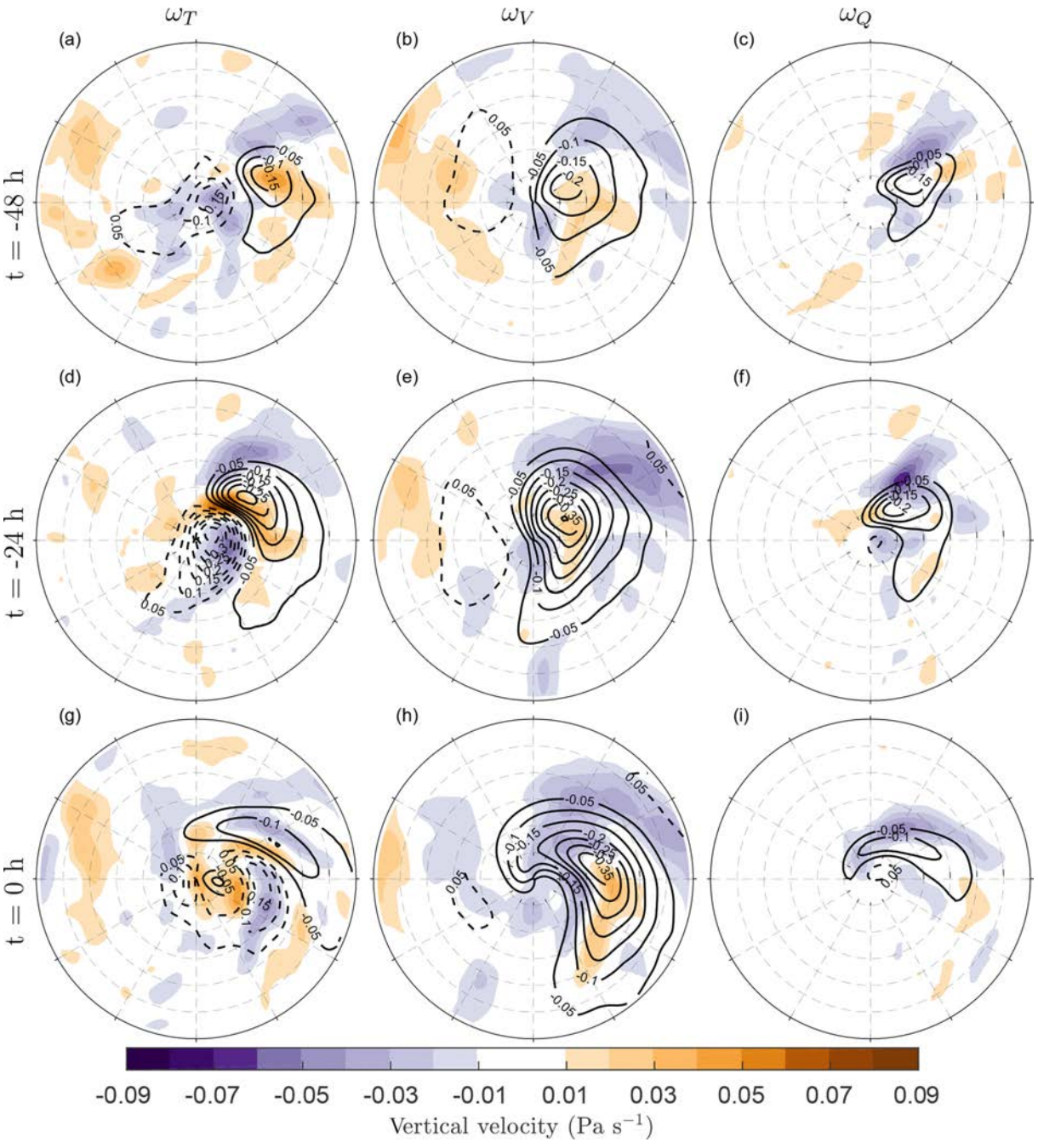

Figure 11. Composite mean and change in 700 hPa vertical velocity in pressure coordinates due to thermal advection (ω_T, **a, d, g**), due to vorticity advection (ω_V, **b, e, h**), and due to diabatic heating (ω_Q, **c, f, i**). Panels **(a)–(c)** are valid 48 h before the time of maximum intensity, panels **(d)–(f)** are valid 24 h before the time of maximum intensity, and panels **(g)–(i)** are valid at the time of maximum intensity. Contours show the control values and shading the difference (SST4 − CNTL). All composites are of the strongest 200 extra-tropical cyclones in each experiment.

reliable estimates of how different physical processes influence the total vertical motion.

Figure 11 shows the contribution to vertical velocity from thermal advection, vorticity advection, and diabatic heating at three offset times in the CNTL experiment. The maximum values of ascent attributed to the different forcing mechanisms in the composite mean cyclones are also shown in Table 2. In the CNTL composite cyclone thermal advection leads to ascent in the warm sector downstream of the cyclone centre and descent behind the cold front (Fig. 11a, d, and g).

Table 2. Maximum values of ascent ($\mathrm{Pa\,s^{-1}}$) at 700 hPa directly from the model (ω) and attributed to vorticity advection (ω_V), thermal advection (ω_T), and diabatic heating (ω_Q) in the CNTL composite mean and the SST4 composite mean at different offset times.

	CNTL				SST4			
Time (h)	ω	ω_V	ω_T	ω_Q	ω	ω_V	ω_T	ω_Q
−48	−0.5016	−0.2279	−0.1808	−0.195	−0.5238	−0.2162	−0.1423	−0.193
−24	−0.6722	−0.401	−0.3179	−0.2311	−0.6965	−0.3816	−0.3013	−0.2339
0	−0.4387	−0.3889	−0.1517	−0.1352	−0.4565	−0.3761	−0.1681	−0.1512
24	−0.1572	−0.1701	−0.0601	−0.0371	−0.1674	−0.1851	−0.054	−0.0358

Ascent and descent due to thermal advection reach a maximum 24 h before the time of maximum intensity (Table 2), and as the composite cyclone evolves in time the region of ascent wraps cyclonically around the poleward side of the cyclone centre. Vorticity advection (Fig. 11b, e, and h) leads to stronger ascent at all offset times compared to either thermal advection or diabatic heating in the CNTL composite cyclone (Fig. 11, Table 2). At all offset times the ascent attributed to vorticity advection covers a large area and is located downstream of the cyclone centre. As the cyclone evolves, the area of maximum ascent moves further away from the cyclone centre and a region of weak ascent wraps cyclonically around the cyclone centre. This cyclonic behaviour, indicative of life cycle 2 (LC2, Thorncroft et al., 1993) cyclone development, occurs as the cyclones are located on the poleward side of the jet at all offset times considered here. The contribution to vertical motion from the diabatic heating term is shown in Fig. 11c, f, and i. Ascent related to diabatic heating is constrained to a smaller area than ascent due to either vorticity or thermal advection and is located in the poleward parts of the warm conveyor belt. The maximum values of ascent related to diabatic heating at $t = -24$ h and the time of maximum intensity are also weaker than those due to either thermal advection or vorticity advection in both the CNTL and SST4 experiments (Table 2). This shows that at 700 hPa diabatic heating has a smaller impact on the cyclone's vertical motion than the dynamical terms.

The response of vertical motion due to the different forcing mechanisms to warming is also shown in Fig. 11 by the shading. At $t = -48$ h, ascent due to thermal advection weakens slightly with warming (orange shading co-located with the maximum ascent in CNTL in Fig. 11a and Table 2), and the descent associated with cold-air advection is also weaker in SST4 than in the CNTL. The ascent due to warm-air advection in the warm sector is slightly more poleward in SST4 compared to CNTL. At $t = -24$ h, the region of ascent due to thermal advection in SST4 has moved poleward and downstream relative to that in the CNTL. This is evident in Fig. 11d as the positive difference values (weaker ascent, orange shading) between the cyclone centre and the maximum ascent in the CNTL and as negative difference values (stronger ascent, purple shading) poleward of the maximum ascent in CNTL. This illustrates that at both $t = -48$ and $t = -24$ h the warm front is more poleward and extends further downstream away from the cyclone centre in SST4 compared to in CNTL. A similar but weaker pattern also remains at the time of maximum intensity (Fig. 11g).

The response of vertical motion due to vorticity advection at 700 hPa has a similar spatial pattern at all offset times considered but is most pronounced in magnitude at $t = -24$ h and at the time of maximum intensity. The most notable feature is that ascent due to vorticity advection in SST4 covers a greater area compared to in CNTL and that the ascent expands polewards and downstream of the cyclone centre. The second notable feature is that at 700 hPa the maximum ascent due to vorticity advection decreases with warming (Fig. 11b, e, and h and Table 2). This indicates that ascent due to positive vorticity advection downstream of the cyclone centre weakens in magnitude but becomes more spatially extensive.

To further understand the change in ascent due to vorticity advection, the 500 hPa geopotential height fields are considered. To compare the 500 hPa geopotential height in the SST4 and CNTL composite cyclones, first the composite cyclone mean (weighted by grid area) at each offset time was subtracted to generate maps of the cyclone relative 500 hPa geopotential height anomaly. This was necessary as in SST4 the 500 hPa heights are higher simply due to the warmer atmosphere, which makes a comparison of the shape and extent of the upper level trough difficult. Figure 12 shows the differences in these anomalies. At $t = -48$ h (Fig. 12a) the negative anomaly to the south of the cyclone centre indicates that the 500 hPa trough is slightly deeper in SST4 compared to in CNTL. Furthermore, the dipole of negative and positive anomalies downstream of the cyclone centre at $t = -48$ h indicates that the 500 hPa trough is sharper in SST4 compared to in CNTL. At $t = -24$ h (Fig. 12b) an asymmetric dipole pattern is evident, which has small positive values upstream and larger negative values downstream of the cyclone centre. This indicates that the 500 hPa trough is shifted downstream relative to the cyclone centre in SST4 compared to in CNTL but also that the trough is broader and extends more downstream in SST4 compared to CNTL. This pattern is also evident at $t = 0$ and $t = +24$ h. The broader upper-level trough in SST4 is thus the likely reason why ascent due to vorticity

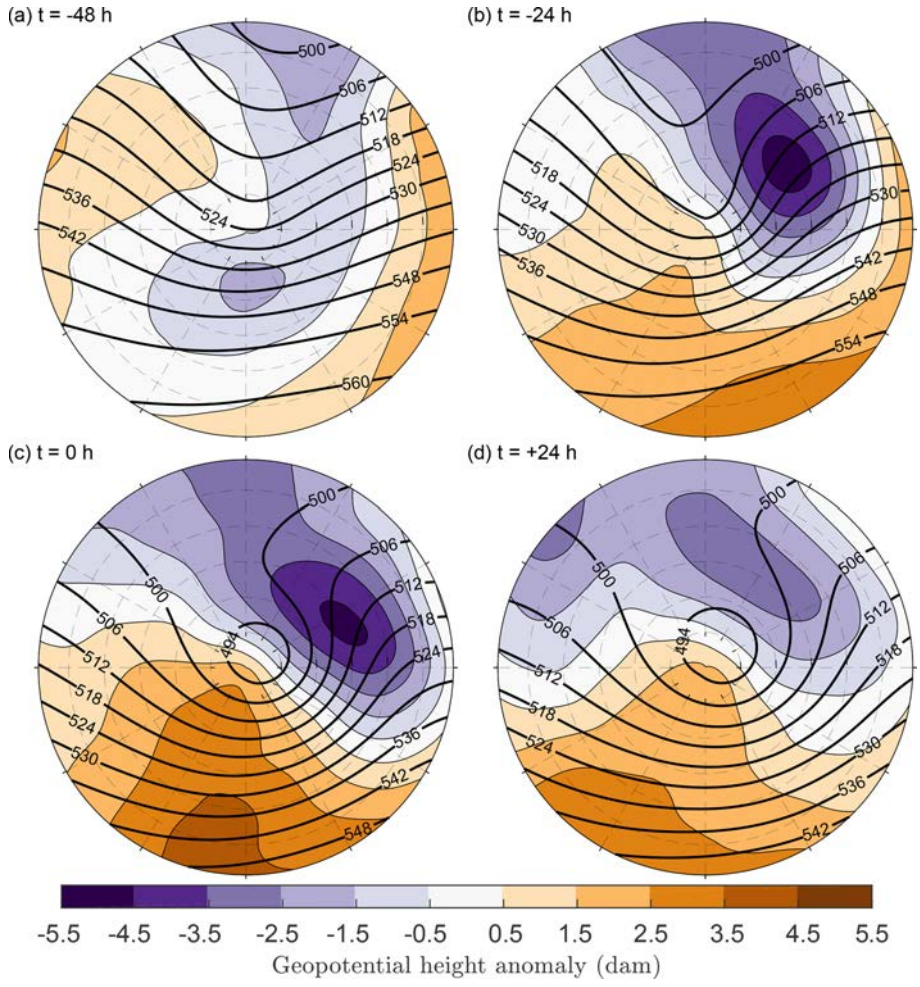

Figure 12. Composite mean of 500 hPa geopotential height (dam) in CNTL (black contours) and the difference (SST4 − CNTL) in the cyclone relative anomalies at **(a)** 48 h before time of maximum intensity, **(b)** 24 h before time of maximum intensity, **(c)** time of maximum intensity, and **(d)** 24 h after the time of maximum intensity.

advection expands over a greater area downstream in SST4 compared to CNTL.

Ascent attributed to diabatic heating has a larger relative increase with warming in the warm front region compared to both dynamical terms (Fig. 11). At all offset times, ascent due to diabatic heating increases poleward of the maximum in the CNTL composite, which combined with the absence of any decrease in ascent results in an expansion of the area where diabatic heating contributes notably to ascent. Furthermore, in contrast to both thermal advection and vorticity advection, there are no coherent regions where descent due to diabatic heating has increased.

The spatial patterns of changes in ascent due to the different forcing mechanisms (Fig. 11) can be compared to the patterns of change in the total model output vertical velocity (Fig. 10). It can therefore be concluded that the increase in ascent poleward and downstream of the cyclone centre occurs due to a combination of all three processes. However, thermal advection and diabatic heating are responsible for most of the increase in ascent close to the cyclone centre, whereas vorticity advection is the main cause of the downstream expansion of the ascent field. The decrease in total ascent near the cyclone centre is found to be due to changes in spatial pattern of thermal advection and the position of the fronts. In the SST4 experiment, the warm front advances further ahead of the cyclone centre than in the CNTL, which results in weaker ascent due to warm air advection close to the cyclone centre. However, the decrease in ascent in the warm sector is a direct result of weaker ascent due to vorticity advection in this location, which arises as a consequence of the broader 500 hPa trough. In contrast, the weaker descent immediately to the south of the cyclone centre is mainly due to weaker cold-air advection in SST4 compared to CNTL, which again relates to changing positions of the fronts. Finally, it should be noted that vertical velocities are likely to

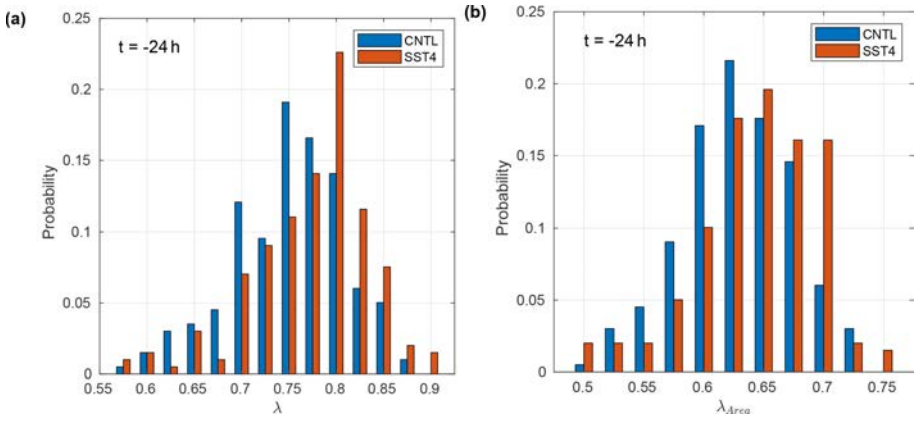

Figure 13. Normalized histograms of the **(a)** asymmetry parameter and **(b)** area asymmetry parameter (see text for more details) valid 24 h before the time of maximum intensity. Both histograms include values for the 200 strongest extra-tropical cyclones in both experiments. Blue shades show CNTL and red SST4.

be weaker for the same forcing in the warmer experiment due to an increase in tropospheric static stability (e.g. Fig. 3c).

7 Asymmetry of vertical motion

Ascent is stronger and occupies a smaller and narrower region than descent, both in the context of extra-tropical cyclones and globally. O'Gorman (2011) proposed two parameters, λ and λ_{Area}, to quantify the asymmetry between upward and downward motions. The asymmetry parameter, λ, is given by

$$\lambda \equiv \frac{\overline{\omega'\omega'^{\uparrow}}}{\overline{\omega'^2}}, \tag{4}$$

where in our study we define ω' to be the perturbation from the mean vertical velocity (Pa s^{-1}) calculated over the 12° cyclone composite area. $\omega^{\uparrow}$ denotes taking the upward part of ω (i.e. applying a Heaviside function). The overbar denotes an average over the cyclone area. λ_{Area} is an alternative (and more approximate) definition of asymmetry, which is based on geometric considerations. λ_{Area} is given by

$$\lambda_{\text{Area}} = \frac{1 - a_u}{1 - \overline{\omega}/\overline{\omega_u}}, \tag{5}$$

where a_u is the fraction of the total area (in this case the 12° cyclone composite area) which is covered by ascent, $\overline{\omega_u}$ is the spatial average over the cyclone area of the ascent, and $\overline{\omega}$ is the spatial average of all vertical motions.

λ and λ_{Area} are both calculated for each of the 200 individual extra-tropical cyclones in both the CNTL and SST4 experiments at different offset times. Only vertical motions at one pressure level, 700 hPa, are considered. Figure 13 shows the distribution of both asymmetry parameters at $t = -24$ h, which reveals that there is considerable spread across the 200 strongest extra-tropical cyclones, particularly in λ, with values ranging from 0.55 to 0.9 in both experiments. However, it is also evident that there are larger values of both λ and λ_{Area} in SST4 compared to in CNTL. The mean values for both parameters are shown in Table 3. At $t = -24$, $t = 0$, and $t = +24$ h, both λ and λ_{Area} are statistically significantly larger in SST4 compared to in CNTL; however the increases are small in magnitude. The fractional area of ascent (a_u) is less than 0.5 at all offset times in both CNTL and SST4 (Table 3), indicating that regions of ascent are smaller relative to areas of descent. Warming does not cause large changes to the fractional area of ascent; a statistically significant decrease occurs at $t = 0$ h, a statistically significant increase occurs at $t = +48$ h, and no significant changes occur at $t = -48$, -24, or $+24$ h. Thus the small changes in both asymmetry parameters occur due to changes in the ratio of mean descent to mean ascent. Small increases in the maximum ascent (minimum ω, Table 2) are found and the mean vertical motion averaged over the 12° cyclone area also becomes more negative in SST4 (Table 3), indicating either stronger ascent or weaker descent. The mean ascent, calculated over areas where $\omega < 0$ in the 12° cyclone area, strengthens slightly at $t = -24$, $t = 0$, and $t = +24$ h (Table 3) while the mean descent, averaged over areas where $\omega > 0$ in the 12° cyclone area, weakens slightly at all offset times. The magnitude of ratio between the mean upward velocity and mean downward velocity (i.e. $|\overline{\omega_u}/\overline{\omega_d}|$) increases at all times, as does the ratio between the mean vertical motion and mean upward velocity (i.e. $|\overline{\omega}/\overline{\omega_u}|$), such that λ increases with warming.

The magnitude of the mean increase in both λ and λ_{Area} is small; for example, at the time of maximum intensity λ increases from 0.74 in CNTL to 0.77 in SST4, and λ_{Area} increases from 0.64 in CNTL to 0.66 in SST4 (Table 3). This result differs slightly from the results of O'Gorman (2011), who, in idealized climate change simulations performed on an aqua planet, found that λ has a value of ~ 0.6 and that

Table 3. Mean values of λ, λ_{Area} (see text for definitions), fractional area of ascent (a_u), mean vertical motion ($\overline{\omega}$), mean ascent ($\overline{\omega_u}$), and mean descent ($\overline{\omega_\mathrm{d}}$) at 700 hPa averaged over the strongest 200 extra-tropical cyclones in CNTL and in SST4 at different offset times.

	CNTL						SST4					
Time (h)	λ_{Area}	λ	a_u	$\overline{\omega}$	$\overline{\omega_u}$	$\overline{\omega_\mathrm{d}}$	λ_{Area}	λ	a_u	$\overline{\omega}$	$\overline{\omega_u}$	$\overline{\omega_\mathrm{d}}$
−48	0.60	0.70	0.30	0.0011	−0.1618	0.1083	0.59	0.70	0.30	0.0006	−0.1578	0.1065
−24	0.63	0.75	0.41	−0.0137	−0.1922	0.1135	0.64	0.77	0.40	−0.0178	−0.1974	0.1091
0	0.64	0.74	0.43	−0.0183	−0.1801	0.1021	0.66	0.77	0.42	−0.0220	−0.1890	0.0966
24	0.60	0.69	0.45	−0.0116	−0.1322	0.0867	0.62	0.73	0.47	−0.0162	−0.1329	0.0805
48	0.59	0.69	0.41	−0.0066	−0.1142	0.0777	0.60	0.71	0.42	−0.0091	−0.1053	0.0703

it does not increase when the global mean surface temperature increases. Tamarin-Brodsky and Hadas (2019), however, find a small increase in λ with warming and no changes to the fractional area of ascent (a_u), which is in agreement with what we find here. Previously Booth et al. (2015) calculated λ, λ_{Area}, and a_u in dry and moist baroclinic life cycle experiments and find that including moisture increases λ from 0.58 to 0.74, increases λ_{Area} from 0.55 to 0.64, and decreases a_u from 0.45 to 0.40. These changes are much more pronounced than those found in this study likely due to the relative difference in the two sets of experiments, e.g. a dry versus moist case compared to a moist case vs. a moist case with 4 K warming.

8 Conclusions

Aqua-planet simulations were performed with a state-of-the-art, full-complexity atmospheric model (OpenIFS) to quantify how the number, characteristics, and structure of extra-tropical cyclones respond to horizontally uniform warming and to identify possible physical reasons for such changes. This simplified climate change experimental method was selected because it provides a very large sample size of cyclones for drawing statistically significant conclusions from and because the initial conditions and experimental design do not exert a strong control on the evolution of the model state.

The aqua-planet model set-up is capable of producing a zonal mean climate that is broadly similar to that observed on Earth. The response of the zonal mean temperature and zonal mean zonal wind to warming is in broad agreement with multi-model mean predictions from CMIP5 models. Namely, the greatest warming is observed in the tropical upper troposphere, the subtropical jet streams intensify, move upwards and polewards with warming, and the eddy-driven jet and mid-latitude storm track moves polewards with warming. The magnitude of the near-surface warming in the aqua-planet SST4 simulation compared to CNTL is approximately 4 K, which is within the CMIP5 multi-model range predicted to occur by 2100 under the RCP8.5 scenario.

Extra-tropical cyclones were tracked using an objective tracking algorithm which identifies localized maxima of 850 hPa relative vorticity truncated to T42 spectral resolution. In both the control (CNTL) and warm (SST4) experiment about 3500 cyclone tracks were identified. Warming the SSTs did not change the cyclone lifetime and led to a 3.3 % decrease in the total number of extra-tropical cyclones. Moreover, the median intensity of cyclones, as measured by the maximum 850 hPa vorticity, does not change significantly when SSTs are warmed uniformly; however, the intensity distribution of extra-tropical cyclones broadens, resulting in more intense and more weaker cyclones. The median deepening rate of all extra-tropical cyclones did not change significantly with warming although the zonal mean Eady growth decreased by 5 %–10 % due to an increase in the hydrostatic stability. This apparent conflict arises as moisture acts to intensify the extra-tropical cyclones in these simulations whereas the Eady growth rate is a measure of dry baroclinicity. In addition, both extra-tropical cyclone genesis and lysis regions move poleward with warming, which is consistent with the poleward shift of the eddy-driven jet.

These results can be compared to those from previous idealized studies as well as to results obtained from full-complexity climate models. Our result that the maximum relative vorticity of the most extreme cyclones increases with warming is in agreement with results from previous aqua-planet simulations (Pfahl et al., 2015). When our results of extra-tropical cyclone intensity are compared to results based on coupled climate models, a complex picture emerges. Our result that the number of extreme cyclones increases with warming agrees with the results from Champion et al. (2011) and the Southern Hemisphere results of Chang et al. (2012) yet disagrees with the results from Bengtsson et al. (2009) and Catto et al. (2011), who both found that the number of intense storms in Europe and the North Atlantic is likely to decrease in the future.

Cyclone composites of the 200 strongest extra-tropical cyclones were created for both the CNTL and the SST4 experiments. The structure of both composite cyclones is qualitatively and even quantitatively very similar to composite cyclones created from reanalysis (Dacre et al., 2012) and historical climate model simulations (Catto et al., 2010). This

strongly highlights the validity and usefulness of aqua-planet simulations. The aim of our composite analysis was to identify how the structure of the most intense extra-tropical cyclones responds to warming. The main focus was on how precipitation and vertical motion respond to warming, and the omega equation was utilized to assess changes to vertical motion forced by thermal and vorticity advection and attributable to diabatic heating. The main results of how the structure of the 200 most intense extra-tropical cyclones change with warming include the following.

1. The total column water vapour (TCWV) increases everywhere within a 12° radius of the cyclone centre, and the meridional TCWV gradient increases. The largest absolute increases in TCWV occur in the warm sector, whereas the largest relative increases occur poleward of the warm front.

2. The 900–700 hPa layer average potential vorticity increases at all stages of the cyclone evolution everywhere within a 12° radius of the cyclone centre. The small absolute increases away from the cyclone centre result from increasing stratification.

3. The 900 hPa wind speed increases in particular in the warm sector and thus the size of the area exposed to wind speeds above a certain fixed threshold increases.

4. The low-level potential vorticity, total and large-scale precipitation, and ascent at 700 hPa ahead of the warm front increase at all times of the cyclone life cycle, which occurs due to an increase in ascent forced by thermal advection and an increase in how diabatic processes enhance ascent.

5. The area of ascent downstream of the cyclone centre expands due to increased ascent forced by vorticity advection. This is related to a downstream shift and broadening of the 500 hPa trough.

6. The maximum values of ascent at 700 hPa decrease slightly due to vorticity and thermal advection during the cyclone intensification phase, and the maximum value of ascent increases slightly due to diabatic heating.

7. The asymmetry of vertical motion (λ and λ_{Area}) increases slightly with warming, and the fractional area of ascent does not notably change. The small increases in asymmetry arise as the absolute magnitude of the increase in ascent is greater than the absolute decrease in the magnitude of the descent.

First, these results show that ascent becomes slightly more diabatically driven in the warmer experiment compared to the CNTL experiment and that cyclone-related precipitation increases by up to 50 % – a value much larger than predicted for global precipitation amounts. Second, these results indicate that the spatial structure of the most intense extra-tropical cyclones does change with warming. The localized maxima of low-level PV, 900 hPa wind speed, maximum precipitation, and vertical velocity associated with the warm front all move northeast relative to the centre of the cyclone. This demonstrates that in the warmer experiment the warm front is farther poleward and downstream of the cyclone centre than in CNTL. Furthermore, the area of ascent also increased with warming, particularly in the downstream region due to changes in ascent forced by vorticity advection and ultimately a broader trough at 500 hPa in SST4 compared to in the CNTL experiment.

The cyclone composite analysis revealed that precipitation increased everywhere relative to the cyclone centre with warming. The same result was obtained by Yettella and Kay (2017), who analysed a 30-member initial condition climate model ensemble. Furthermore, Yettella and Kay (2017) find that precipitation in a cyclone composite of Northern Hemisphere wintertime extra-tropical cyclones increases from maximum values of ∼9 mm per day to 11 mm d^{-1} in the far-future (2081–2100) simulations forced with RCP8.5. The relative increase is thus smaller than that found in our aqua-planet simulations, which is likely due to the fact that in the real world evaporation over land is limited, whereas there is always a limitless source of moisture at the surface in an aqua planet.

The most striking similarity found between our results and previous studies is the downstream shift in the low-level vorticity anomaly and precipitation relative to the cyclone centre. Kirshbaum et al. (2018) and Tierney et al. (2018) both find very similar results of how extra-tropical cyclone structure responds to warming in their baroclinic life cycle experiments. Kirshbaum et al. (2018) show that with increasing environmental temperature the cyclonic potential vorticity associated with the warm front strengthened and moved downstream, while Tierney et al. (2018) show that in warmer simulations the upper-level PV anomaly is much farther west relative to the low-level PV anomaly than in colder and drier simulations. Thus, this spatial change appears to be a robust feature of how extra-tropical cyclones respond to warming. We thus speculate that in a warmer climate the classical coupling and mutual intensification of lower- and upper-level anomalies may be disrupted and that extra-tropical cyclone dynamics and associated weather may be notably different.

This study prioritized in-depth understanding of changes to the dynamics and structure of extra-tropical cyclones with warming, rather than quantifying extra-tropical cyclone structure in specific future climate scenarios. Thus, the simulations included numerous simplifications, and consequently there are some caveats to this study. First, the aqua-planet simulations contain no polar amplification, and thus the low-level temperature gradient does not change with warming. Chang et al. (2012) show that CMIP5 models predict a sig-

nificant increase in the frequency of extreme cyclones during the winter in the Southern Hemisphere, a result which is in general agreement with our aqua-planet results. This means that (1) our results may be more applicable to the Southern Hemisphere and (2) our results, together with further additional simulations, could be used to ascertain the impact of polar amplification on extra-tropical cyclone intensity. Second, as there is no land in our simulations, the potential impact of differential changes in land–sea temperatures on extra-tropical cyclone dynamics is not considered, meaning that our results are likely more applicable to oceanic extra-tropical cyclones. Third, we applied uniform SST warming, which neglects localized oceanic cooling that occurs in the northern North Atlantic and parts of the high-latitude Southern Ocean in several CMIP5 models (Fig. 12.9, Collins et al., 2013). Fourth, the simulations were performed at a resolution more typical of a climate model (125 km) than of a numerical weather prediction model, meaning that in both the CNTL and SST4 experiments extra-tropical cyclones may be weaker and precipitation areas broader than if the simulations had been conducted at higher resolution. Nevertheless it appears unlikely that repeating the experiments at higher resolution would fundamentally change the main conclusions as Jung et al. (2012) find that increasing the resolution of the IFS from T159 to T1279 only increases the amount of precipitation by 6 % and does not alter the ratio of convective to large-scale precipitation. Lastly, cyclone composites were created from the strongest 200 storms and clearly the results would differ if we considered a larger or smaller number.

We conclude by noting that the results obtained here can be used as a stepping stone to better understand predictions from coupled climate models of how the structure of extra-tropical cyclones is likely to change in the future. A logical next step would be to analyse climate model projections for evidence of the downstream shift relative to the cyclone centre of increased low-level potential vorticity, vertical velocity, and precipitation.

Code availability. OpenIFS is available under license from the European Centre for Medium-Range Weather Forecasts (ECMWF). See https://confluence.ecmwf.int/display/OIFS (ECMWF, 2015) for more details. Information on how to obtain the cyclone identification and tracking algorithm (TRACK) can be found from http://www.nerc-essc.ac.uk/~kih/TRACK/Track.html. The version of the omega equation code applied here is available from Mika Rantanen on request.

Supplement. The supplement related to this article is available online at: https://doi.org/10.5194/wcd-1-1-2020-supplement.

Author contributions. VAS designed and performed the numerical experiments, analysed the data, and wrote the paper. MR performed the omega equation calculations. PH performed the cyclone tracking and ran the cyclone composite code. JR and HJ provided guidance on interpreting the results. All authors commented on the paper.

Competing interests. The authors declare that they have no conflict of interest.

Acknowledgements. We acknowledge ECMWF for making the OpenIFS model available and CSC – IT Center for Science Ltd. for the allocation of computational resources. We thank Glenn Carver, Filip Vánˆa, and Gabriela Szépszó for assistance with OpenIFS and for creating the initial conditions for the simulations. We also thank Kevin Hodges for providing the cyclone tracking code, TRACK, and Helen Dacre for providing the cyclone composite code.

Financial support. This research has been supported by the Academy of Finland (grant no. 307331).

Review statement. This paper was edited by Sebastian Schemm and reviewed by two anonymous referees.

References

Bengtsson, L., Hodges, K. I., and Keenlyside, N.: Will extratropical storms intensify in a warmer climate?, J. Climate, 22, 2276–2301, 2009.

Binder, H., Boettcher, M., Joos, H., and Wernli, H.: The role of warm conveyor belts for the intensification of extratropical cyclones in Northern Hemisphere winter, J. Atmos. Sci., 73, 3997–4020, 2016.

Bjerknes, J.: On the structure of moving cyclones, Mon. Weather Rev., 47, 95–99, 1919.

Booth, J. F., Wang, S., and Polvani, L.: Midlatitude storms in a moister world: Lessons from idealized baroclinic life cycle experiments, Clim. Dynam., 41, 787–802, 2013.

Booth, J. F., Polvani, L., O'Gorman, P. A., and Wang, S.: Effective stability in a moist baroclinic wave, Atmos. Sci. Lett., 16, 56–62, 2015.

Boutle, I. A., Belcher, S. E., and Plant, R. S.: Moisture transport in midlatitude cyclones, Q. J. Roy. Meteorol. Soc., 137, 360–373, 2011.

Browning, K. A., Hardman, M. E., Harrold, T. W., and Pardoe, C. W.: The structure of rainbands within a mid-latitude depression, Q. J. Roy. Meteorol. Soc., 99, 215–231, 1973.

Carlson, T. N.: Airflow through midlatitude cyclones and the comma cloud pattern, Mon. Weather Rev., 108, 1498–1509, 1980.

Catto, J. L., Shaffrey, L. C., and Hodges, K. I.: Can climate models capture the structure of extratropical cyclones?, J. Climate, 23, 1621–1635, 2010.

Catto, J. L., Shaffrey, L. C., and Hodges, K. I.: Northern Hemisphere extratropical cyclones in a warming climate in the

HiGEM high-resolution climate model, J. Climate, 24, 5336–5352, 2011.

Champion, A. J., Hodges, K. I., Bengtsson, L. O., Keenlyside, N. S., and Esch, M.: Impact of increasing resolution and a warmer climate on extreme weather from Northern Hemisphere extratropical cyclones, Tellus A, 63, 893–906, 2011.

Chang, E. K., Guo, Y., and Xia, X.: CMIP5 multimodel ensemble projection of storm track change under global warming, J. Geophys. Res., 117, D23118, https://doi.org/10.1029/2012JD018578, 2012.

Collins, M., Knutti, R., Arblaster, J., Dufresne, J.-L., Fichefet, T., Friedlingstein, P., Gao, X., Gutowski, W. J., Johns, T., Krinner, G., Shongwe, M., Tebaldi, C., Weaver, A. J., and Wehner, M.: Long-term Climate Change: Projections, Commitments and Irreversibility, in: Climate Change 2013: The Physical Science Basis, Contribution of Working Group I to the Fifth Assessment Report of the Intergovernmental Panel on Climate Change, chap. 12, edited by: Stocker, T. F., Qin, D., Plattner, G.-K., Tignor, M., Allen, S. K., Boschung, J., Nauels, A., Xia, Y., Bex, V., and Midgley, P. M., Cambridge University Press, Cambridge, UK and New York, NY, USA, 1029–1136, https://doi.org/10.1017/CBO9781107415324.024, 2013.

Dacre, H. F., Hawcroft, M. K., Stringer, M. A., and Hodges, K. I.: An extratropical cyclone atlas: A tool for illustrating cyclone structure and evolution characteristics, B. Am. Meteorol. Soc., 93, 1497–1502, 2012.

Eckhardt, S., Stohl, A., Wernli, H., James, P., Forster, C., and Spichtinger, N.: A 15-year climatology of warm conveyor belts, J. Climate, 17, 218–237, 2004.

ECMWF: Part IV: Physical Processes, in: chap. 4, IFS Documentation, operational implementation 12 May 2015, ECMWF, Reading, UK, 1–190, 2015.

Field, P. R. and Wood, R.: Precipitation and cloud structure in midlatitude cyclones, J. Climate, 20, 233–254, 2007.

Fink, A. H., Brücher, T., Ermert, V., Krüger, A., and Pinto, J. G.: The European storm Kyrill in January 2007: synoptic evolution, meteorological impacts and some considerations with respect to climate change, Nat. Hazards Earth Syst. Sci., 9, 405–423, https://doi.org/10.5194/nhess-9-405-2009, 2009.

Govekar, P. D., Jakob, C., and Catto, J.: The relationship between clouds and dynamics in Southern Hemisphere extratropical cyclones in the real world and a climate model, J. Geophys. Res., 119, 6609–6628, 2014.

Harrold, T. W.: Mechanisms influencing the distribution of precipitation within baroclinic disturbances, Q. J. Roy. Meteorol. Soc., 99, 232–251, 1973.

Hawcroft, M. K., Shaffrey, L. C., Hodges, K. I., and Dacre, H. F.: How much Northern Hemisphere precipitation is associated with extratropical cyclones?, Geophys. Res. Lett., 39, L24809, https://doi.org/10.1029/2012GL053866, 2012.

Hodges, K. I.: A general method for tracking analysis and its application to meteorological data, Mon. Weather Rev., 122, 2573–2586, 1994.

Hodges, K. I.: Feature tracking on the unit sphere, Mon. Weather Rev., 123, 3458–3465, 1995.

Holton, J. R. and Hakim, G. J.: An introduction to dynamic meteorology, in: vol. 88, Academic Press, Oxford, UK, 2012.

Hoskins, B. J. and Hodges, K. I.: New perspectives on the Northern Hemisphere winter storm tracks, J. Atmos. Sci., 59, 1041–1061, 2002.

Hoskins, B. J., McIntyre, M., and Robertson, A. W.: On the use and significance of isentropic potential vorticity maps, Q. J. Roy. Meteorol. Soc., 111, 877–946, 1985.

Jung, T., Miller, M. J., Palmer, T. N., Towers, P., Wedi, N., Achuthavarier, D., Adams, J. M., Altshuler, E. L., Cash, B. A., Kinter III, J. L., Marx, L., Stan, C., and Hodges, K. I.: High-resolution global climate simulations with the ECMWF model in Project Athena: Experimental design, model climate, and seasonal forecast skill, J. Climate, 25, 3155–3172, 2012.

Kirshbaum, D., Merlis, T., Gyakum, J., and McTaggart-Cowan, R.: Sensitivity of idealized moist baroclinic waves to environmental temperature and moisture content, J. Atmos. Sci., 75, 337–360, 2018.

Lau, W. K.-M., Wu, H.-T., and Kim, K.-M.: A canonical response of precipitation characteristics to global warming from CMIP5 models, Geophys. Res. Lett., 40, 3163–3169, 2013.

Michaelis, A. C., Willison, J., Lackmann, G. M., and Robinson, W. A.: Changes in Winter North Atlantic Extratropical Cyclones in High-Resolution Regional Pseudo – Global Warming Simulations, J. Climate, 30, 6905–6925, 2017.

Naud, C. M., Del Genio, A. D., Bauer, M., and Kovari, W.: Cloud vertical distribution across warm and cold fronts in CloudSat–CALIPSO data and a general circulation model, J. Climate, 23, 3397–3415, 2010.

Naud, C. M., Booth, J. F., Lebsock, M., and Grecu, M.: Observational constraint for precipitation in extratropical cyclones: Sensitivity to data sources, J. Appl. Meteorol. Clim., 57, 991–1009, 2018.

Neale, R. B. and Hoskins, B. J.: A standard test for AGCMs including their physical parametrizations: I: The proposal, Atmos. Sci. Lett., 1, 101–107, 2000.

Neu, U., Akperov, M. G., Bellenbaum, N., Benestad, R., Blender, R., Caballero, R., Cocozza, A., Dacre, H. F., Feng, Y., Fraedrich, K., Grieger, J., Gulev, S., Hanley, J., Hewson, T., Inatsu, M., Keay, K., Kew, S. F., Kindem, I., Leckebusch, G. C., Liberato, M. L. R., Lionell, P., Mokhov, I. I., Pinto, J. G., Raible, C. C., Reale, M., Rudevaia, I., Schuster, M., Simmonds, I., Sinclair, M., Sprenger, M., Tilinina, N. D., Trigo, I. F., Ulbrich, S., Ulbrich, U., Wang, X. L., and Wernli, H.: IMILAST: A community effort to intercompare extratropical cyclone detection and tracking algorithms, B. Am. Meteorol. Soc., 94, 529–547, 2013.

O'Gorman, P. A.: The effective static stability experienced by eddies in a moist atmosphere, J. Atmos. Sci., 68, 75–90, 2011.

Pfahl, S., O'Gorman, P. A., and Singh, M. S.: Extratropical cyclones in idealized simulations of changed climates, J. Climate, 28, 9373–9392, 2015.

Räisänen, J.: Factors affecting synoptic-scale vertical motions: A statistical study using a generalized omega equation, Mon. Weather Rev., 123, 2447–2460, 1995.

Rantanen, M., Räisänen, J., Lento, J., Stepanyuk, O., Räty, O., Sinclair, V. A., and Järvinen, H.: OZO v.1.0: software for solving a generalised omega equation and the Zwack–Okossi height tendency equation using WRF model output, Geosci. Model Dev., 10, 827–841, https://doi.org/10.5194/gmd-10-827-2017, 2017.

Rantanen, M., Räisänen, J., Sinclair, V. A., and Järvinen, H.: Sensitivity of idealised baroclinic waves to mean atmospheric temper-

ature and meridional temperature gradient changes, Clim. Dynam., 52, 2703–2719, 2019.

Schemm, S. and Wernli, H.: The linkage between the warm and the cold conveyor belts in an idealized extratropical cyclone, J. Atmos. Sci., 71, 1443–1459, 2014.

Schemm, S., Wernli, H., and Papritz, L.: Warm conveyor belts in idealized moist baroclinic wave simulations, J. Atmos. Sci., 70, 627–652, 2013.

Schultz, D. M., Bosart, L. F., Colle, B. A., Davies, H. C., Dearden, C., Keyser, D., Martius, O., Roebber, P. J., Steenburgh, W. J., Volkert, H., and Winters, A. C.: Extratropical Cyclones: A Century of Research on Meteorology's Centerpiece, Meteorol. Monogr., 59, 16.1–16.56, 2019.

Shapiro, M. A. and Keyser, D.: Fronts, jet streams and the tropopause., in: Extratropical Cyclones, The Erik Palmén Memorial Volume, Amer. Meteor. Soc., Boston, USA, 167–191, 1990.

Shepherd, T. G.: Atmospheric circulation as a source of uncertainty in climate change projections, Nat. Geosci., 7, 703–708, https://doi.org/10.1038/ngeo2253, 2014.

Simmonds, I. and Keay, K.: Mean Southern Hemisphere extratropical cyclone behavior in the 40-year NCEP–NCAR reanalysis, J. Climate, 13, 873–885, 2000.

Simmons, A. J. and Hoskins, B. J.: The life cycles of some nonlinear baroclinic waves, J. Atmos. Sci., 35, 414–432, 1978.

Sinclair, V. A. and Keyser, D.: Force balances and dynamical regimes of numerically simulated cold fronts within the boundary layer, Q. J. Roy. Meteorol. Soc., 141, 2148–2164, 2015.

Stoelinga, M. T.: A potential vorticity-based study of the role of diabatic heating and friction in a numerically simulated baroclinic cyclone, Mon. Weather Rev., 124, 849–874, 1996.

Tamarin-Brodsky, T. and Hadas, O.: The asymmetry of vertical velocity in current and future climate, Geophys. Res. Lett., 46, 374–382, 2019.

Thorncroft, C., Hoskins, B., and McIntyre, M.: Two paradigms of baroclinic-wave life-cycle behaviour, Q. J. Roy. Meteorol. Soc., 119, 17–55, 1993.

Tierney, G., Posselt, D. J., and Booth, J. F.: An examination of extratropical cyclone response to changes in baroclinicity and temperature in an idealized environment, Clim. Dynam., 51, 3829, https://doi.org/10.1007/s00382-018-4115-5, 2018.

Wernli, H. and Davies, H. C.: A Lagrangian-based analysis of extratropical cyclones. I: The method and some applications, Q. J. Roy. Meteorol. Soc., 123, 467–489, 1997.

Wernli, H. and Schwierz, C.: Surface cyclones in the ERA-40 dataset (1958–2001). Part I: Novel identification method and global climatology, J. Atmos. Sci., 63, 2486–2507, 2006.

Yettella, V. and Kay, J. E.: How will precipitation change in extratropical cyclones as the planet warms? Insights from a large initial condition climate model ensemble, Clim. Dynam., 49, 1765–1781, 2017.

Zappa, G., Shaffrey, L. C., and Hodges, K. I.: The ability of CMIP5 models to simulate North Atlantic extratropical cyclones, J. Climate, 26, 5379–5396, 2013a.

Zappa, G., Shaffrey, L. C., Hodges, K. I., Sansom, P. G., and Stephenson, D. B.: A multimodel assessment of future projections of North Atlantic and European extratropical cyclones in the CMIP5 climate models, J. Climate, 26, 5846–5862, 2013b.

ILMATIETEEN LAITOS
METEOROLOGISKA INSTITUTET
FINNISH METEOROLOGICAL INSTITUTE

FINNISH METEOROLOGICAL INSTITUTE
Erik Palménin aukio 1
P.O. Box 503
FI-00560 HELSINKI
tel. +358 29 539 1000
WWW.FMI.FI

FINNISH METEOROLOGICAL INSTITUTE
CONTRIBUTIONS No. 165
ISSN 0782-6117
ISBN 978-952-336-105-8 (paperback)
ISBN 978-952-336-106-5 (pdf)
https://doi.org/10.35614/isbn.9789523361065

Helsinki, 2020
Edita Prima Oy